THE UNIVERSITY OF TULSA
THE GRADUATE SCHOOL

ANALYSIS OF SLUG AND DRILLSTEM TESTS

by
Alvaro Marcello Marco Peres

A dissertation submitted in partial fulfillment of
the requirements for the degree of Doctor of Philosophy
in the Discipline of Petroleum Engineering
The Graduate School
The University of Tulsa
1989

THE UNIVERSITY OF TULSA
THE GRADUATE SCHOOL

ANALYSIS OF SLUG AND DRILLSTEM TESTS

A DISSERTATION
APPROVED FOR THE DISCIPLINE OF
PETROLEUM ENGINEERING

By Dissertation Committee

Albert C. Reynolds Jr., Chairperson

James Matthews Chase

Ram S. Agarwal

ABSTRACT

Peres, Alvaro Marcello Marco (Doctor of Philosophy in Petroleum Engineering)
Analysis of Slug and Drillstem Tests (235 pp. - Chapter V)
Directed by Dr. Albert C. Reynolds, Jr.

(349 words)

This work presents new procedures for the analysis of slug and drillstem tests. The proposed methods account for the flow rate variation, however, no direct measurement of the sandface rate or its determination from the liquid recovery are needed.

A new general method for determining the formation flow capacity and the skin factor from slug test data is presented. It is shown that the slug test response can be converted to the response for an equivalent constant surface rate, wellbore storage and skin problem. The equivalent constant rate pressure data is obtained by integrating the measured slug test pressure over producing time, whereas, multiplication of the slug test pressure data by the producing time yields the equivalent constant surface rate pressure derivative data. After the constant surface rate pressure data and its derivative are generated by our procedure, the converted data can be analyzed by using existent wellbore storage and skin type curves for the particular reservoir model represented by the data. Therefore, slug test type curves are no longer needed. It is also shown that the well known rate normalization procedure and the traditional superposition method can also be applied to the converted pressure data to greatly improve the reliability of the analysis.

Two new straight-line methods for analyzing pressure buildup data obtained from drillstem tests are presented. The new methods apply for cases where the produced fluid does not reach the surface during the flowing period. From the slope

of the straight line obtained by either method, it is shown that the flow capacity, the skin factor and the initial reservoir pressure can be determined. If the beginning of the straight-line is delayed by wellbore storage and skin effects, it is shown that a multi-rate equivalent time can be constructed so that standard type-curve matching can be performed to obtain estimates of the flow capacity and the skin factor.

New deconvolution schemes for the analysis of slug and drillstem test pressure data are also proposed. The new algorithms do not require the measurement or direct computation of the sandface flow rate during the flow and buildup periods.

ACKNOWLEDGEMENTS

I wish to thank Dr. Albert C. Reynolds Jr. for the continuous assistance, guidance and encouragement I have received throughout my graduate studies. The comments and suggestions of the Dissertation Committee members, Dr. R. Agarwal, Dr. L. Macias-Chapa, Dr. R. Cerro and Dr. L. Thompson are gratefully acknowledged.

I would like to extend my appreciation to the management of Petrobras - Petróleo Brasileiro for providing financial support. Also, I am grateful to the Petroleum Engineering Department at The University of Tulsa for providing the computer facilities. Portions of this research were conducted under the auspices of the University of Tulsa Petroleum Reservoir Exploitation Projects (TUPREP).

Special thanks goes to Mustafa Onur for many stimulating discussions in the difficult aspects of well testing analysis.

Finally, I wish to thank my parents Marcello and Nelly for teaching me that there is no merit in easy accomplishments.

This work is dedicated to my loving wife Vania, my son Fabio and my daughter Daniela for their infinite patience, understanding and trust.

TABLE OF CONTENTS

LIST OF TABLES

List of Figures

CHAPTER I
INTRODUCTION

In a slug test, an instantaneous pressure drop is imposed on the formation face by either adding or removing a small amount of fluid from the wellbore. The instantaneous pressure drop can also be obtained by a sudden compression or decompression of the wellbore fluid. The wellbore pressure recovery towards equilibrium can be analyzed for determining reservoir properties.

The analysis of slug test data is considered in Chapter II. The original slug test procedure and an analysis method was proposed by Ferris and Knowles[1] for ground water applications. By deriving a long-time asymptotic solution, they showed that the formation flow capacity could be estimated from the slope of a Cartesian plot of the wellbore pressure versus the reciprocal of time. The analytical solution used in Ref. 1 assumes a line source well. Cooper et al.[2] presented the finite wellbore radius solution and showed that Ferris and Knowles' method[1] becomes valid only for large values of time. Cooper et al.[2] presented semilog type curves from which the reservoir permeability and the porosity-compressibility product could be determined by type-curve matching. However, they pointed out that because of the similarity of the shapes of the type curve solutions, the porosity-compressibility product obtained from this type curve matching procedure is of questionable accuracy.

Cooper et al.'s[2] slug test type curves were introduced in the petroleum engineering literature by van Poollen and Weber[3] and by Kohlhaas[4]. Ramey and Agarwal[5] incorporated the skin effect into the slug test solutions using the infinitesimally thin skin concept of van Everdingen[6] and Hurst[7]. Later, Ramey et al.[8] presented semilog and log-log slug test type curves using the correlating group $C_D \exp(2s)$ suggested by Earlougher and Kersch[9]. Since then, type-curve matching has become the standard procedure for analyzing slug test pressure data. Although the correlating group used in construction of these type curves is not mathematically

rigorous, it has been verified that, for all practical purposes, the correlation is reliable for large values of the wellbore storage coefficient. The validity of Earlougher and Kersch's[9] correlating group was further investigated by Sageev[10]. Based on early time asymptotic approximations, Ref. 10 proposed one type curve for zero skin cases and a different type curve for the case where the skin factor is nonzero.

The presence of a finite thickness skin was considered by Faust and Mercer[11] and by Moench and Hsieh[12]. Ref. 12 showed that when the wellbore storage coefficient is large, the solutions for finite thickness skin are indistinguishable from those obtained by Ramey et al.[8] They pointed out that for small values of the wellbore storage coefficient, the early time response is controlled by the skin zone properties, whereas the late time response is affected by the unaltered reservoir properties.

A procedure for testing low transmissibility reservoirs was suggested by Bredehoeft and Papadopulos[13]. In their procedure, an instantaneous pressure drop is created by a sudden pressurization of the liquid in the wellbore. The pressure response is related to wellbore liquid compressibility which substantially reduces the test response duration. Similar procedures have been used in the petroleum industry (e.g., surge tests, closed chamber tests, etc).

The Ramey et al.[8] slug test type curves are strictly applicable only for a fully-penetrating well in a homogeneous infinite reservoir, therefore specific slug test type curves have to be generated for different flow geometries (e.g. linear, spherical) and reservoir models. The slug test pressure response in a double-porosity reservoir has been investigated by Barker and Black[14], Mateen and Ramey[15] and Sageev and Ramey[16] for a fully-penetrating well. Dougherty and Babu[17] derived slug test solutions for a restricted-entry well. Karasaki et al.[18] presented slug test type curves for various geometries in heterogeneous systems.

Chapter II presents a completely new approach to the slug test problem. It is shown that the slug test response can be converted to an equivalent constant rate, wellbore storage and skin problem. The equivalent constant rate pressure data is obtained by integrating the measured slug test pressure over the producing

time, whereas the multiplication of the slug test pressure data by the producing time yields the equivalent constant surface rate pressure derivative data. Once the equivalent data is obtained, reservoir parameters can be estimated using well known constant rate analysis techniques such as type curve matching[19–23], rate normalization[24–28] and convolution[29–31]. More importantly, it is shown that the new analysis procedure is applicable for any reservoir/well geometry. Therefore, slug test type curves are no longer needed.

Chapter III is concerned with the analysis of DST data. A drillstem test (DST) is a temporary well completion with the specific purposes of rock and fluid characterization under dynamic reservoir conditions. DST's are by far the most common testing procedure and are extensively used for exploratory purposes as well as for monitoring reservoir and well conditions in developed productive zones. Ideally, reservoir parameters such as reservoir pressure, formation damage, permeability, reservoir boundaries and heterogeneities can be determined from DST data.

Standard DST equipment and operational procedures have been described elsewhere in the literature[32–37]. Essentially, the testing tool consists of a packer and a tester valve attached to the tail of the drill pipe or production tubing. After the packer is set in position, the opening of the DST valve imposes a sudden pressure drop at formation face causing the reservoir fluid to flow into the wellbore, increasing the liquid level in the string. For the cases where the string above the valve is empty, the initial flowing pressure approaches atmospheric pressure. In some cases a certain volume of fluid (known as cushion) is added in the string above the tester valve in order to avoid mechanical failure of the tools and damage to the formation (such as sand production). In this work, we only consider cases where the wellbore fluid does not reach the surface during the flowing period and thus, the flow period represents a slug test. In such a case, the DST flow period data can be analyzed using the techniques described in Chapter II. When the tester valve is closed for the buildup period, the wellbore storage coefficient decreases from one for a rising-liquid-level to one for fluid-compression, which typically represents a reduction of two orders of magnitude in the storage coefficient[36].

For wells in which the liquid level does not reach the surface, the DST flow period shows a continuously decreasing flow rate. The combined effects of variable flow rate and short producing time generally make it difficult to analyze buildup data by conventional constant rate methods, such as the Horner plot. Buildup analysis following a variable rate drawdown has been the object of several investigations[38–44]. When the flow rate history is known, the multi-rate method of Ref. 38 can be used to analyze pressure buildup data. Horner[38] also proposed a simplified approach to account for a variable rate production. In this approach, the actual producing time is replaced by the ratio of the cumulative production to the last flow rate. Odeh and Selig[39] presented expressions for correcting both the rate and flowing time in order to account for the flow rate variation on pressure buildup calculations. Dolan et al.[40] verified that if the rate variation during the DST flow period is not severe, the use of the average production rate in the equation for the semilog slope of a Horner plot yields an accurate estimate of the flow capacity. Streltsova[41] showed that for small shut-in times, the buildup response is affected by the last flow rate before shut-in. Ref. 41 also showed that for large shut-in times the Horner semilog slope does not depend upon the rate-history but only upon its average value. Several authors[37,41,42] indicated that the rate variation effect on the shape of semilog plots can be erroneously interpreted as reservoir heterogeneity. Soliman[43] proposed a continuous multi-rate method for DST applications, which approximates the flow rates by a polynomial expression. Correa and Ramey[44] presented an analytical solution for the buildup response following a rising-liquid-level flow period. A long time approximation to the analytical solution indicated that by plotting buildup pressures versus the reciprocal of the total time, one could obtain estimates for the flow capacity and initial reservoir pressure. The same plotting technique was suggested by Soliman[45] for the analysis of buildup data obtained after a short flow period.

New DST buildup analysis procedures are presented in Chapter III. Although the new methods do account for the rate variation during the flow period, no direct measurement of sandface rates or its determination from the liquid recovery are

needed. This fact represents the major advantage of the proposed methods over the traditional multi-rate method of Ref. 38. Our procedures are also independent of the length of the flow period compared to the shut-in period.

The development of some of the methods presented in Chapters II and III assume that a particular flow regime prevails in the reservoir. In particular, the straight-line methods derived from the superposition principle (convolution) are strictly applicable for radial flow geometry. In Chapter IV, we present methods based on the deconvolution approach. In this approach, no assumption regarding the well/reservoir flow geometry is needed and represents the most general method for handling pressure data affected by a variable flow rate.

In any deconvolution method, Duhamel's principle[46] is used to generate the equivalent pressure data that would be obtained for production at a constant sand-face rate. Several numerical schemes have been proposed[47–53]. Though the first deconvolution algorithm was proposed as early as 1965 by Jargon and van Poollen[47], this method did not become popular in the industry until recently. Pascal and Quillian[48] applied a deconvolution method for the analysis of variable rate drawdown tests of low-permeability gas reservoirs. In their procedure, the continuously variable gas rate is approximated by an exponential equation. Bostic et al.[49] presented and applied a deconvolution scheme in the analysis of massive hydraulic fractured gas wells. Kuĉuk and Ayestaran[50] proposed a improved deconvolution algorithm which, in contrast with the scheme of Ref. 49, does not require interpolation and iteration. Thompson et al.[51] considered the numerical aspects of the schemes of Refs. 49 and 50. Ref. 51 showed that for a monotonically decreasing flow rate both schemes are stable. Thompson and Reynolds[52] presented the application of deconvolution methods for several well testing problems.

All the deconvolution schemes discussed thus far solve for the equivalent constant rate pressure data using a recursive formula and all computations are performed in real space. Based on the work of Ref. 50, Roumboutsos and Stewart[53] presented a deconvolution scheme in Laplace space which eliminates the recursive calculation and hence, improves the stability of the numerical procedure. In their

approach, the measured pressure and rate data are transformed into Laplace space using a piecewise linear approximation, and the resulting equivalent constant rate pressure drop is inverted from Laplace space by a numerical inversion algorithm.

The application of the previously described schemes assumes that the rate data is available. In Chapter IV, we present deconvolution schemes for drillstem test data which does not requires direct measurement of sandface rates or its determination from the liquid recovery. Both real and Laplace space approaches are considered.

In Chapter V we summarize the results of this work and discuss possible extensions.

CHAPTER II
SLUG TEST ANALYSIS

A general solution of the slug test problem in terms of the constant rate solution is presented in this Chapter. New analysis procedures based on this relationship are presented. Some practical aspects are discussed and several field examples are offered for illustrative purposes.

2.1 Definitions

Different dimensionless pressure solutions are considered in the course of this work. In this Chapter, p_{wD} denotes the dimensionless wellbore pressure drop solution of the slug test problem under consideration and p_{wcD} denotes the dimensionless wellbore pressure drop solution that would be obtained for the same wellbore/reservoir problem if the well were produced at a constant surface flow rate. This p_{wcD} solution incorporates wellbore storage effects. The corresponding dimensionless wellbore pressure solution for production at a constant sandface rate is denoted by p^*_{wcD} and represents the solution obtained when wellbore storage effects are negligible.

All definitions given here are in oil field units. Dimensionless time, dimensionless radial distance and the dimensionless wellbore storage coefficient are defined, respectively, by

$$t_D = \frac{2.637 \times 10^{-4} kt}{\phi \mu c_t r_w^2}, \tag{2.1.1}$$

$$r_D = \frac{r}{r_w}, \tag{2.1.2}$$

and

$$C_D = \frac{5.615C}{2\pi \phi c_t h r_w^2}, \tag{2.1.3}$$

where C denotes the wellbore storage coefficient in RB/psi, due to either the compressibility of the fluid in the wellbore or a change in the wellbore fluid level. For the conventional slug test procedure, C is given by

$$C = \frac{144\pi r_p^2}{5.615\rho g/g_c}, \tag{2.1.4}$$

where r_p is the radius of the drill pipe and ρ is the density of the fluid being produced into the wellbore. If wellbore storage effects are caused by the compression or expansion of the wellbore fluid, the wellbore storage coefficient C is given by

$$C = V_w c_{wf}, \tag{2.1.5}$$

where V_w is the volume of the pressurized wellbore and c_{wf} denotes the isothermal compressibility of the fluid in the wellbore. Throughout this work, the subscript w is used to denote properties related to the wellbore.

The dimensionless pressure drop for the slug test problem is defined by

$$p_D = \frac{p_i - p(r,t)}{p_i - p_o}, \tag{2.1.6}$$

where $p(r,t)$ denotes the pressure at a distance r at time t, p_i represents the initial pressure throughout the reservoir and p_o denotes the imposed initial bottom-hole pressure. As mentioned previously, p_{wD} represents the dimensionless pressure drop that occurs at the wellbore for the slug test solution and is obtained by replacing $p(r,t)$ in Eq. 2.1.6 by $p_{wf}(t)$, that is,

$$p_{wD} = \frac{p_i - p_{wf}(t)}{p_i - p_o} = \frac{\Delta p}{p_i - p_o}, \tag{2.1.7}$$

where Δp is given by

$$\Delta p = p_i - p_{wf}(t). \tag{2.1.8}$$

The dimensionless sandface rate is defined as

$$q_D = \frac{141.2 q_{sf}(t)\mu}{kh(p_i - p_o)}, \tag{2.1.9}$$

where $q_{sf}(t)$ (in RB/day) denotes the sandface flow rate obtained during the slug test as a function of time.

The skin factor definition is based on the infinitesimally thin skin zone concept[6,7] and is given by

$$s = \frac{kh}{141.2 q_{sf}(t)\mu} \Delta p_{skin}, \tag{2.1.10}$$

where Δp_{skin} represents the additional pressure drop which occurs due to formation damage (or improvement) around the wellbore.

Later in this Chapter, we establish a relation between the slug test solution and the classical constant rate wellbore storage and skin solution. The dimensionless pressure drop definition for the constant surface rate wellbore storage and skin problem is given by

$$p_{cD} = \frac{kh\,[p_i - p(r,t)]}{141.2 qB\mu}. \tag{2.1.11}$$

Note p_{cD} given by Eq. 2.1.11 represents the dimensionless pressure drop solution that would be obtained at a point r at time t in the reservoir if the well were produced at a constant surface rate q. This solution includes the effects of wellbore storage and skin. Similarly, p_{wcD} would represent the dimensionless wellbore pressure drop solution for the constant surface rate wellbore storage and skin problem, and is given by

$$p_{wcD} = \frac{kh\Delta p}{141.2 qB\mu}, \tag{2.1.12}$$

where Δp is given by Eq. 2.1.8.

The logarithmic time derivative of the constant surface rate dimensionless wellbore pressure is defined by

$$p'_{wcD} = \frac{dp_{wcD}}{d\ln t_D} = \frac{kh\Delta p'}{141.2 qB\mu}, \tag{2.1.13}$$

where $\Delta p'$ denotes the derivative of Δp with respect to the natural logarithm of time. In this work, the symbol $'$ is always used to denote differentiation with respect to the natural logarithm of time.

The dimensionless sandface rate for constant surface rate wellbore storage and skin problems is defined by

$$q_{cD} = \frac{q_{sfc}(t)}{qB}, \tag{2.1.14}$$

where q_{sfc} represents the sandface rate (in RB/day) under constant surface rate production.

2.2 Background and Theory

In this section, the basic derivation of the new procedure for analyzing slug test data is presented. We first review the slug test and constant rate solutions for plane radial flow. Then, we establish a relationship between the two solutions which is valid for any well/reservoir flow geometry.

2.2.1 Slug Test Solution

In the following, we consider a fully-penetrating well in an infinite, homogeneous and isotropic reservoir of uniform thickness. Initially, the pressure is constant throughout the reservoir and equal to p_i whereas, at the wellbore, the pressure is set instantaneously equal to p_o. In addition, it is assumed that momentum and inertial effects in the wellbore can be neglected.

Under the stated assumptions and using the dimensionless variables defined earlier, the slug test initial boundary value problem (IBVP) can be formulated as

$$\frac{1}{r_D}\frac{\partial}{\partial r_D}\left(r_D\frac{\partial p_D}{\partial r_D}\right) = \frac{\partial p_D}{\partial t_D}, \tag{2.2.1}$$

$$p_D(r_D,0) = 0; \qquad 1 < r_D < \infty, \tag{2.2.2}$$

$$\lim_{r_D\to\infty} p_D(r_D,t_D) = 0; \qquad t_D \geq 0, \tag{2.2.3}$$

$$p_{wD}(0) = 1, \tag{2.2.4}$$

$$p_{wD} = \left[p_D - s\left(r_D\frac{\partial p_D}{\partial r_D}\right)\right]_{r_D=1}, \tag{2.2.5}$$

and

$$\left(r_D\frac{\partial p_D}{\partial r_D}\right)_{r_D=1} = C_D\frac{\partial p_{wD}}{\partial t_D}. \tag{2.2.6}$$

The Laplace space solution of the IBVP specified by Eqs. 2.2.1-2.2.6 is given by[5]

$$\bar{p}_{wD} = C_D\frac{K_0(\sqrt{u}) + s\sqrt{u}K_1(\sqrt{u})}{\sqrt{u}K_1(\sqrt{u}) + C_D u[K_0(\sqrt{u}) + s\sqrt{u}K_1(\sqrt{u})]}, \tag{2.2.7}$$

where $\bar{p}_{wD}$ denotes the Laplace transform of p_{wD}, u denotes the Laplace variable, and K_0 and K_1 denote, respectively, the modified Bessel functions of the second kind of order zero and order one.

The real inversion of Eq. 2.2.7 was presented by Ramey and Agarwal[5] and is given by

$$p_{wD} = \frac{4C_D}{\pi^2} \int_0^\infty \frac{\exp(-u^2 t_D)}{u f(u)} du, \tag{2.2.8}$$

where

$$f(u) = \left[uC_D J_0(u) - (1 - u^2 s C_D) J_1(u)\right]^2 + \left[uC_D Y_0(u) - (1 - u^2 s C_D) Y_1(u)\right]^2. \tag{2.2.9}$$

Here, J_0, J_1, Y_0 and Y_1 are Bessel functions of the first and second kind of order zero and one.

Ramey et al.[8] presented slug test type curves in which the p_{wD} solution given by Eq. 2.2.8 is plotted versus t_D/C_D for a range of values of the correlating group $C_D \exp(2s)$. Fig. 2.2.1 presents Ramey et al.'s semilog type curve where the p_{wD} solution, represented by the solid lines, is plotted versus t_D/C_D for the specified values of $C_D \exp(2s)$. The dimensionless pressure solution presented in Fig. 2.2.1 was obtained by numerical inversion of Eq. 2.2.7 using the Stehfest algorithm[54]. The dashed lines shown in Fig. 2.2.1 represents the complementary solution of p_{wD}, that is, $1 - p_{wD}$. Ref. 8 also presented log-log type curves of the p_{wD} and $1 - p_{wD}$ solutions which are combined in Fig. 2.2.2. Note that the type curves of Figs. 2.2.1 and 2.2.2 represent the same basic solution. Type-curve matching of field data with the dimensionless solutions of Figs. 2.2.1 and 2.2.2 has become the standard procedure for analyzing slug test data.

When the initial wellbore flowing pressure is known, type-curve matching of field data is obtained by moving the field data plot only in the horizontal direction. If p_o is not known, type-curve matching can only by accomplished with the log-log type curves of Fig. 2.2.2; the type curves of Fig. 2.2.1 cannot be used. However, in such a case, the type-curve matching procedure using Fig. 2.2.2 requires movement of the

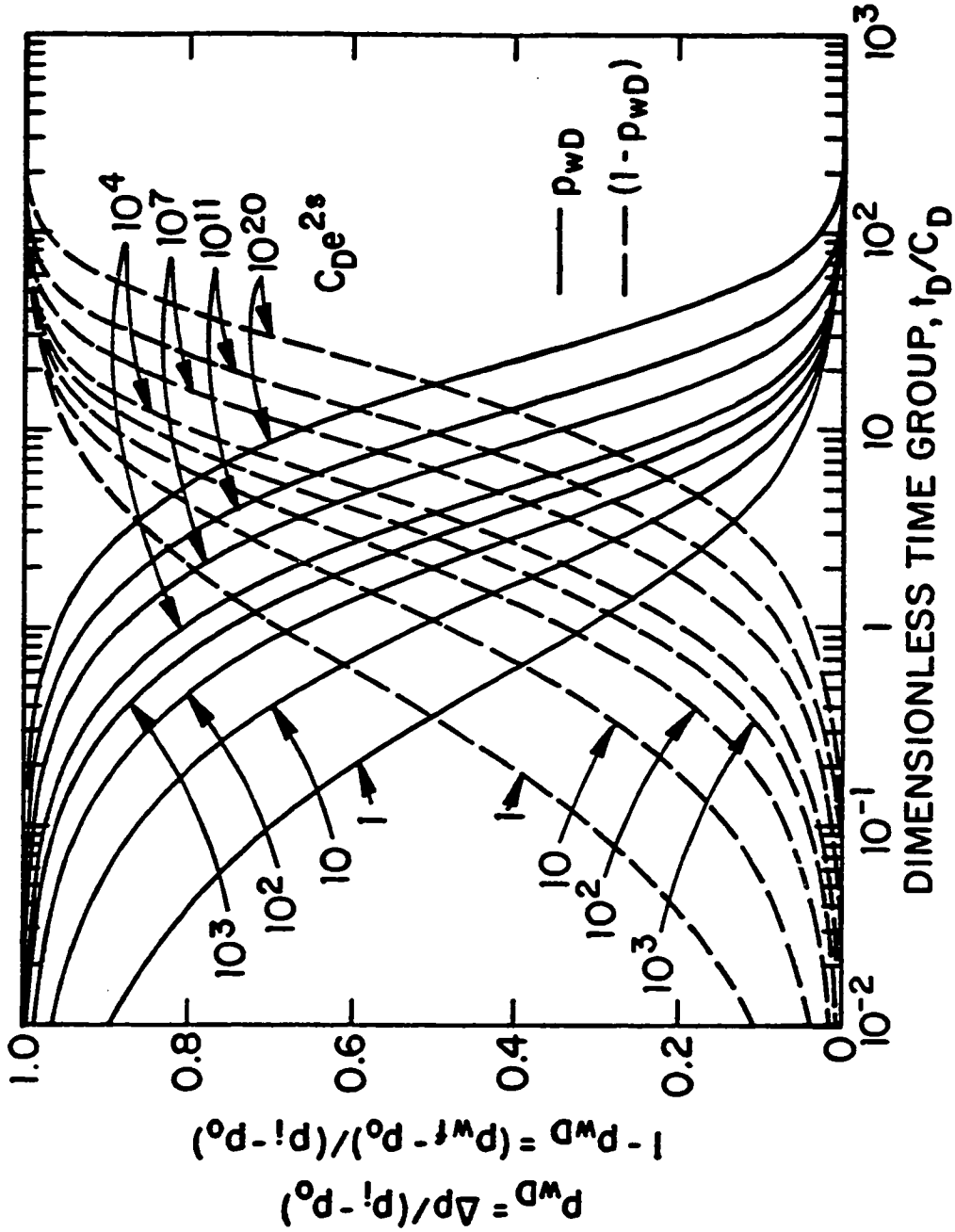

Fig. 2.2.1 - Ramey et al. slug test semilog type curve.

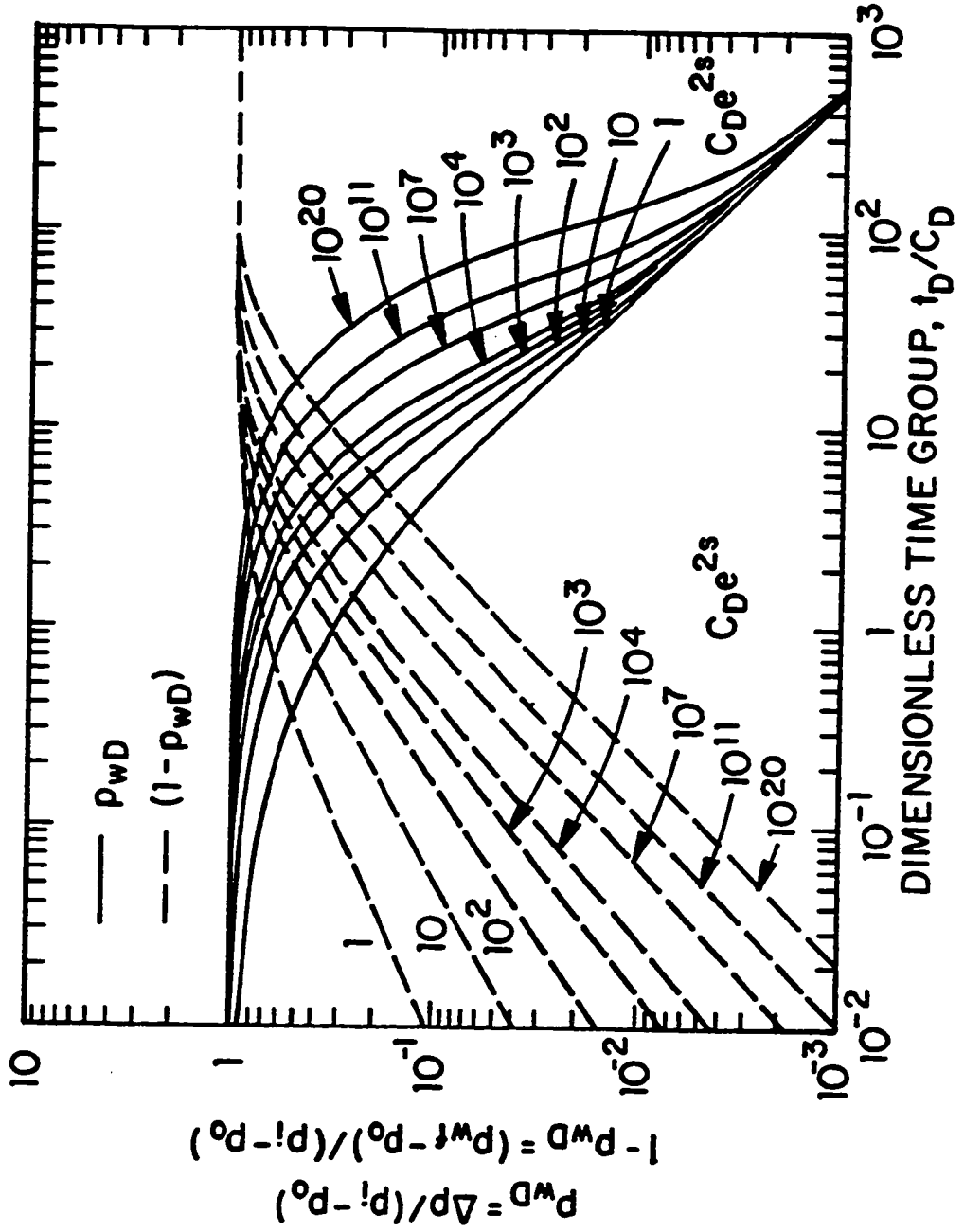

Fig. 2.2.2 - Kamey et al. slug test log-log type curve.

field data in both the horizontal and vertical directions which reduces the likelihood of obtaining a unique match. Later in this Chapter, we present an improved type curve matching procedure which only requires horizontal movement of the field data plot and does not require an accurate estimate of the initial wellbore pressure, p_o.

2.2.2 Constant Rate Solution

In this sub-section, we briefly review the basic constant rate solution for radial flow problems.

A wellbore storage type curve was presented by van Everdingen and Hurst[55]. Their type curve is based on the line source well assumption, and skin effects are not considered. Later, van Everdingen[6] incorporated the skin effect into this solution. Unfortunately, these type curves never gained popularity as an interpretation technique.

Papadopulos and Cooper[56] introduced the finite wellbore radius and wellbore storage type curve in the ground water literature. Reservoir parameters could be determined by the type-curve matching of measured data with the type curve solutions. They also indicated that the type curve matching procedure could be difficult due to the similarity in the shapes of the type curve solutions.

The finite wellbore radius problem considering both wellbore storage and skin effects for a fully-penetrating well in an infinite, homogeneous and isotropic reservoir of uniform thickness, is given by

$$\frac{1}{r_D}\frac{\partial}{\partial r_D}\left(r_D\frac{\partial p_{cD}}{\partial r_D}\right)=\frac{\partial p_{cD}}{\partial t_D}, \tag{2.2.10}$$

$$p_{cD}(r_D,0)=0; \qquad 1<r_D<\infty, \tag{2.2.11}$$

$$\lim_{r_D\to\infty} p_{cD}(r_D,t_D)=0; \qquad t_D\geq 0, \tag{2.2.12}$$

$$p_{wcD}=\left[p_{cD}-s\left(r_D\frac{\partial p_{cD}}{\partial r_D}\right)\right]_{r_D=1}, \tag{2.2.13}$$

and

$$-\left(r_D\frac{\partial p_{cD}}{\partial r_D}\right)_{r_D=1}=1-C_D\frac{\partial p_{wcD}}{\partial t_D}. \tag{2.2.14}$$

The Laplace space solution of the dimensionless wellbore pressure drop is[19]

$$\bar{p}_{cwD} = \frac{1}{u} \frac{K_0(\sqrt{u}) + s\sqrt{u}K_1(\sqrt{u})}{\sqrt{u}K_1(\sqrt{u}) + C_D u[K_0(\sqrt{u}) + s\sqrt{u}K_1(\sqrt{u})]}, \tag{2.2.15}$$

where $\bar{p}_{wcD}$ denotes the Laplace transform of p_{wcD}. The real inversion of Eq. 2.2.15 is[19]

$$p_{wcD} = \frac{4}{\pi^2} \int_0^\infty \frac{1 - \exp(-u^2 t_D)}{u^3 f(u)} du, \tag{2.2.16}$$

where $f(u)$ is given by Eq. 2.2.9.

Agarwal et al.[19] presented a type curve based on the solution given by Eq. 2.2.16 for various values of the wellbore storage coefficient and the skin factor. Gringarten et al.[20] utilized the correlating group $C_D \exp(2s)$ in the construction of a new wellbore storage and skin type curve. The major feature of the Gringarten et al.[20] type curves is that the number of curves presented is greatly reduced. However, it is difficult to obtain a unique match of field pressure data with either type curve due the similar shape of the dimensionless pressure solutions.

Bourdet et al.[21] incorporated the derivative of the dimensionless wellbore pressure, p'_{wcD}, into the Gringarten et al.[20] type curve. Fig. 2.2.3 presents the Bourdet et al.[21] wellbore storage and skin type curve for a homogeneous reservoir. Type curves incorporating both dimensionless pressure and its logarithmic derivative have two main advantages over conventional types curves. First, the pressure derivative solution has more curvature than the pressure solution which increases the likelihood of obtaining a unique match. Second, such type curves require a simultaneous match of the pressure change and the derivative of the pressure change which also increases the likelihood of obtaining a unique match. However, the application of these type curves requires the computation of pressure derivatives by numerical differentiation of measured pressure data.

Recently, a new derivative type curve construction was proposed by Onur and Reynolds[22] and by Duong[23]. These authors presented new wellbore storage and skin type curves by defining a dimensionless group given by the ratio of the wellbore pressure to two times its logarithmic derivative. Fig. 2.2.4 shows Onur and

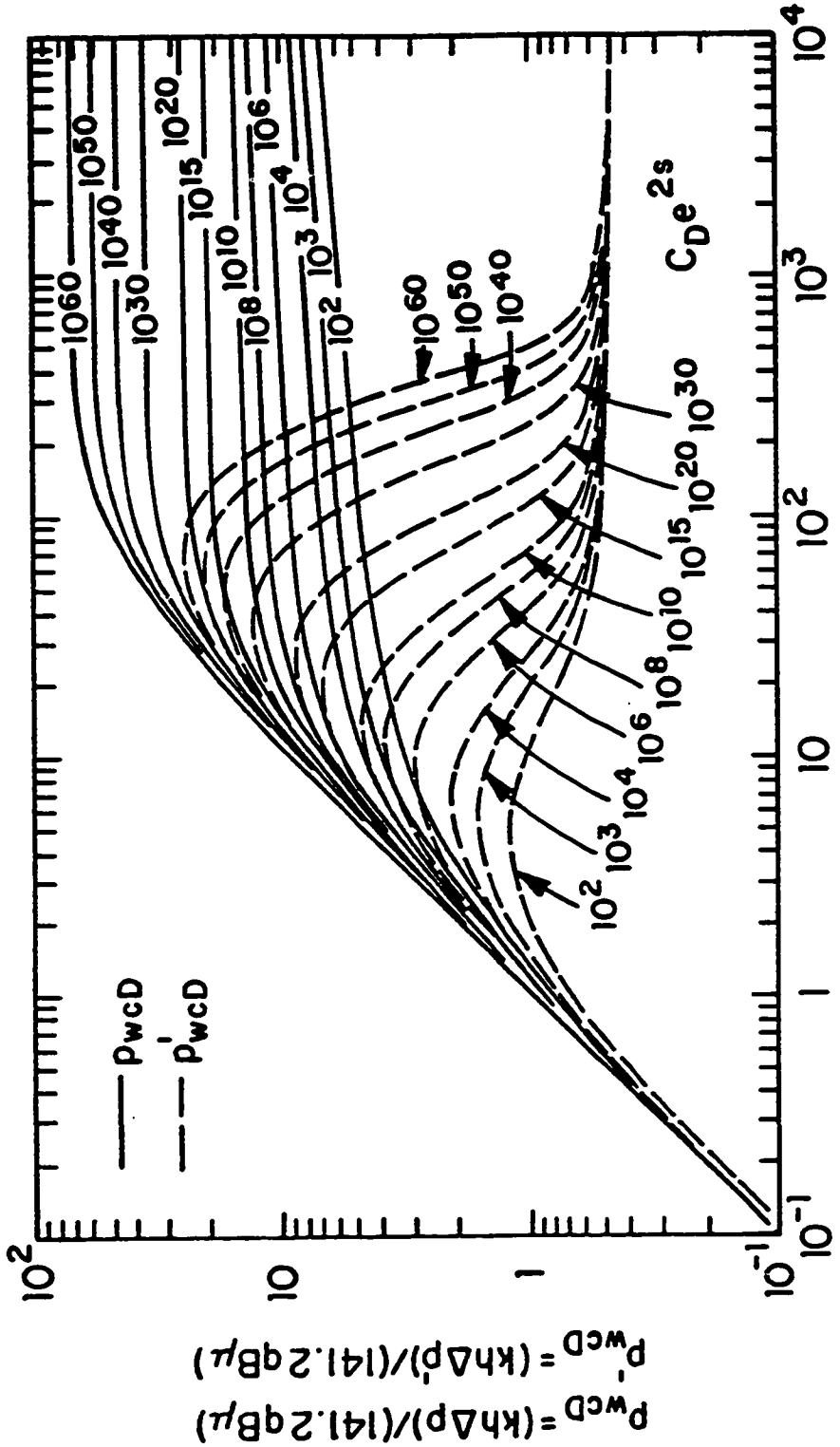

Fig. 2.2.3 - Bourdet et al. wellbore storage and skin type curve.

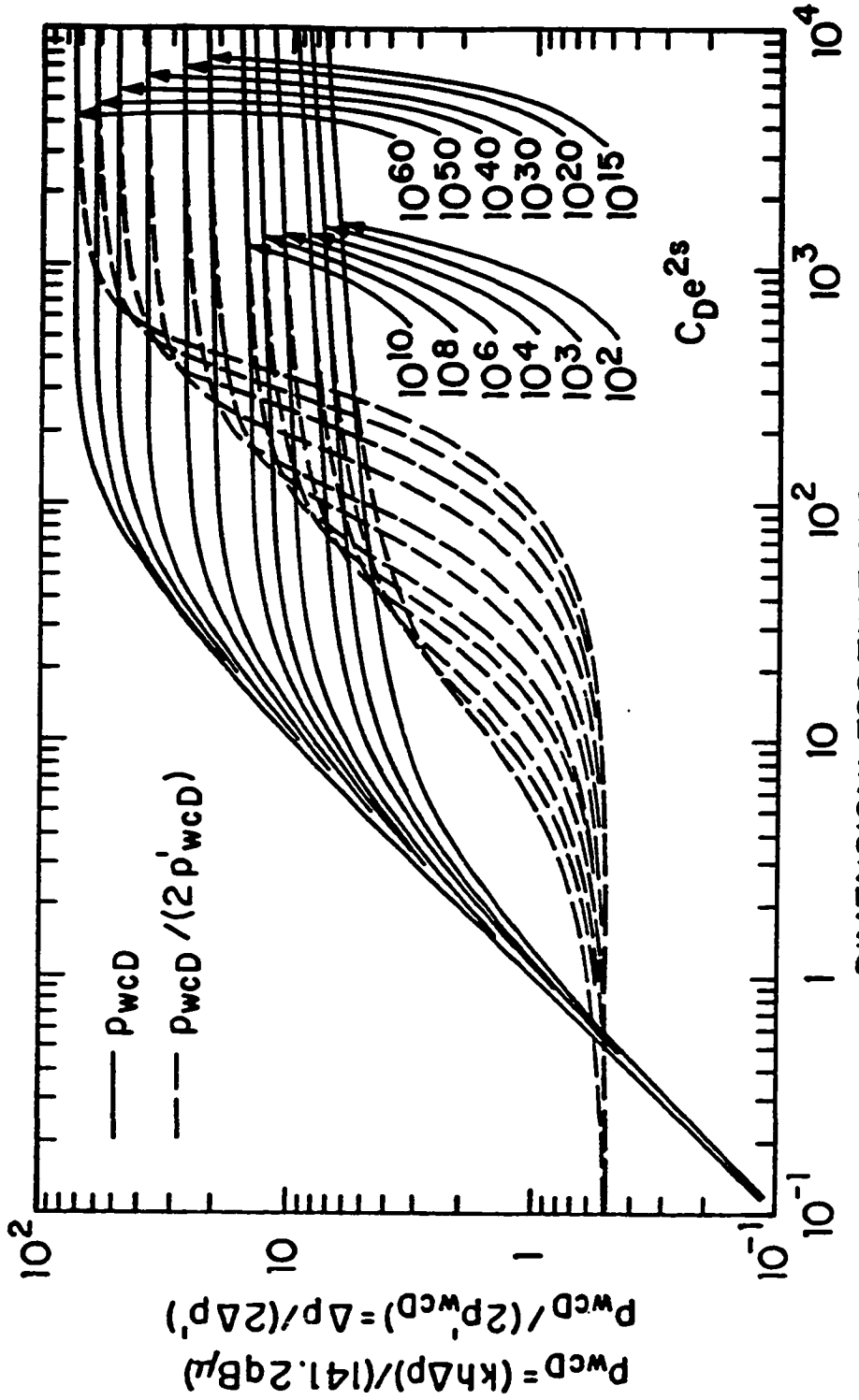

Fig. 2.2.4 - Onur-Reynolds wellbore storage and skin type curve.

Reynolds' constant rate wellbore storage and skin type curve for homogeneous reservoirs (Duong's type curve is similar to Fig. 2.2.4, except Duong uses a vertical scale which is two times the one used by Onur and Reynolds). Note that the group $\Delta p/(2\Delta p')$ is dimensionless, therefore, the vertical scale of the pressure derivative type curves of Fig. 2.2.4 is automatically aligned with the vertical scale of the field pressure derivative ratio data. Thus, the type-curve matching of field pressure derivative data requires that the plot of $\Delta p/(2\Delta p')$ versus t be moved only the horizontal direction which simplifies the type-curve matching procedure. Moreover, as discussed in Ref. 22, this unique correspondence between the vertical scales of the type curves and the $\Delta p/(2\Delta p')$ versus t plot helps to determine whether given field data actually represents the solution assumed by the type curves of Fig. 2.2.4. Later in this Chapter, we show how the type curves of Figs. 2.2.3 and 2.2.4 can be used to analyze slug test field data.

2.2.3 General Slug Test Solution

Based on the dimensionless solutions given by Eqs. 2.2.8 and 2.2.16, Refs. 5 and 19 realized that the slug test dimensionless wellbore solution could be written as

$$p_{wD}(t_D, C_D, s) = C_D \frac{dp_{wcD}}{dt_D}(t_D, C_D, s), \tag{2.2.17}$$

that is, the slug test wellbore pressure solution, p_{wD}, can be obtained directly from the time derivative of the constant rate wellbore storage and skin solution, p_{wcD}. Eq. 2.2.17 can be obtained from Eq. 2.2.16 by using Leibnitz's rule for the differentiation of integrals. One can also obtain Eq. 2.2.17 by comparing the Laplace space solution of the slug test and the constant rate problem given by Eqs. 2.2.7 and 2.2.15, respectively. Although this result has been known for a long time, the relation provided by Eq. 2.2.17 has not been fully explored.

Before the novel procedure for analyzing slug test data is presented, we derive the general relation between the slug test and the constant rate problem. The derivation of Eq. 2.2.17 given here and presented in Refs. 5 and 19 assumes a fully-penetrating well in an infinite homogeneous, isotropic reservoir of uniform thickness.

In the following, it is shown that Eq. 2.2.17 is also valid for any reservoir/well system and holds at any position within the reservoir.

A general slug test solution can be written in terms of Duhamel's principle[46] as

$$p_D(t_D, r_D, C_D, s) = \int_0^{t_D} q_D(\tau) \frac{\partial p^*_{cD}}{\partial t_D}(t_D - \tau, r_D) d\tau, \qquad (2.2.18)$$

where q_D represents the dimensionless slug test sandface rate, defined by Eq. 2.1.9, and $\partial p^*_{cD}/\partial t_D$ denotes the time derivative of the constant sandface rate solution without wellbore storage effects evaluated at $t_D - \tau$. In Eq. 2.2.18, p_D and p^*_{cD} denote, respectively, the slug test solution and the constant sandface rate solution (no wellbore storage) for a general well/reservoir geometry.

From a material balance on the wellbore and using the definitions of dimensionless variables given previously, it follows that the dimensionless slug test sandface rate is given by

$$q_D(t_D) = -C_D \frac{dp_{wD}}{dt_D}(t_D, C_D, s). \qquad (2.2.19)$$

Eq. 2.2.19 represents a material balance in the wellbore and therefore, applies for any well/reservoir flow geometry. Using this result in Eq. 2.2.18 gives

$$p_D(t_D, r_D, C_D, s) =$$

$$-\int_0^{t_D} C_D \frac{dp_{wD}}{d\tau}(\tau, C_D, s) \frac{\partial p^*_{cD}}{\partial t_D}(t_D - \tau, r_D) d\tau. \qquad (2.2.20)$$

Note that Eq. 2.2.20 is completely general, that is, it represents the slug test solution for any reservoir/well geometry since the derivation is based on Duhamel's principle and a material balance in the wellbore.

Similarly, the general dimensionless pressure drop solution for production at a constant surface rate is given by

$$p_{cD}(t_D, r_D, C_D, s) = \int_0^{t_D} q_{cD}(\tau) \frac{\partial p^*_{cD}}{\partial t_D}(t_D - \tau, r_D) d\tau, \qquad (2.2.21)$$

where q_{cD} represents the dimensionless sandface rate for the constant surface rate problem, defined by Eq. 2.1.14, and is given by

$$q_{cD} = 1 - C_D \frac{dp_{wcD}}{dt_D}. \qquad (2.2.22)$$

Note that Eq. 2.2.22 also represents a material balance in the wellbore and therefore, is a valid expression for any flow geometry. Using Eq. 2.2.22 in Eq. 2.2.21, we obtain

$$p_{cD}(t_D, r_D, C_D, s) = \int_0^{t_D} \left[1 - C_D \frac{dp_{wcD}}{d\tau}(\tau, C_D, s)\right] \frac{\partial p^*_{cD}}{\partial t_D}(t_D - \tau, r_D) d\tau. \quad (2.2.23)$$

The objective now is to establish a relation between Eqs. 2.2.20 and 2.2.23. By taking the Laplace transforms of Eqs. 2.2.20 and 2.2.23 and performing some algebraic manipulations, the p^*_{cD} solution can be eliminated from these Equations. Upon application of the inverse Laplace transform, one can then obtain the following result (details are given in the Appendix A)

$$p_D(t_D, r_D, C_D, s) = C_D \frac{\partial p_{cD}}{\partial t_D}(t_D, r_D, C_D, s), \quad (2.2.24)$$

which is a generalization of the result obtained by Refs. 5 and 19, that is, Eq. 2.2.24 is valid for any well/reservoir geometry and applies at any location within the reservoir.

Eq. 2.2.24 provides the basis of the new general procedure for analyzing slug test data. Integrating both sides of Eq. 2.2.24 from zero to t_D gives

$$p_{cD}(t_D, r_D, C_D, s) = \frac{1}{C_D} \int_0^{t_D} p_D(\tau, r_D, C_D, s) d\tau. \quad (2.2.25)$$

Multiplying both sides of Eq. 2.2.24 by t_D/C_D gives

$$t_D \frac{\partial p_{cD}}{\partial t_D} = p'_{cD} = \frac{t_D}{C_D} p_D. \quad (2.2.26)$$

Eqs. 2.2.25 and 2.2.26 indicate that measured slug test pressure data can be directly converted to data that would be obtained for the corresponding constant surface rate wellbore storage and skin problem. Note that by integrating the slug test pressure response over the producing time (Eq. 2.2.25) one generates the equivalent pressure change data that would be obtained if the well were produced at constant surface flow rate. Moreover, the multiplication of the slug test pressure data by the producing time (Eq. 2.2.26) yields the equivalent constant surface rate pressure

derivative data without applying any numerical differentiation technique. Note that interference data caused by a slug test performed in an active well can also be converted to constant rate data by the same procedure.

At the wellbore, Eqs. 2.2.25 and 2.2.26 are given, respectively, by

$$p_{wcD}(t_D, C_D, s) = \frac{I(p_{wD})}{C_D} \tag{2.2.27}$$

and

$$p'_{wcD} = \frac{t_D}{C_D} p_{wD}. \tag{2.2.28}$$

In Eq. 2.2.27, $I(p_{wD})$ denotes the slug test pressure integral and is defined by

$$I(p_{wD}) = \int_0^{t_D} p_{wD}(\tau, C_D, s) d\tau. \tag{2.2.29}$$

2.3 Analysis Procedures

After generating the equivalent pressure and pressure derivative data from the measured slug test pressure data by means of Eqs. 2.2.27 and 2.2.28, desired reservoirs properties can be easily determined from well known and available constant rate analysis techniques. These analysis techniques are discussed in this section. First, we investigate the applicability of the existent wellbore storage and skin type curves to the "converted" data. Then, we discuss the applicability of rate-normalization and convolution methods.

2.3.1 Type-Curve Matching

As mentioned previously, derivative type curves improve the matching procedure by reducing the non-uniqueness problem typical of type curves which utilize only the pressure change. Here, we illustrate the use of the derivative type curves shown in Figs. 2.2.3 and 2.2.4 to analyze the converted slug test data. The extension to other flow geometries follows essentially the same guidelines given here. It is important to note that slug test type curves are no longer needed to analyze the measured slug test pressure data.

The dimensional version of Eqs. 2.2.27 and 2.2.28 are given, respectively, by

$$p_{wcD} = \frac{2.95 \times 10^{-4}}{C(p_i - p_o)} \frac{kh}{\mu} I(\Delta p) \tag{2.3.1}$$

and

$$p'_{wcD} = \frac{2.95 \times 10^{-4}}{C(p_i - p_o)} \frac{kh}{\mu} t\Delta p. \tag{2.3.2}$$

In Eq. 2.3.1, $I(\Delta p)$ denotes the time integral of the measured slug test pressure data, that is

$$I(\Delta p) = \int_0^t \Delta p(\tau) d\tau, \tag{2.3.3}$$

where $I(\Delta p)$ is in psi-hour. Note that the field application of Eq. 2.3.3 requires a numerical integration scheme. This point is addressed later in this Chapter.

A procedure for using the Bourdet et al. type curve[21] (see Fig. 2.2.3) to analyze the converted slug test data follows:

(1) Compute $I(\Delta p)$ and $t\Delta p$ as functions of time from the measured slug test pressure data;

(2) Make a log-log plot of $I(\Delta p)$ and $t\Delta p$ versus t on tracing paper using the basic scales of the type curve shown in Fig. 2.2.3;

(3) Perform a simultaneous type-curve match of the two sets of converted data $I(\Delta p)$ and $t\Delta p$ with the dimensionless pressure and the dimensionless pressure derivative type curves. This match determines the value of $[C_D \exp(2s)]_M$, as well as the pressure match-point values, $[p_{wcD}]_M$ and $[I(\Delta p)]_M$, and the time match-point values $(t_D/C_D)_M$ and $(t)_M$. Here, and throughout this work, the subscript M refers to a match point value;

(4) Estimate the transmissibility from the pressure match-point values by the following equation:

$$\frac{kh}{\mu} = 141.2(24C)\ (p_i - p_o) \frac{[p_{wcD}]_M}{[I(\Delta p)]_M}. \tag{2.3.4}$$

The transmissibility can also be determined (or checked) using the time match-point values from the following equation:

$$\frac{kh}{\mu} = 141.2(24C) \frac{(t_D/C_D)_M}{(t)_M}; \tag{2.3.5}$$

(5) Using the value of $[C_D \exp(2s)]_M$ associated with the curve matched (see step 3), the skin factor can be determined by

$$\begin{aligned} s &= \frac{1}{2} \ln \left(\frac{[C_D \exp(2s)]_M}{C_D} \right) \\ &= \frac{1}{2} \ln \left(\frac{2\pi \phi c_t h r_w^2}{5.615C} [C_D \exp(2s)]_M \right). \end{aligned} \tag{2.3.6}$$

Alternatively, one can use Onur and Reynolds' wellbore storage and skin type curve[22] (Fig. 2.2.4) in the analysis of the converted data. It follows directly from Eqs. 2.3.1 and 2.3.2 that

$$\frac{p_{wcD}}{2p'_{wcD}} = \frac{I(\Delta p)}{2t\Delta p}. \tag{2.3.7}$$

Type-curve matching using Onur and Reynolds' type curves requires a two step procedure:

(i) First, the matching of the plot $I(\Delta p)/[2t\Delta p]$ versus t is accomplished by moving the field data plot only in the horizontal direction. This step determines the time match-point values $(t_D/C_D)_M$ and $(t)_M$ and determines the value of $[C_D \exp(2s)]_M$ from the specific type curve matched.

(ii) The plot $I(\Delta p)$ versus t is then matched with the dimensionless pressure solution by moving the field plot only in the vertical direction. This step determines the equivalent pressure match-point values. Well/reservoir properties can then be determined by Eqs. 2.3.4 - 2.3.6.

Note that the analysis of the converted slug test data can be completed by using the time match-point values only, that is, one can directly determine the transmissibility and the skin factor from Eqs. 2.3.5 and 2.3.6, respectively.

A somewhat similar type-curve matching procedure for analyzing build-up data has been proposed by Cinco et al.[57] and Ayoub et al.[58]. These authors showed that if the producing time is very short, the subsequent buildup pressure response is approximately equal to the drawdown cartesian pressure derivative response. Therefore, by multiplying the buildup pressure drop by the elapsed time, one can directly compute the drawdown logarithmic pressure derivative, p'_{wcD}. Ref. 57 only used this fact to properly identify reservoir flow regimes, whereas, Ref. 58 proposed

a buildup analysis procedure based on the type-curve matching of the pressure-derivative using the Bourdet et al. type curves[21]. Ref. 58 also pointed out that such technique might be applicable to the analysis of slug test data; however, they recognize that a match based only on the pressure derivative may not be unique. Our procedure utilizes both equivalent pressure and pressure-derivative data (Eqs. 2.3.1 and 2.3.2) in the analysis of slug test data, and as shown in the following sections, it is not restricted to type-curve matching techniques.

2.3.2 Rate-Normalization

If the slug test is not sufficiently long, most of the converted slug test data is dominated by wellbore storage effects. In such cases, it is difficult to obtain a unique match of the converted data with the constant rate type curves of Figs. 2.2.3 and 2.2.4. Here, we explore the applicability of methods which eliminate the wellbore storage effects from the converted slug test data.

The effects of a continuously changing flow rate can be accounted for by the so called "deconvolution" methods. Different numerical schemes have been proposed[47–53] in which Duhamel's principle is used to generate the equivalent pressure data that would be obtained for production at a constant sandface rate. The application of such methods for the analysis of slug test data is considered in Chapter IV.

An approximate deconvolution procedure is given by the rate-normalization method proposed by Gladfelter et al.[24]; also see Aron and Scott[25], Winestock and Colpitts[26] and Ramey[27]. In this method, the constant sandface rate solution is approximated by the ratio of the pressure drop to the instantaneous sandface rate. The straightforward implementation of this method makes it very attractive from a field application point of view.

For the wellbore slug test data, the rate-normalization method is defined as

$$p^{*}_{wcD} \approx \frac{p_{wD}(t_D)}{q_D(t_D)} = -\frac{p_{wD}}{C_D\,(dp_{wD}/dt_D)} = -\frac{2.95\times10^{-4}kh}{\mu C}\frac{\Delta p}{[d\Delta p/dt]}, \tag{2.3.8}$$

where the first equality of Eq. 2.3.8 follows from Eq. 2.2.19 and the second equality follows directly from the dimensionless definitions given previously. There are two disadvantages associated with the use of Eq. 2.3.8. First, it requires the use of pressure derivatives which might complicate the analysis of the rate-normalization method due the oscillatory behavior generally exhibited by derivative data. Second, as shown in Ref. 59, and illustrated here with computer generated data, the rate normalized response p_{wD}/q_D is approximately equal to p^*_{wcD} only for times corresponding to $t_D/C_D \leq 1$. For larger values of time, the approximation given by Eq. 2.3.8 becomes highly inaccurate and the rate-normalization method applied directly to the slug test data fails.

Fig. 2.3.1 presents a comparison of the rate-normalization method, p_{wD}/q_D, for $C_D = 10^4$ and $s = 0$ with the constant sandface rate solution, p^*_{wcD}. The solid line represents p^*_{wcD}, which was computed directly from Eq. 2.2.15 with $C_D = 0$ using the Stehfest algorithm[54]. The circular data points through a solid line represent the rate-normalized group, p_{wD}/q_D. This group was evaluated by numerically inverting Eq. 2.2.7 for p_{wD} and dp_{wD}/dt_D, and then by computing q_D from Eq. 2.2.19. It is apparent that p_{wD}/q_D correlates reasonably well with the constant rate solution for dimensionless times less than or equal to 10^4, departing rapidly from p^*_{wcD} at times corresponding to $t_D/C_D > 1$. Note that at early times the rate-normalized data exhibits a nearly correct semilog straight line of slope 1.151, therefore, this portion of the data can be analyzed by the classical semilog method.

Ramey[28] investigated the rate-normalization method for the constant rate, wellbore storage and skin problem. Ref. 28 concluded that for all practical purposes, the rate-normalization method is a good approximation for handling a variable sandface rate due to the influence of wellbore storage. The rate-normalized procedure for the constant rate problem can be written as

$$p^*_{wcD} \approx \frac{p_{wcD}(t_D)}{q_{cD}(t_D)}. \tag{2.3.9}$$

Ref. 28 indicated that at early times Eq. 2.3.9 gives the correct semilog slope but shifted 0.4 units below the actual constant sandface rate solution. At

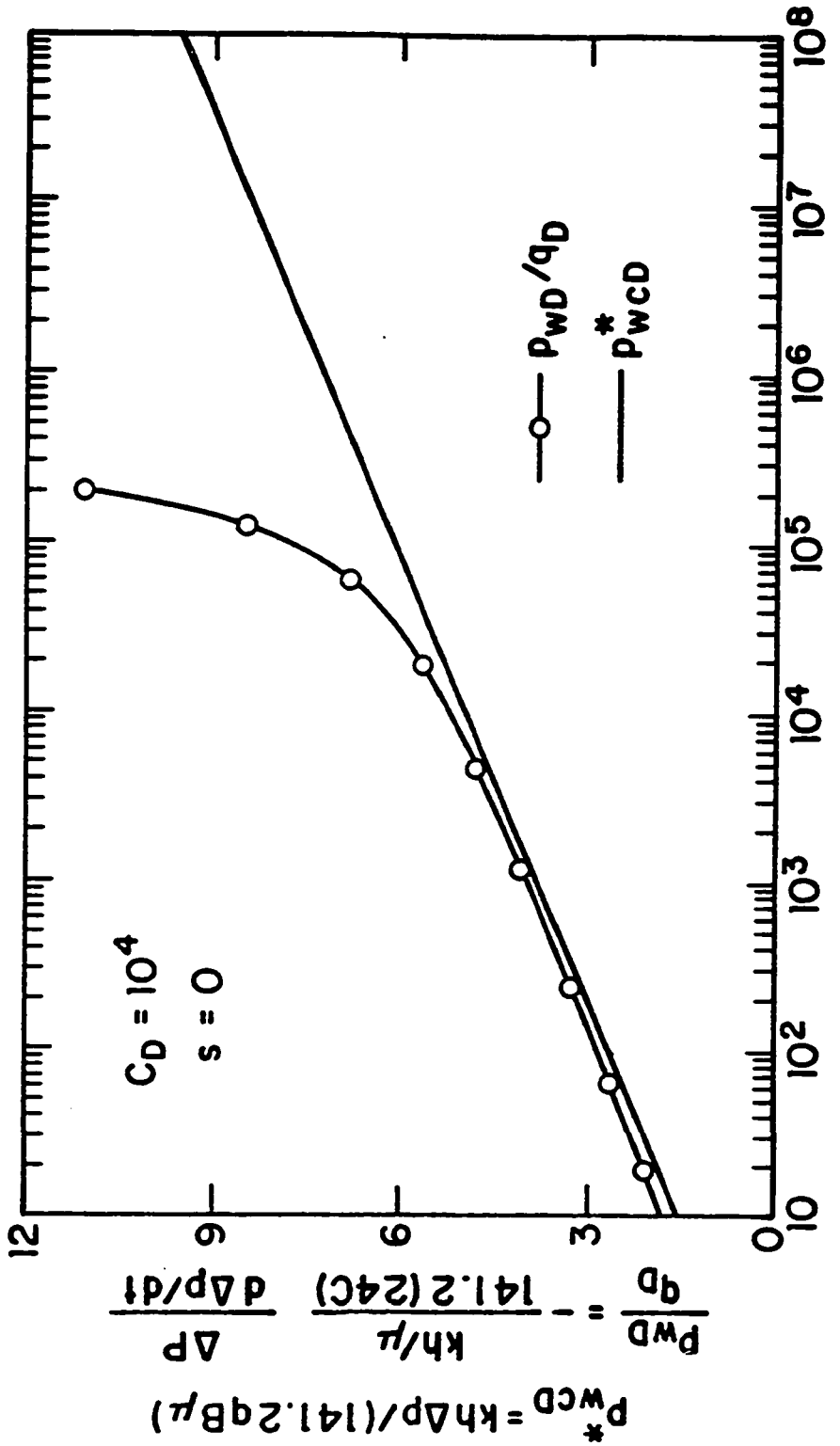

Fig. 2.3.1 - Comparison of the slug test rate-normalized response with the constant sandface rate solution.

intermediate times, a transition period one log-cycle long occurs and eventually the rate-normalized solution becomes identical to the constant sandface rate solution.

Fig. 2.3.2 presents computer generated data for a homogeneous reservoir with $C_D = 10^4$ and $s = 0$. The solid line in Fig. 2.3.2 represents the constant sandface rate solution, that is, p^*_{wcD}, and the square data points connected by a solid line represent p_{wcD}/q_{cD}. In constructing the rate-normalized group, the p_{wcD} solution is obtained by the numerical inversion of Eq. 2.2.15 and q_{cD} is computed from Eq. 2.2.22. At early times the normalized response is displaced approximately 0.4 units below the p^*_{wcD} solution. At intermediate times, a transition period occurs for approximately one log cycle and eventually the two solutions become identical. A semilog straight line fit through any span of the data shown in Fig. 2.3.2 would have a slope close to the desired 1.151 value. The skin factor obtained from such a straight line would slightly underestimate the true skin factor. Since $C_D = 10^4$, data corresponding to $t_D \leq 10^4$ corresponds to $t_D/C_D \leq 1$. Inspection of Fig. 2.2.3 shows that p_{wcD} for $t_D/C_D \leq 1$ *appears* to lie on the unit slope line. Theoretically, data will lie on the unit slope line only when $q_{cD} = 0$, that is, when no fluid flows from the reservoir into the wellbore. If $q_{cD} = 0$, Eq. 2.2.22 indicates that the logarithmic derivative of p_{wcD} will also lie on the unit slope line. The results of Fig. 2.2.3 show that p'_{wcD} falls below the unit slope line at all times, thus $q_{cD} \neq 0$ for all $t_D > 0$ even though the pressure solution *appears* to lie on the unit slope line for $t_D/C_D \leq 1$. In this work, data corresponding to this time period is referred to as wellbore storage dominated data. The results of Fig. 2.3.2 show that the rate-normalization method can be applied to data dominated by wellbore storage effects.

A comparison of the results of Figs. 2.3.1 and 2.3.2 indicates that the rate-normalization method based on the constant rate solution with wellbore storage and skin (see Eq. 2.3.9) agrees longer with p^*_{wcD} than does the rate-normalization applied to the slug test solution (see Eq. 2.3.8). Therefore, one should first convert the measured slug test pressure data into the equivalent constant rate data, and then apply the rate-normalization to this converted data in order to obtain the best

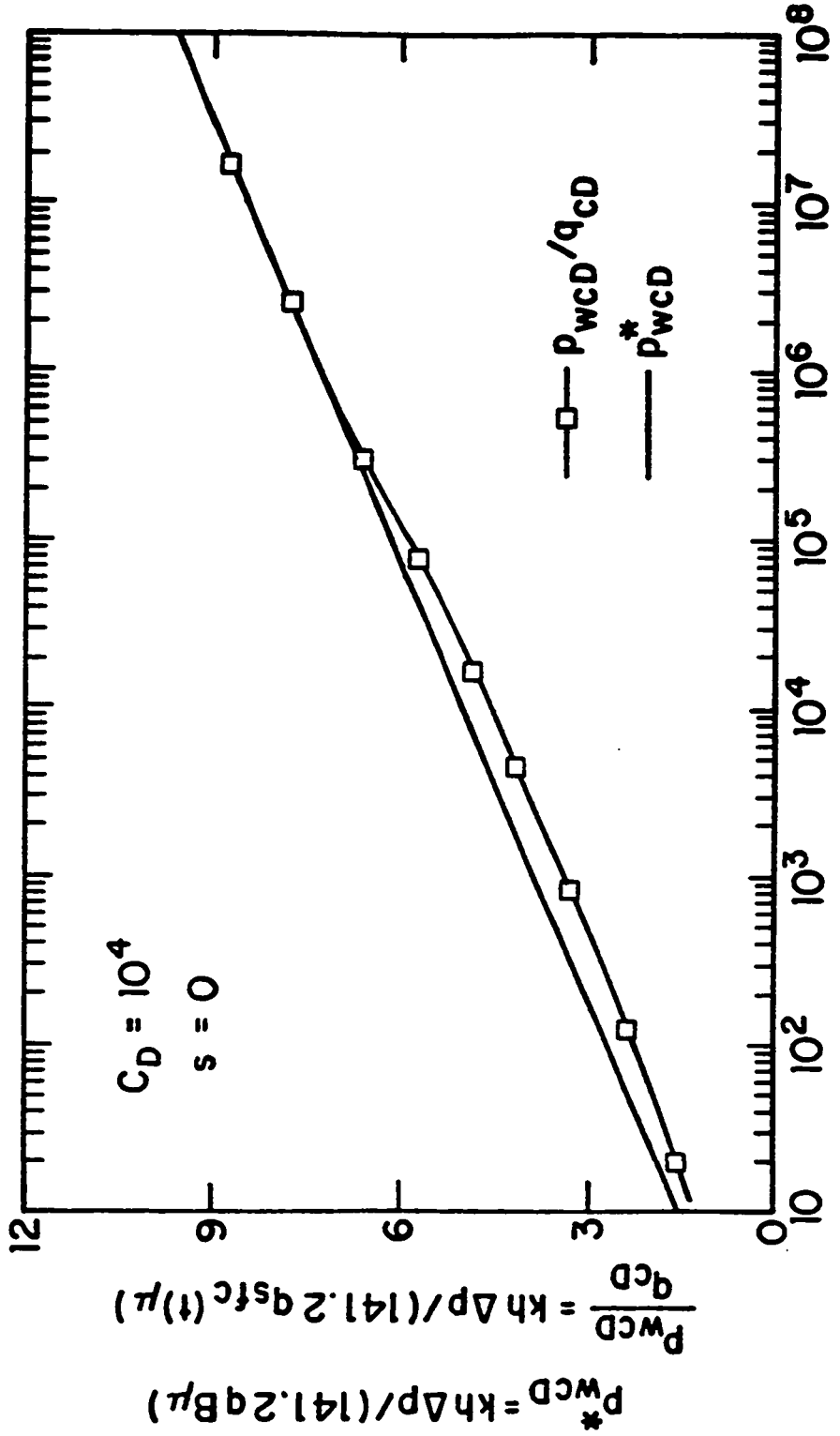

Fig. 2.3.2 - Comparison of the wellbore storage and skin rate-normalized response with the constant sandface rate solution.

approximation to the constant sandface rate solution. Using Eqs. 2.2.17 and 2.2.27 in Eq. 2.3.9, gives the form of the converted slug test rate-normalization method:

$$p^{\bullet}_{wcD} \approx \frac{I(p_{wD})}{C_D\,[1-p_{wD}]} = \frac{2.95\times10^{-4}kh}{\mu C}\,\frac{I(\Delta p)}{(p_{wf}-p_o)}, \tag{2.3.10}$$

For radial flow problems, $p^{\bullet}_{wcD}$ is given by the standard semilog equation and Eq. 2.3.10 becomes

$$\frac{2.95\times10^{-4}kh}{\mu C}\,\frac{I(\Delta p)}{(p_{wf}-p_o)} = 1.151\log\left(\frac{4t_D}{e^{\gamma}}\right)+\ s, \tag{2.3.11}$$

which suggests that a semilog plot of $I(\Delta p)/[p_{wf}(t)-p_o]$ versus t should yield a semilog straight line with a slope m given by

$$m = \frac{162.6(24)\mu C}{kh}, \tag{2.3.12}$$

where the slope m is in hours. The flow capacity, kh can be obtained from the rearrangement of Eq. 2.3.12. The skin factor can be estimated by the following equation

$$s = 1.151\left[\frac{[I(\Delta p)/(p_{wf}-p_o)]_{t^*}}{m} - \log\left(\frac{kt^*}{\phi\mu c_t r_w^2}\right)+3.23\right], \tag{2.3.13}$$

where $(t^*, [I(\Delta p)/(p_{wf}-p_o)]_{t^*})$ is any point on the straight line.

For nonradial flow problems, $I(\Delta p)/(p_{wf}-p_o)$ versus t data can be analyzed using type curves based on constant sandface rate solutions.

2.3.3 Convolution Methods

Once the flow geometry in the reservoir is properly identified by type-curve or rate-normalization procedures, the variable rate data can be analyzed by direct convolution (superposition, multi-rate) methods. In these methods, a particular solution is assumed for $p^{\bullet}_{wcD}$ and the continuously variable rate is replaced by a piecewise approximation[29–31]. Application of these methods to slug and closed

chamber test field data can be found in Refs. 60 and 61. In Refs. 60 and 61, p^*_{wcD} is replaced by the logarithmic approximation and the flow rate is calculated by means of numerical differentiation of the wellbore pressure (see Eq. 2.2.19). However, application of convolution directly to measured slug test data often results in scattered data due to noisy flow rate data. As discussed in the following paragraph, the noise is substantially reduced if convolution is applied instead to the converted slug test data. Consider the partition of the interval $[0, t_D]$ given by

$$0 = t_{0D} < t_{1D} < \cdots < t_{nD} < t_{n+1,D} = t_D. \tag{2.3.14}$$

Then, Duhamel's principle applied at the wellbore for constant surface rate wellbore storage and skin problems can be written as

$$p_{wcD}(t_D) = \int_0^{t_D} q_{cD}(\tau) \frac{dp^*_{wcD}}{dt_D}(t_D - \tau) d\tau =$$

$$\sum_{j=0}^{n} \int_{t_{jD}}^{t_{j+1,D}} q_{cD}(\tau) \frac{dp^*_{wcD}}{dt_D}(t_D - \tau) d\tau =$$

$$\sum_{j=0}^{n} q_{cD}(\hat{t}_{j+1,D}) \left[p^*_{wcD}(t_D - t_{jD}) - p^*_{wcD}(t_D - t_{j+1,D}) \right], \tag{2.3.15}$$

where $\hat{t}_{j+1,D}$ is a point selected in the interval

$$t_{jD} \le \hat{t}_{j+1,D} \le t_{j+1,D} \; ; \qquad j = 0, 1, \cdots, n \tag{2.3.16}$$

accordingly to the expression

$$\hat{t}_{j+1,D} = \theta_{j+1} t_{j+1,D} + (1 - \theta_{j+1}) t_{jD}. \tag{2.3.17}$$

Equation 2.3.15 can be rearranged to give

$$\frac{p_{wcD}(t_D)}{q_{cD}(\hat{t}_{n+1,D})} = \frac{\text{sum 1}}{q_{cD}(\hat{t}_{n+1,D})}. \tag{2.3.18}$$

Here,

$$\text{sum 1} = \sum_{j=0}^{n} \left[q_{cD}(\hat{t}_{j+1,D}) - q_{cD}(\hat{t}_{jD}) \right] p^*_{wcD}(t_D - t_{jD}), \tag{2.3.19}$$

and

$$q_{cD}(\hat{t}_{0D}) = 0. \tag{2.3.20}$$

The success of the rate-normalization procedure applied to problems where the variable sandface rate is due to wellbore storage effects suggests that we should choose $\hat{t}_{j+1,D} = t_{j+1,D}$, or equivalently, take $\theta_{j+1} = 1$ for all j. With this choice,

$$q_{cD}(\hat{t}_{j+1,D}) = q_{cD}(t_{j+1,D}), \tag{2.3.21}$$

and then the group on the left hand side of Eq. 2.3.18 is identical to the rate-normalized solution, $p_{wcD}(t_D)/q_{cD}(t_D)$; see Eq. 2.3.9. Note that, the resulting form of Eq. 2.3.18 is identical to the multi-rate method presented by Odeh and Jones[30]. Combining Eqs. 2.2.17, 2.2.22, 2.2.27, 2.3.19 and 2.3.21 in Eq. 2.3.18 gives

$$\frac{I(p_{wD})}{C_D\,[1 - p_{wD}(t_D)]} = \frac{\text{sum 2}}{[1 - p_{wD}(t_D)]}, \tag{2.3.22}$$

where

$$\text{sum 2} = \sum_{j=0}^{n} \left[p_{wD}(t_{jD}) - p_{wD}(t_{j+1,D})\right] p^{\bullet}_{wcD}(t_D - t_{jD}), \tag{2.3.23}$$

which is the working convolution equation for the converted slug test data. By replacing $p^{\bullet}_{wcD}$ in Eq. 2.3.23 by the constant sandface rate solution of interest, a analysis method can be constructed. For transient radial flow, the $p^{\bullet}_{wcD}$ term may be replaced by the standard logarithmic approximation and Eq. 2.3.22 becomes

$$\frac{I(p_{wD})}{C_D\,[1 - p_{wD}(t_{n+1,D})]} = 1.151\left[t_{msD} + \log\left(\frac{4}{e^{\gamma}}\right)\right] + s, \tag{2.3.24}$$

where the converted slug test multi-rate dimensionless time, t_{msD}, is defined by

$$t_{msD} = \sum_{j=0}^{n}\left[\frac{p_{wD}(t_{jD}) - p_{wD}(t_{j+1,D})}{1 - p_{wD}(t_{n+1,D})}\right]\log\left(t_{n+1,D} - t_{jD}\right). \tag{2.3.25}$$

The dimensional form of Eq. 2.3.24 for analyzing data is given by

$$\frac{2.95 \times 10^{-4} kh}{\mu C}\,\frac{I(\Delta p)}{[p_{wf}(t_{n+1}) - p_o]} = 1.151\, t_{ms} + \tilde{s}, \tag{2.3.26}$$

where t_{ms} and $\tilde{s}$ are given, respectively, by

$$t_{ms} = \sum_{j=0}^{n} \log(t_{n+1} - t_j) \left[\frac{p_{wf}(t_{j+1}) - p_{wf}(t_j)}{p_{wf}(t_{n+1}) - p_o} \right] \tag{2.3.27}$$

and

$$\tilde{s} = 1.151 \left[\log\left(\frac{k}{\phi \mu c_t r_w^2} \right) - 3.23 + 0.87s \right]. \tag{2.3.28}$$

A plot of $I(\Delta p)/[p_{wf}(t) - p_o]$ versus the converted slug test multi-rate time, t_{ms}, yields a slope m, given by

$$m = \frac{162.6(24)\mu C}{kh}, \tag{2.3.29}$$

where the slope m is in hours. Note that the slope equation of the convolution method is identical to the slope of the rate-normalization method.

The skin factor can be estimated by the following equation

$$s = 1.151 \left[\frac{[I(\Delta p)/(p_{wf} - p_o)]_{t^*_{ms}}}{m} - t^*_{ms} - \log\left(\frac{k}{\phi \mu c_t r_w^2} \right) + 3.23 \right], \tag{2.3.30}$$

where $(t^*_{ms}, [I(\Delta p)/(p_{wf} - p_o)]_{t^*_{ms}})$ is any point on the straight line.

Before closing this section, it is important to note that our analysis procedures (see Eqs. 2.3.1, 2.3.2, 2.3.7, 2.3.10, 2.3.22 and 2.3.26) utilize converted data. Since our method avoids numerical differentiation of data and the converted pressure data is obtained by integration of the measured slug test data, the converted data we analyze will normally be free of noise. This is a desirable property for field applications and is even more important when the raw pressure data exhibits oscillatory behavior as in one of the field examples presented later in this Chapter.

2.3.4 Results

In this section, computer generated data is used to verify the analysis procedure previously presented. The slug test pressure response considered here is based on a fully-penetrating well in a homogeneous, infinite reservoir. The p_{wD} solutions were obtained by numerical inversion of Eq. 2.2.7 for the following cases:

Case 1 - $t_{pD} = 10^4$; $C_D = 10^3$; $s = 0$.

Case 2 - $t_{pD} = 10^4$; $C_D = 10^3$; $s = 10$.

Fig. 2.3.3 presents a comparison of the converted slug test data with the wellbore storage and skin constant rate solutions for $C_D = 10^3$ and $s = 0$. This case represents a typical behavior of a slug test with good fluid level recovery during the producing time ($p_{wD}(t_{pD}) = 0.15$); see Fig. 2.2.1. The solid curve represents the constant rate dimensionless wellbore pressure, p_{wcD}, whereas the logarithmic derivative of p_{wcD} is shown by the dashed curve. The circular data points in Fig. 2.3.3 represent the converted slug test pressure, $I(p_{wD})/C_D$, given by Eq. 2.2.27. Note that an exact match with the p_{wcD} curve is obtained. The converted pressure derivative obtained from Eq. 2.2.28, shown by the triangular data points, is in perfect agreement with the constant rate pressure derivative p'_{wcD}. Thus, Fig. 2.3.3 illustrates the validity of the expressions which relate the slug test response and the constant rate solution under wellbore storage and skin effects.

Fig. 2.3.4 presents the application of the converted slug test rate-normalization method for Case 1. As discussed previously, the slug test rate-normalized group (Eq. 2.3.10), shown by the circular data points, is displaced below the constant sandface solution, p^*_{wcD}, represented by the solid line. The slug test rate-normalization method presents the correct 1.151 slope value at early times, indicated in the Figure by the dashed straight line. For times greater than $t_D = 3 \times 10^3$ ($t_D/C_D = 3$), the rate-normalized data points begins to deviate from the straight line and corresponds to the intermediate region presented by the rate-normalization method; see Fig. 2.3.2.

The convolution method applied to the slug test data of Case 1 is presented in Fig. 2.3.5. The group $I(p_{wD})/[C_D(1 - p_{wD})]$ versus the multi-rate time t_{msD}, which forms the basis of the converted convolution method, is shown by the circular data points, whereas the constant rate solution with no wellbore storage, p^*_{wcD}, is graphed as the solid line. The proposed convolution method presents a nearly perfect agreement as expected from the theoretical development of Eq. 2.3.24. The slight difference presented at early times is possibly due to errors introduced by the approximation of the integrals in the construction of the multi-rate time t_{msD} and by the fact that the logarithmic approximation is used to replace p^*_{wcD}.

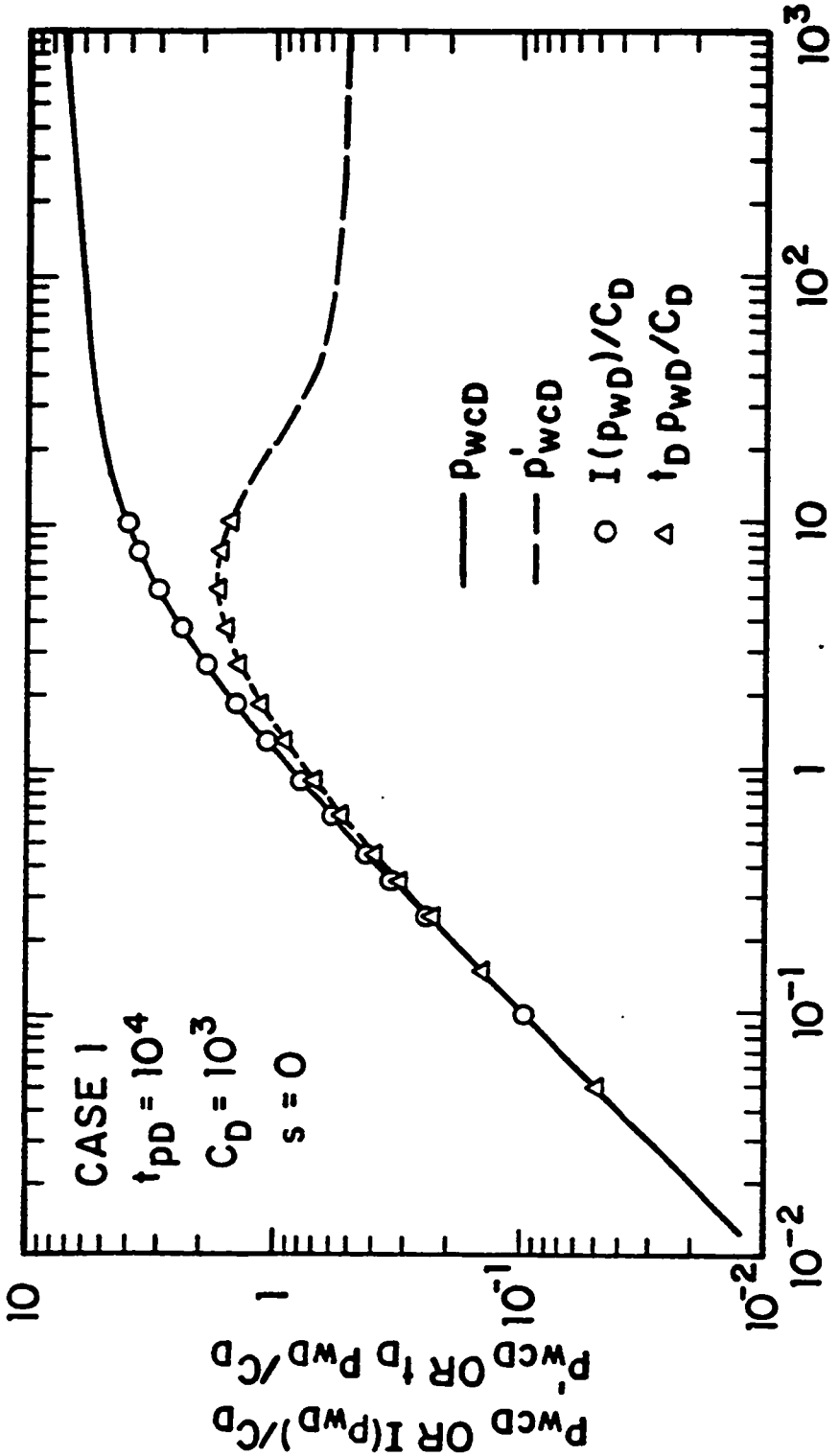

Fig. 2.3.3 - Comparison of the converted slug test response with the wellbore storage and skin constant rate solution; Case 1.

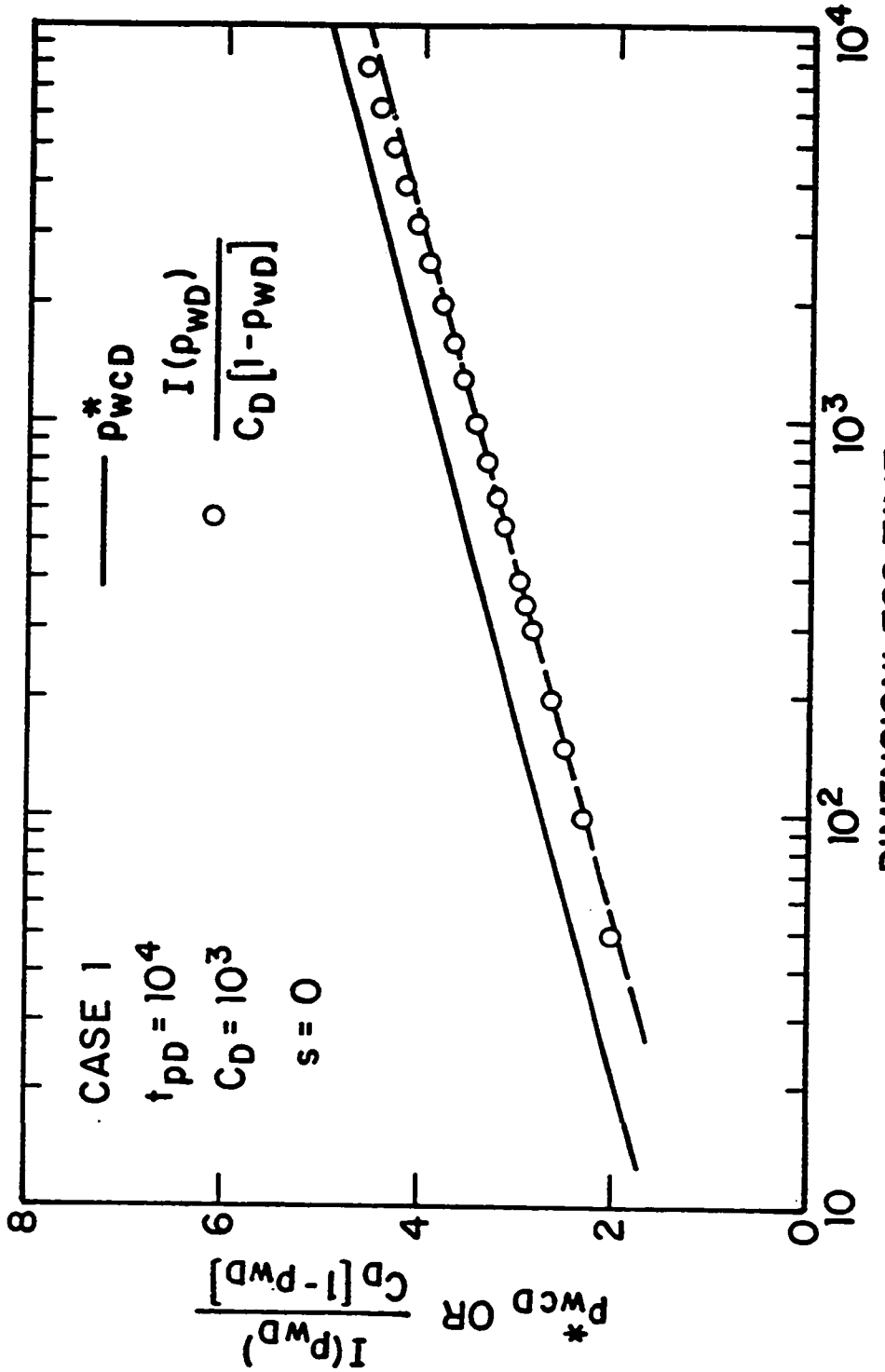

Fig. 2.3.4 - Correlation of the converted slug test rate-normalized response with the constant sandface rate solution; Case 1.

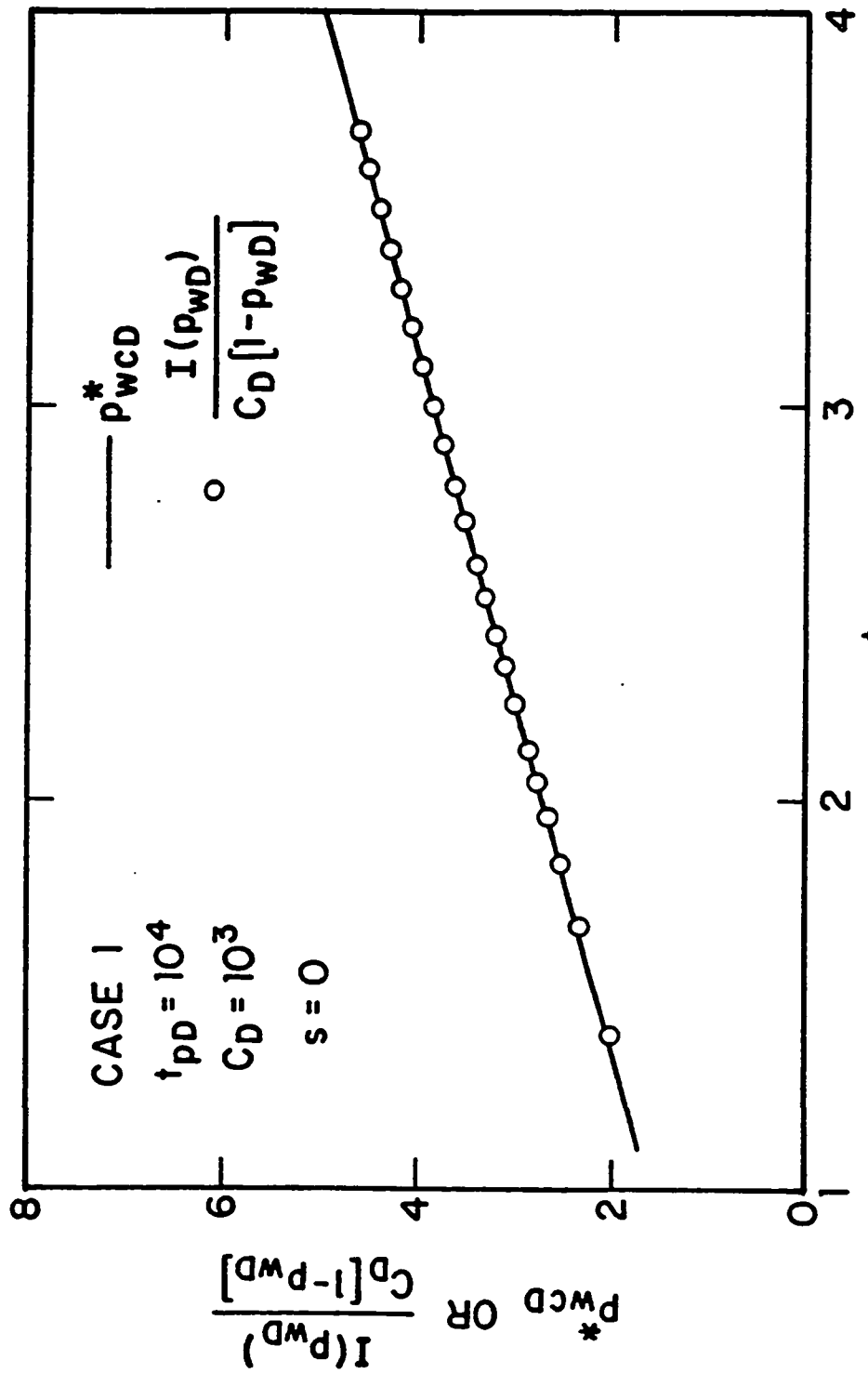

Fig. 2.3.5 - Correlation of the converted slug test convolution method with the constant sandface rate solution; Case 1.

Case 2 represents a case of much less fluid recovery ($p_{wD}(t_{pD}) = 0.51$) as can be seen by a quick inspection of Fig. 2.2.1. Case 2 represents the case of formation damage but a low permeability formation may also yield a low recovery during the testing time. The results of Figs. 2.3.6 - 2.3.8 are similar to those of Case 1 and are discussed in less detail.

The converted pressure and pressure derivative, shown in Fig. 2.3.6 by the circular and triangular data points, present an excellent agreement with the constant rate solutions p_{wcD} and p'_{wcD}. Note that most the converted data lie in the unit slope line region, which indicates that, in such a case, a unique type-curve match cannot be easily obtained with the derivative type curves of Figs. 2.2.3 and 2.2.4.

Fig. 2.3.7 presents the rate-normalization method for Case 2. The symbols convention used in this Figure are the same as in Fig. 2.3.4. Note that the straight line of slope 1.151 obtained for this case is slightly longer than in Case 1. As shown in Ref. 28, for the same value of the wellbore storage coefficient, the existence a positive skin factor delays the departure of the rate-normalized data from the initial straight line.

Fig. 2.3.8 illustrates the application of the converted convolution method for Case 2. Similar to Case 1, most of the $I(p_{wD})/[C_D(1-p_{wD})]$ versus t_{mscD} data points lie on the p^*_{wcD} solution. The results of Figs. 2.3.7 and 2.3.8 indicate that, for cases of low fluid recovery, or equivalently, when most of the converted data are dominated by wellbore storage effects, the rate-normalization and convolution methods can be successfully applied for parameter estimation.

2.3.4 Practical Considerations

In this section, we discuss some of the practical aspects of the new slug test analysis procedure.

The results of Figs. 2.3.3 and 2.3.6 indicate that the span of converted data obtained for type-curve matching is very limited when compared to the typical span of data available for type-curve matching obtained from constant rate tests. Although the converted slug test data of Figs. 2.3.3 and 2.3.6 are constructed from

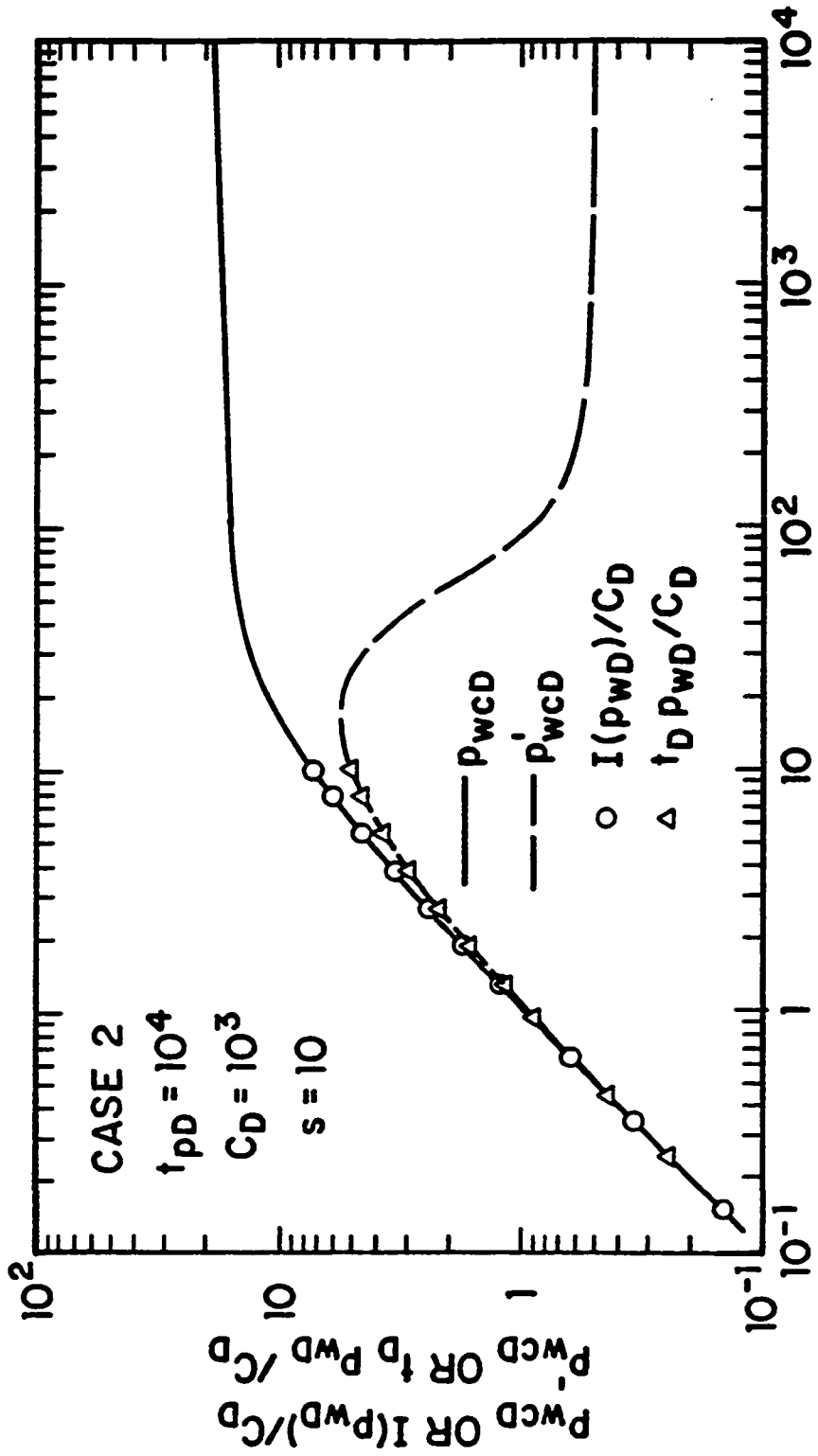

Fig. 2.3.6 - Comparison of the converted slug test response with the wellbore storage and skin constant rate solution; Case 2.

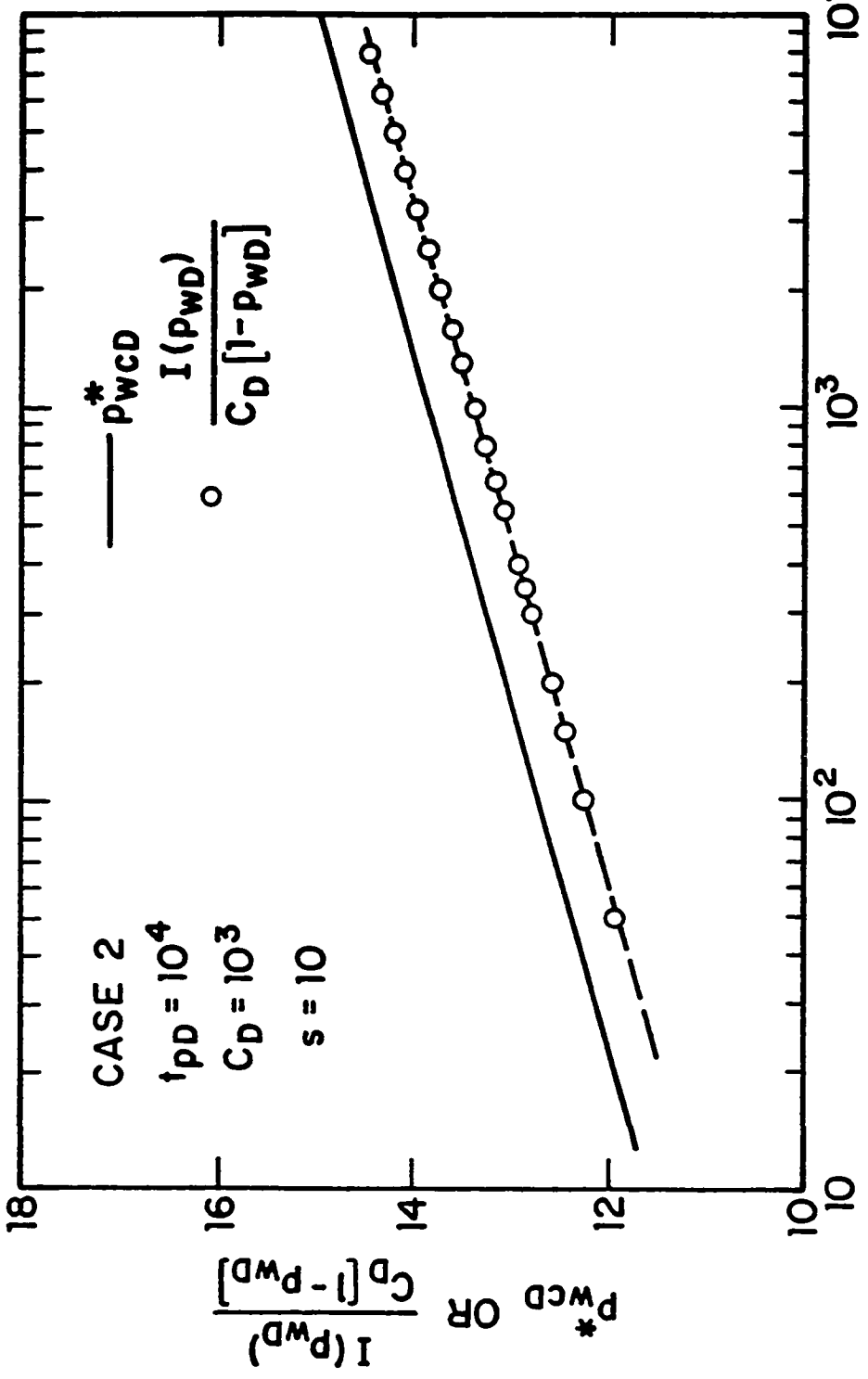

Fig. 2.3.7 - Correlation of the converted slug test rate-normalized response with the constant sandface rate solution; Case 2.

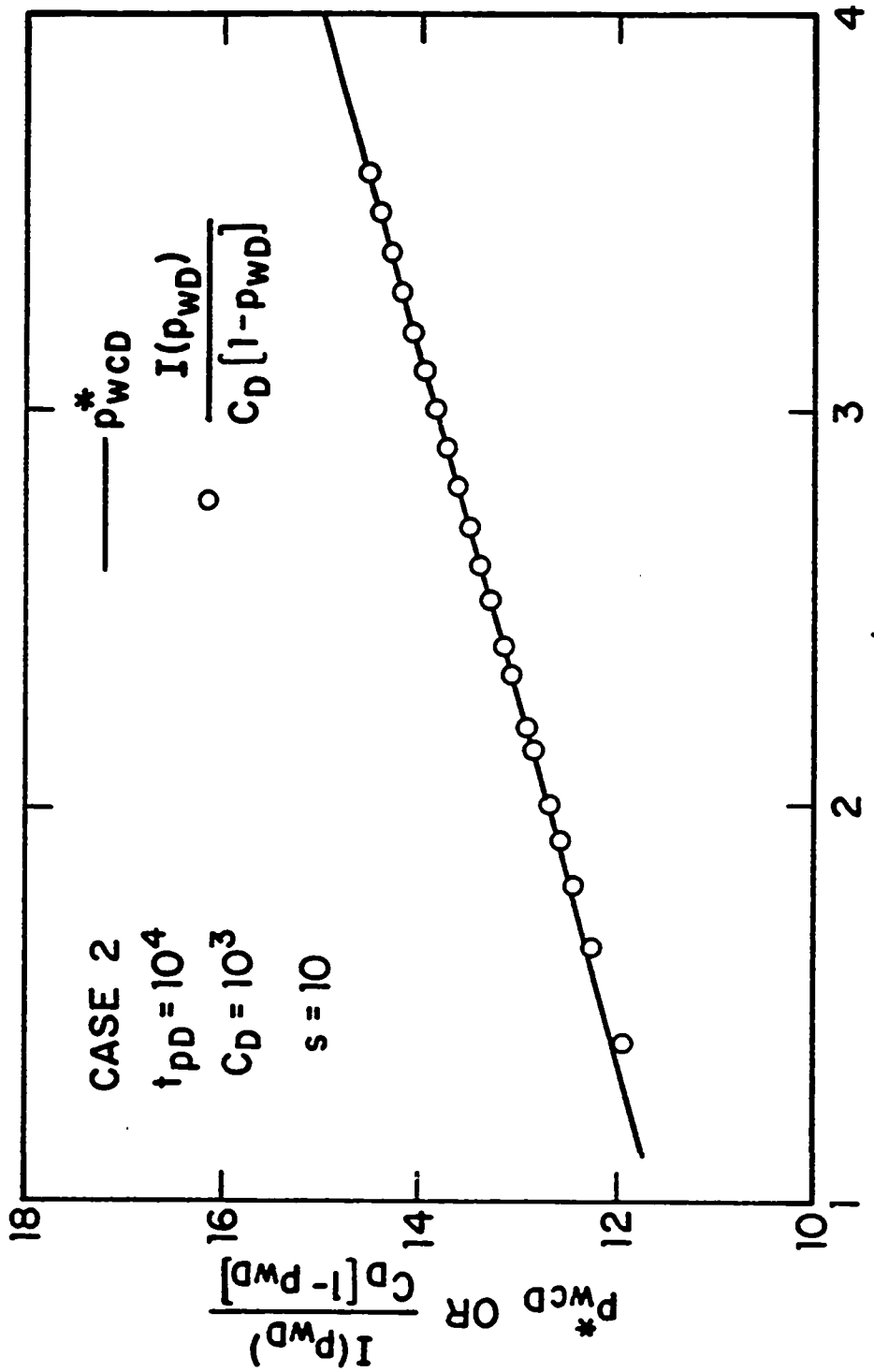

Fig. 2.3.8 - Correlation of the converted slug test convolution method with the constant sandface rate solution; Case 2.

computer generated data, they represent typical responses of slug test or DST flow period data obtained in field operations; see the Field Applications section. Note that the converted slug test data represent an equivalent constant rate test of short duration, in which most of the data is strongly affected by wellbore storage. In terms of field application, this means that a unique match with the wellbore storage and skin type curves cannot be easily obtained, especially with the Bourdet et al.[21] type curves, which requires movement of the field data plot in both the horizontal and vertical directions. In this regard, the use of the type curve of Fig. 2.2.4 improves the likelihood of obtaining a unique match of the converted data since the field data plot is moved only in one direction as previously discussed. However, a field log-log plot of $I(\Delta p)$ and $t\Delta p$ versus t can help to identify when a type-curve match is most likely to be successful. If the converted pressure derivative, $t\Delta p$, achieves a maximum and starts to decline, as in Case 1 (see Fig. 2.3.3), then a reasonably good match can be obtained with the Onur and Reynolds' derivative type curve for most of the cases. If the converted derivative data $t\Delta p$ barely departs from the converted pressure data $I(\Delta p)$ and from the unit slope line, as in Case 2 (see Fig. 2.3.6), then a reliable type curve match is not feasible. In this case, rate-normalization and convolution represent the only methods of analysis.

The field application of the new slug test procedure requires the use of some numerical integration scheme to evaluate the time integral of the measured slug test pressure data; see Eq. 2.3.2. A very simple algorithm to implement for practical purposes is given by the composite trapezoidal rule and its application is discussed here.

With the partition of the interval $[0, t_D]$ given by Eq. 2.3.14, Eq. 2.2.29 can be written as

$$\begin{aligned} I(p_{wD}) &= \int_0^{t_D} p_{wD}(\tau)d\tau \\ &= \sum_{j=0}^{n} \int_{t_{jD}}^{t_{j+1,D}} p_{wD}(\tau)d\tau. \end{aligned} \tag{2.3.31}$$

The trapezoidal rule formula[62] applied to the interval $[t_{jD}, t_{j+1,D}]$ of the partition, gives

$$\int_{t_{jD}}^{t_{j+1,D}} p_{wD}(\tau)d\tau = \left[\frac{p_{wD}(t_{jD}) + p_{wD}(t_{j+1,D})}{2}\right](t_{j+1,D} - t_{jD}) \; -$$

$$\frac{1}{12}\left(t_{j+1,D}-t_{jD}\right)^3\frac{d^2p_{wD}}{dt_D^2}(\xi_{j+1}), \tag{2.3.32}$$

where ξ_{j+1} satisfies

$$t_{jD}<\xi_{j+1}<t_{j+1,D}. \tag{2.3.33}$$

The error introduced by trapezoidal rule formula is given by the last term in the right hand side of Eq. 2.3.32. Using the trapezoidal rule in Eq. 2.3.31, one obtains

$$I(p_{wD})=\sum_{j=0}^{n}\left[\frac{p_{wD}(t_{jD})+p_{wD}(t_{j+1,D})}{2}\right]\left(t_{j+1,D}-t_{jD}\right)-$$

$$\frac{1}{12}\sum_{j=0}^{n}\left(t_{j+1,D}-t_{jD}\right)^3\frac{d^2p_{wD}}{dt_D^2}(\xi_{j+1})$$

$$\approx\sum_{j=0}^{n}\left[\frac{p_{wD}(t_{jD})+p_{wD}(t_{j+1,D})}{2}\right]\left(t_{j+1,D}-t_{jD}\right). \tag{2.3.34}$$

The numerical integration scheme for field applications is given by the following expression

$$I(\Delta p)\approx\sum_{j=0}^{n}\left[\frac{\Delta p(t_j)+\Delta p(t_{j+1})}{2}\right]\left(t_{j+1}-t_j\right). \tag{2.3.35}$$

Note that the last term on the right hand side of Eq. 2.3.32 represents the local error of the trapezoidal rule whereas the global error of the composite trapezoidal rule is given by the second summation term on the right hand side of Eq. 2.3.34. For homogeneous, infinite-acting systems the second derivative of the dimensionless slug test pressure solution is a positive, decreasing function for all times. Therefore, the local error term in Eq. 2.3.32 is always negative and the integral of the dimensionless slug test pressure solution is overestimated by the trapezoidal rule. Note that the numerical integration of the field slug test pressure data from Eq. 2.3.35 will also be overestimated. A question of practical interest concerns whether a given collection of pressure measurements has enough data points so that an accurate estimate of the pressure integral is obtained.

Fig. 2.3.9 presents a comparison of the constant rate solution p_{wcD}, shown as a solid line, versus the converted slug test pressure data represented by the circular data points. In this Figure, the $I(p_{wD})/C_D$ values were obtained by first evaluating

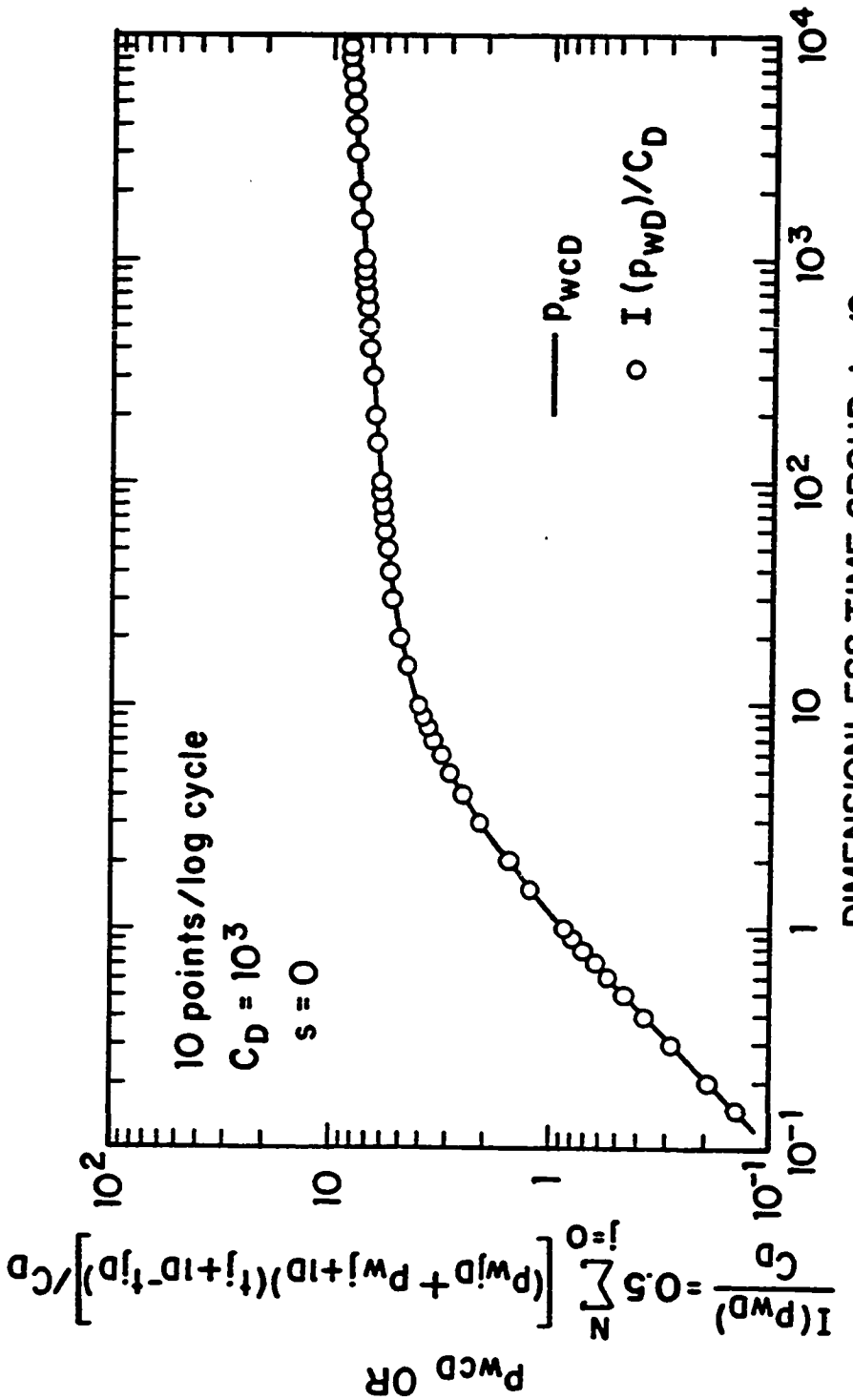

Fig. 2.3.9 - Correlation of the converted slug test data obtained by the trapezoidal rule formula; log-log plot.

p_{wD} from Eq. 2.2.7 and then applying the composite integration procedure of Eq. 2.3.34 using 10 data points per logarithmic cycle. Note that for comparison purposes, we extended the converted data beyond the range normally observed in field applications. The results of Fig. 2.3.9 indicate that a density of 10 points per log-cycle is accurate enough for type-curve matching applications.

Fig. 2.3.10 presents a semilog plot for the same results shown in Fig. 2.3.9. Note that the converted pressure group $I(p_{wD})/C_D$ presents a good agreement with the constant rate solution for $t_D/C_D \leq 20$, which corresponds to $t_D \leq 2 \times 10^4$. After this time, the converted pressure data obtained from the trapezoidal rule slightly overestimates the correct constant rate solution. Note that the use of a log-based data density forces the time step to be increased at the beginning of each log-cycle. Most of field slug test data is limited to times correspondent to $t_D/C_D \leq 20$, therefore, 10 points per log-cycle will be sufficiently accurate for straight-line analysis, such as the rate-normalization and convolution methods discussed in the Analysis Procedure section.

Given a collection of field pressure measurements, an average data-density can be calculated by the following expression

$$d_{avg} = \frac{\mathrm{n}}{\log\left(t_{n+1}/t_1\right)}, \tag{2.3.36}$$

where n denotes the number of data points and t_{n+1} and t_1 are the times of the last and first data measurements. As a rule of thumb, if the calculated d_{avg} is greater than 10, the application of the composite integration as described here will, in general, provide an accurate value of $I(\Delta p)$. For a sparse data set, a more powerful numerical integration scheme is required. The discussion of these techniques is beyond the scope of this work.

The field implementation of the new slug test analysis procedure requires the knowledge of both p_i and p_o. The initial reservoir pressure p_i is required in the computation of the converted groups $I(\Delta p)$ and $t\Delta p$; see Eqs. 2.3.1 - 2.3.3. The initial wellbore pressure p_o is also required in the calculation of $I(\Delta p)$ when the numerical scheme given by Eq. 2.3.35 is used. However, the p_o value is used only

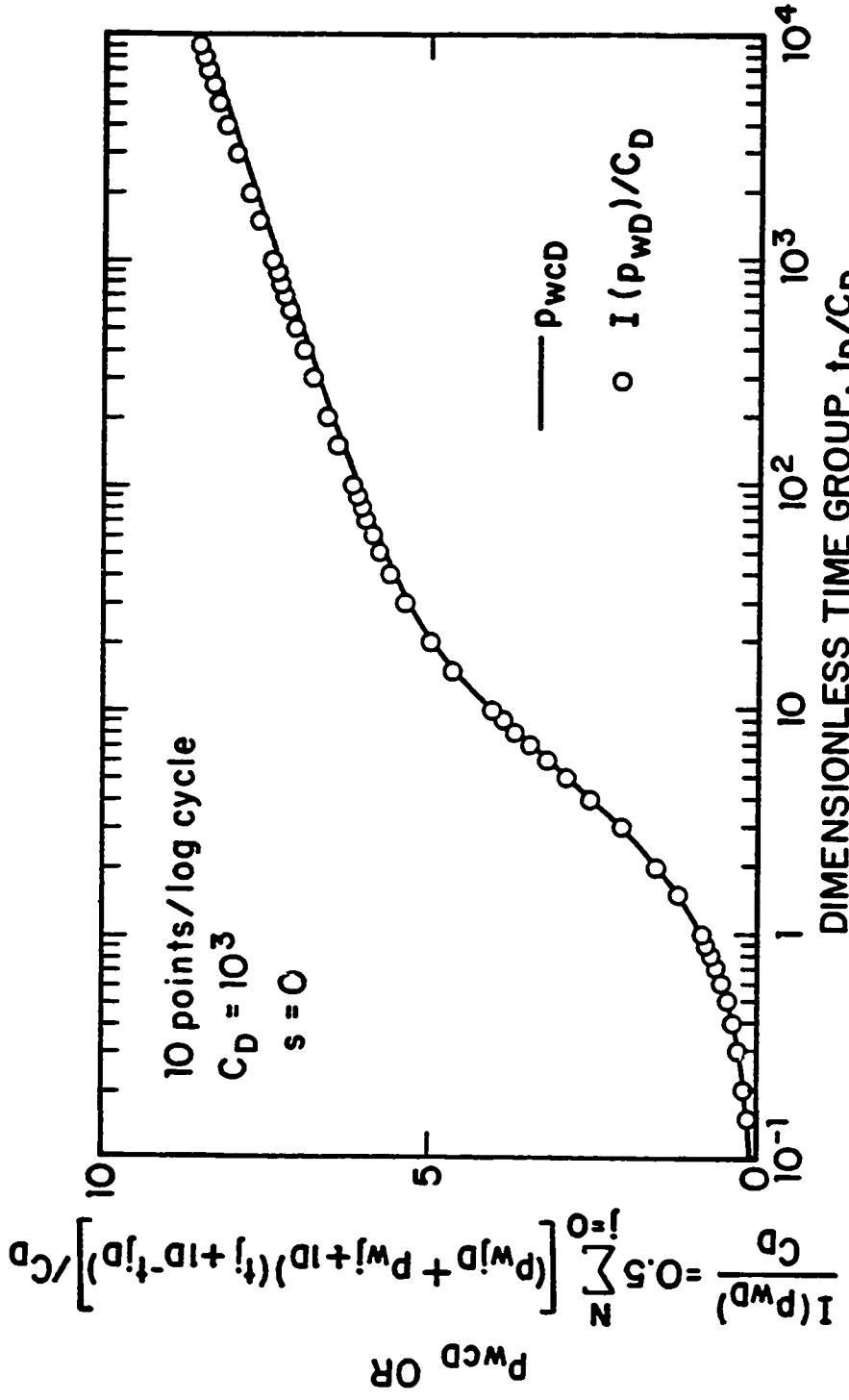

Fig. 2.3.10 - Correlation of the converted slug test data obtained by the trapezoidal rule formula; semilog plot.

once in the computations therefore, the error introduced by the choice of p_o is a constant. Note that at early times $I(\Delta p)$ increases linearly with time and the error quickly becomes less important in the computations. There is a class of numerical integration schemes, known as open Newton-Cotes formulas, which does not require an estimate of p_o. An example of such a scheme is given by the midpoint rule[62]. Therefore, an accurate estimate of p_o is not needed for the analysis of the slug test converted data by type-curve analysis. However, both rate-normalization and convolution methods require an estimate of p_o; see Eqs. 2.3.11 and 2.3.26.

For DST flow period data, the initial reservoir pressure p_i can be obtained from the buildup pressure response using methods which are described in Chapter III. For the conventional slug test, p_i has to be estimated from other sources. The initial wellbore pressure p_o is generally measured or can be estimated to a good degree of accuracy. For example, for a DST with a cushion, the imposed initial pressure is given by the hydrostatic pressure exerted by the fluid column of the cushion. In some ground water operations, the instantaneous pressure drop is obtained by first immersing an object into the water well, and then, after stabilization of the water level, by removing it quickly. As shown in Ref. 2, from the knowledge of the object weight, the pressure p_o can easily be estimated. In the following, we present a procedure for determining p_o for cases when it cannot be estimated by any other means.

At early times the constant rate pressure solution can be approximated by

$$p_{wcD} = \frac{t_D}{C_D}, \tag{2.3.37}$$

which gives the well known unit slope line equation during wellbore storage dominated flow. Combining Eq. 2.3.37 and Eq. 2.2.27, and using the dimensionless definitions given before, one obtains

$$t = \frac{I(\Delta p)}{p_i - p_o}. \tag{2.3.38}$$

The above result indicates that at early times, a log-log plot of $I(\Delta p)$ versus t exhibits a unit slope line. Any point in the unit slope line can be used to estimate p_o from the following equation

$$p_o = p_i - \frac{[I(\Delta p)]_M}{t_M}, \tag{2.3.39}$$

where $(t_M, [I(\Delta p)]_M)$ represents any point on the unit slope line. Some remarks about the application of Eq. 2.3.39 are in order:

(i) The value of the initial reservoir pressure p_i does not affect the value of p_c obtained from Eq. 2.3.39, as one can see by expanding the $[I(\Delta p)]_M$ term.

(ii) Strictly speaking, no data points lie exactly on the unit slope line, therefore Eq. 2.3.39 will normally tend to overestimate p_o.

(iii) Eq. 2.3.39 may not work if the computed $I(\Delta p)$ values are obtained from a closed Newton-Cotes formula. For example, if the unit slope is drawn through the first $I(\Delta p)$ point calculated from the trapezoidal rule, the p_o value obtained from Eq. 2.3.39 is equal to the arithmetic average of the p_o used in Eq. 2.3.35 and $p_{wf}(t_1)$. Because of this behavior, Eq. 2.3.39 should be applied with caution.

In the Field Applications section, we present a case in which the application of Eq. 2.3.39 yields a good estimate of p_o.

2.4 Field Applications

2.4.1 Example A

The field example considered here was presented by Waller and Krase[63] and corresponds to a slug test conducted during a perforating run in an underbalanced condition. This type of test typically shows a highly oscillatory pressure behavior at early times due the explosion of the perforating charges, and most of the time, one has to smooth the data before any conventional analysis techniques can be applied[60]. This example illustrates that the new procedure can be successfully applied to raw pressure data as collected in the field.

The measured pressure and the converted pressure versus time data are presented in Table 2.4.1. Other test data are also presented in Table 2.4.1. Columns 2, 3 and 4 of Table 2.4.1, respectively, show the measured pressure data, the equivalent (or converted) pressure data and the equivalent logarithmic derivative of the converted pressure data. The converted pressure data shown in Column 3 was calculated from Eq. 2.3.35. The average data-density for this field example evaluate from Eq. 2.3.36 gives $d_{avg} = 28$, therefore, based on previous discussion, the composite trapezoidal integration will provide accurate results. The pressure derivative of converted data given in Column 4, was computed by multiplying the measured slug test pressure drop, Δp, by the correspondent time t; see Eq. 2.3.2. Column 5 gives values of the converted pressure derivative group $\Delta p/(2\Delta p')$ used in the type curves of Fig. 2.2.4 which were obtained by dividing Column 3 by twice the value of Column 4; see Eq. 2.3.7. The converted rate-normalized data is presented in the last column of Table 2.4.1 and represents the ratio of the values of Column 3, $I(\Delta p)$, to the pressure difference $(p_{wf} - p_o)$; see Eq. 2.3.10. Note that two values in Column 6 are not shown. They correspond to measured pressures which are smaller than p_o, so the rate-normalized group becomes negative at those pressures.

Fig. 2.4.1 shows a log-log plot of the converted pressure drop (Column 3 of Table 2.4.1) and the equivalent pressure derivative (Column 4) versus time. The converted data in Fig. 2.4.1 presents the characteristic behavior of Bourdet et al.'s type curve solutions (Fig. 2.2.3). Note that slug test was run long enough so that the converted derivative clearly displays a maximum around 13 minutes, therefore, one may attempt to determine reservoir parameters using the type-curve matching procedure presented earlier. Fig. 2.4.1 also shows a fairly well defined unit slope line through the early time data points, which was used to determine the initial wellbore flowing pressure, $p_o = 3165$ psi; see Eq. 2.3.39. As discussed in Ref. 63, the explosion of the perforating charges remove mass from the wellbore. Therefore, the wellbore pressure measured just prior to perforating should not be used as p_o. Ref. 63 determined $p_o = 3185$ psi by extrapolating the early pressure trend to time zero, which is reasonably close to our estimated value. Actually, our type curve

Table 2.4.1

Field Example A

$p_i = 3427.5$ psi $\quad p_o = 3165.0$ psi $\quad c_{wf} = 7.3 \times 10^{-6}$ psi^{-1}

$V_w = 331$ bbl $\quad h = 39.37$ ft $\quad c_t = 23 \times 10^{-6}$ psi^{-1}

$\mu = 0.409$ cp $\quad r_w = 0.354$ ft $\quad \phi = 0.45$

time min	p_{wf} psi	$I(\Delta p)$ psi-min	$t\Delta p$ psi-min	$I(\Delta p)/2t\Delta p$ dimensionless	$I(\Delta p)/(p_{wf} - p_o)$ min
0.0833	3209	2.003E+01	1.820E+01	5.503E-01	4.553E-01
0.1667	3071	4.401E+01	5.943E+01	3.703E-01	-
0.2500	3192	6.867E+01	5.888E+01	5.832E-01	2.543E+00
0.3333	3157	8.974E+01	9.016E+01	4.977E-01	-
0.4167	3208	1.102E+02	9.147E+01	6.023E-01	2.562E+00
0.5000	3229	1.276E+02	9.925E+01	6.427E-01	1.994E+00
0.6667	3230	1.606E+02	1.317E+02	6.098E-01	2.471E+00
0.7500	3243	1.765E+02	1.384E+02	6.378E-01	2.263E+00
0.8333	3207	1.934E+02	1.837E+02	5.262E-01	4.604E+00
0.9167	3235	2.106E+02	1.765E+02	5.967E-01	3.008E+00
1.0000	3252	2.259E+02	1.755E+02	6.436E-01	2.597E+00
1.0833	3232	2.414E+02	2.118E+02	5.699E-01	3.603E+00
1.1667	3245	2.517E+02	2.129E+02	6.038E-01	3.214E+00
1.2500	3251	2.721E+02	2.206E+02	6.166E-01	3.164E+00
1.3333	3244	2.871E+02	2.447E+02	5.867E-01	3.634E+00
1.4167	3255	3.019E+02	2.444E+02	6.177E-01	3.355E+00
1.5000	3251	3.165E+02	2.648E+02	5.977E-01	3.680E+00
1.5833	3254	3.310E+02	2.747E+02	6.025E-01	3.720E+00
1.6667	3260	3.453E+02	2.792E+02	6.184E-01	3.643E+00
1.7500	3255	3.594E+02	3.019E+02	5.953E-01	3.994E+00
1.8333	3262	3.735E+02	3.034E+02	6.155E-01	3.850E+00
1.9167	3264	3.872E+02	3.134E+02	6.178E-01	3.912E+00
2.0000	3262	4.009E+02	3.310E+02	6.056E-01	4.133E+00
2.0833	3268	4.145E+02	3.323E+02	6.234E-01	4.024E+00
2.1667	3268	4.278E+02	3.456E+02	6.189E-01	4.153E+00
2.2500	3269	4.410E+02	3.566E+02	6.183E-01	4.240E+00
2.3333	3273	4.540E+02	3.605E+02	6.297E-01	4.204E+00
2.5000	3274	4.797E+02	3.838E+02	6.250E-01	4.401E+00
2.5833	3278	4.923E+02	3.862E+02	6.374E-01	4.357E+00
2.6667	3279	5.048E+02	3.960E+02	6.373E-01	4.428E+00
2.7500	3280	5.171E+02	4.056E+02	6.374E-01	4.496E+00
2.8333	3282	5.293E+02	4.122E+02	6.420E-01	4.524E+00
2.9167	3284	5.413E+02	4.185E+02	6.467E-01	4.549E+00
3.0000	3285	5.533E+02	4.275E+02	6.471E-01	4.610E+00
3.5000	3295	6.220E+02	4.638E+02	6.706E-01	4.785E+00
4.0000	3302	6.865E+02	5.020E+02	6.838E-01	5.011E+00
4.5000	3310	7.473E+02	5.288E+02	7.066E-01	5.153E+00
5.5000	3322	8.588E+02	5.803E+02	7.400E-01	5.470E+00
6.0000	3329	9.098E+02	5.910E+02	7.697E-01	5.547E+00
6.5000	3334	9.578E+02	6.078E+02	7.880E-01	5.667E+00

Table 2.4.1 (cont'd)

time min	p_{wf} psi	$I(\Delta p)$ psi-min	$t\Delta p$ psi-min	$I(\Delta p)/2t\Delta p$ dimensionless	$I(\Delta p)/(p_{wf}-p_o)$ min
7.0000	3339	1.003E+03	6.195E+02	8.097E-01	5.766E+00
7.5000	3344	1.046E+03	6.263E+02	8.353E-01	5.845E+00
8.0000	3348	1.087E+03	6.360E+02	8.546E-01	5.940E+00
8.5000	3352	1.126E+03	6.418E+02	8.771E-01	6.020E+00
9.0000	3355	1.163E+03	6.525E+02	8.910E-01	6.120E+00
9.5000	3359	1.198E+03	6.508E+02	9.205E-01	6.175E+00
10.000	3362	1.232E+03	6.550E+02	9.401E-01	6.251E+00
10.500	3365	1.264E+03	6.563E+02	9.627E-01	6.318E+00
11.000	3368	1.294E+03	6.545E+02	9.885E-01	6.374E+00
11.500	3370	1.323E+03	6.613E+02	1.001E+00	6.455E+00
12.000	3373	1.351E+03	6.540E+02	1.033E+00	6.496E+00
12.500	3375	1.378E+03	6.563E+02	1.050E+00	6.562E+00
13.000	3377	1.404E+03	6.565E+02	1.069E+00	6.621E+00
13.500	3378	1.429E+03	6.683E+02	1.069E+00	6.708E+00
14.000	3380	1.453E+03	6.650E+02	1.092E+00	6.758E+00
14.500	3382	1.476E+03	6.598E+02	1.119E+00	6.803E+00
15.000	3384	1.499E+03	6.525E+02	1.148E+00	6.842E+00
15.500	3387	1.520E+03	6.278E+02	1.210E+00	6.845E+00
16.000	3387	1.540E+03	6.480E+02	1.188E+00	6.936E+00
17.000	3390	1.579E+03	6.375E+02	1.238E+00	7.017E+00
18.000	3392	1.615E+03	6.390E+02	1.264E+00	7.116E+00
19.000	3394	1.650E+03	6.365E+02	1.296E+00	7.204E+00
20.000	3397	1.682E+03	6.100E+02	1.378E+00	7.249E+00
21.000	3398	1.712E+03	6.195E+02	1.382E+00	7.347E+00
22.000	3400	1.740E+03	6.050E+02	1.438E+00	7.405E+00
23.000	3401	1.767E+03	6.095E+02	1.450E+00	7.488E+00
24.000	3403	1.793E+03	5.880E+02	1.524E+00	7.533E+00
25.000	3403	1.817E+03	6.125E+02	1.483E+00	7.636E+00
26.000	3405	1.841E+03	5.850E+02	1.573E+00	7.670E+00
27.000	3406	1.863E+03	5.805E+02	1.604E+00	7.729E+00
28.000	3407	1.884E+03	5.740E+02	1.641E+00	7.784E+00
29.000	3408	1.904E+03	5.655E+02	1.683E+00	7.834E+00
30.000	3409	1.923E+03	5.550E+02	1.732E+00	7.880E+00
35.000	3412	2.008E+03	5.425E+02	1.850E+00	8.129E+00
40.000	3415	2.078E+03	5.000E+02	2.078E+00	8.311E+00
45.000	3417	2.135E+03	4.725E+02	2.260E+00	8.473E+00
50.000	3419	2.183E+03	4.250E+02	2.568E+00	8.594E+00
54.500	3421	2.217E+03	3.543E+02	3.128E+00	8.658E+00
59.500	3422	2.247E+03	3.273E+02	3.432E+00	8.741E+00
64.500	3422	2.274E+03	3.548E+02	3.205E+00	8.848E+00
69.500	3424	2.297E+03	2.433E+02	4.720E+00	8.867E+00
74.500	3424	2.314E+03	2.608E+02	4.437E+00	8.934E+00

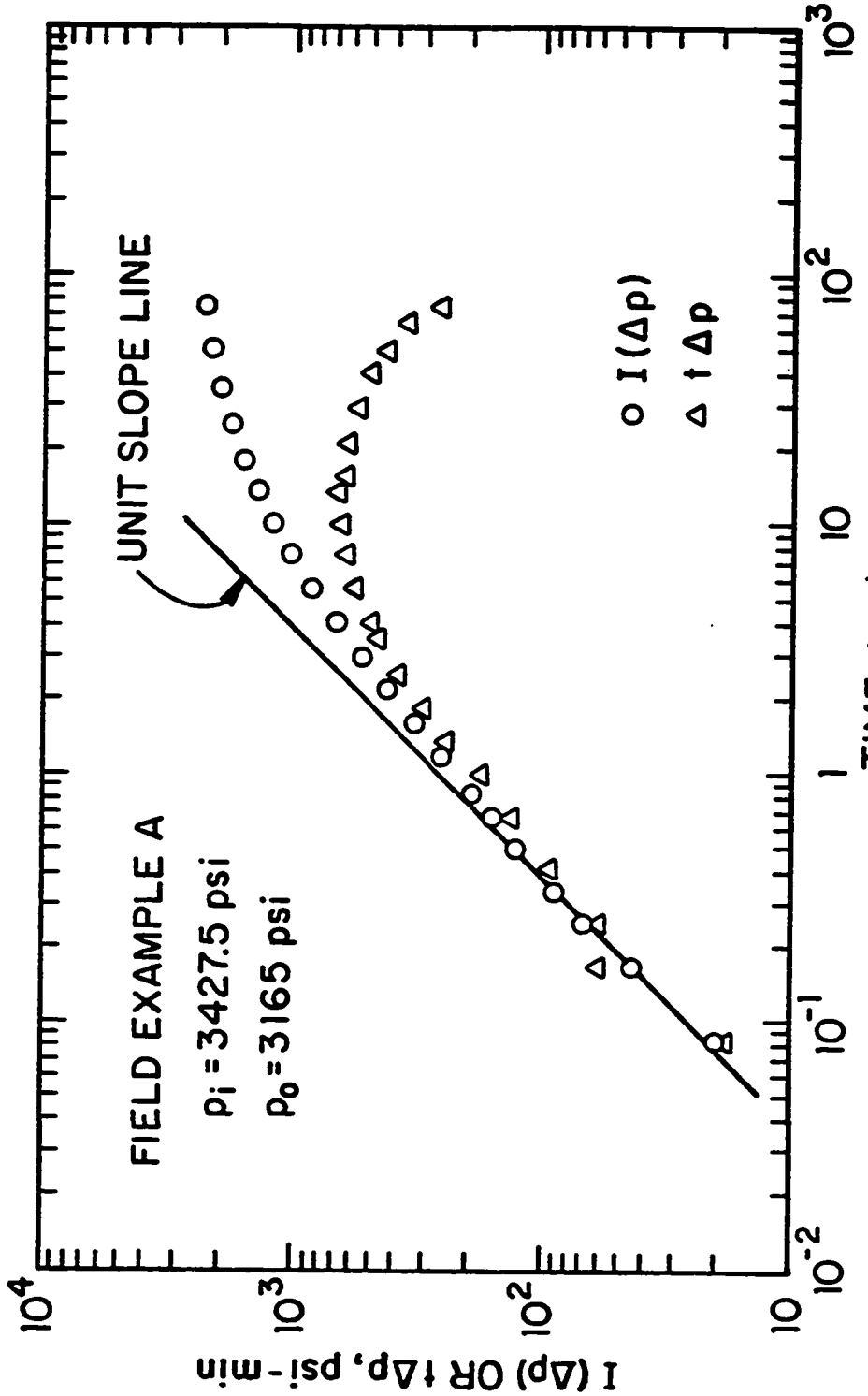

Fig. 2.4.1 - Log-log plot of the converted pressure drop and its derivative; Field Example.

analysis was performed in two steps. First, based on the p_o value estimated by Ref. 63, $I(\Delta p)$ was calculated using Eq. 2.3.35. Upon construction of a log-log plot similar to Fig. 2.4.1, the unit slope analysis provided $p_o = 3165$ psi and the calculations were repeated for consistency. Note that, the successful application of Eq. 2.3.39 in this field data is due to the oscillatory behavior shown by the wellbore pressure at early times.

Fig. 2.4.2 shows a type-curve match of a log-log plot of $I(\Delta p)/[2t\Delta p]$ (Column 5 of Table 2.4.1) versus t with the type curve solutions of Fig. 2.2.4 which was obtained by moving the field data plot only in the horizontal direction. The solid curve shown in Fig. 2.4.2 corresponds to the pressure derivative ratio type curves of Fig. 2.2.4 for $C_D \exp(2s) = 40$. The early part of the converted data cannot be accurately matched with the type curve solution due the strong oscillation in the measured pressure during that period. At late times, the data bend upward because the pressure difference, $\Delta p = p_i - p_{wf}$, that appears in the denominator of the pressure derivative ratio, is less accurate as p_{wf} approaches p_i. This loss of accuracy in Δp occurs because the pressure data presented in Ref. 63 does not contain enough accurate digits. At intermediate times, the match obtained is excellent and indicates that the measured data is representative of the radial flow geometry assumed in constructing the type curves. The match shown in Fig. 2.4.2 yields the time match-point values, $(t_D/C_D)_M = 4.0$ and $(t)_M = 10$ minutes. Using these time-match point values, the transmissibility can be computed directly from Eq. 2.3.5 as follows

$$\begin{aligned} \frac{kh}{\mu} &= 141.2\frac{(24)(331)(7.3\times 10^{-6})(4.0)}{(10/60)} \\ &= 196.6 \text{ md-ft/cp}, \end{aligned} \tag{2.4.1}$$

which gives $kh = 80.4$ md-ft. The wellbore storage coefficient C used in Eq. 2.4.1 was determined directly from Eq. 2.1.5 using the values of V_w and c_{wf} given in Table 2.4.1.

The type curve match of Fig. 2.4.2 fixes the correspondence between the time scales, therefore the equivalent pressure drop $I(\Delta p)$ can be type-curve matched by

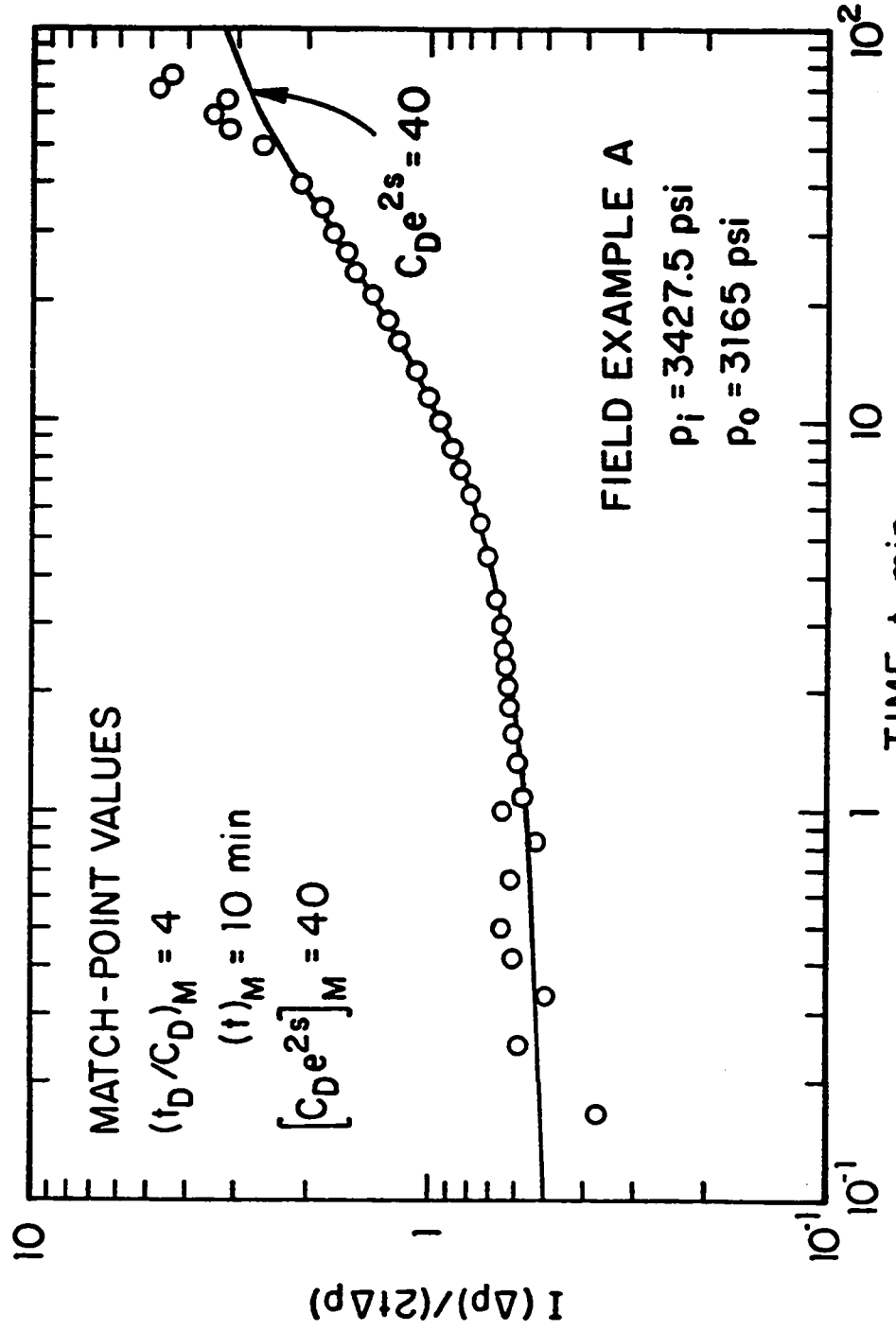

Fig. 2.4.2 - Type-curve match of the converted pressure derivative ratio; Field Example A.

moving the field plot only in the vertical direction. The type curve match is shown in Fig. 2.4.3, where the three solid curves represent the dimensionless wellbore pressure solutions of Fig. 2.2.4 for $C_D \exp(2s) = 10$, 40 and 100. Note that the converted data is matched with the $C_D \exp(2s) = 40$ type curve solution. As mentioned before, for the slug test problem, this step is not necessary but it provides a check on the estimate of kh obtained from the time match-point values. As indicated in Fig. 2.4.3, the match-point values are $(p_{wcD})_M = 1.6$ and $[I(\Delta p)]_M = 1000$ psi-min. The transmissibility can be computed from Eq. 2.3.4 as

$$\frac{kh}{\mu} = 141.2\frac{(24)(331)(7.3\times 10^{-6})(3427.5-3165)(1.6)}{(1000/60)} = 206.4 \text{ md-ft/cp}, \tag{2.4.2}$$

which yields $kh = 84.4$ md-ft. The results obtained by Eqs. 2.4.1 and 2.4.2 are in good agreement.

From Eqs. 2.1.3 and 2.1.5 and the data given in Table 2.4.1, one obtains $C_D = 42.3$. The skin factor calculated from Eq. 2.3.6 is

$$s = \frac{1}{2}\ln\left(\frac{40}{42.3}\right) = -0.03. \tag{2.4.3}$$

From the type-curve match of the converted field data shown in Figs. 2.4.2 and 2.4.3, it appears that the field data is representative of radial flow in a homogeneous reservoir. Thus, for all practical purposes, p^*_{wcD} is given by the well known semilog equation and the rate-normalization method, given by Eq. 2.3.11, can be applied to analyze the converted data.

Fig. 2.4.4 presents a semilog plot of the rate-normalized converted data, $I(\Delta p)/[p_{wf}(t) - p_o]$ versus t. The circular data points represent the converted field data shown in Column 6 of Table 2.4.1. A well-defined semilog straight line is obtained with a slope $m = 3.259$ minutes. Note that some scatter is obtained in the data at early times and the last points deviate from the straight line; see the related discussion of Fig. 2.4.2. The transmissibility can be estimated from the obvious rearrangement of Eq. 2.3.12 and is given by

$$\frac{kh}{\mu} = \frac{162.6(24)(331)(7.3\times 10^{-6})}{(3.259/60)} = 173.6 \text{ md-ft/cp}, \tag{2.4.4}$$

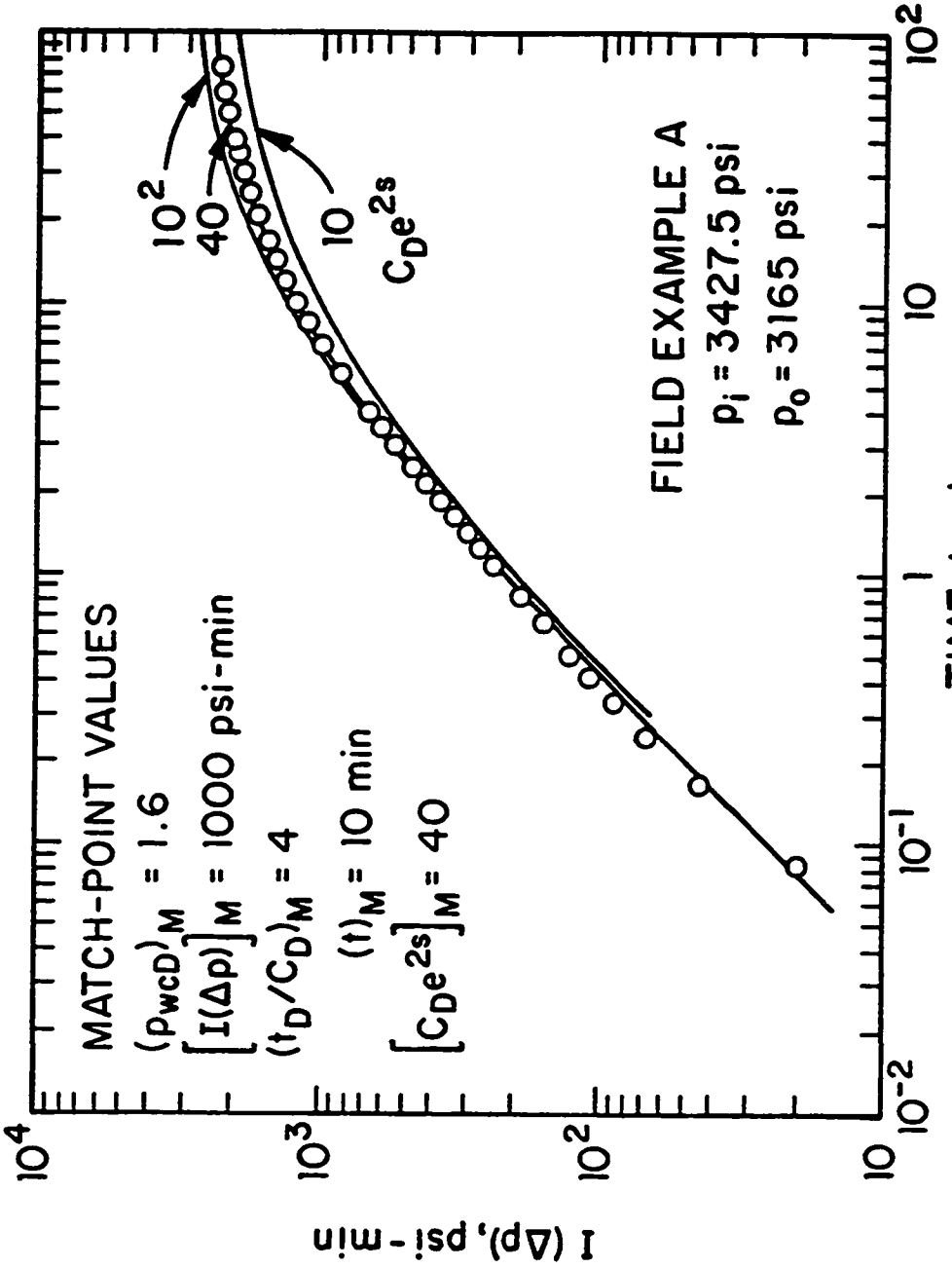

Fig. 2.4.3 - Type-curve match of the converted pressure drop; Field Example A.

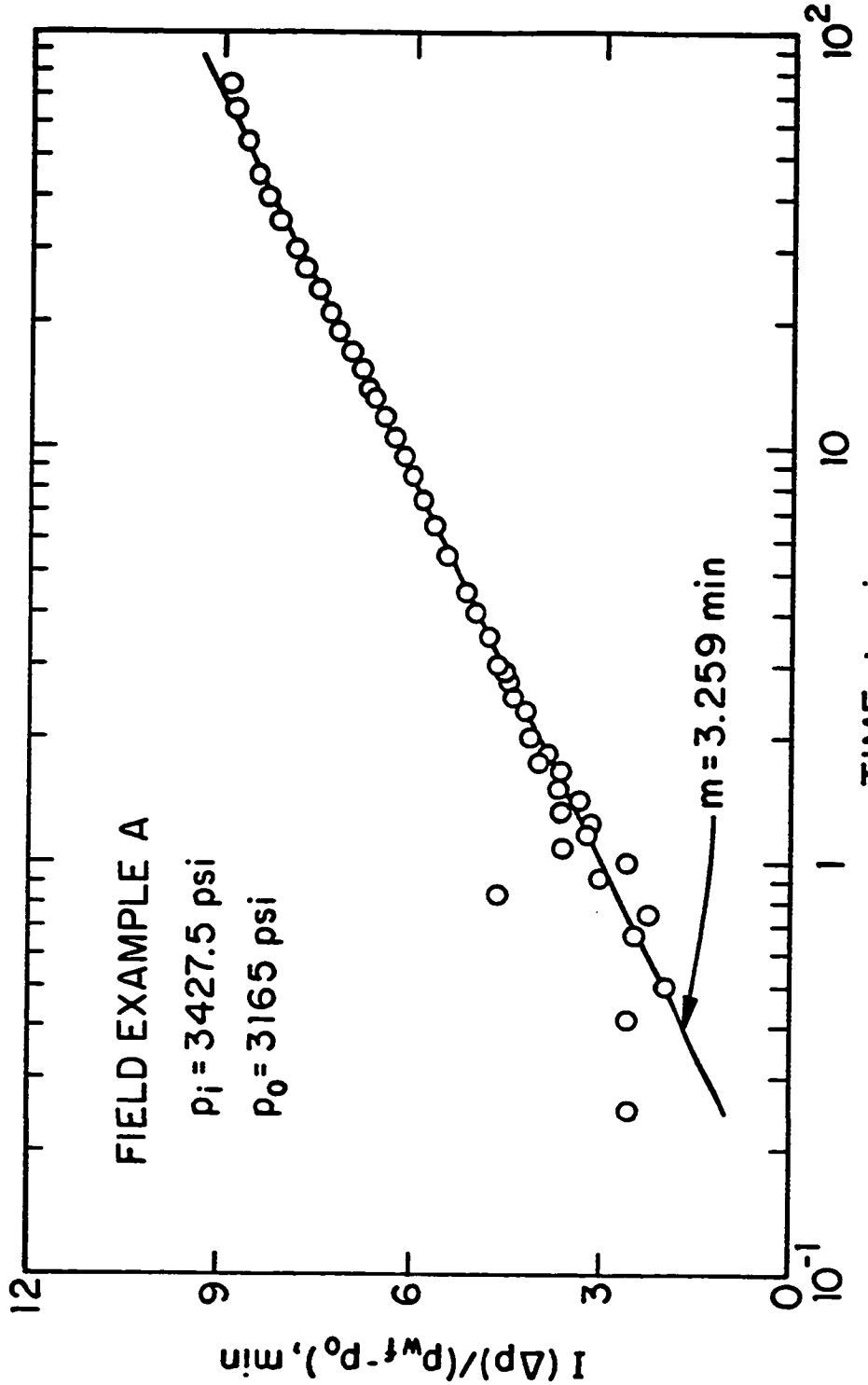

Fig. 2.4.4 - Semilog plot of the converted rate-normalized pressure drop; Field Example A.

which gives kh = 71 md-ft. Selecting a point on the straight line, say t^* = 10 minutes and $[I(\Delta p)/(p_{wf}-p_o)]_{t^*}$ = 6.29 minutes, the skin factor can be estimated from Eq. 2.3.13 as follows

$$s = 1.151\left[\frac{6.29}{3.259} - \log\left(\frac{173.6(10/60)}{(0.45)(39.37)(23\times10^{-6})(0.354)^2}\right) + 3.23\right], \qquad (2.4.5)$$

that is, $s = -0.68$.

We also applied the convolution method, Eq. 2.3.26, to the converted data as discussed previously. Fig. 2.4.5 presents a plot of $I(\Delta p)/[p_{wf}(t)-p_o]$ versus the slug test multi-rate time coordinate of Eq. 2.3.27. The converted data in Column 6 of Table 2.4.1 are plotted as circular data points. A good straight line with slope m = 2.962 minutes is obtained and even the scatter in the data at early times is reduced; compare Fig. 2.4.5 with Fig. 2.4.4. Using this slope value in Eq. 2.3.29 we obtain (kh/μ) = 191.0 md-ft/cp and kh = 78.1 md-ft. At the multi-rate time t^*_{ms} = 1.0, the correspondent value of $[I(\Delta p)/(p_{wf}-p_o)]_{t^*_{ms}}$ on the straight line is 6.825 minutes. Therefore, from Eq. 2.3.30, we have

$$s = 1.151\left[\frac{6.825}{2.962} - 1.00 - \log\left(\frac{(191.0/60)}{(0.45)(39.37)(23\times10^{-6})(0.354)^2}\right) + 3.23\right], \quad (2.4.6)$$

which yields $s = -0.31$.

In Table 2.4.2, we summarize the results obtained for this field example. For comparison purposes, Table 2.4.2 also includes the results presented by Waller and Krase[63] which were obtained from a conventional slug test type-curve match. The results obtained by our new analysis procedure using type-curve matching, rate-normalization and convolution methods are all in good agreement, but differ somewhat from the analysis results of Ref. 63. Note that the difference in the calculated skin factors obtained from the rate-normalization and from the convolution method is approximately 0.4 as predicted by theory.

2.4.1 Example B

The field data considered in this section was presented in Ref. 44 and corresponds to pressure data measured during a drill stem test operation. Here, we will

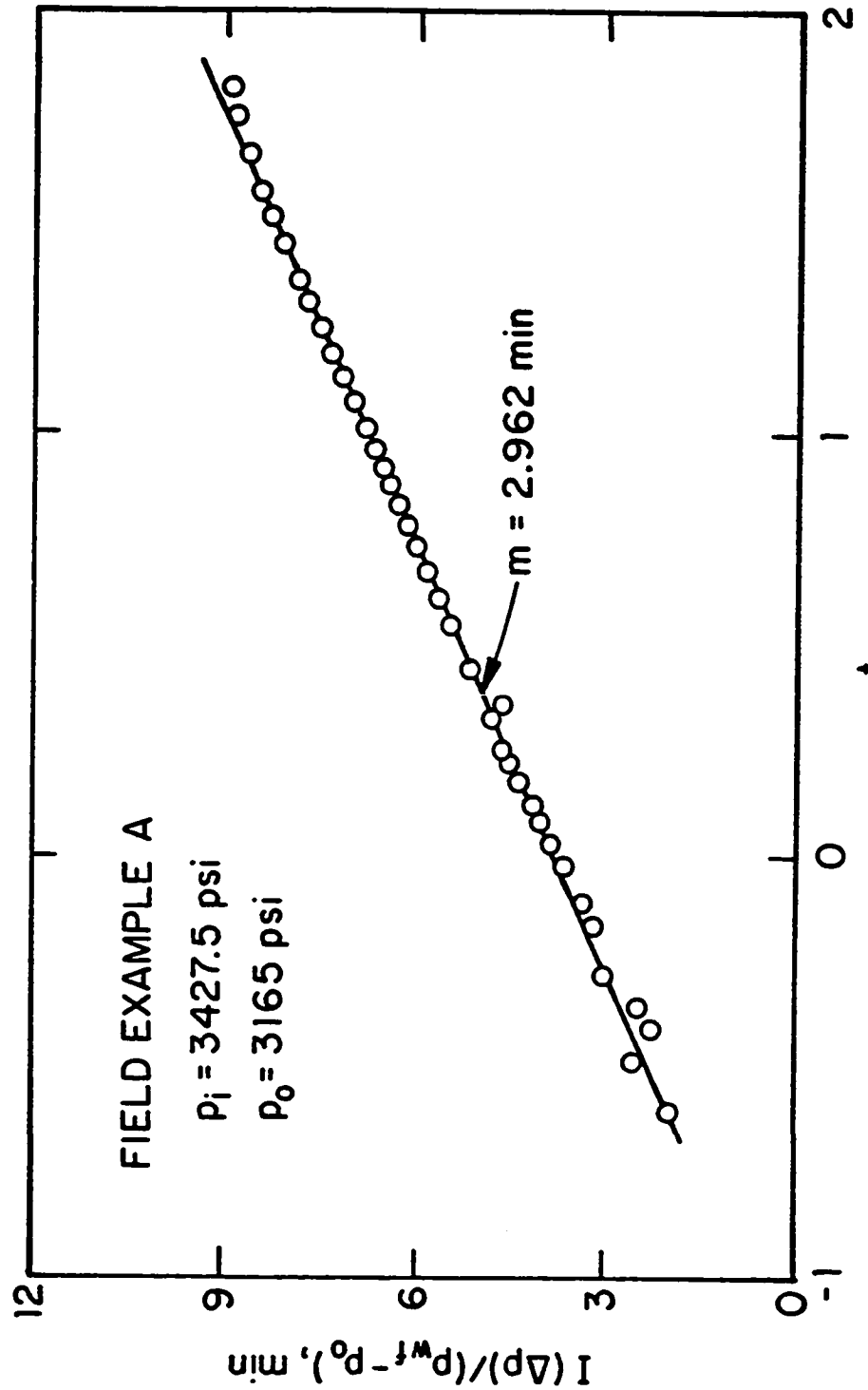

Fig. 2.4.5 - Convolution plot of the converted pressure drop; Field Example A.

Table 2.4.2

Field Example A - Comparison of Results

Reservoir Parameters	Waller and Krase Slug test type curve	This work		
		Type curve	Rate-normalization	Convolution
kh/μ, md-ft/cp	257.7	196.6	173.6	191.0
kh, md-ft	105.4	80.4	71.0	78.1
s	0.78	- 0.03	- 0.68	- 0.31
$C_D \exp(2s)$	200	40	11	23

consider the analysis of the DST flow period; the pressure response of the buildup period will be analyzed in Chapter III. Pressure data measured during the DST flow period is generally not used for quantitative analysis and the interpretation is concentrated on the buildup period. This example illustrate that data from the flow period can be analyzed as well and provides a source of additional information.

The measured pressure, the converted pressure and other test data are presented in Table 2.4.3. The initial reservoir pressure p_i shown in the table was obtained from the analysis of the buildup period, whereas the initial wellbore pressure, p_o, is a measured value.

The measured pressure data of the DST flow period is presented in Column 2. The converted pressure and pressure-derivative data are shown in Columns 3 and 4, respectively; see Eqs. 2.3.1 and 2.3.2. The average point-density calculated from Eq. 2.3.36 gives $d_{avg} = 16$, thus the trapezoidal rule is sufficiently accurate for the $I(\Delta p)$ calculation. Column 5 gives the values of the group defined by Eq. 2.3.7, which forms the basis of the type curves of Fig. 2.2.4. The converted rate-normalized data is presented in the last column of Table 2.4.3.

Fig. 2.4.6 shows the log-log plot of the converted pressure and pressure-derivative data. It appears that the converted derivative data had just achieved its maximum when the well was shut-in for the buildup period, therefore, this field example presents the minimum amount of data necessary for reliable type curve matching. Even though a well defined unit slope line is shown in Fig. 2.4.6, the p_o value calculated from this straight line does not match the p_o value used in the $I(\Delta p)$ calculations; see item (iii) in the discussion of Eq. 2.3.39.

The type-curve match of the log-log plot of the converted group $I(\Delta p)/[2t\Delta p]$ is shown in Fig. 2.4.7. The solid curves shown in Fig. 2.4.7 corresponds to the type curves dimensionless solutions of Fig. 2.2.4 for $C_D \exp(2s) = 10, 10^2$ and 10^3. Note that the field data is matched with the $C_D \exp(2s) = 10^2$ dimensionless solution. Using the match-point values indicated in the Fig. 2.4.7, the transmissibility is estimated from Eq. 2.3.5 as shown below

$$\begin{aligned} \frac{kh}{\mu} &= 141.2\frac{(24)(0.0365)(4.7)}{(1.0)} \\ &= 581 \text{ md-ft/cp.} \end{aligned} \tag{2.4.7}$$

Table 2.4.3

Field Example B - Flow Period

$p_i = 892$ psi $\quad p_o = 142.4$ psi $\quad c_t = 10.2 \times 10^{-6}$ psi^{-1}

$h = 38$ ft $\quad C = 3.65 \times 10^{-2}$ bb/psi

$\mu = 60$ cp $\quad r_w = 0.354$ ft $\quad \phi = 0.062$

time hour	p_{wf} psi	$I(\Delta p)$ psi-hour	$t\Delta p$ psi-hour	$I(\Delta p)/2t\Delta p$ dimensionless	$I(\Delta p)/(p_{wf} - p_o)$ hour
0.022	1.862E+02	1.60094E+01	1.55276E+01	5.15514E-01	3.65511E-01
0.026	1.951E+02	1.88148E+01	1.81194E+01	5.19189E-01	3.57017E-01
0.034	2.099E+02	2.43308E+01	2.31914E+01	5.24565E-01	3.60456E-01
0.041	2.216E+02	2.90646E+01	2.74864E+01	5.28708E-01	3.66977E-01
0.053	2.393E+02	3.70031E+01	3.45931E+01	5.34834E-01	3.81869E-01
0.067	2.618E+02	4.59835E+01	4.22234E+01	5.44526E-01	3.85121E-01
0.084	2.823E+02	5.65226E+01	5.12148E+01	5.51819E-01	4.04021E-01
0.106	3.105E+02	6.96258E+01	6.16390E+01	5.64787E-01	4.14193E-01
0.132	3.334E+02	8.44471E+01	7.37352E+01	5.72638E-01	4.42131E-01
0.166	3.640E+02	1.02919E+02	8.76480E+01	5.87117E-01	4.64437E-01
0.187	3.800E+02	1.13839E+02	9.57440E+01	5.94498E-01	4.79122E-01
0.209	3.949E+02	1.24939E+02	1.03894E+02	6.01284E-01	4.94810E-01
0.235	4.122E+02	1.37639E+02	1.12753E+02	6.10357E-01	5.10152E-01
0.264	4.303E+02	1.51291E+02	1.21889E+02	6.20610E-01	5.25498E-01
0.295	4.496E+02	1.65304E+02	1.30508E+02	6.33311E-01	5.38100E-01
0.334	4.709E+02	1.82143E+02	1.40647E+02	6.47515E-01	5.54468E-01
0.372	4.910E+02	1.97763E+02	1.49172E+02	6.62868E-01	5.67305E-01
0.418	5.111E+02	2.15746E+02	1.59216E+02	6.77526E-01	5.85154E-01
0.470	5.377E+02	2.34861E+02	1.66521E+02	7.05201E-01	5.94135E-01
0.528	5.610E+02	2.54735E+02	1.74768E+02	7.28781E-01	6.08541E-01
0.590	5.839E+02	2.74547E+02	1.81779E+02	7.55168E-01	6.21851E-01
0.662	6.073E+02	2.95888E+02	1.88471E+02	7.84968E-01	6.36455E-01
0.774	6.302E+02	3.26492E+02	2.02633E+02	8.05623E-01	6.69315E-01
0.835	6.551E+02	3.41702E+02	1.97811E+02	8.63707E-01	6.66476E-01
0.938	6.772E+02	3.64965E+02	2.01482E+02	9.05699E-01	6.82433E-01
1.051	6.989E+02	3.88011E+02	2.02948E+02	9.55937E-01	6.97235E-01
1.126	7.122E+02	4.01995E+02	2.02455E+02	9.92802E-01	7.05502E-01

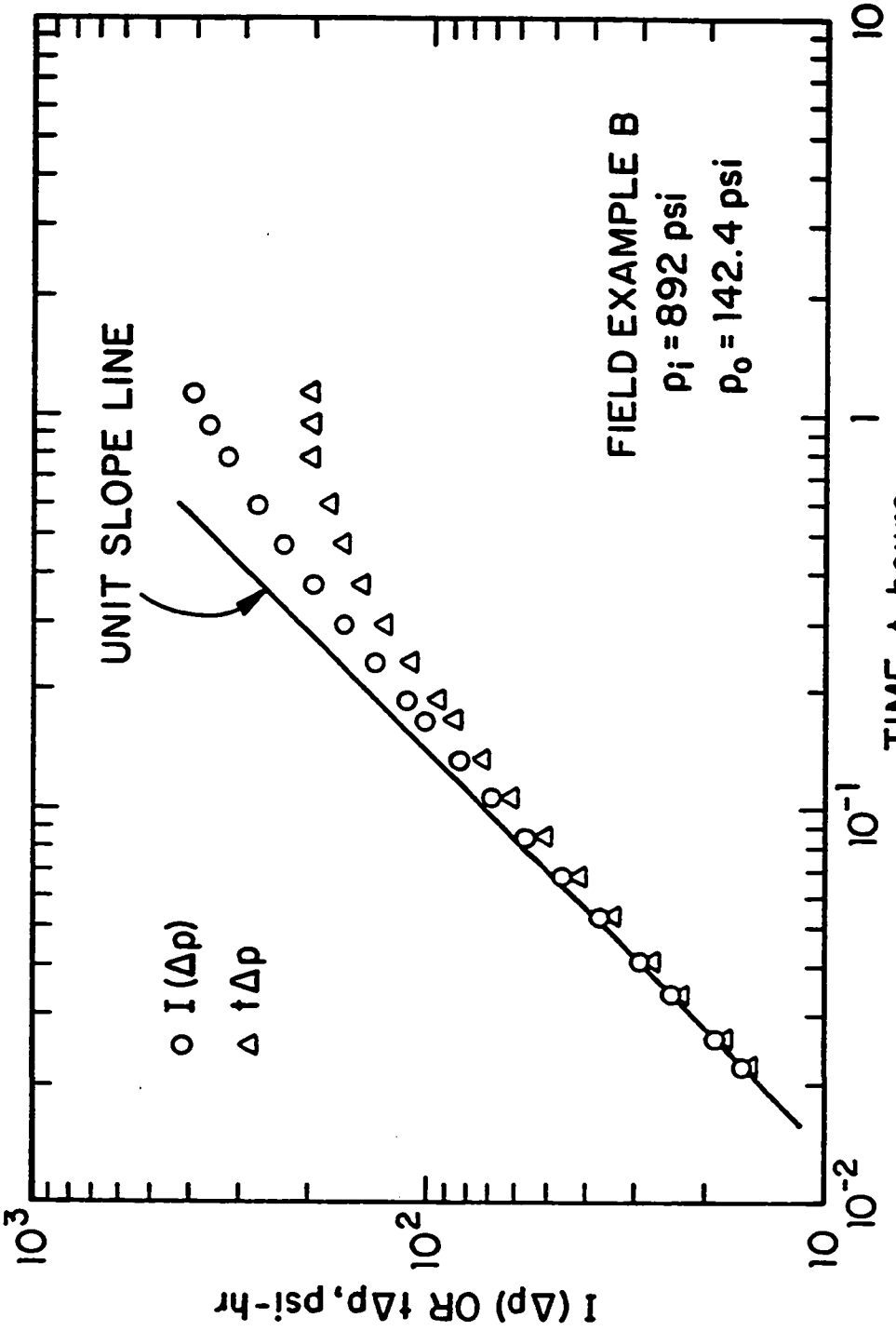

Fig. 2.4.6 - Log-log plot of the converted pressure drop and its derivative; Field Example B.

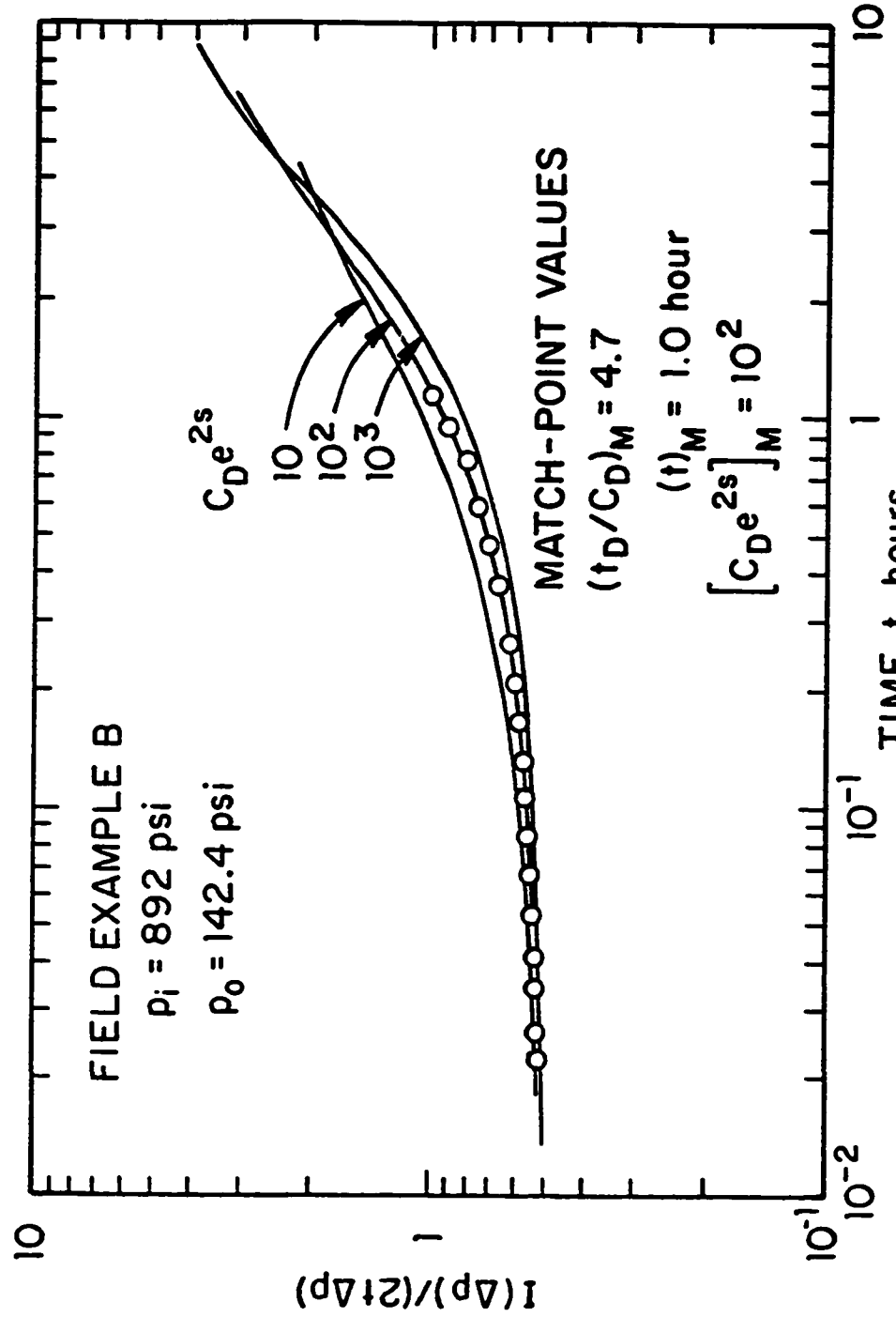

Fig. 2.4.7 - Type-curve match of the converted pressure derivative ratio; Field Example B.

The type-curve match of $I(\Delta p)$ versus t is shown in Fig. 2.4.8 and was obtained by moving the field plot only in the vertical direction by using the time-match points of Fig. 2.4.7. The three solid curves represent the same dimensionless solutions shown in Fig. 2.4.7. As indicated in Fig. 2.4.8, the match-point values are $(p_{wcD})_M = 0.62$ and $[I(\Delta p)]_M = 100$ psi-hour. The transmissibility is estimated from Eq. 2.3.4 as

$$\frac{kh}{\mu} = 141.2\frac{(24)(0.0365)(892-142.4)(0.62)}{(100)} = 575 \text{ md-ft/cp}, \tag{2.4.8}$$

which is in good agreement with the result of Eq. 2.4.7.

Using Eqs. 2.1.3 and 2.1.4, the parameters of Table 2.4.3 gives $C_D = 10831$. The skin factor can be estimated by

$$s = \frac{1}{2}\ln\left(\frac{100}{10831}\right) = -2.3. \tag{2.4.9}$$

The semilog plot of the converted rate-normalization method is shown in Fig. 2.4.9. The circular data points represent the $I(\Delta p)/\left[p_{wf}(t) - p_o\right]$ values shown in the last Column of Table 2.4.3. For times greater than 0.1 hours, Fig. 2.4.9 shows a well defined straight line with slope $m = 0.29$ hours. Using this slope value in Eq. 2.3.12 gives

$$\frac{kh}{\mu} = \frac{162.6(24)(0.0365)}{(0.29)} = 491 \text{ md-ft/cp}. \tag{2.4.10}$$

Taking a point on the straight line, say $t^* = 1.05$ hours and $[I(\Delta p)/(p_{wf} - p_o)]_{t^*} = 0.698$ hours, the skin factor can be calculated from Eq. 2.3.13 as

$$s = 1.151\left[\frac{0.698}{0.29} - \log\left(\frac{491(1.05)}{(0.062)(38)(10.2\times10^{-6})(0.354)^2}\right) + 3.23\right], \tag{2.4.11}$$

which gives $s = -3.0$.

Fig. 2.4.10 presents a Cartesian plot of the converted convolution method. A good straight line is obtained for times corresponding to $t_{ms} > -0.1$, and yields a slope $m = 0.274$. Using this value in Eq. 2.3.29 gives $(kh/\mu) = 520$ md-ft/cp. At the multi-rate time $t^*_{ms} = -0.3$, the value of $[I(\Delta p)/(p_{wf} - p_o)]_{t^*_{ms}}$ on the straight line is 0.667 hours. Using this values in Eq. 2.3.30 yields $s = -2.6$.

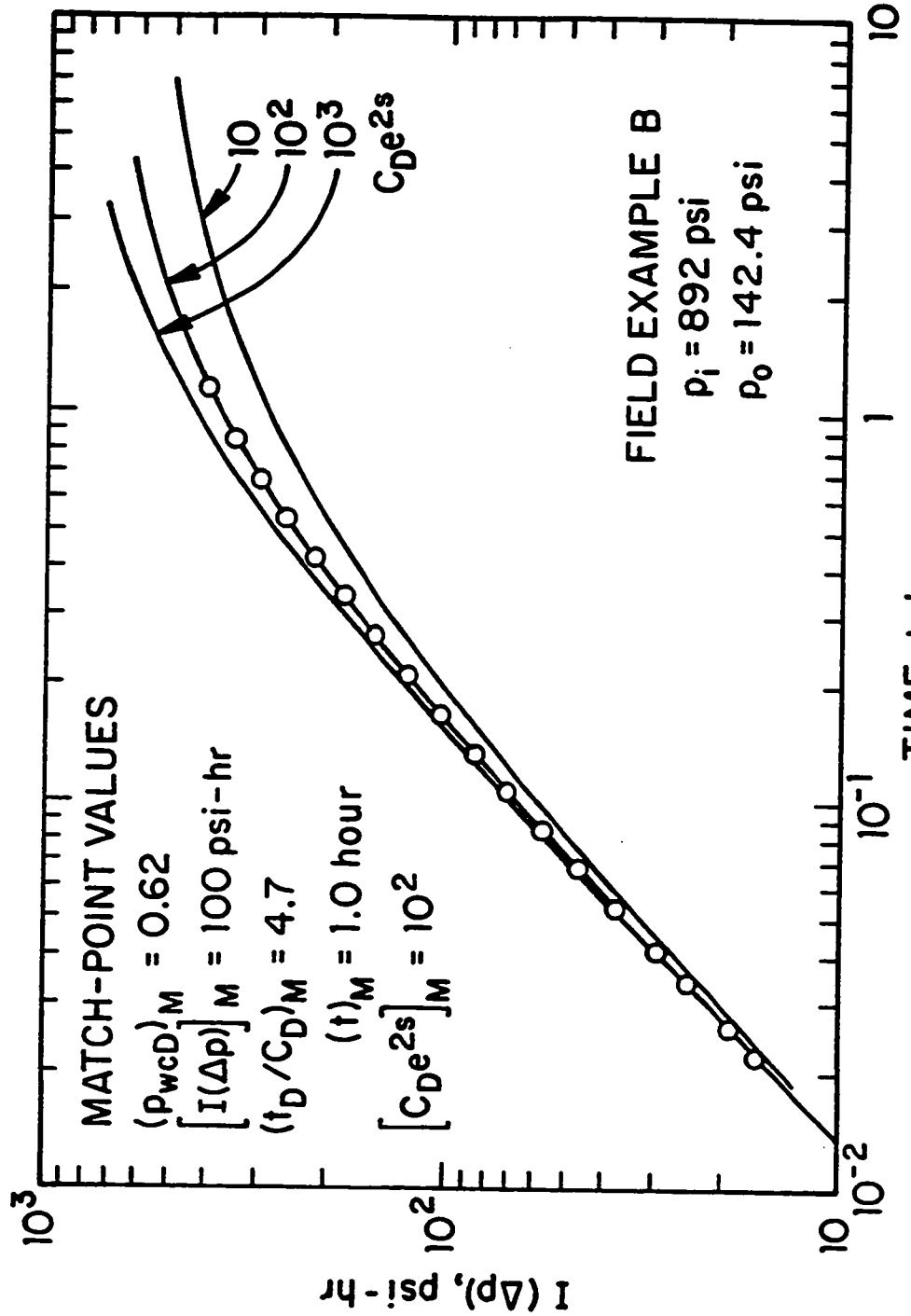

Fig. 2.4.8 - Type-curve match of the converted pressure drop; Field Example B.

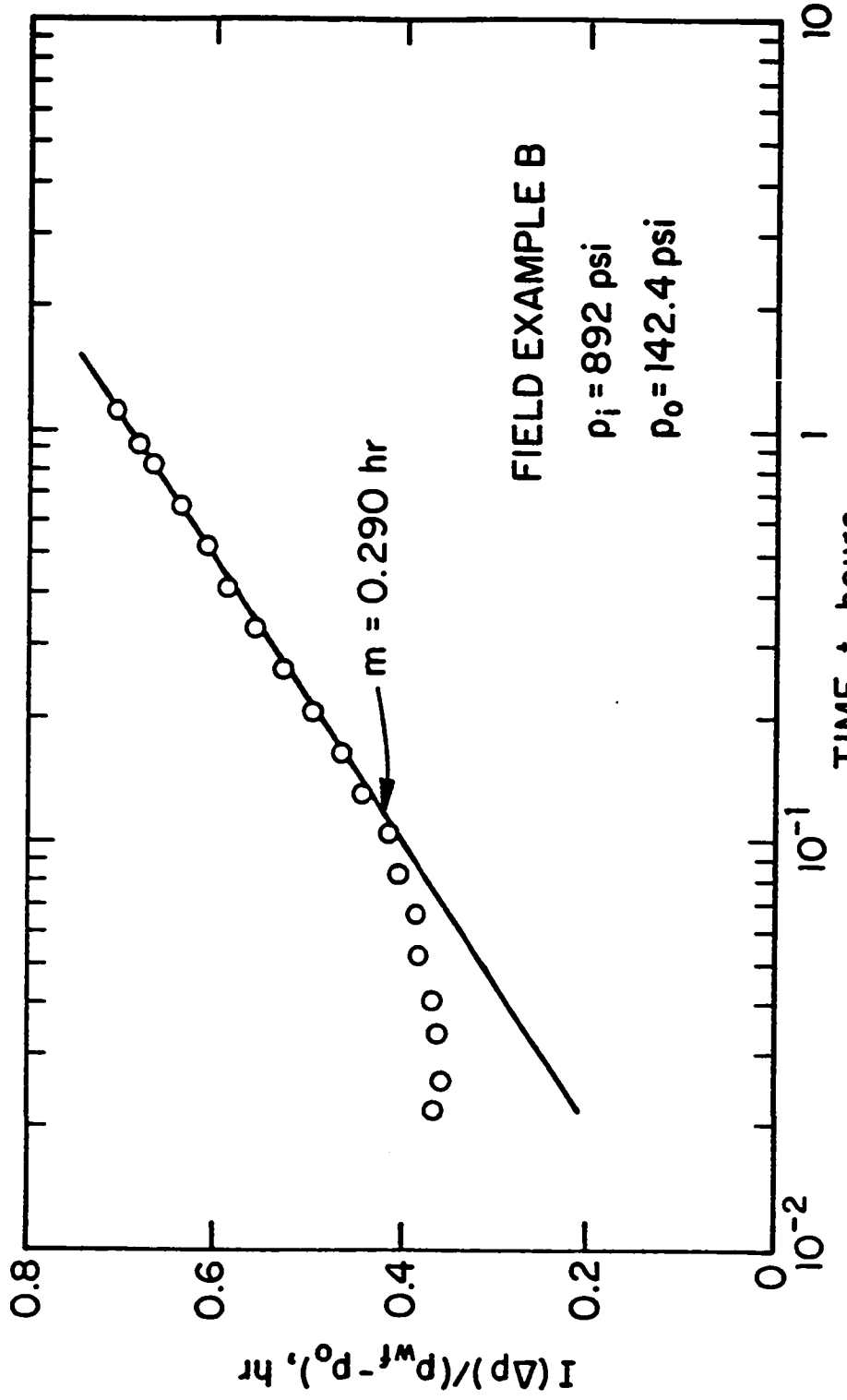

Fig. 2.4.9 - Semilog plot of the converted rate-normalized pressure drop; Field Example B.

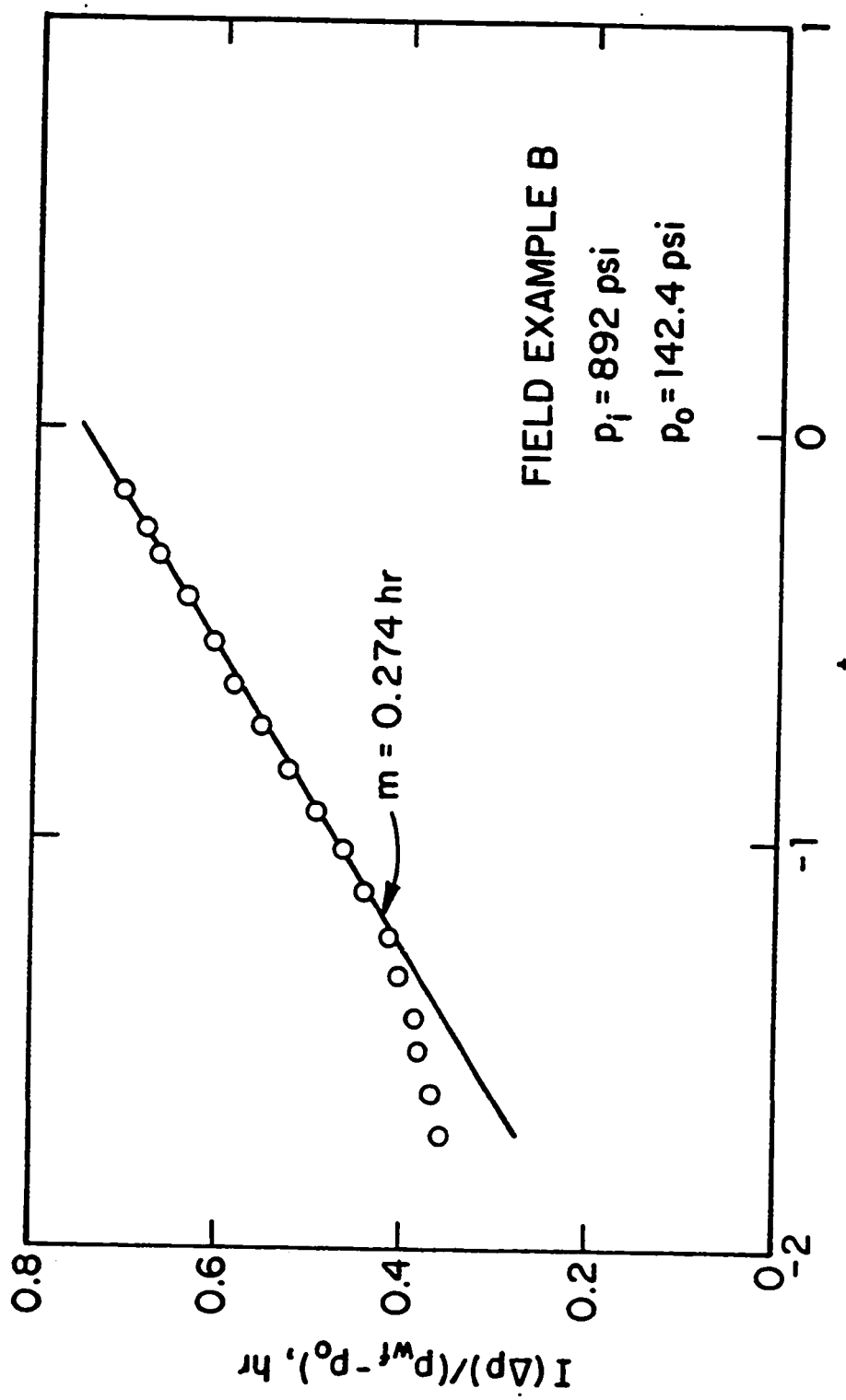

Fig. 2.4.10 - Convolution plot of the converted pressure drop; Field Example B.

Note that for times less than 5 minutes, the data of Fig. 2.4.9 and 2.4.10 do not follow the straight line equations predicted by our theoretical development even though this early data presents a good match with the dimensionless type curve solutions as shown in Figs. 2.4.7 and 2.4.8. This may be caused by early non-radial flow geometry or some other short duration phenomenon (such as momentum effects).

The summary of the quantitative analysis of Example B is shown in Table 2.4.4. The results by type-curve matching, rate-normalization and convolution are all in good agreement. Note that the skin obtained by the rate-normalization method is 0.4 units smaller than the one calculated by the convolution method as expected.

2.4.1 Example C

The field example presented here corresponds to data measured during the flow period of a conventional DST. The buildup data will be analyzed in in the Field Applications section of Chapter III. This example presents much less fluid recovery than the previous field case and illustrates a case in which the short span of the data does not allow a reliable type curve analysis.

The test data and computations are presented in Table 2.4.5. The p_i value presented in the table corresponds to the value obtained from the pressure analysis of the buildup period. The initial wellbore pressure p_o was obtained directly from the DST chart.

Note that the presentation of Table 2.4.5 is slightly different from previous examples. The measured pressure versus time data is shown in Column 2. The multi-rate time t_{ms} calculated from Eq. 2.3.27 is presented in Column 3. The converted pressure data and the rate-normalized group are shown in Columns 4 and 5, respectively. The average data-density d_{avg} for this field example is around 15, thus the integration scheme of Eq. 2.3.35 should be sufficiently accurate for practical purposes.

Fig. 2.4.11 shows the log-log plot of the converted pressure, $I(\Delta p)$, and converted pressure-derivative data, $t\Delta p$. Note that the converted derivative data did

Table 2.4.4

Field Example B - Comparison of Results

Parameters	Type-curve	Rate-normalization	Convolution
kh/μ, md-ft/cp	581	491	520
kh, md-ft	34860	29460	31200
s	-2.3	-3.0	-2.6
$C_D \exp(2s)$	100	27	60

Table 2.4.5

Field Example C - Flow Period

$p_i = 3315.2$ psi $\quad p_o = 263.1$ psi $\quad c_t = 1.47 \times 10^{-5}$ psi^{-1}

$h = 23$ ft $\quad C = 1.609 \times 10^{-2}$ bbl/psi

$\mu = 0.43$ cp $\quad r_w = 0.354$ ft $\quad \phi = 0.13$

time hour	p_{wf} psi	t_{ms} dimensionless	$I(\Delta p)$ psi-hour	$I(\Delta p)/(p_{wf} - p_o)$ hour
2.4000E-01	4.7580E+02	-6.1979E-01	7.0698E+02	3.3238E+00
4.8000E-01	5.2045E+02	-3.7098E-01	1.3831E+03	5.3744E+00
7.2000E-01	5.8478E+02	-2.6253E-01	2.0461E+03	6.3607E+00
9.6000E-01	6.8457E+02	-2.1946E-01	2.6894E+03	6.3811E+00
1.2000E+00	7.6597E+02	-1.4992E-01	3.3110E+03	6.5842E+00
1.4400E+00	8.5263E+02	-9.8071E-02	3.9124E+03	6.6366E+00
1.6800E+00	9.2747E+02	-4.1096E-02	4.4945E+03	6.7650E+00
1.9200E+00	9.9968E+02	8.1283E-03	5.0589E+03	6.8680E+00
2.1600E+00	1.0601E+03	6.0057E-02	5.6073E+03	7.0358E+00
2.4000E+00	1.1073E+03	1.1381E-01	6.1429E+03	7.2762E+00
2.6400E+00	1.1704E+03	1.4373E-01	6.6652E+03	7.3465E+00
2.8800E+00	1.2216E+03	1.8246E-01	7.1738E+03	7.4846E+00
3.1200E+00	1.2780E+03	2.1124E-01	7.6695E+03	7.5567E+00
3.3600E+00	1.3319E+03	2.4006E-01	8.1520E+03	7.6275E+00
3.6000E+00	1.3778E+03	2.7244E-01	8.6225E+03	7.7351E+00
3.8400E+00	1.4211E+03	3.0262E-01	9.0822E+03	7.8427E+00
4.0800E+00	1.4671E+03	3.2716E-01	9.5313E+03	7.9164E+00
4.3200E+00	1.5131E+03	3.4983E-01	9.9693E+03	7.9758E+00
4.5600E+00	1.5564E+03	3.7289E-01	1.0397E+04	8.0390E+00
4.8576E+00	1.6063E+03	4.0346E-01	1.0913E+04	8.1245E+00

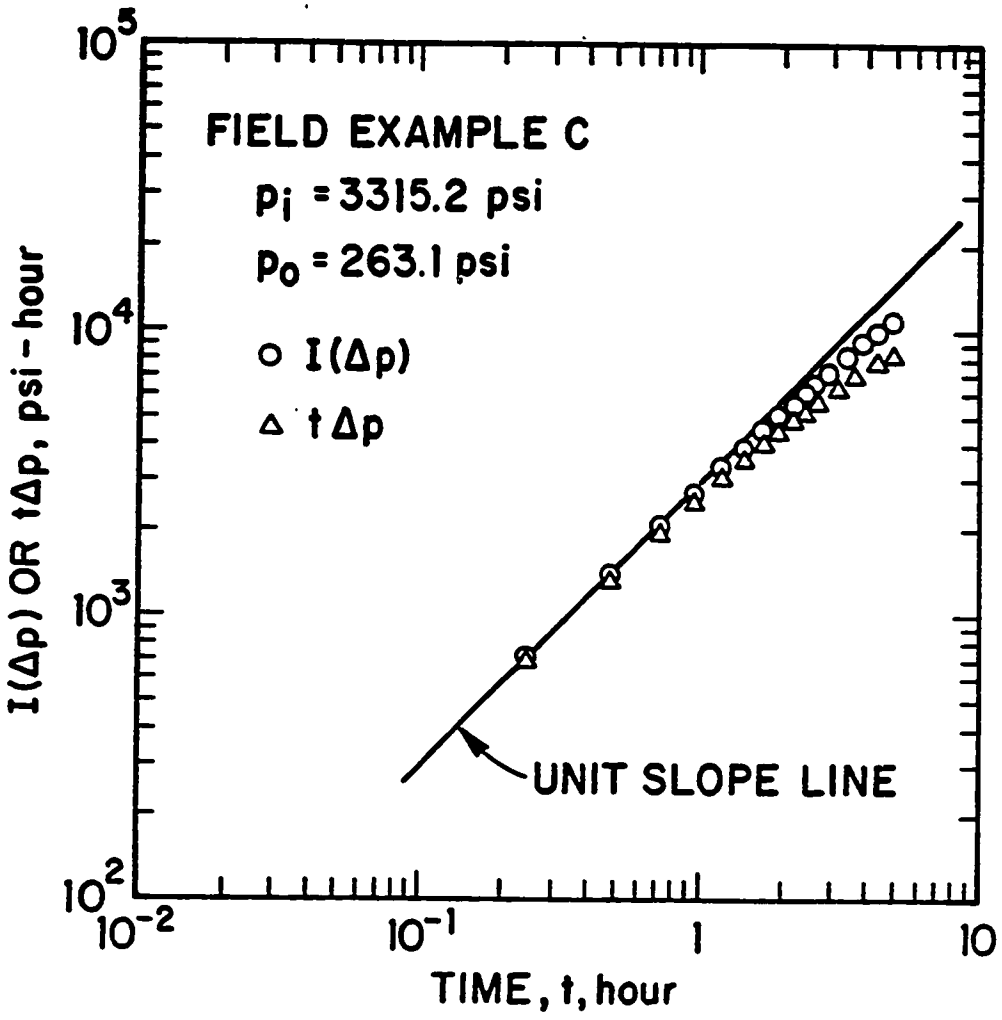

Fig. 2.4.11 - Log-log plot of the converted pressure drop and its derivative; Field Example C.

not achieved the maximum and most of the converted data are within the wellbore storage dominated region. Although the flow period was relatively long (about 5 hours), the slug test dimensionless wellbore pressure at the end of the flow period, $p_{wD}(t_{pD})$, is equal to 0.56; see Eq. 2.1.7. This result indicates that the liquid recovery was only 44% of the maximum column recovery. Therefore, a reliable type curve analysis of the field data cannot be performed. However, the field data can be analyzed by the rate-normalization and convolution methods.

The converted rate-normalized semilog plot is shown in Fig. 2.4.12. A good semilog straight line is drawn through the data points correspondent to times greater than 1.5 hours. Using the semilog slope value indicated in Fig. 2.4.12 in Eq. 2.3.12, gives

$$\frac{kh}{\mu} = \frac{162.6(24)(0.01609)}{(2.92)} = 21.5 \text{ md-ft/cp.} \qquad (2.4.12)$$

Using the straight line point $\{[I(\Delta p)/(p_{wf} - p_o)]_{t^*} = 8.04, t^* = 4.56\}$, the skin equation gives

$$s = 1.151\left[\frac{8.04}{2.92} - \log\left(\frac{21.5(4.56)}{(0.13)(23)(1.47\times 10^{-5})(0.354)^2}\right) + 3.23\right], \qquad (2.4.13)$$

which gives $s = -1.5$.

Fig. 2.4.13 presents a Cartesian plot of $I(\Delta p)/[p_{wf}(t) - p_o]$ versus the multi-rate time t_{ms} shown in Column 3 of Table 2.4.5. A well defined straight-line with slope $m = 2.98$ hours is obtained. Using this value in Eq. 2.3.29 gives

$$\frac{kh}{\mu} = \frac{162.6(24)(0.01609)}{(2.98)} = 21.1 \text{ md-ft/cp.} \qquad (2.4.14)$$

At the multi-rate time $t^*_{ms} = 0.373$ the correspondent value of $[I(\Delta p)/(p_{wf} - p_o)]_{t^*_{ms}}$ on the straight line is 8.04 hours. Therefore, the skin factor can be estimated by

$$s = 1.151\left[\frac{8.04}{2.98} - 0.373 - \log\left(\frac{21.1}{(0.13)(23)(1.47\times 10^{-5})(0.354)^2}\right) + 3.23\right], \qquad (2.4.15)$$

which yields $s = -1.2$.

Note that the transmissibility estimate from Eqs. 2.4.12 and 2.4.14 are in excellent agreement and the difference in the skin factors of Eqs. 2.4.13 and 2.14.15

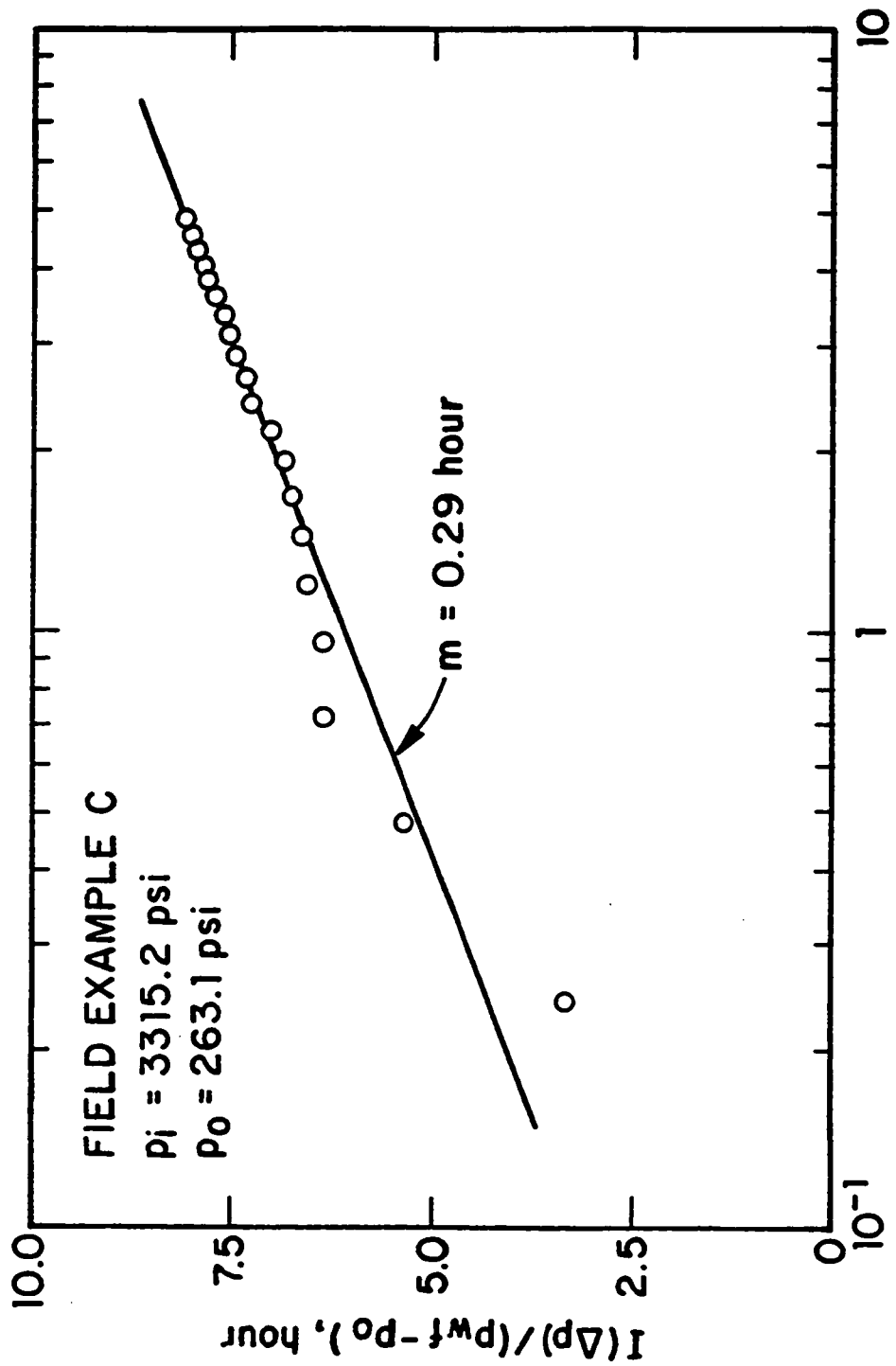

Fig. 2.4.12 - Semilog plot of the converted rate-normalized pressure drop; Field Example C.

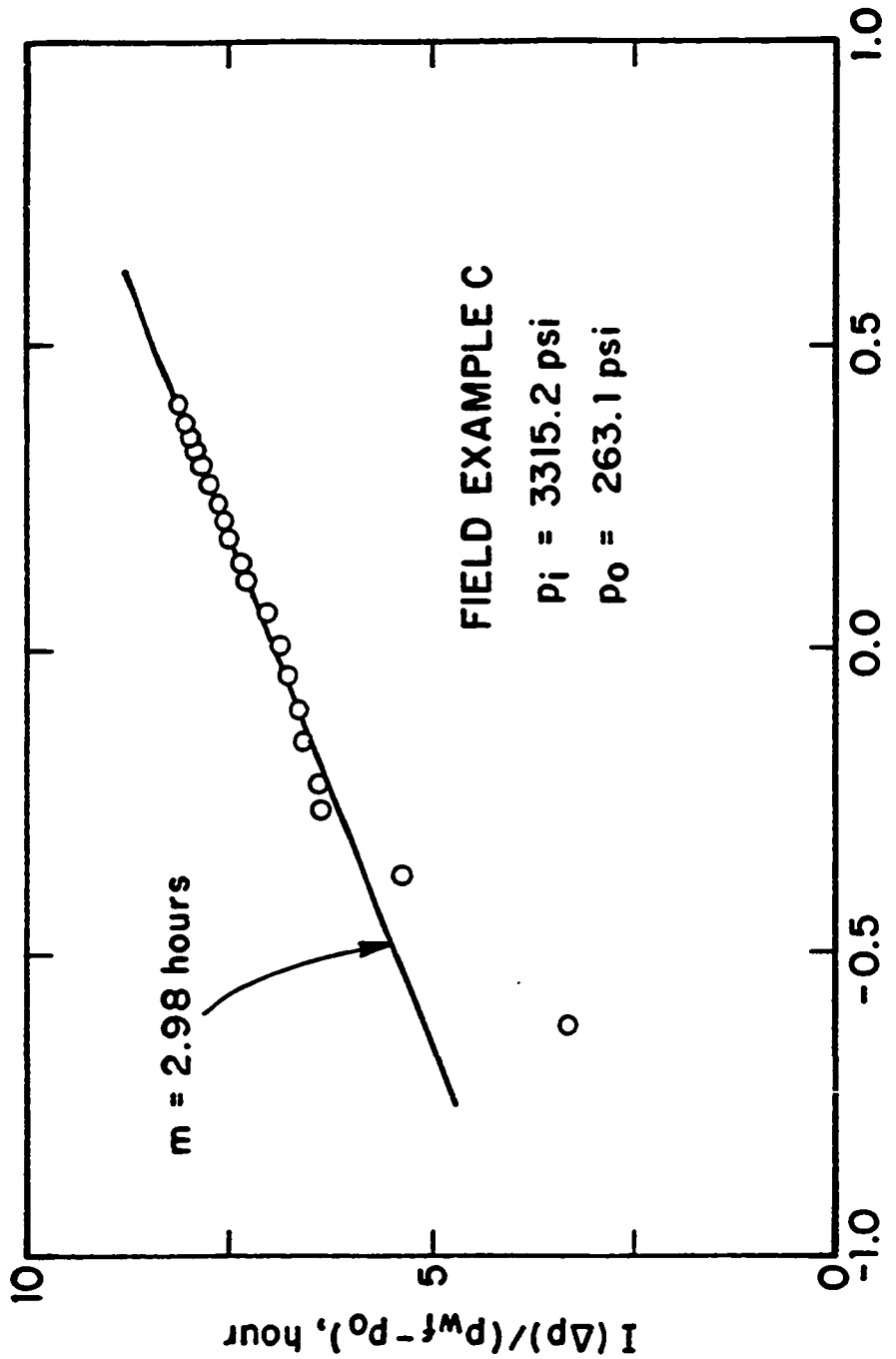

Fig. 2.4.13 - Convolution plot of the converted pressure drop; Field Example C.

is close to the one predicted by theory. Similarly to the Example B, the converted data in Figs. 2.4.12 and 2.4.13 do not follow the straight lines at early times. In this example the converted data presents a slight S-shape behavior around the straight line, especially in Fig. 2.4.12. At later times this effect dies out and a well defined straight line is obtained in Figs. 2.4.12 and 2.4.13.

CHAPTER III
DRILLSTEM TEST BUILDUP ANALYSIS

This Chapter presents new procedures for analyzing pressure buildup data obtained from drillstem tests. The new techniques presented here apply for cases where the produced fluid does not reach the surface during the flowing period so that, the flow period represents the slug test considered in Chapter II. Field and computer generated data are used to compare the performance of the proposed methods versus traditional techniques.

3.1 Definitions

In this Chapter, p_{wD} denotes the dimensionless wellbore pressure drop solution for either the flow or buildup period of the DST problem under consideration. The constant surface rate dimensionless wellbore pressure drop solution is always denoted by p_{wcD} and incorporates the skin and wellbore storage effects. As before, p^{*}_{wcD} denotes the dimensionless wellbore pressure solution for constant sandface production and represents the solution when wellbore storage effects are negligible.

The dimensionless time and dimensionless shut-in time are defined, respectively, by

$$t_D = \frac{2.637 \times 10^{-4} kt}{\phi \mu c_t r_w^2}; \quad \text{for } 0 < t \leq t_p + \Delta t, \tag{3.1.1}$$

and

$$\Delta t_D = \frac{2.637 \times 10^{-4} k \Delta t}{\phi \mu c_t r_w^2}; \quad \text{for } \Delta t > 0, \tag{3.1.2}$$

where t_p represents the producing time and Δt denotes the elapsed time since the well was shut-in, whereas, t represents the total elapsed time since the start of the DST.

As mentioned previously, the DST problem is characterized by a step change in the wellbore storage coefficient. The opening of the DST valve allows the reservoir

fluid to flow into the wellbore and the liquid level in the string increases accordingly. The dimensionless wellbore storage coefficient under this condition is defined as

$$C_{FD} = \frac{5.615 C_F}{2\pi\phi c_t h r_w^2}, \tag{3.1.3}$$

where C_F denotes the slug test wellbore storage coefficient, in RB/psi, due to the change in the wellbore fluid level. The wellbore storage coefficient can be computed directly from the completion and fluid data by the following expression

$$C_F = \frac{144\pi r_p^2}{5.615\rho g/g_c}, \tag{3.1.4}$$

where r_p is the radius of the drill pipe and ρ is the density of the fluid being produced into the wellbore. The subscript F is used to indicate that C_F is the wellbore storage coefficient during the flow period.

When the bottom-hole valve is closed for the buildup period, the wellbore storage coefficient decreases from one due to a changing liquid-level to one due to fluid-compression. The dimensionless wellbore storage coefficient for the buildup period is defined by

$$C_{SD} = \frac{5.615 C_S}{2\pi\phi c_t h r_w^2}, \tag{3.1.5}$$

where C_S denotes the buildup wellbore storage coefficient, in RB/psi, due to the compressibility of the fluid in the wellbore and is given by

$$C_S = V_w c_{wf}, \tag{3.1.6}$$

where V_w is the volume of the pressurized wellbore for the buildup period and c_{wf} denotes the isothermal compressibility of the fluid in the wellbore. The subscript S indicates that C_S is the wellbore storage coefficient for the shut-in period. Field practice indicates that the buildup wellbore storage coefficient C_S cannot be accurately estimated from wellbore and fluid data. However, in DST operations C_{SD} is typically two orders of magnitude smaller than C_{FD} and its effects on the buildup response can be neglected in many cases.

The dimensionless wellbore pressure drop at any time t_D during the DST is defined by

$$p_{wD} = \frac{p_i - p_w(t)}{p_i - p_o}, \tag{3.1.7}$$

where $p_w(t)$ denotes the wellbore pressure at any time t and may represent a drawdown or buildup pressure; however for the drawdown case, $p_w = p_{wf}$ and for the buildup case, $p_w = p_{ws}$. As mentioned previously, p_i represents the initial reservoir pressure and p_o denotes the imposed initial bottom-hole pressure.

It is also convenient to define a dimensionless pressure buildup change for the DST problem by

$$p_{sD} = \frac{p_i - p_{ws}(\Delta t)}{p_i - p_o}, \tag{3.1.8}$$

where p_{ws} represents the shut-in wellbore pressure.

The dimensionless sandface rate is defined as

$$q_D = \frac{141.2 q_{sf}(t)\mu}{kh(p_i - p_o)}, \tag{3.1.9}$$

where $q_{sf}(t)$ is in RB/day and denotes the sandface flow rate obtained during the DST (either flow or buildup period) as a function of time.

3.2 Background and Theory

In this major section, we briefly review the current status of buildup analysis procedures for drillstem tests. All results presented in this work assume single phase flow of a slightly compressible fluid of constant viscosity. In addition, it is assumed that momentum and inertial effects in the wellbore can be neglected.

3.2.1 Basic Buildup Solutions

From the superposition principle, the basic buildup equation following a *constant* rate flow period can be written as

$$p_{scD}(\Delta t_D) = p_{wcD}(t_D) - p_{wcD}(\Delta t_D), \tag{3.2.1}$$

where p_{scD} denotes the constant rate dimensionless pressure buildup change which is defined by

$$p_{scD} = \frac{kh(p_i - p_{ws})}{141.2qB\mu}. \tag{3.2.2}$$

In Eq. 3.2.2, q (in STB/day), represents the constant surface rate before shut-in. Eq. 3.2.1 assumes that wellbore storage is negligible, or that the wellbore storage coefficient has the same value for both drawdown and buildup, therefore, it does not apply for varying wellbore storage problems.

For homogeneous, infinite-acting reservoirs, if wellbore storage effects are negligible, then p_{wcD} is given by the logarithmic approximation and Eq. 3.2.1 becomes[38]

$$p_{scD}(\Delta t_D) = \frac{1}{2} \ln\left(\frac{t_{pD} + \Delta t_D}{\Delta t_D}\right). \tag{3.2.3}$$

Using the dimensionless definitions given before, the working form of Eq. 3.2.3 is given by

$$p_{ws}(\Delta t) = p_i - m \log\left(\frac{t_p + \Delta t}{\Delta t}\right) = p_i - \frac{m}{2.303} \ln\left(\frac{t_p + \Delta t}{\Delta t}\right), \tag{3.2.4}$$

where m is defined by

$$m = \frac{162.6qB}{(kh/\mu)}. \tag{3.2.5}$$

Eq. 3.2.4 indicates that a semilog plot of p_{ws} versus the ratio $(t_p + \Delta t)/\Delta t$ yields a straight line with slope m (in psi). Once the slope value is obtained, the transmissibility kh/μ can be estimated by the obvious rearrangement of Eq. 3.2.5. The reservoir pressure p_i can be obtained by extrapolating the straight line to $(t_p + \Delta t)/\Delta t = 1$. This plotting technique is known in the petroleum industry as the Horner method[38] whereas in the ground water literature it is referred to as the Theis method[64].

During the DST flow period, the rising liquid level causes the flow rate to decrease throughout that period, and thus, strictly speaking, the Horner method is not applicable for the analysis of DST buildup pressure data. The results of Refs. 40 and 41 (see also Refs. 35 and 36) suggest that for DST applications, the constant

flow rate qB should be replaced by the average flow rate. This average rate, q_{avg} (RB/day), is given by

$$q_{avg} = \frac{1}{t_p}\int_0^{t_p}(24)C_F\frac{dp_{wf}}{d\tau}(\tau)d\tau = \frac{(24)C_F[p_{wf}(t_p)-p_o]}{t_p}. \tag{3.2.6}$$

Note that Eq. 3.2.6 represents the cumulative production obtained in the flow period divided by the producing time t_p.

A dimensionless slope m_D can be defined as

$$\begin{aligned} m_D &= \frac{141.2q_{avg}}{2(kh/\mu)[p_i-p_o]} = \frac{141.2(24)C_F}{2(kh/\mu)\,t_p}\left[\frac{p_{wf}(t_p)-p_o}{p_i-p_o}\right] \\ &= \frac{C_{FD}\left[1-p_{wD}(t_{pD})\right]}{2\,t_{pD}}, \end{aligned} \tag{3.2.7}$$

where the last equality of Eq. 3.2.7 follows directly from the dimensionless definitions. Replacing qB by q_{avg} in Eq. 3.2.5 and using Eq. 3.2.7, Eq. 3.2.4 can be rewritten as

$$\begin{aligned} \frac{p_{sD}(\Delta t_D)}{m_D} &= \ln\left(\frac{t_{pD}+\Delta t_D}{\Delta t_D}\right) \\ &= t_{HD}, \end{aligned} \tag{3.2.8}$$

which represents the dimensionless Horner method for DST applications. The second equality of Eq. 3.2.8 is used to define the dimensionless time t_{HD}.

A more rigorous procedure for handling the effects of a variable rate schedule is through the use of the conventional multi-rate method[38,36]. Consider the partition of the interval $[0, t_{pD}]$ given by

$$0 = t_{0,pD} < t_{1,pD} < \cdots < t_{n,pD} < t_{n+1,pD} = t_{pD}. \tag{3.2.9}$$

Using the superposition principle, the multi-rate dimensionless buildup pressure solution for transient radial flow is given by[38,36]

$$\frac{p_{sD}(\Delta t_D)}{q_D(\hat{t}_{n+1,pD})} = \frac{1}{2}\sum_{j=0}^{n}\frac{q_D(\hat{t}_{j+1,pD})}{q_D(\hat{t}_{n+1,pD})}\ln\left(\frac{t_{pD}+\Delta t_D-t_{j,pD}}{t_{pD}+\Delta t_D-t_{j+1,pD}}\right), \tag{3.2.10}$$

where $\hat{t}_{j+1,pD}$ is a point selected in the interval

$$t_{j,pD} \le \hat{t}_{j+1,pD} \le t_{j+1,pD}\ ; \qquad j = 0, 1, \cdots, n. \tag{3.2.11}$$

The derivation of Eq. 3.2.10 assumes that the flow rate is zero during the buildup period, that is, it does not consider afterflow production. The dimensional version of Eq. 3.2.10 is given by

$$p_{ws}(\Delta t) = p_i - m_H \; t_{mH}, \tag{3.2.12}$$

where

$$t_{mH} = \sum_{j=0}^{n} \frac{q_{sf}(\hat{t}_{j+1,p})}{q_{sf}(\hat{t}_{n+1,p})} \log\left(\frac{t_p + \Delta t - t_{j,p}}{t_p + \Delta t - t_{j+1,p}}\right) \tag{3.2.13}$$

and

$$m_H = \frac{162.6 \; q_{sf}(\hat{t}_{n+1,p})}{(kh/\mu)}. \tag{3.2.14}$$

Application of Eq. 3.2.10 to DST data requires the determination of the flow rates from the liquid level recovery by the following expression (see Eq. 2.2.19)

$$q_D\left(\hat{t}_{j+1,pD}\right) = -C_{FD}\left[\frac{dp_{wD}}{dt_D}\right]_{\hat{t}_{j+1,pD}}, \tag{3.2.15}$$

or, in dimensional form,

$$q_{sf}\left(\hat{t}_{j+1,p}\right) = (24)C_F\left[\frac{dp_{wf}}{dt}\right]_{\hat{t}_{j+1,p}}. \tag{3.2.16}$$

Note that the use of pressure derivatives in Eq. 3.2.16, may complicate the analysis of the multi-rate buildup method due the oscillatory behavior generally exhibited by raw derivative data. This represents the major disadvantage associated with the use of Eq. 3.2.12. Later in this Chapter, we present alternative multi-rate procedures which obtain the rate information without resorting to pressure derivatives.

3.2.2 Drillstem Test Buildup Solution

Here we consider the same well/reservoir geometry described in section 2.2.1 of Chapter II, that is, we assume a fully-penetrating well in an infinite, homogeneous and isotropic reservoir of uniform thickness. At initial conditions, the pressure is uniform throughout the reservoir and equal to p_i. At the wellbore, the pressure is set instantaneously equal to p_o. Under these assumptions, the drillstem test initial boundary value problem can be formulated as

$$\frac{1}{r_D}\frac{\partial}{\partial r_D}\left(r_D\frac{\partial p_D}{\partial r_D}\right)=\frac{\partial p_D}{\partial t_D}, \tag{3.2.17}$$

$$p_D(r_D,0)=0; \qquad 1<r_D<\infty, \tag{3.2.18}$$

$$\lim_{r_D\to\infty} p_D(r_D,t_D)=0; \qquad t_D\geq 0, \tag{3.2.19}$$

$$p_{wD}(0)=1, \tag{3.2.20}$$

$$p_{wD}=\left[p_D-s\left(r_D\frac{\partial p_D}{\partial r_D}\right)\right]_{r_D=1}, \tag{3.2.21}$$

and

$$\left(r_D\frac{\partial p_D}{\partial r_D}\right)_{r_D=1}=\begin{cases} C_{FD}\dfrac{dp_{wD}}{dt_D}, & t_D<t_{pD}; \\ C_{SD}\dfrac{dp_{wD}}{dt_D}, & t_D>t_{pD}. \end{cases} \tag{3.2.22}$$

A solution for the above DST problem can be written directly from Duhamel's principle as

$$p_{wD}(t_D)=\int_0^{t_D} q_D(\tau)\frac{dp^*_{wcD}}{dt_D}(t_D-\tau)d\tau=$$

$$\int_0^{t_{pD}} q_D(\tau)\frac{dp^*_{wcD}}{dt_D}(t_D-\tau)d\tau+\int_{t_{pD}}^{t_D} q_D(\tau)\frac{dp^*_{wcD}}{dt_D}(t_D-\tau)d\tau, \tag{3.2.23}$$

for $t_D > t_{pD}$. The solution for $t_D < t_{pD}$ was considered in Chapter II. In Eq. 3.2.23, q_D represents the dimensionless sandface flow rate defined by Eq. 3.1.9, whereas dp^*_{wcD}/dt_D denotes the time derivative of the constant sandface rate solution evaluated at $t_D - \tau$. From a material balance on the wellbore and using the dimensionless definitions given previously, the DST sandface flow rate is given by

$$q_D(t_D)=\begin{cases} -C_{FD}\dfrac{dp_{wD}}{dt_D}, & t_D<t_{pD}; \\ -C_{SD}\dfrac{dp_{wD}}{dt_D}, & t_D>t_{pD}. \end{cases} \tag{3.2.24}$$

Using Eq. 3.2.24 and the definition of the dimensionless pressure buildup change, p_{sD}, Eq. 3.2.23 can be written as

$$p_{sD}(\Delta t_D)=-C_{FD}\int_0^{t_{pD}}\frac{dp_{wD}}{d\tau}(\tau)\frac{dp^*_{wcD}}{dt_D}(t_{pD}+\Delta t_D-\tau)d\tau$$

$$-C_{SD}\int_0^{\Delta t_D}\frac{dp_{sD}}{d\tau}(\tau)\frac{dp^*_{wcD}}{d\Delta t_D}(\Delta t_D-\tau)d\tau. \tag{3.2.25}$$

Note that Eq. 3.2.25 represents a implicit solution, that is, p_{sD} appears in both sides of the equation. Upon rewriting the second integral in the right hand side of Eq. 3.2.25 in a discrete from, a recursive algorithm can be obtained to generate the DST dimensionless pressure buildup solutions.

An explicit analytical solution for the DST buildup problem given by Eqs. 3.2.17 - 3.2.22 was obtained by Correa and Ramey[44] and is given by

$$p_{wD}(t_D) = C_{SD}\frac{dp_{wcD}}{dt_D}(t_D, C_{SD}, s)+$$

$$(C_{SD} - C_{FD})\int_0^{t_{pD}} \frac{dp_{wD}}{d\tau}(\tau)\frac{dp_{wcD}}{dt_D}(t_D - \tau, C_{SD}, s)d\tau; \quad \text{for } t_D > t_{pD}. \quad (3.2.26)$$

Note that the solution presented by Eq. 3.2.26 is given in terms of the constant surface solution, p_{wcD}, and no pressure buildup solutions appears in the right hand side of Eq. 3.2.26. Thus, the computation of the buildup solution by means of Eq. 3.2.26 is more efficient and easier to implement than Eq. 3.2.25. The integral that appears in Eq. 3.2.26 can be evaluated by standard numerical methods presented elsewhere[65]. It is important to realize that both Eqs. 3.2.25 and 3.2.26 are general solutions for the DST problem and are not restricted to the radial flow problem considered in this section.

Based on Eq. 3.2.26, Ref. 44 proposed a method for the analysis of DST pressure buildup data. For shut-in times such that $t_D \gg t_{pD}$ and assuming that p_{wcD} is given by the logarithmic approximation, Ref. 44 showed that Eq. 3.2.26 becomes

$$\frac{p_{sD}(\Delta t_D)}{m_{cD}} = \frac{t_{pD}}{t_{pD} + \Delta t_D} = t_{cD}, \quad (3.2.27)$$

where t_{cD} is defined by the second equality of Eq. 3.2.27, and m_{cD} is defined by

$$m_{cD} = \frac{C_{FD}\left[1 - p_{wD}(t_{pD})\right] + C_{SD}p_{wD}(t_{pD})}{2\, t_{pD}}. \quad (3.2.28)$$

The dimensional form of Eqs. 3.2.27 and 3.2.28 for analyzing field data are given, respectively, by

$$p_{ws}(\Delta t) = p_i - m_c \frac{t_p}{t_p + \Delta t} \quad (3.2.29)$$

and

$$m_c = \frac{141.2(24)}{2(kh/\mu)\ t_p}\left\{C_F\left[p_{wf}(t_p) - p_o\right] + C_S\left[p_i - p_{wf}(t_p)\right]\right\} \qquad (3.2.30)$$

Eqs. 3.2.29 and 3.2.30 suggest that the reservoir flow capacity and the initial reservoir pressure can be determined from a Cartesian plot of p_{ws} versus $t_c = t_p/(t_p+\Delta t)$ provided that $C_S \ll C_F$. Throughout this work, this plotting technique is referred to as the Cartesian Method.

Using an approximation of the logarithmic function in Eq. 3.2.3, Soliman[45] derived the same plotting technique given in Ref. 44 for cases in which the buildup is preceded by a short flow period. Following Soliman's approach, the long time approximation of Eq. 3.2.8 becomes

$$\frac{p_{sD}(\Delta t_D)}{m_D} = -\ln\left(1 - \frac{t_{pD}}{t_{pD}+\Delta t_D}\right) \approx \frac{t_{pD}}{t_{pD}+\Delta t_D}, \qquad (3.2.31)$$

for the DST problem. If C_{FD} is much larger than C_{SD}, which is often the case for DST's, then from Eqs. 3.2.7 and 3.2.28, we see that $m_D \approx m_{cD}$, and then Eqs. 3.2.27 and 3.2.31 are identical. The above development is intended to show that there is no advantage in using the Cartesian Method of Ref. 44 instead of the Horner plot given by Eq. 3.2.8. Both methods fail to consider the effect of rate variation during the flow period, lumping all the rate history into the average flow rate.

3.3 Analysis Procedures

In this section the theoretical foundation of the new buildup methods for drill-stem tests are presented. First, new straight-line methods are proposed. Then, a buildup type-curve matching procedure is discussed.

3.3.1 Straight-line Method 1

As discussed in the previous section, a general solution for the DST problem can be obtained from the Duhamel's formula and is given by Eq. 3.2.25. Eq. 3.2.23 can also be written as[46]

$$p_{wD}(t_D) = \frac{d}{dt_D}\int_0^{t_D} q_D(\tau)\ p^*_{wcD}(t_D - \tau)d\tau. \qquad (3.3.1)$$

Eq. 3.3.1 represents another form of the Duhamel's principle and is equivalent to Eq. 3.2.23. To obtain Eq. 3.2.23 from Eq. 3.3.1, one can apply Leibnitz's rule for the differentiation of integrals. Eq. 3.3.1 is starting point in the development of the Method 1.

Integrating both sides of Eq. 3.3.1, gives

$$\int_0^{t_D} p_{wD}(\tau)d\tau = \int_0^{t_D} q_D(\tau)\; p^*_{wcD}(t_D-\tau)d\tau. \tag{3.3.2}$$

For $t_D > t_{pD}$, Eq. 3.3.2 can be written as

$$\int_0^{t_D} p_{wD}(\tau)d\tau =$$

$$\int_0^{t_{pD}} q_D(\tau)\; p^*_{wcD}(t_D-\tau)d\tau \; + \int_{t_{pD}}^{t_D} q_D(\tau)\; p^*_{wcD}(t_D-\tau)d\tau. \tag{3.3.3}$$

Note that the first integral in the right hand side of Eq. 3.3.3 accounts for the rate change during the flow period, whereas the second integral accounts for the flow rate variation after shut-in.

At the instant of shut-in, i.e., when $t_D = t_{pD}$, Eq. 3.3.2 gives

$$\int_0^{t_{pD}} p_{wD}(\tau)d\tau = \int_0^{t_{pD}} q_D(\tau)\; p^*_{wcD}(t_{pD}-\tau)d\tau. \tag{3.3.4}$$

Neglecting afterflow for the shut-in period (that is, assuming $q_D = 0$ for $t_D > t_{pD}$ or equivalently, assuming $C_{SD} = 0$) and subtracting Eq. 3.3.4 from Eq. 3.3.3, one obtains

$$I(p_{sD}) = \int_0^{t_{pD}} q_D(\tau)\left[p^*_{wcD}(t_D-\tau) - p^*_{wcD}(t_{pD}-\tau)\right]d\tau, \tag{3.3.5}$$

where $I(p_{sD})$ represents the integral of the pressure buildup change defined by

$$\begin{aligned} I(p_{sD}) &= \int_{t_{pD}}^{t_D} p_{wD}(\tau)d\tau \\ &= \int_0^{\Delta t_D} p_{sD}(\tau)d\tau. \end{aligned} \tag{3.3.6}$$

The second equality in Eq. 3.3.6 indicates that the integration is carried over the shut-in times, thus only buildup pressures are involved in the computation of $I(p_{sD})$.

Using the partition of the interval $[0, t_{pD}]$ given by Eq. 3.2.9, Eq. 3.3.5 can be written as

$$I(p_{sD}) = \sum_{j=0}^{n} \int_{t_{j,pD}}^{t_{j+1,pD}} q_D(\tau)\left[p^*_{wcD}(t_D - \tau) - p^*_{wcD}(t_{pD} - \tau)\right] d\tau$$

$$\approx \sum_{j=0}^{n} \left\{ \left[p^*_{wcD}(t_D - \hat{t}_{j+1,pD}) - p^*_{wcD}(t_{pD} - \tilde{t}_{j+1,pD})\right] \int_{t_{j,pD}}^{t_{j+1,pD}} q_D(\tau) d\tau \right\}, \tag{3.3.7}$$

where $\hat{t}_{j+1,pD}$ and $\tilde{t}_{j+1,pD}$ are points selected in the interval

$$t_{j,pD} \leq \tau \leq t_{j+1,pD} \; ; \qquad j = 0, 1, \cdots, n, \tag{3.3.8}$$

accordingly to the following expressions

$$\hat{t}_{j+1,pD} = \theta_{j+1} t_{j+1,pD} + (1 - \theta_{j+1}) t_{j,pD} \tag{3.3.9}$$

and

$$\tilde{t}_{j+1,pD} = \xi_{j+1} t_{j+1,pD} + (1 - \xi_{j+1}) t_{j,pD} \tag{3.3.10}$$

In this work, we always select $\theta_{j+1} = \xi_{j+1}$ for all j and thus $\hat{t}_{j+1,pD} = \tilde{t}_{j+1,pD}$.

The sandface flow rate at any time τ such that $\tau \leq t_{pD}$, is given by

$$q_D(\tau) = -C_{FD} \left[\frac{dp_{wD}}{dt_D}\right]_{\tau}. \tag{3.3.11}$$

Using Eq. 3.3.11 in the second equality of Eq. 3.3.7 and performing the integration yields the following equation

$$I(p_{sD}) = -C_{FD} \sum_{j=0}^{n} \left\{ \left[p^*_{wcD}(t_D - \hat{t}_{j+1,pD})\right.\right.$$

$$\left.\left. - p^*_{wcD}(t_{pD} - \hat{t}_{j+1,pD})\right] \left[p_{wD}(t_{j+1,pD}) - p_{wD}(t_{j,pD})\right] \right\}. \tag{3.3.12}$$

Note that the last step eliminates flow rate from the equations however, its effect is still properly accounted for by the last term between brackets in Eq. 3.3.12. The wellbore pressure difference in that term multiplied by $-C_{FD}$ gives the cumulative production on the time interval from $t_{j,pD}$ to $t_{j+1,pD}$.

By replacing $p^{\bullet}_{wcD}$ in Eq. 3.3.12 by the appropriate constant sandface rate solution of interest, a buildup analysis method can be constructed. For transient radial flow, the $p^{\bullet}_{wcD}$ terms may be replaced by the standard log approximation and then Eq. 3.3.12 can be rewritten as

$$\frac{1}{m_D \Delta t_D} I(p_{sD}) = t_{1D}, \tag{3.3.13}$$

where m_D is given by Eq. 3.2.7 and t_{1D} is the multi-rate dimensionless time of Method 1 defined by

$$t_{1D} = -\sum_{j=0}^{n} \left\{ \frac{t_{pD}}{\Delta t_D} \ln \left(\frac{t_D - \hat{t}_{j+1,pD}}{t_{pD} - \hat{t}_{j+1,pD}} \right) \left[\frac{p_{wD}(t_{j+1,pD}) - p_{wD}(t_{j,pD})}{1 - p_{wD}(t_{pD})} \right] \right\}. \tag{3.3.14}$$

Using the dimensionless definitions given previously and rearranging Eq. 3.3.13, it can be shown that

$$\frac{I(p_{ws})}{\Delta t} = p_i - m_1 t_1, \tag{3.3.15}$$

where

$$t_1 = \sum_{j=0}^{n} \left\{ \frac{t_p}{\Delta t} \log \left(\frac{t_p + \Delta t - t_{j,p}}{t_p - t_{j,p}} \right) \left[\frac{p_{wf}(t_{j+1,p}) - p_{wf}(t_{j,p})}{p_{wf}(t_p) - p_o} \right] \right\}, \tag{3.3.16}$$

and

$$m_1 = \frac{162.6}{(kh/\mu)} \frac{24 C_F \left[p_{wf}(t_p) - p_o \right]}{t_p}. \tag{3.3.17}$$

Note that in Eq. 3.3.16 it is assumed that $\theta_{j+1} = 0$ for all j. Also note that the multi-rate time t_1 is dimensionless. In Eq. 3.3.15, $I(p_{ws})$ denotes the time integral of the measured buildup pressure data, that is

$$I(p_{ws}) = \int_0^{\Delta t} p_{ws}(\tau) d\tau, \tag{3.3.18}$$

where $I(p_{ws})$ is in psi-hour.

Eq. 3.3.15 indicates that a plot of $I(p_{ws})/\Delta t$ versus the multi-rate time t_1 yields a straight line with slope m_1 (in psi). The permeability, k, can be obtained from the slope m_1 by the obvious rearrangement of Eq. 3.3.17. Note that by

extrapolating this straight line to $t_1 = 0$, one obtains the initial reservoir pressure p_i.

An equation for estimating the skin factor can be obtained as follows. Using the partition given by Eq. 3.2.9, Eq. 3.3.4 becomes

$$\int_0^{t_{pD}} p_{wD}(\tau)d\tau = \sum_{j=0}^{n}\left\{ p^{\bullet}_{wcD}(t_{pD} - \hat{t}_{j+1,pD}) \int_{t_{j,pD}}^{t_{j+1,pD}} q_D(\tau)d\tau \right\} =$$

$$= C_{FD}\sum_{j=0}^{n}\left\{ p^{\bullet}_{wcD}(t_{pD} - \hat{t}_{j+1,pD})\left[p_{wD}(t_{j,pD}) - p_{wD}(t_{j+1,pD})\right] \right\}, \qquad (3.3.19)$$

where $\hat{t}_{j+1,pD}$ is given by Eq. 3.3.9. Note that the second equality in Eq. 3.3.19 follows directly from Eq. 3.3.11. Assuming radial flow geometry so that $p^{\bullet}_{wcD}$ is given by the standard semilog equation, Eq. 3.3.19 can be rearranged to obtain

$$\frac{1}{C_{FD}\left[1 - p_{wD}(t_{pD})\right]} \int_0^{t_{pD}} p_{wD}(\tau)d\tau =$$

$$1.151\left\{ \sum_{j=0}^{n}\left(\log\left(t_{pD} - t_{j,pD}\right)\left[\frac{p_{wD}(t_{j,pD}) - p_{wD}(t_{j+1,pD})}{1 - p_{wD}(t_{pD})}\right]\right) + \log\left(\frac{4}{e^{\gamma}}\right)\right\} + s. \qquad (3.3.20)$$

Eq. 3.3.20 assumes $\hat{t}_{j+1,pD} = t_{jpD}$ for all j.

Multiplying and dividing the left hand side of Eq. 3.3.20 by t_{pD}, using the dimensionless definitions and solving the resulting equation for the skin factor, one obtains

$$\begin{aligned} s = 1.151\Bigg\{ & \frac{p_i - p_{avg}}{m_1} - \log\left(\frac{k}{\phi\mu c_t r_w^2}\right) + 3.23 \\ & - \sum_{j=0}^{n} \log\left(t_p - t_{j,p}\right)\left[\frac{p_{wf}(t_{j+1,p}) - p_{wf}(t_{j,p})}{p_{wf}(t_p) - p_o}\right]\Bigg\}, \end{aligned} \qquad (3.3.21)$$

where p_{avg} denotes the average flowing pressure, and is given by

$$p_{avg} = \frac{1}{t_p}\int_0^{t_p} p_{wf}(\tau)d\tau. \qquad (3.3.22)$$

A careful inspection of Eq. 3.3.21 shows that the above skin equation is identical to skin equation given by Eq. 2.3.30 evaluated at $t_{n+1} = t_p$.

The field application of Method 1 requires a scheme for performing the numerical integration of Eq. 3.3.18. Even though more accurate schemes exists, the composite trapezoidal rule discussed in Chapter II is very simple to implement and is accurate enough for most field applications. With the partition of the buildup period $[0, \Delta t]$ given by

$$0 = \Delta t_0 < \Delta t_1 < \cdots < \Delta t_m < \Delta t_{m+1} = \Delta t, \tag{3.3.23}$$

integrating Eq. 3.3.18 with the trapezoidal rule gives

$$I(p_{ws}) = \sum_{i=0}^{m} \left[\frac{p_{ws}(\Delta t_{i+1}) + p_{ws}(\Delta t_i)}{2} \right] (\Delta t_{i+1} - \Delta t_i), \tag{3.3.24}$$

where $p_{ws}(\Delta t_0) = p_{wf}(t_p)$.

The development of Method 1 was obtained by expanding Eq. 3.3.2 for times such that $t_D > t_{pD}$, that is, the development was restricted to the buildup period. If a similar procedure is carried out for the flow period instead, the resulting equation is identical to the converted slug test convolution method presented in section 2.3.3. Compare, for instance, Eq. 3.3.20 with Eqs. 2.3.24 and 2.3.25. Therefore, we may consider Method 1 as the buildup analog of the slug test convolution method presented in Chapter II.

3.3.2 Straight-line Method 2

In the previous section, a new DST multi-rate method was presented which does not require the computation of sandface flow rates from pressure derivatives. The procedure was obtained by rearranging Duhamel's principle so that the pressure derivatives were eliminated by integration of the sandface flow rate over a time partition. The same procedure will be followed here, however, the starting point is from the Duhamel's formula given by Eq. 3.2.23.

Assuming that the sandface rate goes immediately to zero at shut-in, Eq. 3.2.23 can be written as

$$p_{sD}(\Delta t_D) = \int_0^{t_{pD}} q_D(\tau) \frac{dp^*_{wcD}}{dt_D}(t_D - \tau) d\tau. \tag{3.3.25}$$

Using the flow period partition presented in Eq. 3.2.9, the discrete version of Eq. 3.3.25 becomes

$$\begin{aligned} p_{sD}(\Delta t_D) &= \sum_{j=0}^{n} \int_{t_{j,pD}}^{t_{j+1,pD}} q_D(\tau) \frac{dp^*_{wcD}}{dt_D}(t_D - \tau) d\tau \\ &= \sum_{j=0}^{n} \frac{dp^*_{wcD}}{dt_D}(t_D - \hat{t}_{j+1,pD}) \int_{t_{j,pD}}^{t_{j+1,pD}} q_D(\tau) d\tau, \end{aligned} \tag{3.3.26}$$

where $\hat{t}_{j+1,pD}$ is given by Eq. 3.3.9. Substituting Eq. 3.3.11 for q_D in the right hand side of Eq. 3.3.26 yields

$$p_{sD}(\Delta t_D) = -C_{FD} \sum_{j=0}^{n} \left\{ \frac{dp^*_{wcD}}{dt_D}(t_D - \hat{t}_{j+1,pD}) \left[p_{wD}(t_{j+1,pD}) - p_{wD}(t_{j,pD}) \right] \right\}. \tag{3.3.27}$$

For a radial flow problem, we may assume that the p^*_{wcD} terms in Eq. 3.3.27 are given by the standard semilog equation so that the derivative is given by $1/[2(t_D - \hat{t}_{j+1,pD})]$. Using this result in Eq. 3.3.27 and performing some algebraic manipulation, it can be shown that

$$\frac{p_{sD}(\Delta t_D)}{m_D} = t_{2D}, \tag{3.3.28}$$

where m_D is given by Eq. 3.2.7 and t_{2D} denotes the Method 2 multi-rate dimensionless time defined by

$$t_{2D} = -\sum_{j=0}^{n} \left\{ \left(\frac{t_{pD}}{t_D - \hat{t}_{j+1,pD}} \right) \left[\frac{p_{wD}(t_{j+1,pD}) - p_{wD}(t_{j,pD})}{1 - p_{wD}(t_{pD})} \right] \right\}. \tag{3.3.29}$$

The form of Eq. 3.3.28 that should be used for analyzing data is given by

$$p_{ws}(\Delta t) = p_i - m_2 t_2, \tag{3.3.30}$$

where

$$t_2 = \sum_{j=0}^{n} \left\{ \left(\frac{t_p}{t_p + \Delta t - t_{j,p}} \right) \left[\frac{p_{wf}(t_{j+1,p}) - p_{wf}(t_{j,p})}{p_{wf}(t_p) - p_o} \right] \right\} \tag{3.3.31}$$

and

$$m_2 = \frac{141.2}{(kh/\mu)} \frac{24 C_F \left[p_{wf}(t_p) - p_o \right]}{2\, t_p}. \tag{3.3.32}$$

Eq. 3.3.31 assumes $\theta_{j+1} = 0$ for all j, i.e., it assumes $\hat{t}_{j+1,p} = t_{j,p}$. Eq. 3.3.30 suggests that a plot of p_{ws} versus the multi-rate time t_2 yields a straight line with slope m_2 (in psi), and the extrapolation of the straight line to $t_2 = 0$ gives the initial reservoir pressure p_i. The permeability k can be obtained from the slope m_2 by the obvious rearrangement of Eq. 3.3.32. Note that the slopes of Methods 1 and 2 are related by

$$m_1 = m_2 \ln 10. \tag{3.3.33}$$

Method 2 does not provide a direct way of determining the skin factor since it is based on the derivative of the constant sandface rate solution, and this derivative is independent of the skin factor. However, we may "borrow" the skin factor equation of Method 1 by substituting Eq. 3.3.33 into Eq. 3.3.21; that is, we compute m_1 from Eq. 3.3.33 and use this value of m_1 in Eq. 3.3.21 to estimate s.

3.3.3 Type-Curve Matching

In the development of Methods 1 and 2, it is assumed that the flow rate during the buildup period is negligible. In cases where the formation is highly damaged, the group $C_{SD}\exp(2s)$ will assume large values, which will delay the beginning of the straight lines of Methods 1 and 2. Here, we present a type-curve matching procedure for drillstem test buildup data. The type curve approach is useful not only for determining the end of the wellbore storage but also for deciding whether the application of Methods 1 and 2 is appropriate. This section starts discussing the application of drawdown type curves for the analysis of buildup data preceded by a constant rate flow period. Then, we extend that discussion to DST buildup data.

The dimensionless wellbore pressure solution for the constant surface rate storage and skin problem is given by[19]

$$p_{wcD}(t_D, C_D, s) =$$

$$\int_0^{t_D} \left[1 - C_D \frac{dp_{wcD}}{d\tau}(\tau)\right] \frac{dp^*_{wcD}}{dt_D}(t_D - \tau)d\tau; \; t_D < t_{pD}, \tag{3.3.34}$$

where C_D represents the dimensionless wellbore storage coefficient for the constant surface problem. All wellbore storage and skin drawdown type curves are based on the solution of Eq. 3.3.34. Agarwal et al.[19], Ramey[66], Gringarten et al.[20] and others discussed the application and restrictions in analyzing buildup pressure data using drawdown type curve solutions obtained from Eq. 3.3.34.

The dimensionless buildup pressure rise under constant surface rate production is given by

$$\tilde{p}_{scD}(\Delta t_D) = p_{wcD}(t_{pD}) - p_{scD}(\Delta t_D)$$

$$= p_{wcD}(t_{pD}) - p_{wcD}(t_D) + p_{wcD}(\Delta t_D);\ t_D > t_{pD}, \tag{3.3.35}$$

where the second equality in Eq. 3.3.35 follows from the definition of the dimensionless pressure buildup change given by Eq. 3.2.1. In Eq. 3.3.35, $\tilde{p}_{scD}(\Delta t_D)$ is defined by

$$\tilde{p}_{scD} = \frac{kh[p_{ws} - p_{wf}(t_p)]}{141.2qB\mu}. \tag{3.3.36}$$

Refs. 19, 66 and 20 indicated that for shut-in times satisfying the condition $\Delta t_D \ll t_{pD}$, we have $p_{wcD}(t_D) \approx p_{wcD}(t_{pD})$ and Eq. 3.3.35 becomes

$$\tilde{p}_{scD}(\Delta t_D) = p_{wcD}(\Delta t_D), \tag{3.3.37}$$

therefore, for shut-in times satisfying the above condition, the pressure difference $[p_{ws} - p_{wf}(t_p)]$ can be analyzed using drawdown type curves. As a rule of thumb, Ref. 66 suggested that drawdown type curves could be used to analyze buildup data if $\Delta t \leq 0.1 t_p$, whereas Ref. 20 pointed out that for large values of $C_D \exp(2s)$ the shut-in time could be as large as the producing time.

The above result on using drawdown type curves to analyze buildup data is based on the second equality of Eq. 3.3.35, which is only valid when the wellbore storage coefficient has the same value for both drawdown and buildup period. When this condition is not satisfied, which is often the case in field applications, a more rigorous justification for using drawdown solutions is necessary and is presented here.

Consider the buildup response preceded by a constant sandface rate drawdown period. The sandface flow rate for this problem is given by

$$q_{cD}(t_D) = \begin{cases} 1 & t_D < t_{pD}; \\ -C_D \dfrac{dp_{scD}}{d\Delta t_D}(\Delta t_D), & t_D > t_{pD}. \end{cases} \tag{3.3.38}$$

Using Duhamel's principle, one can write

$$p_{scD}(\Delta t_D) = \int_0^{t_D} q_{cD}(\tau) \frac{dp^*_{wcD}}{dt_D}(t_D - \tau) d\tau =$$

$$\int_0^{t_{pD}} q_{cD}(\tau) \frac{dp^*_{wcD}}{dt_D}(t_D - \tau) d\tau + \int_{t_{pD}}^{t_D} q_{cD}(\tau) \frac{dp^*_{wcD}}{dt_D}(t_D - \tau) d\tau. \tag{3.3.39}$$

Combining Eq. 3.3.38, Eq. 3.3.39 and the first equality of Eq. 3.3.35, one obtains

$$\tilde{p}_{scD}(\Delta t_D) = p^*_{wcD}(t_{pD}) - p^*_{wcD}(t_D) + p^*_{wcD}(\Delta t_D) +$$

$$\int_0^{\Delta t_D} \left[C_D \frac{dp_{scD}}{d\tau}(\tau) \right] \frac{dp^*_{wcD}}{d\Delta t_D}(\Delta t_D - \tau) d\tau. \tag{3.3.40}$$

In the above derivation we used the fact that the sandface flow rate is constant before shut-in, thus $p_{wcD}(t_{pD}) = p^*_{wcD}(t_{pD})$. Differentiating both sides of Eq. 3.3.35 with respect to the shut-in time, one obtains the following expression

$$\frac{d\tilde{p}_{scD}}{d\Delta t_D}(\Delta t_D) = -\frac{dp_{scD}}{d\Delta t_D}(\Delta t_D). \tag{3.3.41}$$

Using Eq. 3.3.41 in the right hand side of Eq. 3.3.40, and considering shut-in times such that $t_D \approx t_{pD}$, Eq. 3.3.40 becomes

$$\begin{aligned} \tilde{p}_{scD}(\Delta t_D) &= p^*_{wcD}(\Delta t_D) - \int_0^{\Delta t_D} \left[C_D \frac{d\tilde{p}_{scD}}{d\tau}(\tau) \right] \frac{dp^*_{wcD}}{d\Delta t_D}(\Delta t_D - \tau) d\tau. \\ &= \int_0^{\Delta t_D} \left[1 - C_D \frac{d\tilde{p}_{scD}}{d\tau}(\tau) \right] \frac{dp^*_{wcD}}{d\Delta t_D}(\Delta t_D - \tau) d\tau. \end{aligned} \tag{3.3.42}$$

Comparing the right hand side of Eq. 3.3.34 with the second equality of Eq. 3.3.42, it is clear that they represent the same basic solution, therefore, the buildup dimensionless pressure rise, $\tilde{p}_{scD}$, when graphed versus the actual shut-in time correlates with the drawdown solutions as long as Δt_D is small compared to t_{pD}.

A different approach for analyzing buildup data with drawdown type curves was presented by Agarwal[67]. Assuming that all p_{wcD} solutions appearing in the right hand side of Eq. 3.3.35 can be replaced by the logarithmic approximation, we have

$$\tilde{p}_{scD}(\Delta t_D) = \left[\frac{1}{2}\ln\left(\frac{4t_{pD}}{e^{\gamma}}\right)+s\right] - \left[\frac{1}{2}\ln\left(\frac{4(t_{pD}+\Delta t_D)}{e^{\gamma}}\right)+s\right]$$

$$+\left[\frac{1}{2}\ln\left(\frac{4\Delta t_D}{e^{\gamma}}\right)+s\right] = \frac{1}{2}\ln\left(\frac{4}{e^{\gamma}}\frac{t_{pD}\Delta t_D}{t_{pD}+\Delta t_D}\right)+s. \qquad (3.3.43)$$

Based on Eq. 3.3.43, Ref. 67 suggested that all buildup data can be correlated with drawdown type curves if the shut-in time is transformed to an equivalent drawdown time, given by

$$t_{eD} = \frac{t_{pD}\Delta t_D}{t_{pD}+\Delta t_D}. \qquad (3.3.44)$$

Strictly speaking, Eq. 3.3.44 is only valid for radial flow and zero wellbore storage. However, Ref. 67 showed through numerical examples that Eq. 3.3.44 also holds for $C_D \neq 0$ if $[t_{pD}/C_D] > 60$, that is, when wellbore storage effects are negligible at the moment of shut-in. The results of Ref. 67 assume that the drawdown and buildup wellbore storage coefficients are identical; here, we briefly indicate that the equivalent time approach can also be extended to cases in which this condition is not satisfied. For small shut-in times, Eq. 3.3.44 shows that $t_{eD} \approx \Delta t_D$, therefore, $\tilde{p}_{scD}$ graphed versus equivalent time will also correlate with the drawdown type curves during the early portions of the buildup; see Eq. 3.3.42. For shut-in times such $[\Delta t_D/C_D]$ is large (say, greater than 60), computations indicate that the integral at the right hand side of Eq. 3.3.40 can be neglected (no satisfactory theoretical proof to confirm this result is known to date), and the equivalent time definition given by Eq. 3.3.44 is obtained by replacing the p^*_{wcD} terms in Eq. 3.3.40 by the logarithmic approximation.

In a drillstem test, the maximum recorded shut-in time is typically two or three times longer than the preceding flow period therefore, in analyzing DST buildup data with drawdown type curves, Agarwal's approach should be followed. Most

importantly, the rate variation during the flow period must be considered. Starting from the general DST solution given by Eq. 3.2.23, one can write

$$p_{wD}(t_{pD}) - p_{wD}(t_D) = \int_0^{t_{pD}} q_D(\tau)\frac{dp^*_{wcD}}{dt_{pD}}(t_{pD}-\tau)d\tau -$$

$$\int_0^{t_{pD}} q_D(\tau)\frac{dp^*_{wcD}}{dt_D}(t_D-\tau)d\tau - \int_{t_{pD}}^{t_D} q_D(\tau)\frac{dp^*_{wcD}}{dt_D}(t_D-\tau)d\tau, \qquad (3.3.45)$$

Combining the definition of the pressure buildup change, p_{sD}, and the buildup boundary condition of Eq. 3.2.24, gives

$$p_{wD}(t_{pD}) - p_{sD}(\Delta t_D) = \int_0^{t_{pD}} q_D(\tau)\left[\frac{dp^*_{wcD}}{dt_{pD}}(t_{pD}-\tau)d\tau - \frac{dp^*_{wcD}}{dt_D}(t_D-\tau)\right]d\tau +$$

$$\int_0^{\Delta t_D}\left[C_{SD}\frac{dp_{sD}}{d\tau}(\tau)\right]\frac{dp^*_{wcD}}{d\Delta t_D}(\Delta t_D-\tau)d\tau. \qquad (3.3.46)$$

Using the flow period partition presented in Eq. 3.2.9, Eq. 3.3.46 becomes

$$p_{wD}(t_{pD}) - p_{sD}(\Delta t_D) =$$

$$\sum_{j=0}^{n} q_D(\hat{t}_{j+1,pD})\int_{t_{j,pD}}^{t_{j+1,pD}}\left[\frac{dp^*_{wcD}}{dt_{pD}}(t_{pD}-\tau)d\tau - \frac{dp^*_{wcD}}{dt_D}(t_D-\tau)\right]d\tau +$$

$$\int_0^{\Delta t_D}\left[C_{SD}\frac{dp_{sD}}{d\tau}(\tau)\right]\frac{dp^*_{wcD}}{d\Delta t_D}(\Delta t_D-\tau)d\tau. \qquad (3.3.47)$$

Integrating term by term and rearranging, one obtains

$$\frac{p_{wD}(t_{pD}) - p_{sD}(\Delta t_D)}{q_D(\hat{t}_{n+1,pD})} =$$

$$\sum_{j=0}^{n}\left(\frac{q_D(\hat{t}_{j+1,pD}) - q_D(\hat{t}_{j,pD})}{q_D(\hat{t}_{n+1,pD})}\right)\left[p^*_{wcD}(t_{pD}-t_{j,pD}) - p^*_{wcD}(t_D-t_{j,pD})\right]$$

$$+p^*_{wcD}(\Delta t_D) + \int_0^{\Delta t_D}\left[\frac{C_{SD}}{q_D(\hat{t}_{n+1,pD})}\frac{dp_{sD}}{d\tau}(\tau)\right]\frac{dp^*_{wcD}}{d\Delta t_D}(\Delta t_D-\tau)d\tau. \qquad (3.3.48)$$

where $\hat{t}_{j+1,pD}$ is given by Eq. 3.3.9 and $q_D(\hat{t}_{0,pD})$ is defined to be zero. The dimensionless buildup pressure rise for the DST problem is defined as

$$\tilde{p}_{sD}(\Delta t_D) = \frac{p_{wD}(t_{pD}) - p_{sD}(\Delta t_D)}{q_D(\hat{t}_{n+1,pD})}, \qquad (3.3.49)$$

thus,

$$\frac{d\tilde{p}_{sD}}{d\Delta t_D}(\Delta t_D) = -\frac{1}{q_D(\hat{t}_{n+1,pD})}\frac{dp_{sD}}{d\Delta t_D}(\Delta t_D). \tag{3.3.50}$$

Using Eqs. 3.3.49 and 3.3.50 in Eq. 3.3.48, we obtain

$$\tilde{p}_{sD}(\Delta t_D) =$$

$$\sum_{j=0}^{n}\left(\frac{q_D(\hat{t}_{j+1,pD}) - q_D(\hat{t}_{j,pD})}{q_D(\hat{t}_{n+1,pD})}\right)\left[p^*_{wcD}(t_{pD} - t_{j,pD}) - p^*_{wcD}(t_D - t_{j,pD})\right]$$

$$+p^*_{wcD}(\Delta t_D) - \int_0^{\Delta t_D}\left[C_{SD}\frac{d\tilde{p}_{sD}}{d\tau}(\tau)\right]\frac{dp^*_{wcD}}{d\Delta t_D}(\Delta t_D - \tau)d\tau. \tag{3.3.51}$$

Note that the $\tilde{p}_{sD}$ definition is based on the rate at the moment of shut-in. For small shut-in times, Eq. 3.3.51 can be approximated by

$$\begin{aligned}\tilde{p}_{sD}(\Delta t_D) &= p^*_{wcD}(\Delta t_D) - \int_0^{\Delta t_D}\left[C_{SD}\frac{d\tilde{p}_{sD}}{d\tau}(\tau)\right]\frac{dp^*_{wcD}}{d\Delta t_D}(\Delta t_D - \tau)d\tau. \\ &= \int_0^{\Delta t_D}\left[1 - C_{SD}\frac{d\tilde{p}_{sD}}{d\tau}(\tau)\right]\frac{dp^*_{wcD}}{d\Delta t_D}(\Delta t_D - \tau)d\tau.\end{aligned} \tag{3.3.52}$$

The comparison of the right hand side of Eq. 3.3.34 with Eq. 3.3.52 indicates that the buildup data following a variable flow rate period can also be correlated with the drawdown type curves if the pressure rise is normalized by the last rate before shut-in. For large shut-in times, computations indicate that the integral at the right hand side of Eq. 3.3.51 becomes less important compared to the other terms, therefore, $\tilde{p}_{sD}$ can be approximated by

$$\tilde{p}_{sD}(\Delta t_D) = p^*_{wcD}(\Delta t_D) +$$

$$\sum_{j=0}^{n}\left(\frac{q_D(\hat{t}_{j+1,pD}) - q_D(\hat{t}_{j,pD})}{q_D(\hat{t}_{n+1,pD})}\right)\left[p^*_{wcD}(t_{pD} - t_{j,pD}) - p^*_{wcD}(t_D - t_{j,pD})\right]. \tag{3.3.53}$$

Assuming radial flow geometry in Eq. 3.3.53, a multi-rate equivalent time can be defined by

$$t_{eMD} = \Delta t_D \prod_{j=0}^{n}\left(\frac{t_{pD} - t_{j,pD}}{t_{pD} + \Delta t_D - t_{j,pD}}\right)^{b_j}, \tag{3.3.54}$$

where the exponent b_j is given by

$$b_j = \frac{q_D(\hat{t}_{j+1,pD}) - q_D(\hat{t}_{j,pD})}{q_D(\hat{t}_{n+1,pD})}. \tag{3.3.55}$$

The multi-rate equivalent time defined by Eq. 3.3.54 was proposed previously by Agarwal[67] for the analysis of multi-rate tests. Note that for small values of Δt_D, we obtain directly from Eq. 3.3.54 that $t_{eMD} \approx \Delta t_D$. Thus, based on the results of Eqs. 3.3.52 and 3.3.53, drawdown type curves can be utilized for analyzing DST buildup data if $\tilde{p}_{sD}$ is graphed versus t_{eMD}. Computations indicate that the multi-rate equivalent time is applicable provided that $t_{pD}/C_{SD} \geq (60+3.5s)$. If derivative type curves are used, one should take the logarithmic derivative of $\tilde{p}_{sD}$ with respect to multi-rate equivalent time. Both $\tilde{p}_{sD}$ and $\tilde{p}'_{sD}$ should be graphed versus t_{eMD} in the log-log plot. Type curve matching is then performed in the usual manner.

One of the drawbacks of the equivalent time approach is that it often shrinks the span of the measured data. This can be seen from Eq. 3.3.44, which shows that t_{eD} approaches t_{pD} for large shut-in times. Thus, for short constant flow rate periods, the practical use of equivalent time is greatly reduced. However, if the rate monotonically decreases during the flow period, the multi-rate equivalent time actually increases the span of the data for most shut-in times of practical interest, and if the rate variation is large, t_{eMD} may be significantly greater than the maximum shut-in time recorded. Note that, in contrast with Methods 1 and 2, the computation of t_{eMD} requires the use of flow rates which are calculated from pressure derivatives (see Eq. 3.2.15). This problem will be addressed in the Practical Considerations section.

3.3.4 Modification of Methods 1 and 2

In the development of Methods 1 and 2, we neglect afterflow effects on the buildup response. However, if the formation is highly damaged, the presence of wellbore storage will delay the beginning of the proper straight line in both Methods 1 and 2. In such a case, if a well defined unit slope line appears on the log-log plot of $\tilde{p}_{sD}$ versus t_{eMD}, the buildup wellbore storage coefficient can be estimated by the following expression:

$$C_S = \frac{q_{sf}(\hat{t}_{n+1,p})}{24} \left[\frac{t^*_{eM}}{\left[p_{ws} - p_{wf}(t_p)\right]_{t^*_{eM}}} \right], \qquad (3.3.56)$$

where $(t^*_{cM}, [p_{ws} - p_{wf}(t_p)]_{t^*_{cM}})$ is any point on the unit slope line. Once C_S is known, afterflow effects can be taken into account by using the modified versions of Methods 1 and 2 presented in this section.

Consider the partition of the buildup period $[0, \Delta t_D]$ given by

$$0 = \Delta t_{0,D} < \Delta t_{1,D} < \cdots < \Delta t_{m,D} < \Delta t_{m+1,D} = \Delta t_D. \tag{3.3.57}$$

Starting from Eqs. 3.3.3 and 3.3.4 and following the procedure of Section 3.3.1, one can write

$$I(p_{sD}) = \sum_{j=0}^{n} \left\{ \left[p^*_{wcD}(t_D - \hat{t}_{j+1,pD}) - p^*_{wcD}(t_{pD} - \hat{t}_{j+1,pD}) \right] \int_{t_{j,pD}}^{t_{j+1,pD}} q_D(\tau) d\tau \right\}$$
$$+ \sum_{i=0}^{m} \left\{ p^*_{wcD}(\Delta t_D - \Delta \hat{t}_{i+1,D}) \int_{\Delta t_{i,D}}^{\Delta t_{i+1,D}} q_D(t_{pD} + \tau) d\tau \right\}, \tag{3.3.58}$$

where $I(p_{sD})$ is given by Eq. 3.3.6, $\hat{t}_{j+1,pD}$ is given by Eq. 3.3.9 and $\Delta \hat{t}_{i+1,D}$ is defined by

$$\Delta \hat{t}_{i+1,D} = \theta_{i+1} \Delta t_{i+1,D} + (1 - \theta_{i+1}) \Delta t_{i,D}. \tag{3.3.59}$$

Using the DST boundary condition given by Eq. 3.2.24, Eq. 3.3.58 becomes

$$I(p_{sD}) = -C_{FD} \times$$

$$\sum_{j=0}^{n} \left\{ \left[p^*_{wcD}(t_D - \hat{t}_{j+1,pD}) - p^*_{wcD}(t_{pD} - \hat{t}_{j+1,pD}) \right] \left[p_{wD}(t_{j+1,pD}) - p_{wD}(t_{j,pD}) \right] \right\}$$

$$- C_{SD} \sum_{i=0}^{m} \left\{ p^*_{wcD}(\Delta t_D - \Delta \hat{t}_{j+1,pD}) \left[p_{sD}(\Delta t_{i+1,D}) - p_{sD}(\Delta t_{i,D}) \right] \right\}. \tag{3.3.60}$$

Replacing the p^*_{wcD} terms by the log approximation and rearranging, one obtains the modified Method 1 which is given by

$$\frac{I(p_{sD})}{C_{FD} \tilde{p}_{sD}} - \frac{C_{SD}}{C_{FD}} \tilde{s}_D = t_{3D}, \tag{3.3.61}$$

where t_{3D} is the multi-rate dimensionless time of the modified Method 1 defined by

$$t_{3D} = -\frac{1}{2\tilde{p}_{sD}} \left\{ \sum_{j=0}^{n} \ln \left(\frac{t_D - \hat{t}_{j+1,pD}}{t_{pD} - \hat{t}_{j+1,pD}} \right) \left[p_{wD}(t_{j+1,pD}) - p_{wD}(t_{j,pD}) \right] + \right.$$

$$\frac{C_{SD}}{C_{FD}}\sum_{i=0}^{m}\ln\left(\Delta t_D-\Delta\hat{t}_{i+1,D}\right)\left[p_{sD}(\Delta t_{i+1,D})-p_{sD}(\Delta t_{i,D})\right]\Bigg\} \tag{3.3.62}$$

and $\tilde{s}_D$ is given by

$$\tilde{s}_D = s+\frac{1}{2}\ln\left(\frac{4}{e^{\gamma}}\right). \tag{3.3.63}$$

The dimensional form of Eq. 3.3.61 for analyzing field data is given by

$$\frac{2.95\times10^{-4}kh}{\mu C_F}\frac{I(p_i-p_{ws})}{[p_{ws}(\Delta t_{m+1})-p_{wf}(t_p)]} = 1.151\ t_3+\frac{C_S}{C_F}\tilde{s}, \tag{3.3.64}$$

where $I(p_i-p_{ws})$ and t_3 are given, respectively, by

$$I(p_i-p_{ws}) = \int_0^{\Delta t}[p_i-p_{ws}(\tau)]d\tau \tag{3.3.65}$$

and

$$t_3 = \sum_{j=0}^{n}\left\{\log\left(\frac{t_p+\Delta t_{m+1}-t_{j,p}}{t_p-t_{j,p}}\right)\left[\frac{p_{wf}(t_{j+1,p})-p_{wf}(t_{j,p})}{p_{ws}(\Delta t_{m+1})-p_{wf}(t_p)}\right]\right\}$$

$$+\frac{C_S}{C_F}\sum_{i=0}^{m}\left\{\log\left(\Delta t_{m+1}-\Delta t_i\right)\left[\frac{p_{ws}(\Delta t_{i+1})-p_{ws}(\Delta t_i)}{p_{ws}(\Delta t_{m+1})-p_{wf}(t_p)}\right]\right\}. \tag{3.3.66}$$

In Eq. 3.3.64, $\tilde{s}$ is defined by Eq. 2.3.28. Note that in Eq. 3.3.66, it is assumed that $\theta_{j+1}=\theta_{i+1}=0$ for all j and i. Eq. 3.3.64 indicates that a plot of $I(p_i-p_{ws})/[p_{ws}(\Delta t)-p_{wf}(t_p)]$ versus the multi-rate time t_3 yields a slope m, given by

$$m = \frac{162.6(24)C_F}{(kh/\mu)}, \tag{3.3.67}$$

where m is in hours. Note that the modified Method 1 is very similar to the slug test convolution method given by Eq. 2.3.26. An equation for the skin factor can be obtained from the obvious rearrangement of Eq. 3.3.64.

The multi-rate time t_3 accounts for the flow rate variation during the flow and buildup periods without resorting to pressure derivatives, however the implementation of this technique requires knowledge of the initial reservoir pressure, p_i; see Eq. 3.3.65.

Using the time partitions given by Eqs. 3.2.9 and 3.3.57, Eq. 3.2.23 can be written as

$$p_{sD}(\Delta t_D) = \sum_{j=0}^{n}\left\{\frac{dp^{*}_{wcD}}{dt_D}(t_D - \hat{t}_{j+1,pD})\int_{t_{j,pD}}^{t_{j+1,pD}} q_D(\tau)d\tau\right\} + \sum_{i=0}^{m}\left\{\frac{dp^{*}_{wcD}}{d\Delta t_D}(\Delta t_D - \Delta\hat{t}_{i+1,D})\int_{\Delta t_{i,D}}^{\Delta t_{i+1,D}} q_D(t_{pD}+\tau)d\tau\right\}, \tag{3.3.68}$$

where $\hat{t}_{j+1,pD}$ and $\Delta\hat{t}_{i+1,D}$ are given, respectively, by Eqs. 3.3.9 and 3.3.59. Using the DST boundary condition, Eq. 3.2.24, yields

$$p_{sD}(\Delta t_D) = -C_{FD}\sum_{j=0}^{n}\left\{\frac{dp^{*}_{wcD}}{dt_D}(t_D - \hat{t}_{j+1,pD})\left[p_{wD}(t_{j+1,pD}) - p_{wD}(t_{j,pD})\right]\right\}$$

$$-C_{SD}\sum_{i=0}^{m}\left\{\frac{dp^{*}_{wcD}}{d\Delta t_D}(\Delta t_D - \Delta\hat{t}_{i+1,D})\left[p_{sD}(\Delta t_{i+1,D}) - p_{sD}(\Delta t_{i,D})\right]\right\}. \tag{3.3.69}$$

Assuming radial flow geometry and rearranging, Eq. 3.3.69 becomes

$$\frac{p_{sD}(\Delta t_D)}{m_D} = t_{4D}, \tag{3.3.70}$$

where m_D is given by Eq. 3.2.7 and t_{4D} denotes the modified Method 2 multi-rate dimensionless time defined by

$$t_{4D} = -\sum_{j=0}^{n}\left\{\left(\frac{t_{pD}}{t_D - \hat{t}_{j+1,pD}}\right)\left[\frac{p_{wD}(t_{j+1,pD}) - p_{wD}(t_{j,pD})}{1 - p_{wD}(t_{pD})}\right]\right\}$$

$$-\frac{C_{SD}}{C_{FD}}\sum_{i=0}^{m}\left\{\left(\frac{t_{pD}}{\Delta t_D - \Delta\hat{t}_{i+1,D}}\right)\left[\frac{p_{sD}(\Delta t_{i+1,D}) - p_{sD}(\Delta t_{i,D})}{1 - p_{wD}(t_{pD})}\right]\right\}. \tag{3.3.71}$$

Using the dimensionless definitions, Eq. 3.3.70 gives

$$p_{ws}(\Delta t) = p_i - m_2 t_4, \tag{3.3.72}$$

where m_2 is given by Eq. 3.3.32 and t_4 is defined by

$$t_4 = \sum_{j=0}^{n}\left\{\left(\frac{t_p}{t_p + \Delta t_{m+1} - \hat{t}_{j+1,p}}\right)\left[\frac{p_{wf}(t_{j+1,p}) - p_{wf}(t_{j,p})}{p_{wf}(t_p) - p_o}\right]\right\} +$$

$$\frac{C_S}{C_F}\sum_{i=0}^{m}\left\{\left(\frac{t_p}{\Delta t_{m+1}-\Delta\hat{t}_{i+1}}\right)\left[\frac{p_{ws}(\Delta t_{i+1})-p_{ws}(\Delta t_i)}{p_{wf}(t_p)-p_o}\right]\right\}. \tag{3.3.73}$$

Eq. 3.3.72 indicates that a a plot of p_{ws} versus the multi-rate time t_4 yields a straight line with slope m_2 (in psi). Note that the extrapolation of the straight line to $t_4 = 0$ gives the initial reservoir pressure p_i and that the reservoir permeability can be estimated directly from Eq. 3.3.32. Similar to Method 2, the plotting technique given by Eq. 3.3.72 does not provide a direct equation for the skin factor. As discussed previously, the skin factor can be estimated from the skin equation obtained for the modified Method 1. In this regard, note that the slopes of these two methods are related by

$$\frac{m}{m_2} = \frac{t_p}{p_{wf}(t_p)-p_o}\ln 10. \tag{3.3.74}$$

Unfortunately, the application of the above method presents numerical difficulties in the computation of the multi-rate time t_{4D} which are discussed in the Results section.

3.3.5 Results

Here, computer generated data is used to illustrate the applications of the new methods. The drillstem test pressure response used here considers a fully penetrating well in a homogeneous, infinite reservoir. The p_{wD} solutions were obtained from Eq. 2.2.17, for the flow period, and from Eq. 3.2.26 for the buildup period. The Stehfest[54] algorithm was used to obtain the p_{wcD} solutions in real space.

Four cases were selected to illustrate the effect of skin and wellbore storage on the DST buildup response.

Case 1 - $t_{pD} = 10^4; C_{FD} = 10^3; C_{SD} = 0; s = 0.$

Case 1A - $t_{pD} = 10^4; C_{FD} = 10^3; C_{SD} = 10; s = 0.$

Case 2 - $t_{pD} = 10^4; C_{FD} = 10^3; C_{SD} = 0; s = 10.$

Case 2A - $t_{pD} = 10^4; C_{FD} = 10^3; C_{SD} = 10; s = 10.$

Note that the producing time and the drawdown wellbore storage coefficient are the same for all cases. Note that Cases 1 and 1A have the same pressure response

during the flow period. Similarly, Cases 2 and 2A give identical responses during the flow period.

Fig. 3.3.1 presents the pressure response for the flow and buildup periods of Case 1A. Note that t_D represents the total test time and p_{wD} denotes the dimensionless pressure for the either flow or buildup period, as defined by Eq. 3.1.7. Cases 1 and 1A represent the typical DST case of high fluid recovery during the flow period.

Fig. 3.3.2 shows a log-log plot of the sandface flow rate versus time for Case 1A. Note that the rate at the moment of shut-in is about ten times smaller than the first rate shown in the figure. After the well is closed in, the sandface rate decreases rapidly to zero.

The drawdown and buildup pressure behavior for Case 2A is shown in Fig. 3.3.3. This figure presents the case of relatively small fluid recovery and shows a typical DST chart representative of a damaged formation. Note that during the flow period, the pressure increases almost linearly with time, indicating a nearly constant flow rate. The sandface flow rate variation for Case 2A is presented in Fig. 3.3.4. This figure shows that the rate at shut-in is about 3 times smaller than the initial flow rate, and, after shut-in, decreases rapidly to zero.

Fig. 3.3.5 shows a comparison of the different analysis techniques discussed in this Chapter when applied to the buildup pressure response of Case 1. As noted previously, a large rate variation occurs during the flow period, however, the rate drops instantaneously to zero ($C_{SD} = 0$) when the well is shut in. The solid triangles in Fig. 3.3.5 represent buildup pressures plotted versus the dimensionless time t_{HD} given by Eq. 3.2.8 (Horner plot). The Cartesian Method is shown as solid circular data points. The proposed new buildup methods are indicated by the open triangular data points (Method 1) and the open circular data points (Method 2). In all cases, the multi-rate times t_{1D} and t_{2D} are computed using $\theta_{j+1} = 0.5$ for all j and $n = 50$ (see Eqs. 3.3.14 and 3.3.29).

As indicated by Eqs. 3.2.8, 3.2.27, 3.3.13 and 3.3.28, all four methods should yield a straight line with unit slope and intercept equal to zero, as shown by the

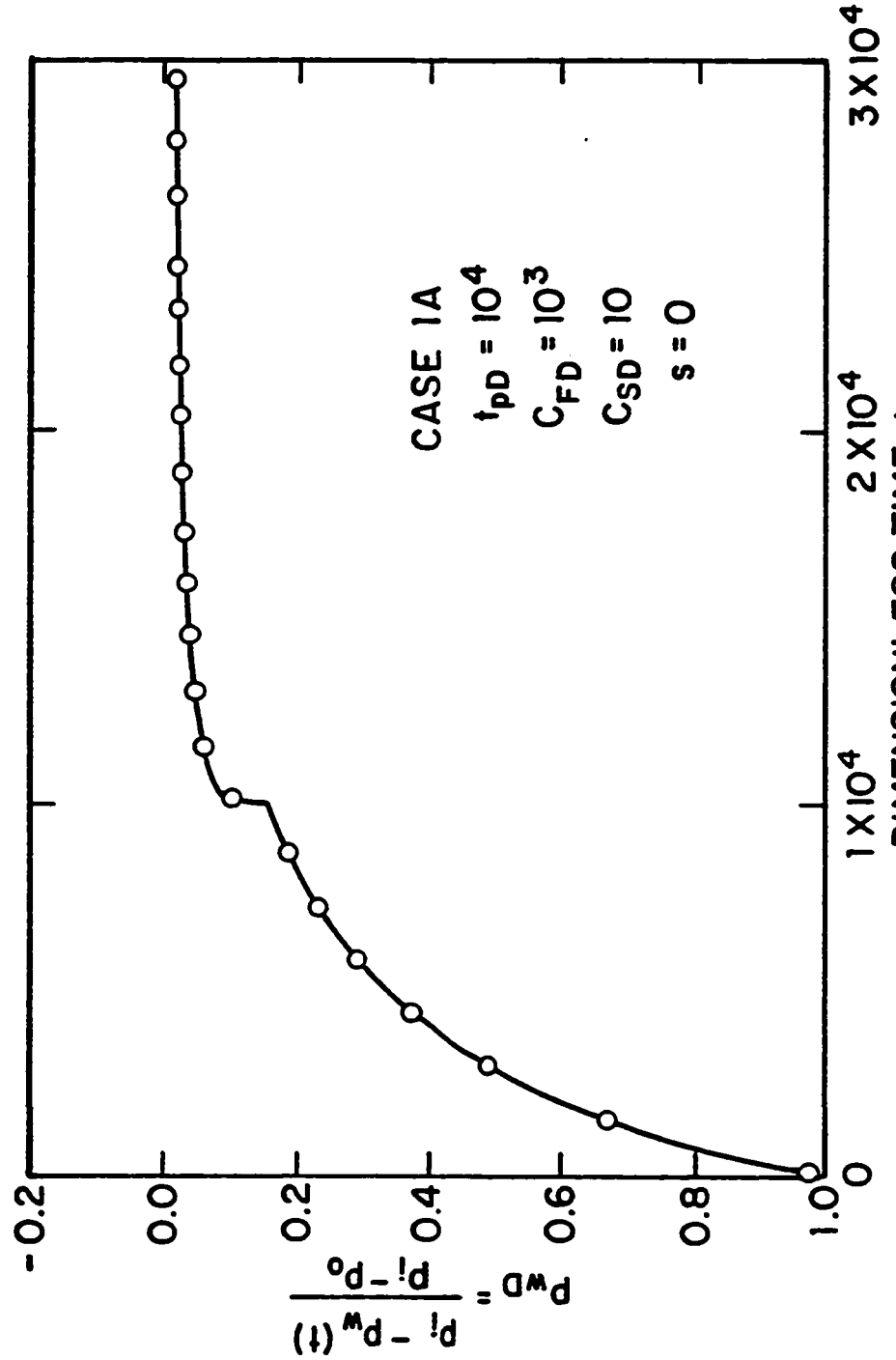

Fig. 3.3.1 - DST dimensionless wellbore pressure response; Case 1A.

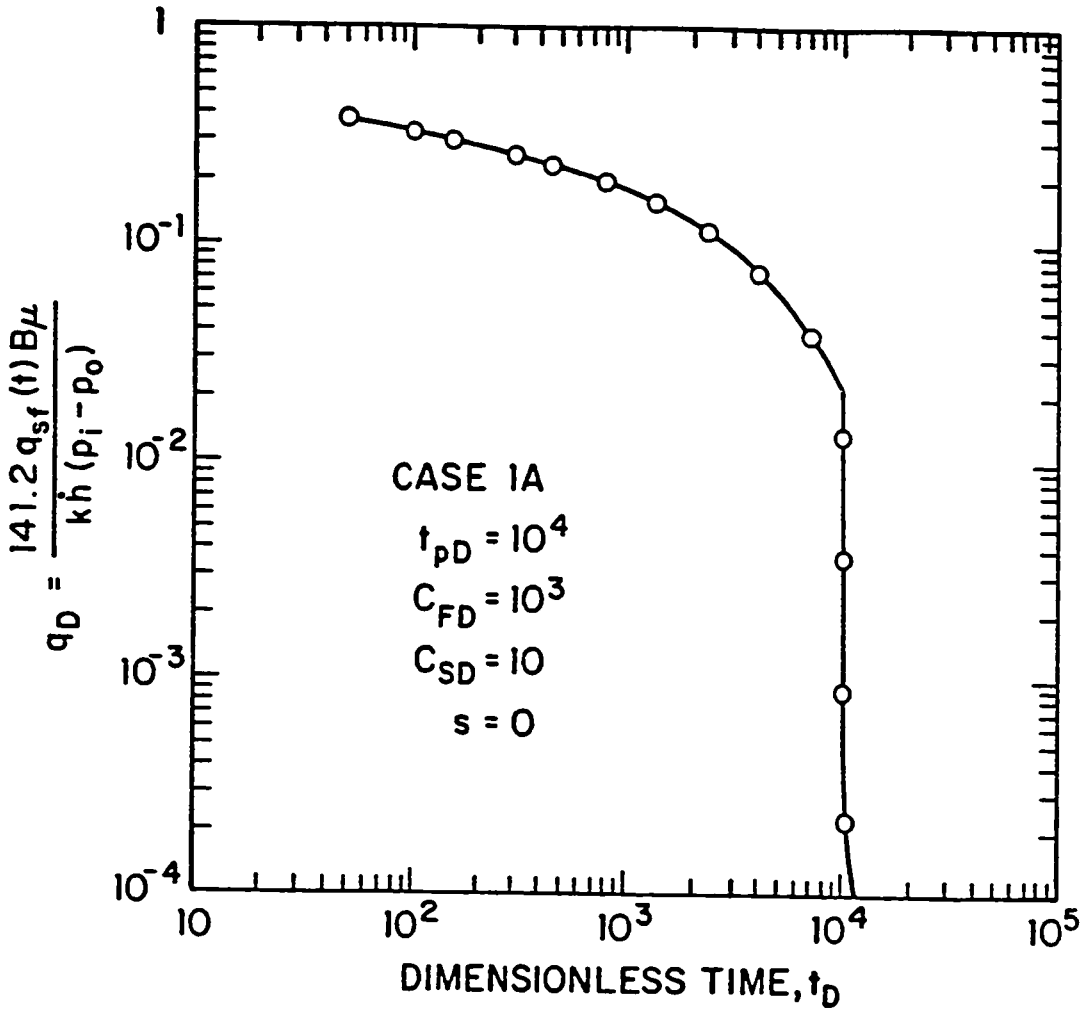

Fig. 3.3.2 - Log-log plot of the dimensionless sandface rate versus dimensionless time; Case 1A.

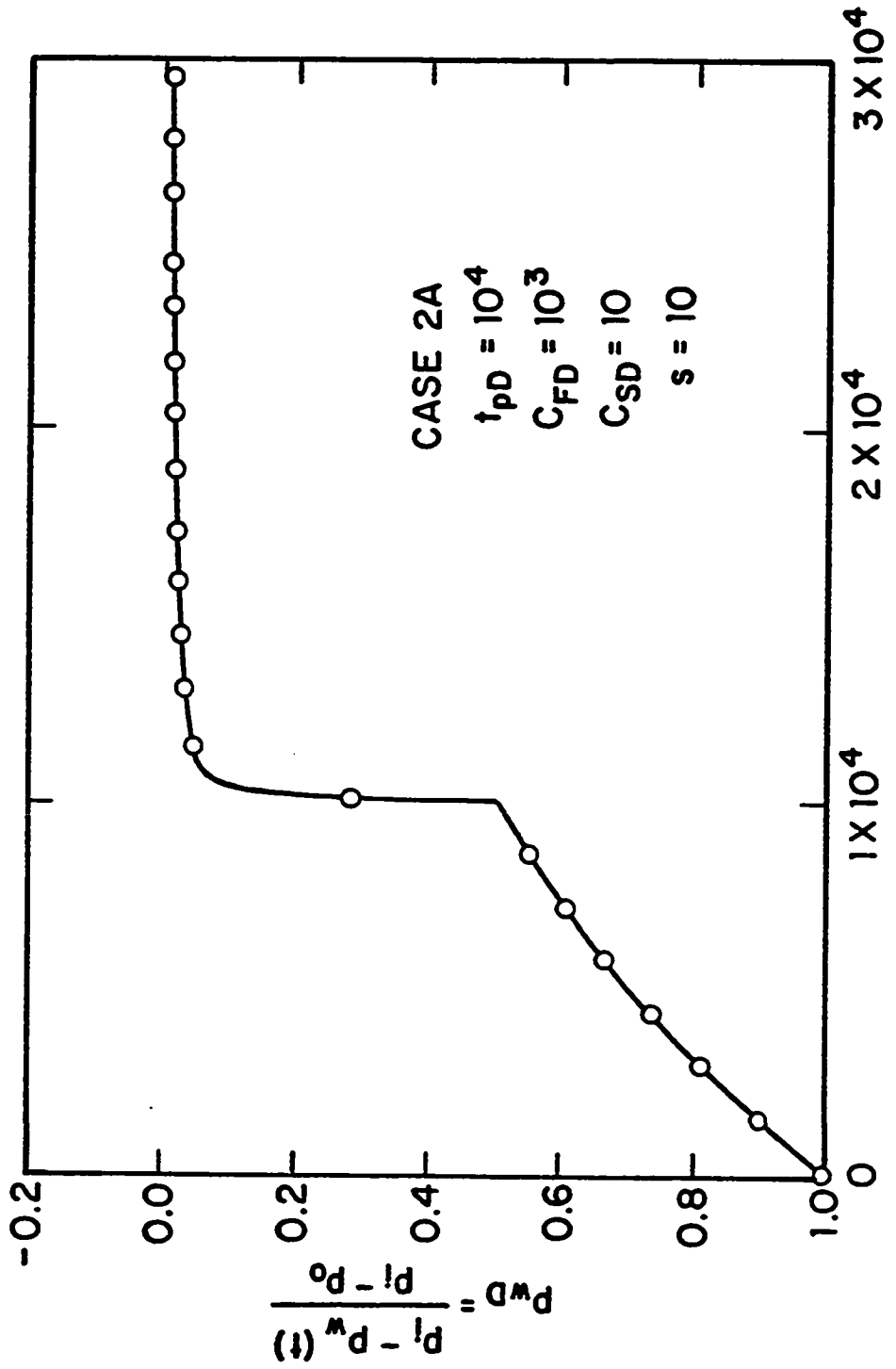

Fig. 3.3.3 - DST dimensionless wellbore pressure response; Case 2A.

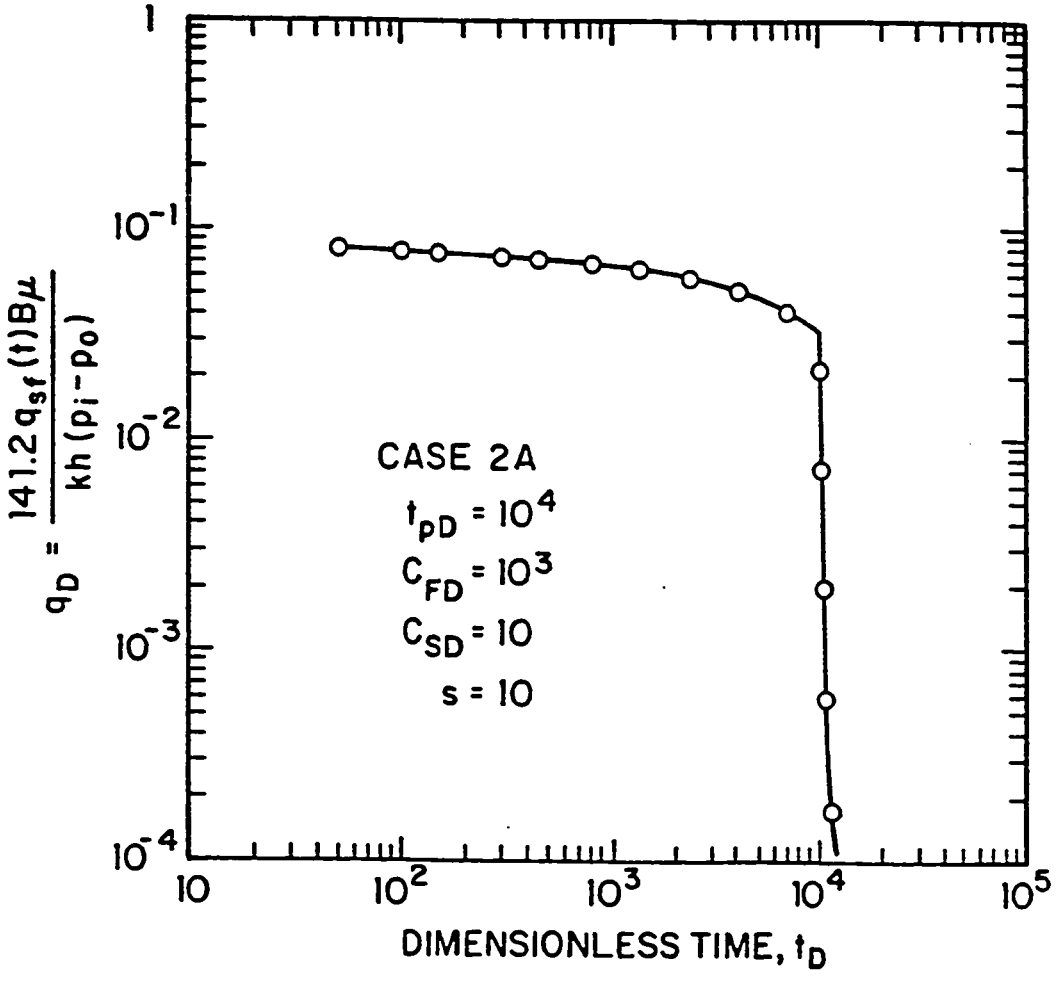

Fig. 3.3.4 - Log-log plot of the dimensionless sandface rate versus dimensionless time; Case 2A.

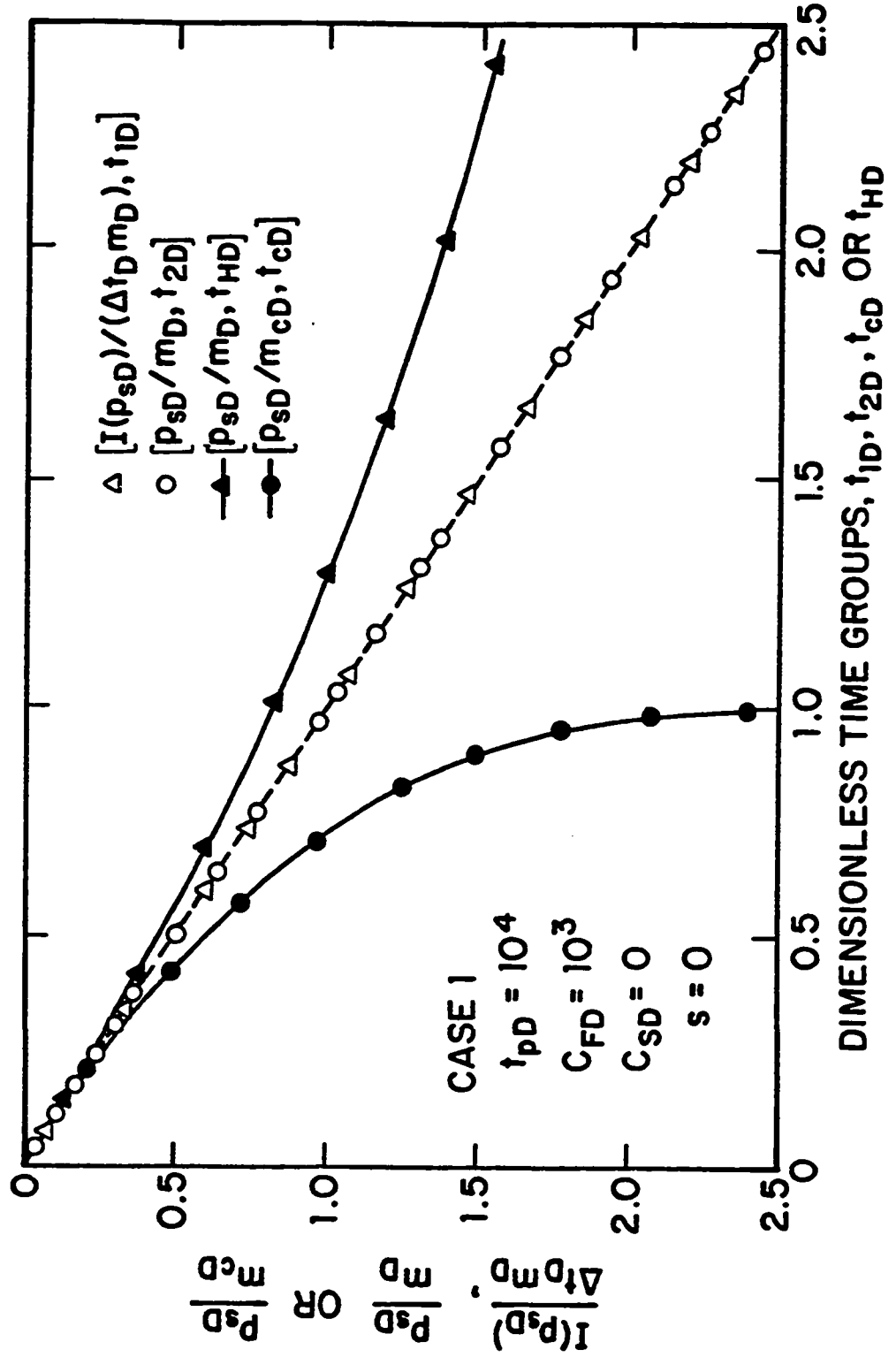

Fig. 3.3.5 - Comparison of straight-line methods; Case 1.

dashed straight line in Fig. 3.3.5. Methods 1 and 2 data points match the theoretical unit slope line as expected. However, due to the large rate variation in the flow rate prior to shut-in, the Horner method, based on the average flow rate (Eq. 3.2.8), and the Cartesian Method (Eq. 3.2.27) require large shut-in times before the proper slope is obtained. The behavior of the Horner plot can be misinterpreted as reservoir heterogeneity, as mentioned previously.

Fig. 3.3.6 presents results for Case 1A. The symbols convention are the same as in Fig. 3.3.5. As the combined wellbore storage and skin effect is small during the buildup period, the data plots for Methods 1 and 2 exhibit the proper straight line shortly after shut-in. Similar to Case 1, the Horner and the Cartesian Method plots provide the correct slope only for large shut-in times.

Fig. 3.3.7 shows a log-log plot of the dimensionless buildup pressure rise, $\tilde{p}_{sD}$, for Case 1A. The solid line in Fig. 3.3.7 represents the constant rate drawdown type curve solution for $C_D = C_{SD} = 10$ and $s = 0$. The circular data points shows that the plot of $\tilde{p}_{sD}$ versus $\Delta t_D/C_{SD}$ correlates with p_{wcD} only at small shut-in times. The plot of $\tilde{p}_{sD}$ versus multi-rate equivalent time (Eq. 3.3.54) divided by C_{SD}, shown as triangular data points, correlates well with the drawdown solution for the whole buildup period. Thus, neglecting the rate variation during the flow period in a DST may lead us to obtain a false type curve match for the buildup data, and consequently, provide erroneous estimates of the flow capacity and skin factor.

Fig. 3.3.8 presents a comparison of the buildup pressure derivatives for the same case of Fig. 3.3.7. The solid curve represents the pressure derivative of the drawdown solution of Fig. 3.3.7. The logarithmic derivative of the dimensionless buildup pressure rise with respect to the actual shut-in time is shown as circular data points, whereas the triangular data points represents the logarithmic derivative of $\tilde{p}_{sD}$ with respect to the multi-rate equivalent time. Fig. 3.3.8 also presents the logarithmic derivative of the buildup pressure with respect to the equivalent time defined by Eq. 3.3.44, shown by the square data points. Note the good agreement of the multi-rate equivalent time method with the drawdown solution. Plotting

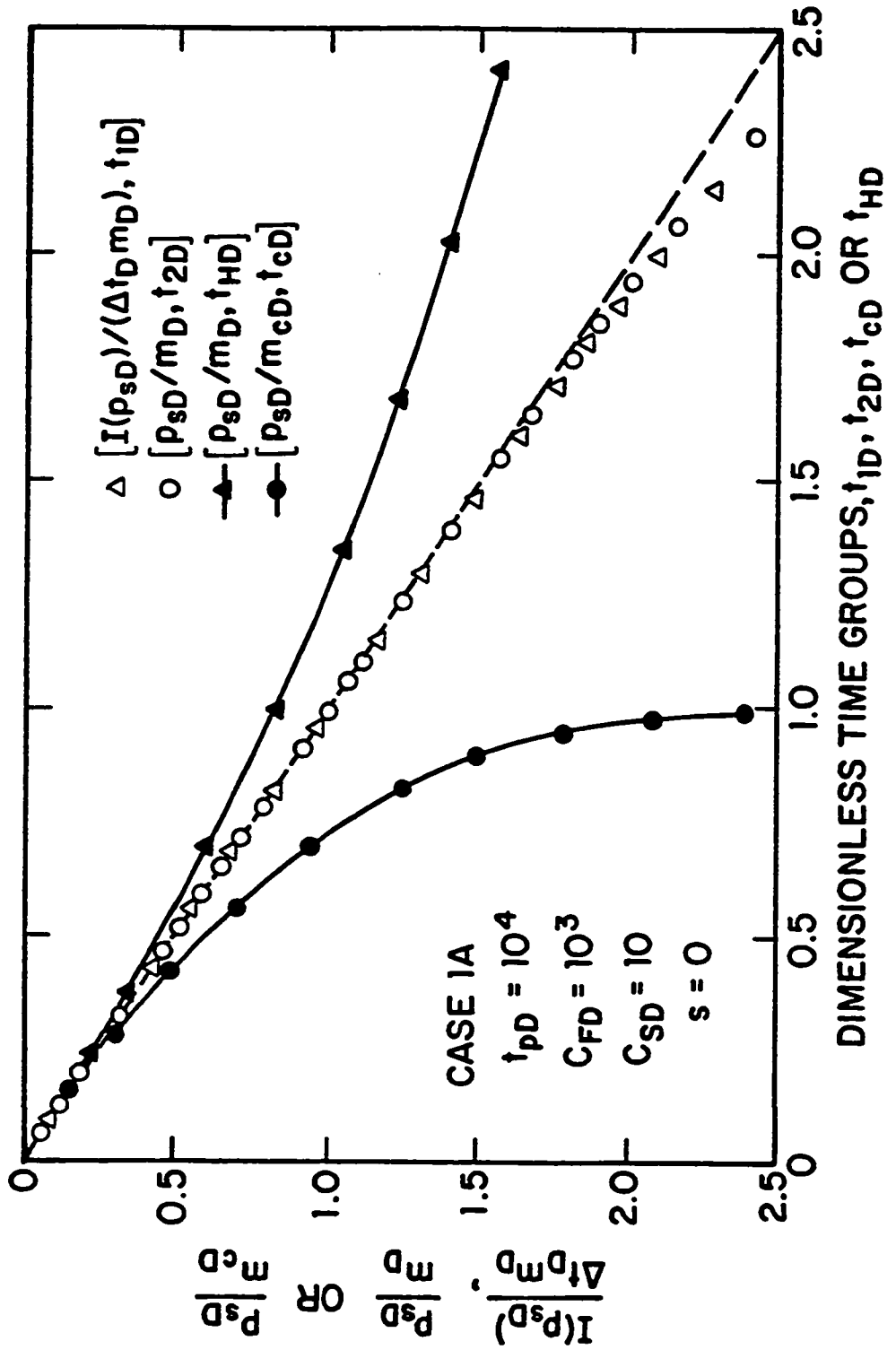

Fig. 3.3.6 - Comparison of straight-line methods; Case 1A.

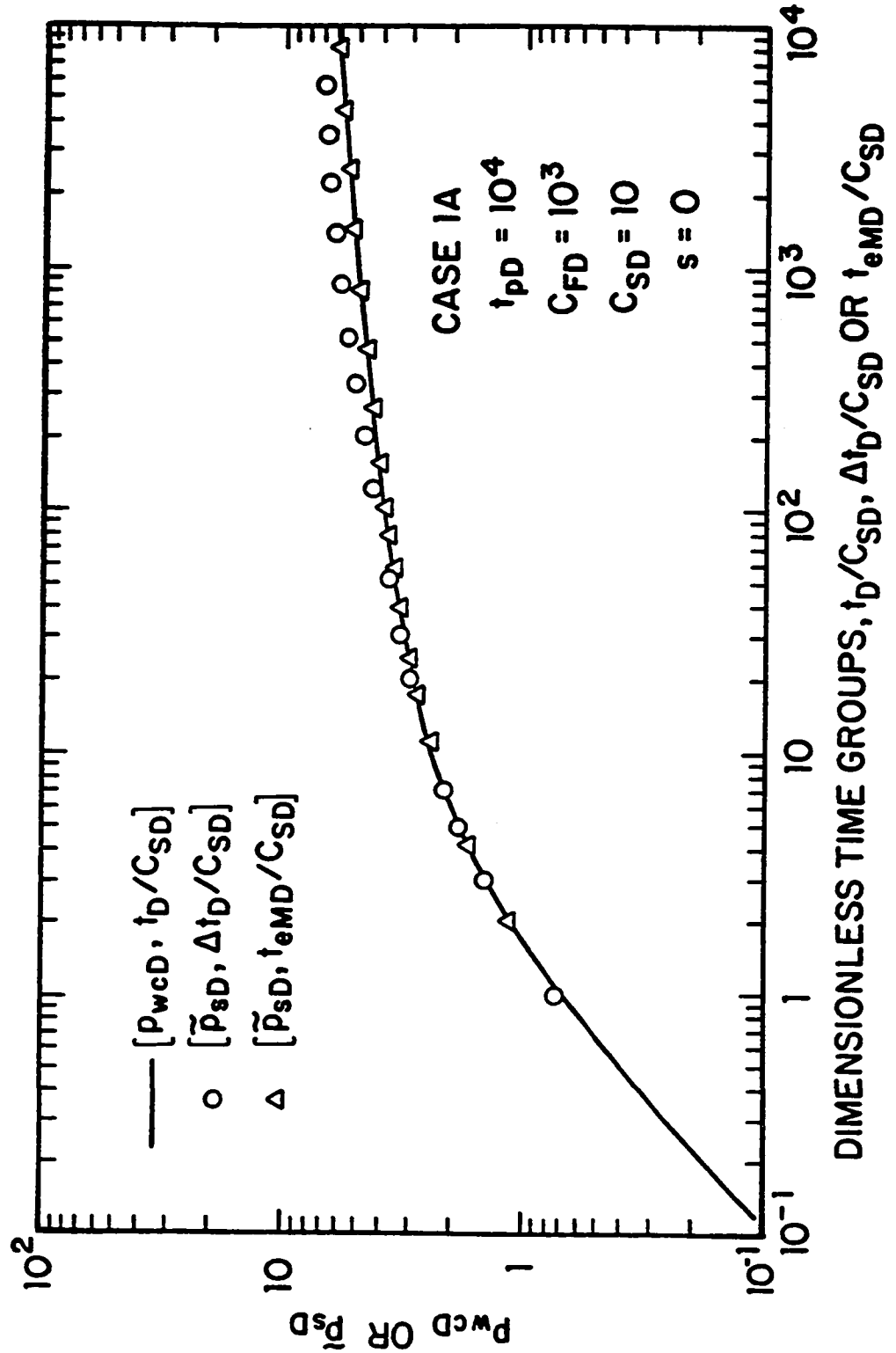

Fig. 3.3.7 - Correlation of DST dimensionless buildup pressure rise; Case 1A.

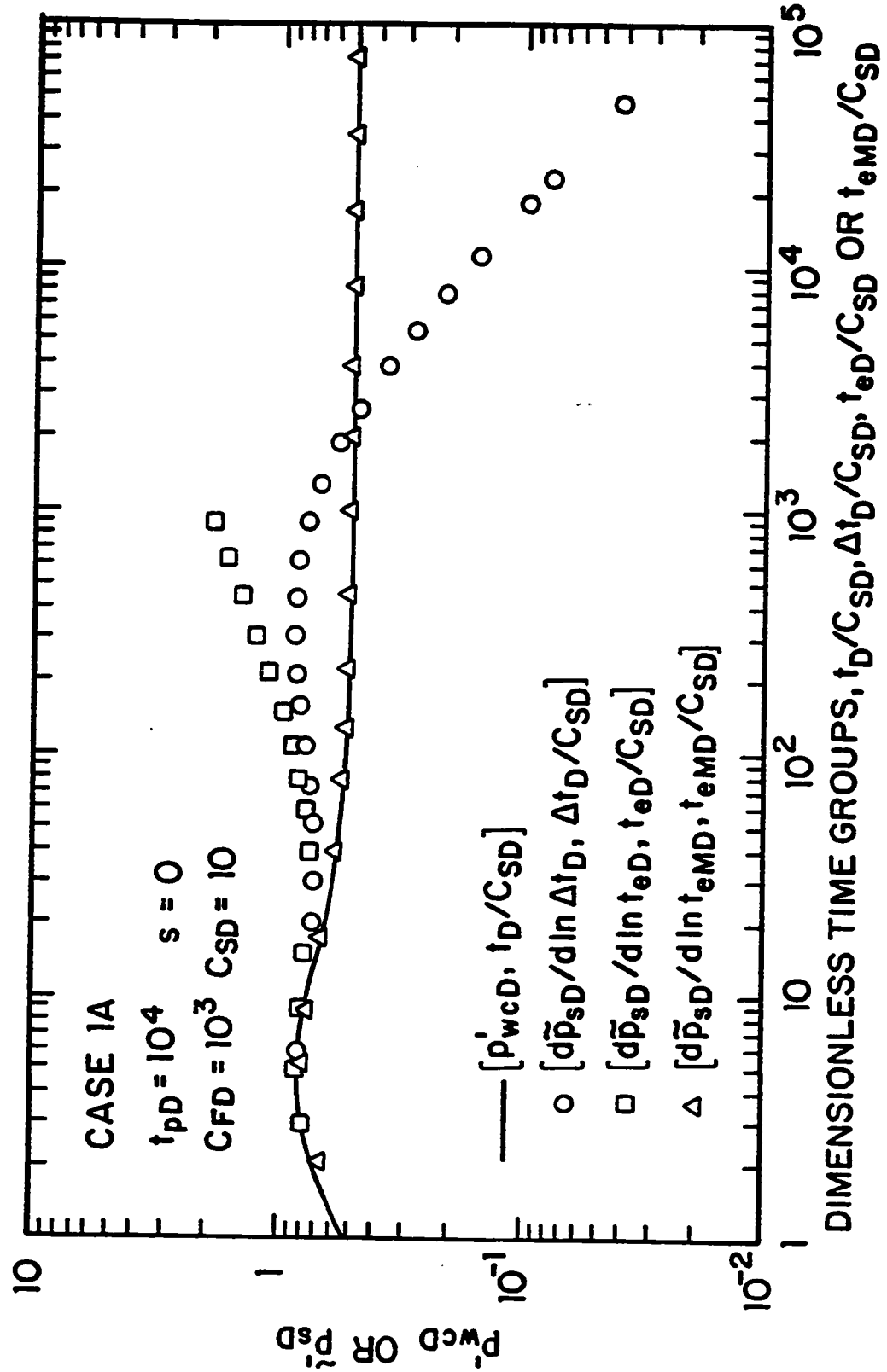

Fig. 3.3.8 - Correlation of dimensionless pressure derivatives; Case 1A.

$\tilde{p}'_{sD}$ versus Δt_D neglects both producing time and rate variation effects, whereas the equivalent time given by Eq. 3.3.44 takes into account the producing time effect but does not account for the flow rate variation. At early times, the semilog slope of the buildup pressure is affected by rate just before shut-in, and at later times, the semilog slope is related to the average flow rate. As the rate decreases during the flow period, the pressure derivative with respect to t_{eD} bends upward as shown in Fig. 3.3.8. Once again, if the change in flow rate is neglected in the buildup analysis, the non-conventional pressure derivative behavior may lead one to conclude that the formation is heterogeneous.

Fig. 3.3.9 presents the application of the straight line methods to the buildup pressure data of Case 2. It can be seen that Methods 1 and 2 match exactly the theoretical straight line shown by the dashed line. Although it still takes long shut-in times to reach the correct slope, the Horner method performs better here than in Cases 1 and 1A. The explanation is obtained from Figs. 3.3.2 and 3.3.4, which show that the sandface rate variation during the flow period for Cases 2 and 2A is less severe than for Cases 1 and 1A. However, even for this more favorable condition, the Cartesian Method requires long shut-in times to reach the correct unit slope line.

The buildup straight line methods for Case 2A are presented in Fig. 3.3.10. The combined effect of the wellbore storage and a positive skin during buildup tend to shift the results obtained by all methods to the left and below the dashed straight line, especially at early shut-in times. The results of Fig. 3.3.10 illustrate that for large values of $C_{SD}\exp(2s)$, the beginning of the proper straight line for Methods 1 and 2 will be also delayed. Fig. 3.3.10 also shows that the combined effect of wellbore storage and skin has a stronger effect on Method 1 than on Method 2. This result is not surprising since Method 1 is based on the integral of p_{sD} which accounts for the entire buildup history. Interestingly enough, the Horner method performs much better for Case 2A than in previous cases. Note that the decreasing flow rate during the flow period causes the buildup pressures to approach the correct slope of the Horner plot from above (see Figs. 3.3.5 and 3.3.9), whereas wellbore storage

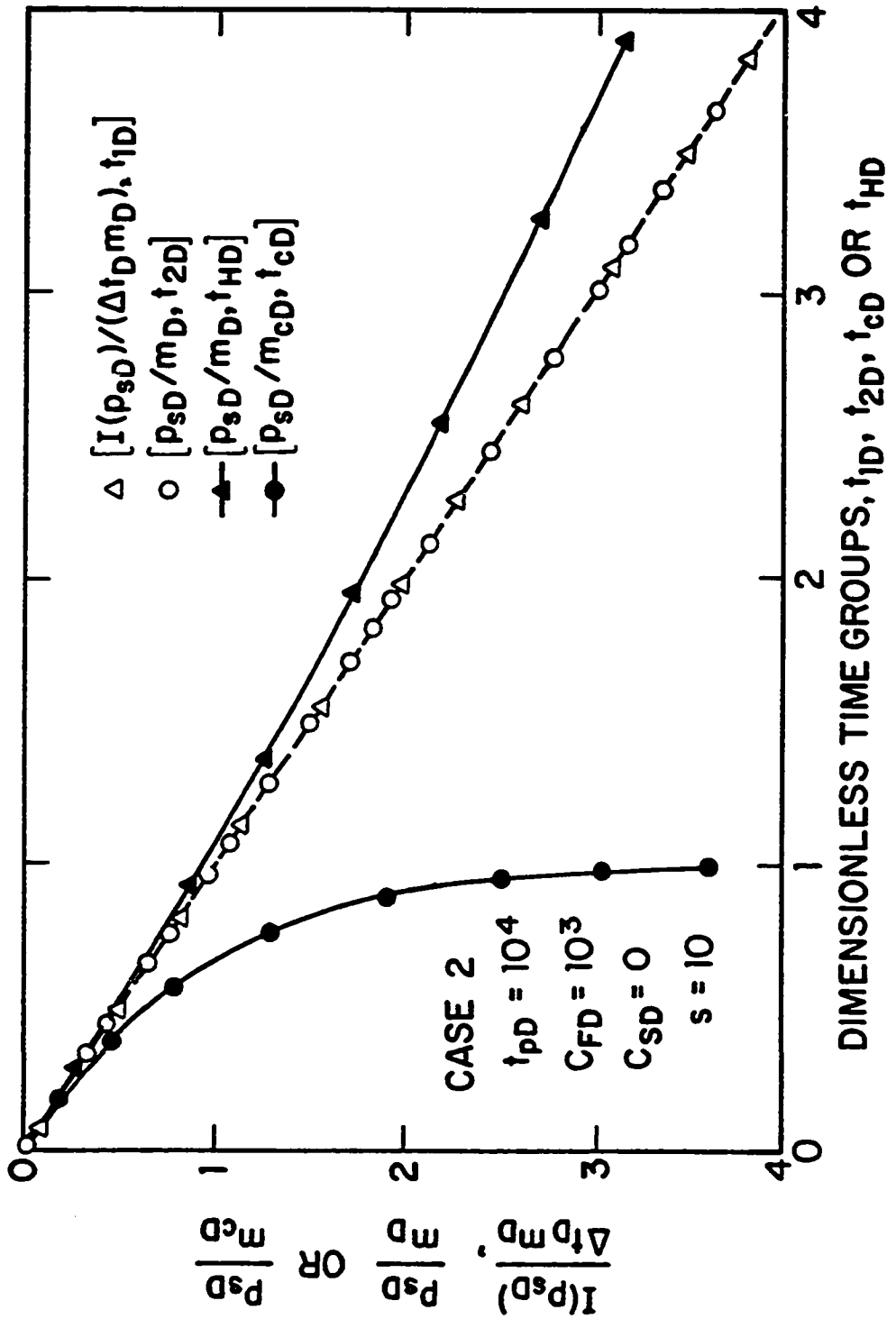

Fig. 3.3.9 - Comparison of straight-line methods; Case 2.

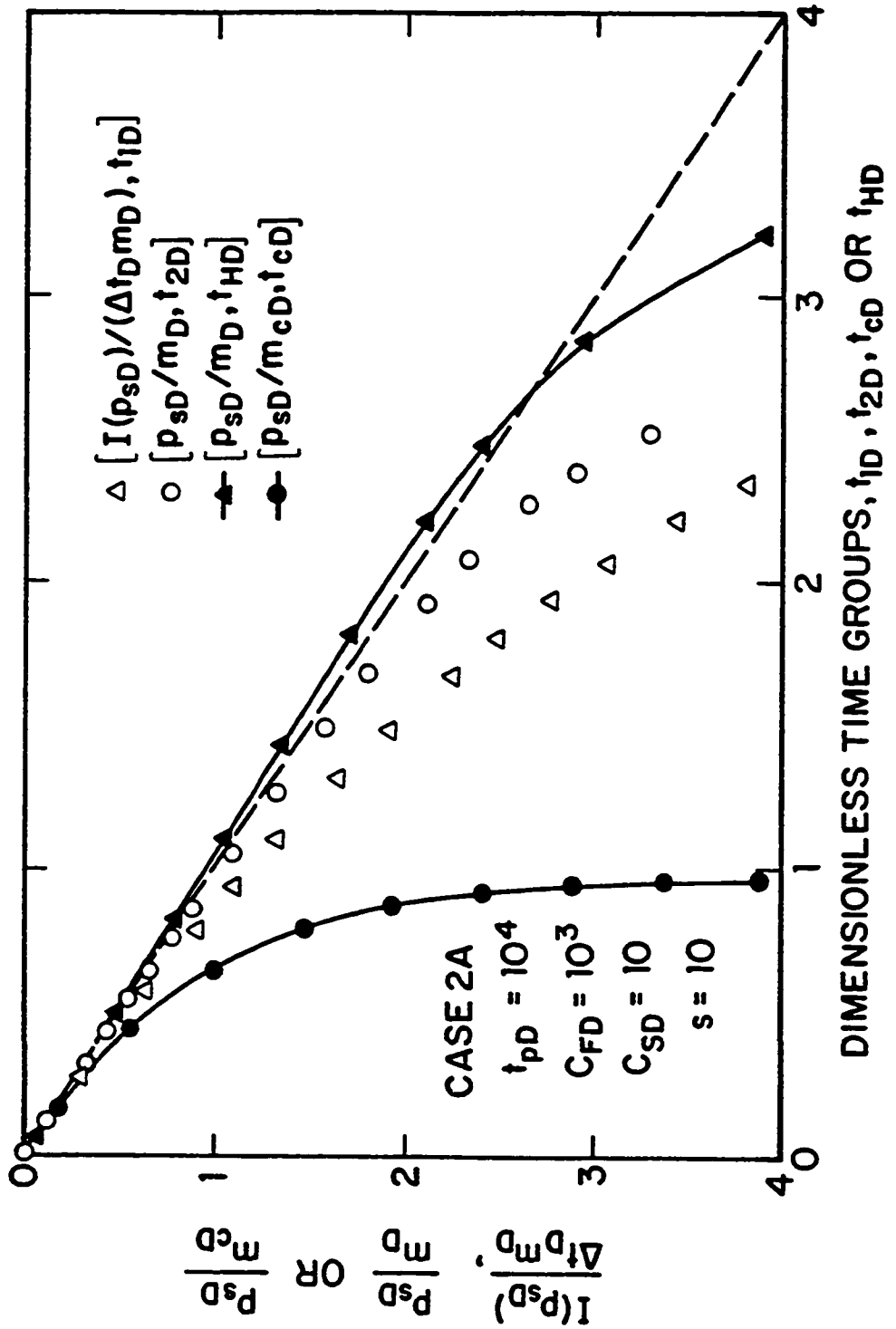

Fig. 3.3.10 - Comparison of straight-line methods; Case 2A.

during buildup causes the pressure to approach the theoretical straight line from below. Therefore, the decreasing flow rate and the buildup wellbore storage have opposite effects on the Horner method, and in the present case, the net effect nearly cancels out. For large values of $C_{SD}\exp(2s)$, log-log plots are useful for estimating the end of wellbore storage and the beginning of the straight lines for Methods 1 and 2.

Fig. 3.3.11 shows the log-log plot of $\tilde{p}_{sD}$ for Case 2A. The constant rate drawdown solution is represented by the solid line. Apparently, $\tilde{p}_{sD}$ presents a good correlation with the drawdown solution when plotted versus Δt_D, as shown by the circular data points. This observation agrees with the results of Ref. 20 for large values of $C_{sD}\exp(2s)$. The correlation of the buildup pressure rise versus the multi-rate equivalent time, shown by the triangular data points, reproduces accurately the drawdown solution for the whole span of the buildup data.

Fig. 3.3.12 presents a comparison of the logarithmic derivatives of $\tilde{p}_{sD}$ for Case 2A. Note that the derivative with respect to the actual shut-in time, shown by the circular data points, diverges from the drawdown solution much earlier than one could predict from Fig. 3.3.11. The plot of $\tilde{p}'_{sD}$ versus multi-rate equivalent time correlates quite well with the theoretical drawdown solution. The plot of $\tilde{p}'_{sD}$ versus the standard equivalent time, t_{eD}, also fails to match the drawdown solution, especially at late times, and the data bend upward for large shut-in times. In Fig. 3.3.12, this upward bend is not as severe as in Case 1A (Fig. 3.3.8), because the ratio of the average rate to the rate at shut-in is smaller for Case 2A than for Case 1A. Using a 10% maximum error in $\tilde{p}'_{sD}$ as a matching criterion, Fig. 3.3.12 indicates that wellbore storage effects end at $[\Delta t_D/C_D] = 300$ which corresponds to $t_{1D} = 2.0$ and $t_{2D} = 1.3$. Note for the corresponding results of Fig. 3.3.10, the beginning of the proper straight line for Method 2 agrees with this estimate. Method 1 requires longer shut-in times than predicted by log-log plots of $\tilde{p}_{sD}$ and $\tilde{p}'_{sD}$ since this method is based on the group $I(p_{sD})/\Delta t_D$ which represents a cumulative average of the pressure buildup change p_{sD}.

As shown in Fig. 3.3.10, the presence of wellbore storage and skin delays the beginning of the straight lines of Methods 1 and 2 for Case 2A. Fig. 3.3.13 presents

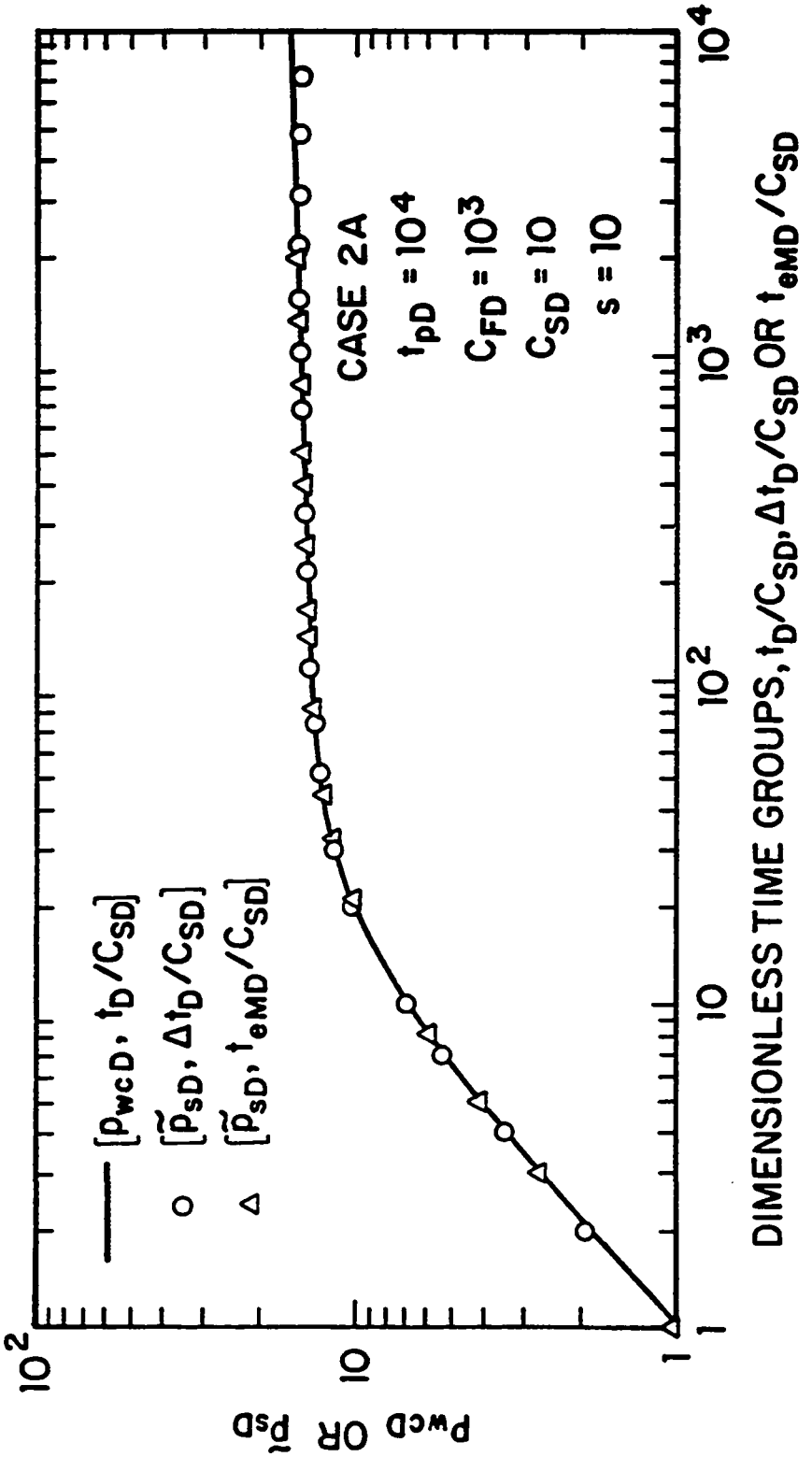

Fig. 3.3.11 - Correlation of DST dimensionless buildup pressure rise; Case 2A.

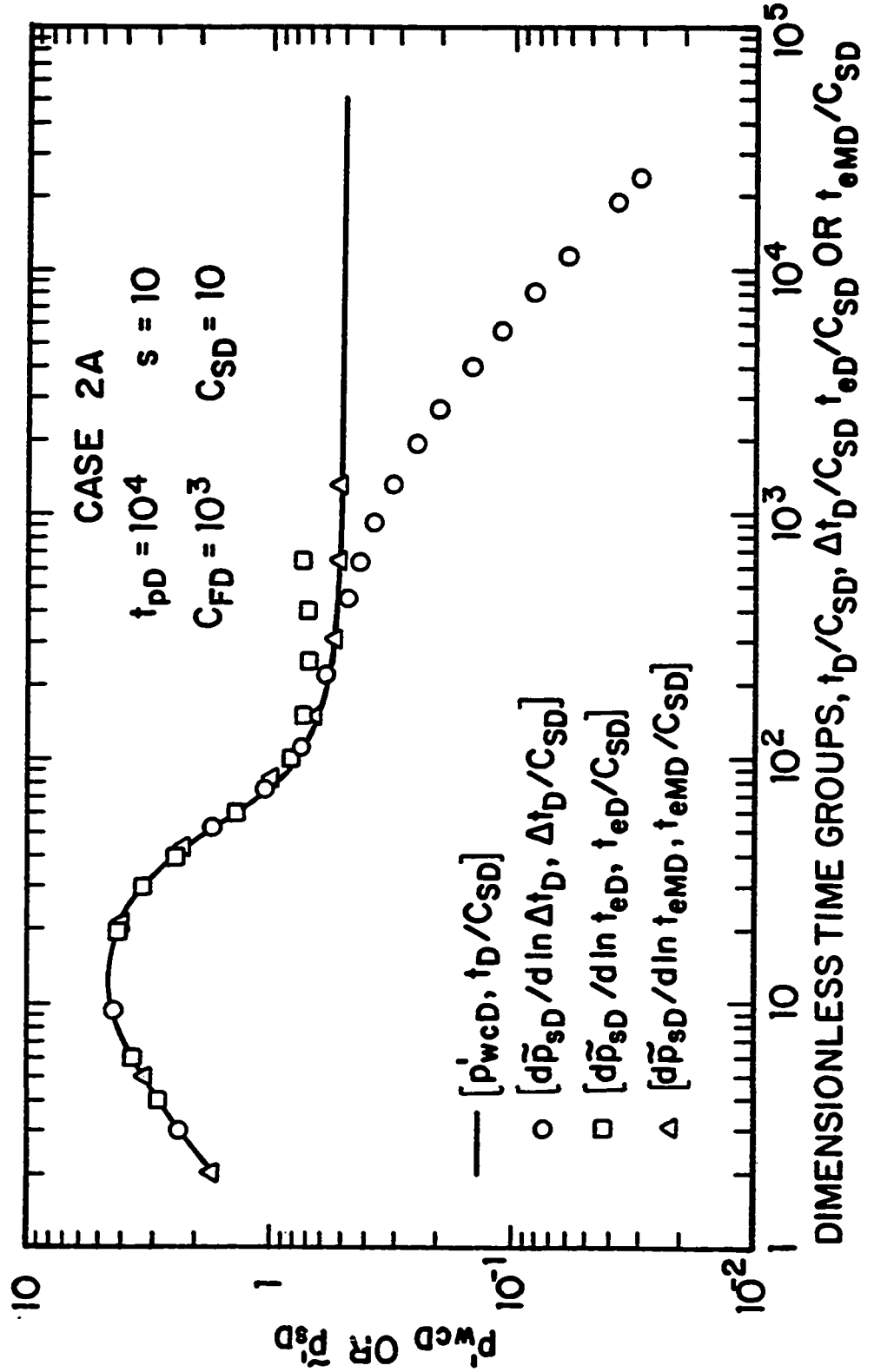

Fig. 3.3.12 - Correlation of dimensionless pressure derivatives; Case 2A.

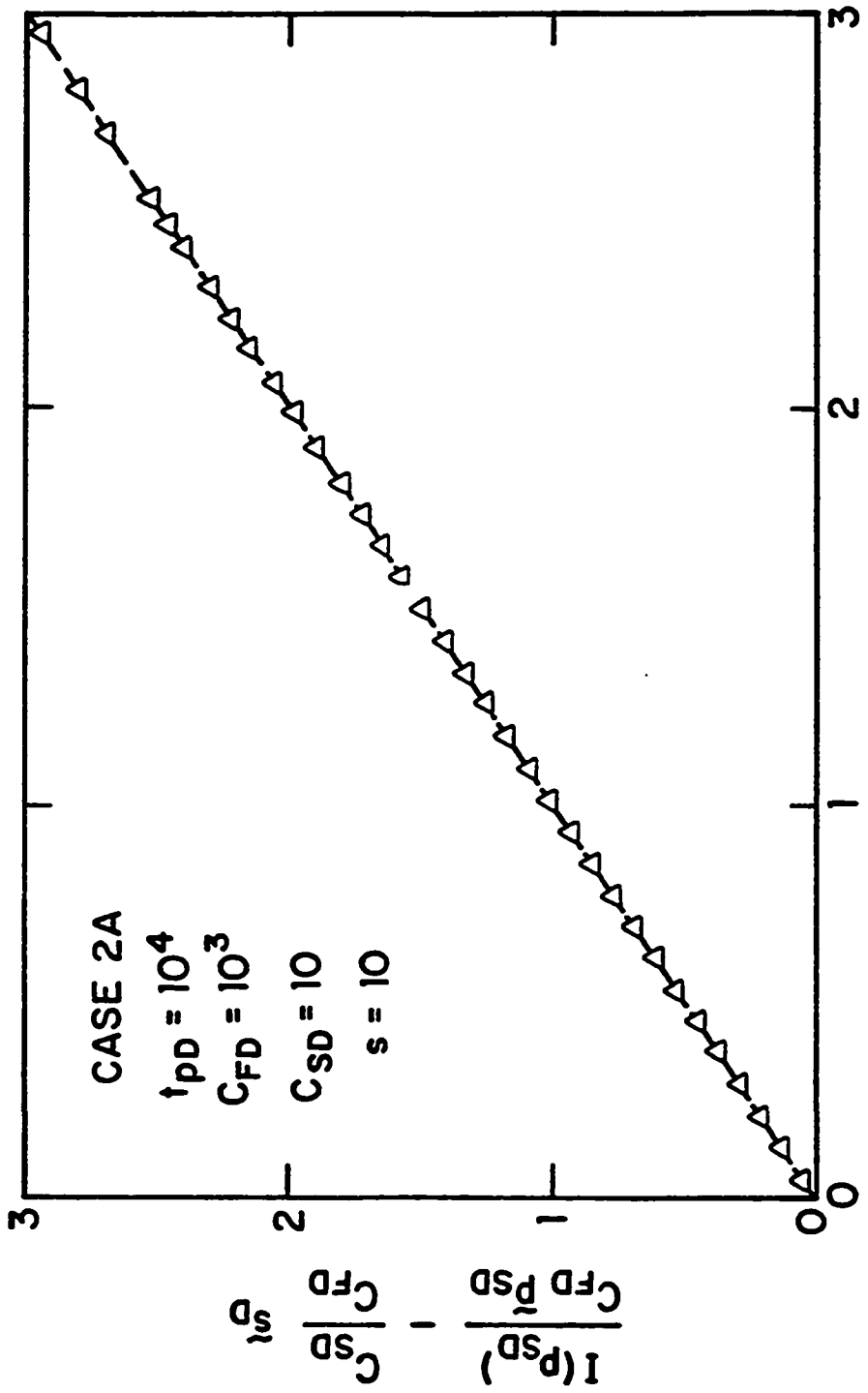

Fig. 3.3.13 - Correlation of the modified Method 1; Case 2A.

the application of the modified Method 1, represented by the triangular data points. As indicated by Eq. 3.3.61, the group at the left hand side plotted versus the multi-rate time t_{3D} should yield a straight line with unit slope and intercept equal to zero, shown by the dashed straight line in Fig. 3.3.13. In this Figure, the shut-in time increases from left to right and the multi-rate time t_{3D} was computed using $\theta_{j+1} = \theta_{i+1} = 0.5$ for all j and i. As can be seen, all data points match the theoretical straight line; compare with Fig. 3.3.10.

The modified Method 2 plot is shown in Fig. 3.3.14. The circular data points presents the group p_{sD}/m_D plotted versus the multi-rate time t_{4D} computed with $\theta_{j+1} = \theta_{i+1} = 0.5$ for all j and i, whereas the results obtained with $\theta_{j+1} = 0.5, \theta_{i+1} = 0.95$ for all j and i is shown by the triangular data points. The dashed straight line represents the theoretical solution; see Eq. 3.3.70. Although the results obtained for $\theta_{i+1} = 0.5$ represent an improvement on the results obtained using Method 2 (see Fig. 3.3.10), the data points do not follow the theoretical solution at early shut-in times. Note that an exact match is obtained if t_{4D} is computed with $\theta_{i+1} = 0.95$. Computations indicate that the optimum θ_{i+1} for the t_{4D} calculations is case dependent and also depends on the buildup partition used. In general, for zero skin cases one should use $\theta_{i+1} = 0.5$ whereas for $s > 0$, $\theta_{i+1} > 0.5$ gives better results. Note that the choice of θ_{i+1} affects the numerical values of the second summation in the right hand side of Eq. 3.3.71 which accounts for the pressure buildup response at early shut-in times.

The multi-rate times t_{1D}, t_{2D} and t_{3D} are not affected as much by the choice of θ_{j+1} and θ_{i+1}, however the best results for computer generated data are always obtained for the choice $\theta_{j+1} = \theta_{i+1} = 0.5$ for any range of skin and wellbore storage coefficient. This difference in behavior is due the fact that the logarithmic functions in Eqs. 3.3.14 and 3.3.62 smooth the effect of $\hat{t}_{j+1,pD}$ and $\Delta\hat{t}_{i+1,D}$, whereas the reciprocal function $1/\Delta t_D$ in Eq. 3.3.71 is more sensitive, especially at low values of m. This observation reduces the practical value of the modified Method 2 for field applications.

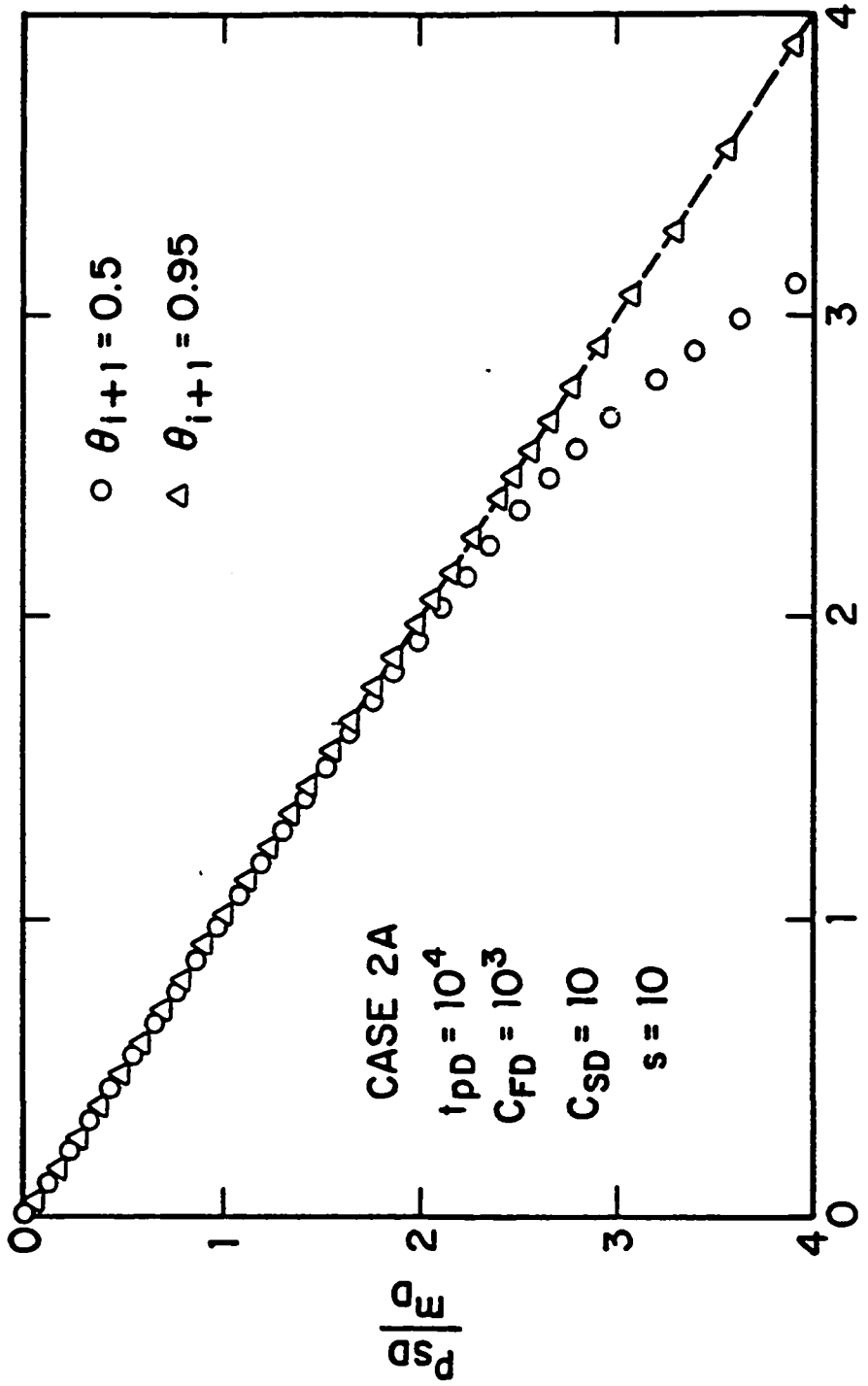

Fig. 3.3.14 - Correlation of the modified Method 2; Case 2A.

3.3.6 Practical Considerations

General guidelines can be extracted from the few cases presented and are discussed here. Because of the smoothing property of integration, application of Method 1 to field data will provide less noisy data than all other methods. However, since the pressure integration accounts for the entire buildup pressure history, if the formation is highly damaged, the presence of the wellbore storage will cause the straight line to begin later than in Method 2. Method 2 is much less affected by wellbore storage and skin than Method 1, however, the skin factor cannot be directly obtained from the working equation of Method 2. It appears reasonable to use the skin equation from Method 1, as discussed in the text and applied in the field examples considered in the next section.

The decline in the flow rate during the DST flow period generally causes the Horner method to approach the correct straight line from above, whereas the Cartesian Method will always reach the proper straight line from below. As a practical consequence, the Horner method often yields an underestimate of the initial reservoir pressure and an overestimate of the flow capacity. The same conclusion was also presented by Kazemi[68] more than 20 years ago. The Cartesian Method tends to overestimate p_i and underestimate kh.

Often in a DST, the extrapolated value of p_i obtained from the Horner analysis of the second shut-in is lower than the p_i estimated from the first buildup period. Different explanations have been presented in the literature (such as the "supercharge"[69] effect). As illustrated in this work, the flow rate decline during the preceding flow period should certainly be considered at the top of the list of plausible causes.

The working equations for Methods 1 and 2 shown in this Chapter (Eqs. 3.3.15, 3.3.16, 3.3.30 and 3.3.31), as well as the Horner and the Cartesian methods, are strictly applicable only for transient radial flow. The validity of these straight line methods should be always verified with log-log plots of $\tilde{p}_{sD}$ and $\tilde{p}'_{sD}$.

The application of the multi-rate equivalent time, given by Eq. 3.3.54, requires the computation of the flow rates from pressure derivatives (see Eq. 3.2.15). The use of some algorithm (such as the three point formula proposed by Bourdet et al.[70]) may provide smooth pressure derivatives but it does not guarantee that the material balance in the wellbore is preserved, that is, the cumulative production obtained from such a computation may not match the measured slug test production. This difference may cause errors when constructing the multi-rate equivalent time, and when applying the conventional multi-rate method given by Eq. 3.2.10. In the following, a simple procedure based on conservation of the produced fluid is presented.

The average flow rate in the time period $[t_{j,pD}, t_{j+1,pD}]$ is given by

$$\begin{aligned}\bar{q}_{j+1,D} &= \frac{1}{t_{j+1,pD}-t_{j,pD}}\int_{t_{j,pD}}^{t_{j+1,pD}} q_D(\tau)d\tau \\ &= \frac{1}{t_{j+1,pD}-t_{j,pD}}\int_{t_{j,pD}}^{t_{j+1,pD}} -C_{FD}\frac{dp_{wD}}{d\tau}(\tau)d\tau \\ &= \frac{C_{FD}}{t_{j+1,pD}-t_{j,pD}}\left[p_{wD}(t_{j,pD})-p_{wD}(t_{j+1,pD})\right],\end{aligned} \tag{3.3.75}$$

where $\bar{q}_{j+1,D}$ denotes the dimensionless average flow rate between two consecutive points of the time partition. Note that the consecutive application of Eq. 3.3.75 for all j also preserves the overall production. In applying Eq. 3.3.54, we now assume that $q_D(\hat{t}j+1, pD) = \bar{q}_{j+1,D}$ is a valid approximation. The dimensional form of Eq. 3.3.75 to be used in the analysis of field data is given by

$$q_{sf}(\hat{t}_{j+1,p}) = (24)C_F\left[\frac{p_{wf}(t_{j+1,p})-p_{wf}(t_{j,p})}{t_{j+1,p}-t_{j,p}}\right]. \tag{3.3.76}$$

Although the flow rate data obtained from Eq. 3.3.76 is generally oscillatory, its application in the computation of the conventional multi-rate time scale t_{mH} has been proved to give results consistent with those obtained from Methods 1 and 2; see the Field Applications section.

3.4 Field Applications

3.4.1 Example C

Here we consider a DST field example, consisting of a 5 hours flow period followed by a buildup 6 hours long. The analysis of the flow period data was considered in Chapter II. The reproduction of the actual DST chart is presented in Fig. 3.4.1. A quick inspection of the DST chart indicates the existence of no damage and a low to moderate flow capacity formation. The measured pressure versus time data of the buildup period are presented in the first two columns of Table 3.4.1. Other test data have been presented in Table 2.4.5. In particular, $C_F = 0.01609$ bbl/psi, $\mu = 0.43$ cp, $\phi = 0.13$ and $r_w = 0.354$ ft.

Columns 3 and 4 of Table 3.4.1 show the calculated values of the multi-rate time scales of Methods 1 and 2, respectively, obtained from Eqs. 3.3.16 and 3.3.31. The last Column of Table 3.4.1 gives the ratio of the time integral of the measured buildup pressure to the elapsed shut-in time. This group is the basis of Method 1; see Eq. 3.3.15. The buildup pressure integral, $I(p_{ws})$, was calculated from the composite trapezoidal integration formula given by Eq. 3.3.24.

Fig. 3.4.2 presents the log-log plot of the buildup pressure rise (circular data points) and its logarithmic derivative (triangular data points) versus the multi-rate equivalent time. The multi-rate time t_{eM} was constructed using the flow rates obtained from Eq. 3.3.76 and the log-derivative, $dp_{ws}/d\ln t_{eM}$, was calculated using Bourdet et al.'s algorithm[70] with no smoothing. The results of Fig. 3.4.2 indicates that the pressure data is not strongly affected by wellbore storage and present the characteristic radial flow behavior.

Fig. 3.4.3 shows the application of Method 1 to the field data. The circular data points represent the data shown in Column 5 of Table 3.4.1 plotted versus the multi-rate time t_1 shown in Column 3. A well defined straight line is obtained with slope $m_1 = 566.8$ psi. As indicated in Fig. 3.4.3, the extrapolation of the straight

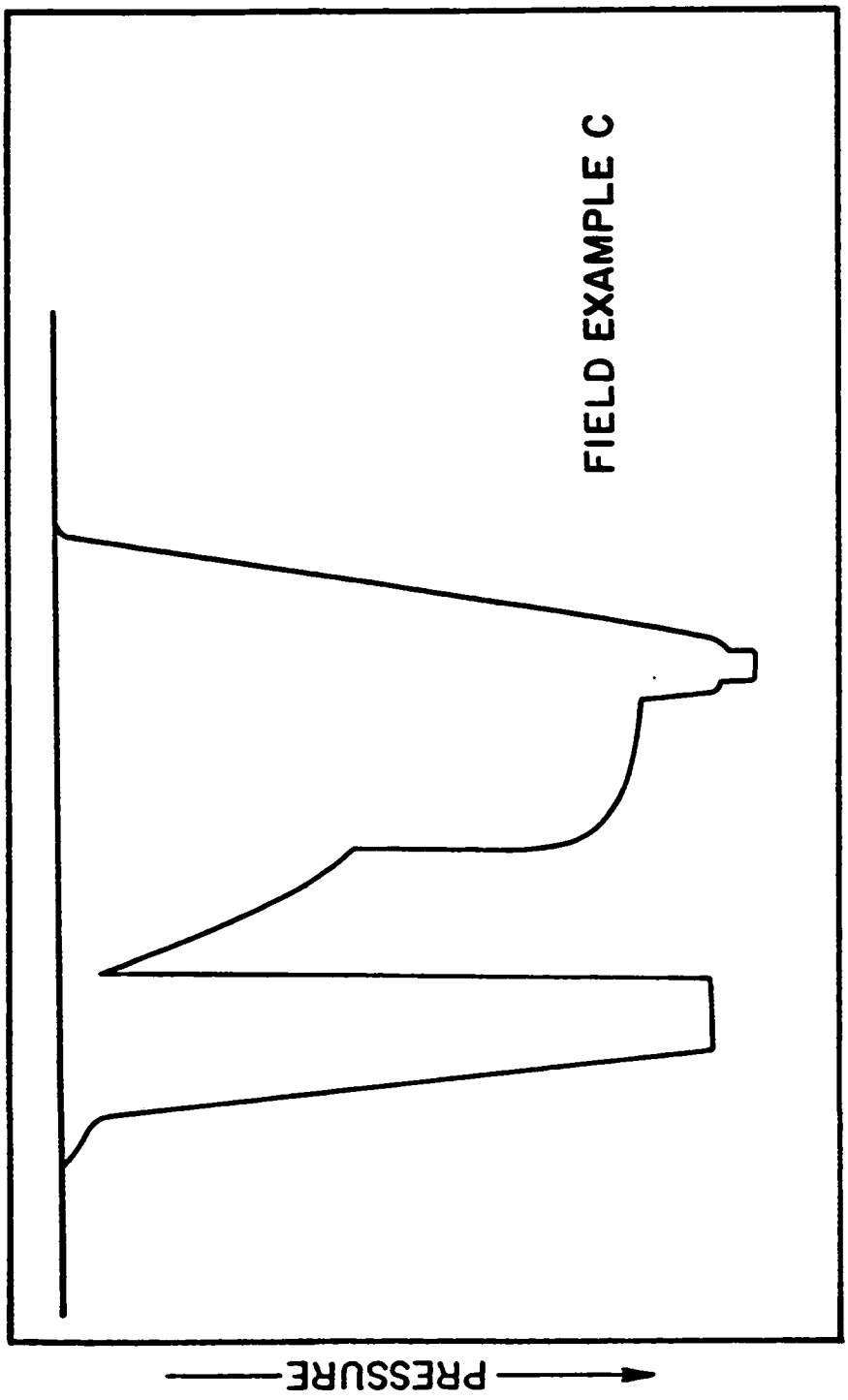

Fig. 3.4.1 - DST chart of the Field Example C.

Table 3.4.1

Field Example C - Buildup Period

Δt hour	p_{ws} psi	t_1 dimensionless	t_2 dimensionless	$I(p_{ws})/\Delta t$ psi
1.9200E-02	2.6028E+03	1.1563E+00	2.6300E+00	2.1046E+03
2.8800E-02	2.6265E+03	1.1493E+00	2.5991E+00	2.2746E+03
3.8400E-02	2.6435E+03	1.1426E+00	2.5694E+00	2.3647E+03
4.8000E-02	2.6540E+03	1.1360E+00	2.5409E+00	2.4215E+03
6.7200E-02	2.6829E+03	1.1233E+00	2.4871E+00	2.4921E+03
8.6400E-02	2.7039E+03	1.1113E+00	2.4370E+00	2.5368E+03
1.0560E-01	2.7210E+03	1.0998E+00	2.3902E+00	2.5687E+03
1.3440E-01	2.7433E+03	1.0835E+00	2.3254E+00	2.6038E+03
1.6320E-01	2.7643E+03	1.0682E+00	2.2661E+00	2.6302E+03
1.8240E-01	2.7774E+03	1.0585E+00	2.2292E+00	2.6450E+03
2.1120E-01	2.7906E+03	1.0446E+00	2.1773E+00	2.6640E+03
2.4000E-01	2.8050E+03	1.0315E+00	2.1291E+00	2.6801E+03
2.6880E-01	2.8168E+03	1.0190E+00	2.0841E+00	2.6941E+03
2.9760E-01	2.8273E+03	1.0071E+00	2.0420E+00	2.7065E+03
3.3600E-01	2.8418E+03	9.9200E-01	1.9896E+00	2.7211E+03
3.7440E-01	2.8549E+03	9.7779E-01	1.9411E+00	2.7342E+03
4.2240E-01	2.8680E+03	9.6108E-01	1.8852E+00	2.7486E+03
4.7040E-01	2.8799E+03	9.4539E-01	1.8337E+00	2.7614E+03
5.2800E-01	2.8930E+03	9.2777E-01	1.7769E+00	2.7751E+03
5.9520E-01	2.9061E+03	9.0865E-01	1.7166E+00	2.7891E+03
6.6240E-01	2.9179E+03	8.9086E-01	1.6615E+00	2.8016E+03
7.4880E-01	2.9311E+03	8.6970E-01	1.5973E+00	2.8158E+03
8.3520E-01	2.9442E+03	8.5017E-01	1.5393E+00	2.8284E+03
1.0560E+00	2.9731E+03	8.0624E-01	1.4128E+00	2.8557E+03
1.1520E+00	2.9849E+03	7.8931E-01	1.3655E+00	2.8659E+03
1.3440E+00	3.0059E+03	7.5860E-01	1.2816E+00	2.8844E+03
1.4880E+00	3.0177E+03	7.3787E-01	1.2262E+00	2.8968E+03
1.6800E+00	3.0322E+03	7.1274E-01	1.1606E+00	2.9114E+03
1.8720E+00	3.0453E+03	6.9002E-01	1.1026E+00	2.9245E+03
2.1120E+00	3.0597E+03	6.6441E-01	1.0387E+00	2.9390E+03
2.3520E+00	3.0729E+03	6.4138E-01	9.8260E-01	2.9520E+03
2.6400E+00	3.0873E+03	6.1653E-01	9.2350E-01	2.9660E+03
2.9760E+00	3.1031E+03	5.9070E-01	8.6364E-01	2.9806E+03
3.3120E+00	3.1149E+03	5.6765E-01	8.1159E-01	2.9936E+03
3.7440E+00	3.1293E+03	5.4134E-01	7.5375E-01	3.0084E+03
4.1760E+00	3.1425E+03	5.1806E-01	7.0401E-01	3.0216E+03
5.2800E+00	3.1661E+03	4.6885E-01	6.0338E-01	3.0494E+03
5.9040E+00	3.1766E+03	4.4594E-01	5.5866E-01	3.0623E+03
6.1824E+00	3.1792E+03	4.3661E-01	5.4083E-01	3.0675E+03

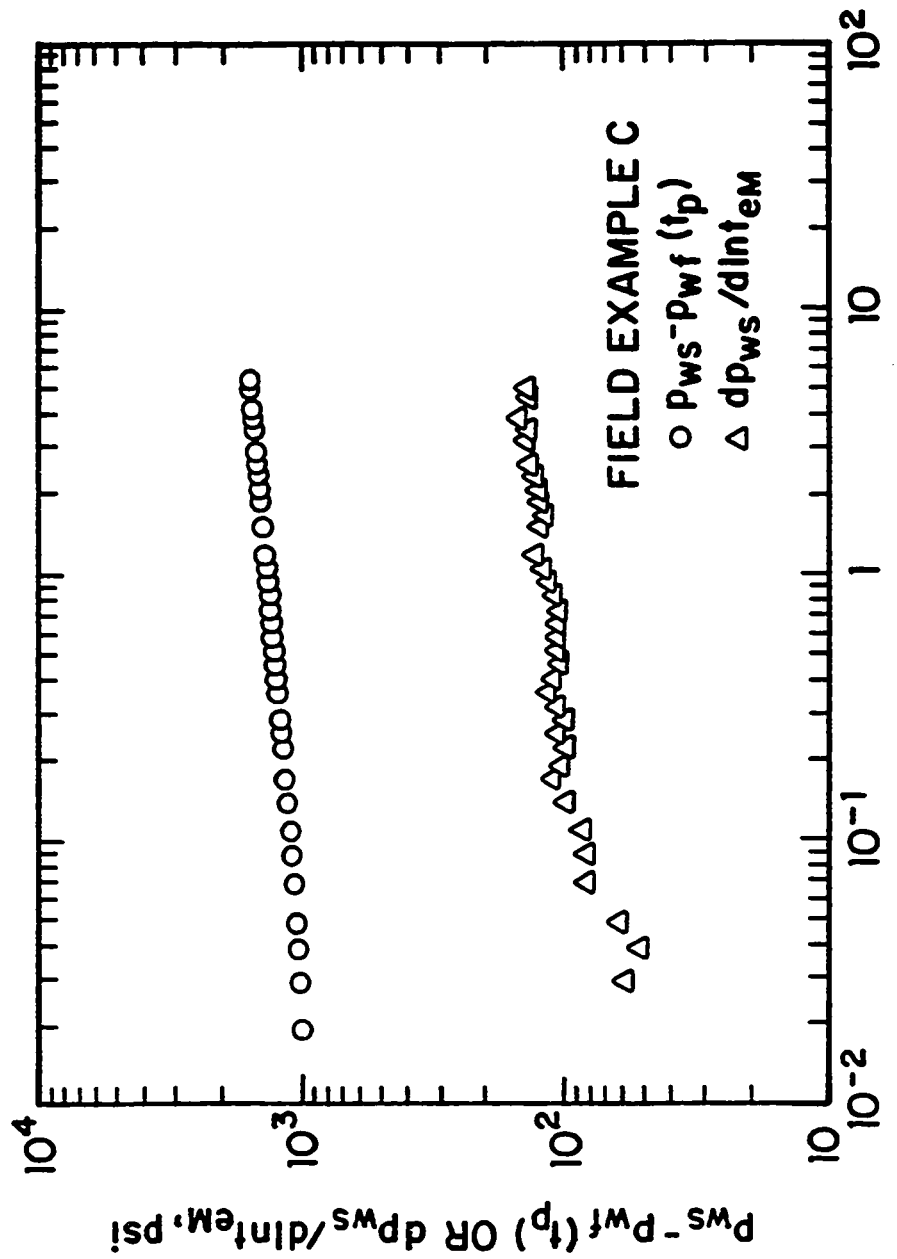

Fig. 3.4.2 - Log-log plot of buildup pressure rise and logarithmic derivative; Field Example C.

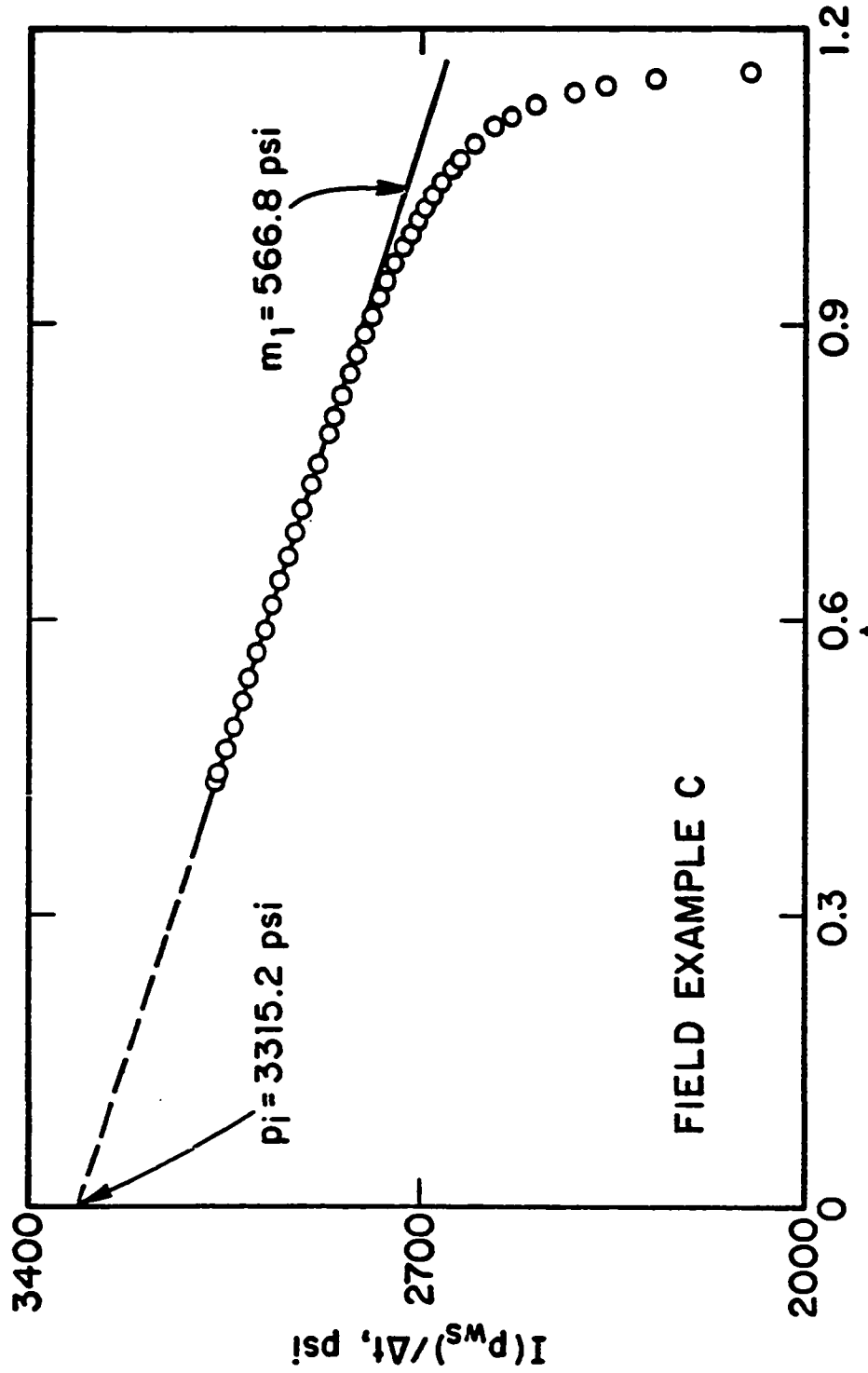

Fig. 3.4.3 - Method 1 Cartesian plot; Field Example C.

line to $t_1 = 0$ provides an estimate of the reservoir initial pressure equal to 3315.2 psi. The transmissibility can be computed from the rearrangement of Eq. 3.3.17 and is given by

$$\frac{kh}{\mu} = \frac{162.6}{566.8}\frac{(24)(0.01609)(1606.3 - 263.1)}{4.86} = 30.6 \text{ md-ft/cp}, \tag{3.4.1}$$

which gives $kh = 13.2$ md-ft. The skin factor can be estimated directly from Eq. 3.3.21

$$s = 1.151\left\{\frac{3315.2 - 1068.7}{566.8} - 0.403 - \log\left(\frac{30.6}{(0.13)(23)(1.47 \times 10^{-5})(0.354)^2}\right) + 3.23\right\} = 0.1. \tag{3.4.2}$$

In Eq. 3.4.2, we used the fact that $p_{avg} = 1068.7$ (obtained from Eq. 3.3.22 using the composite trapezoidal rule) and that the summation term which appears in the right hand side of the skin equation (Eq. 3.3.21) is given by the last entry of Column 3 in Table 2.4.5 (i.e., 0.40346).

Fig. 3.4.4 presents a comparison between Method 2 and the Cartesian Method proposed by Refs. 44 and 45. The buildup pressure versus the multi-rate time t_2 data (Column 4 of Table 3.4.1) are plotted as circular data points. The Cartesian Method is represented by the triangular data points. As can be seen in Fig. 3.4.4, a good straight line with slope $m_2 = 238.4$ psi is obtained for Method 2. This Figure clearly shows that longer shut-in times would be required to obtain a straight line from the Cartesian Method. Using the slope obtained from Method 2 in Eq. 3.3.32, gives

$$\frac{kh}{\mu} = \frac{162.6}{238.4}\frac{(24)(0.01609)(1606.3 - 263.1)}{(2.3)4.86} = 31.6 \text{ md-ft/cp}, \tag{3.4.3}$$

which yields $kh = 13.6$ md-ft. Extending the straight line to $t_2 = 0$ gives $p_i = 3309$ psi, which is reasonably close to the initial reservoir pressure estimated from Method 1. Upon combination of Eqs. 3.3.21 and 3.3.33 and using the above values of p_i, kh/μ and m_2 in the resulting expression, the skin factor is given by

$$s = 1.151\left\{\frac{3309 - 1068.7}{(2.3)238.4} - 0.403\right.$$

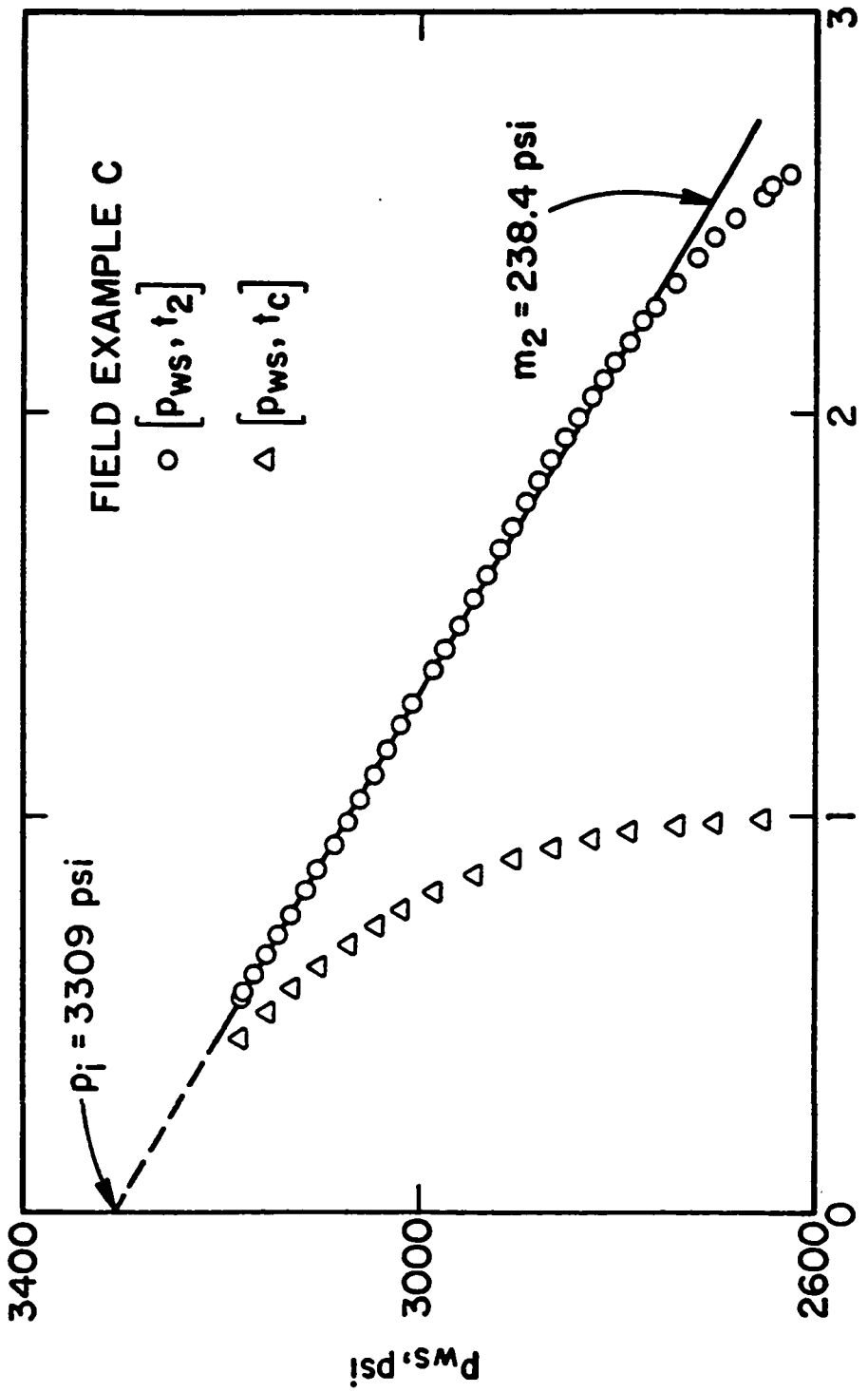

Fig. 3.4.4 - Comparison of Method 2 and Cartesian Method; Field Example C.

$$-\log\left(\frac{31.6}{(0.13)(23)(1.47\times10^{-5})(0.354)^2}\right)+3.23\Big\}=0.2. \qquad (3.4.4)$$

The kh and s values calculated from Method 2 are in excellent agreement with those obtained by Method 1.

Fig. 3.4.5 presents the Horner plot of the field example. The shape of the plot is similar to the theoretical Horner plots shown previously, which indicates the effect of the rate variation before shut-in. However, a fairly good semilog straight line can be fit through the last 10 data points with slope $m = 458.7$ psi. The transmissibility can be estimated by

$$\begin{aligned}\frac{kh}{\mu} &= \frac{162.6}{458.7}\frac{(24)(0.01609)(1606.3-263.1)}{4.86} \\ &= 37.8 \text{ md-ft/cp},\end{aligned} \qquad (3.4.5)$$

which gives $kh = 16.3$ md-ft. Note that in the above computation we used the fact that the average flow rate is given by Eq. 3.2.6. The extrapolation of the straight line in Fig. 3.4.5 yields $p_i = 3295.6$ psi. The skin factor can be estimated from the standard equation using the modification presented by Ref. 35. For the cases in which the flow rate is not constant, the pressure at the moment of shut-in which appears in the skin equation should be replaced by some average flowing pressure[35]. Using the arithmetic average of the initial flowing pressure (p_o) and the last pressure before shut-in, one obtains

$$s = 1.151\Big\{\frac{3295.6-934.7}{458.7}$$

$$-\log\left(\frac{37.8(4.86)}{(0.13)(23)(1.47\times10^{-5})(0.354)^2}\right)+3.23\Big\}=1.0. \qquad (3.4.6)$$

We also applied the the conventional buildup multi-rate method to the field data. Fig. 3.4.6 presents a Cartesian plot of the shut-in pressures versus t_{mH}. This multi-rate time scale was computed directly from Eq. 3.2.13, using the flow rates obtained from the material balance criteria; see Eq. 3.3.76. The straight line shown in Fig. 3.4.6 is slightly longer than the semilog straight line of Fig. 3.4.5 and apparently, there is no other significant difference between the two methods. Using

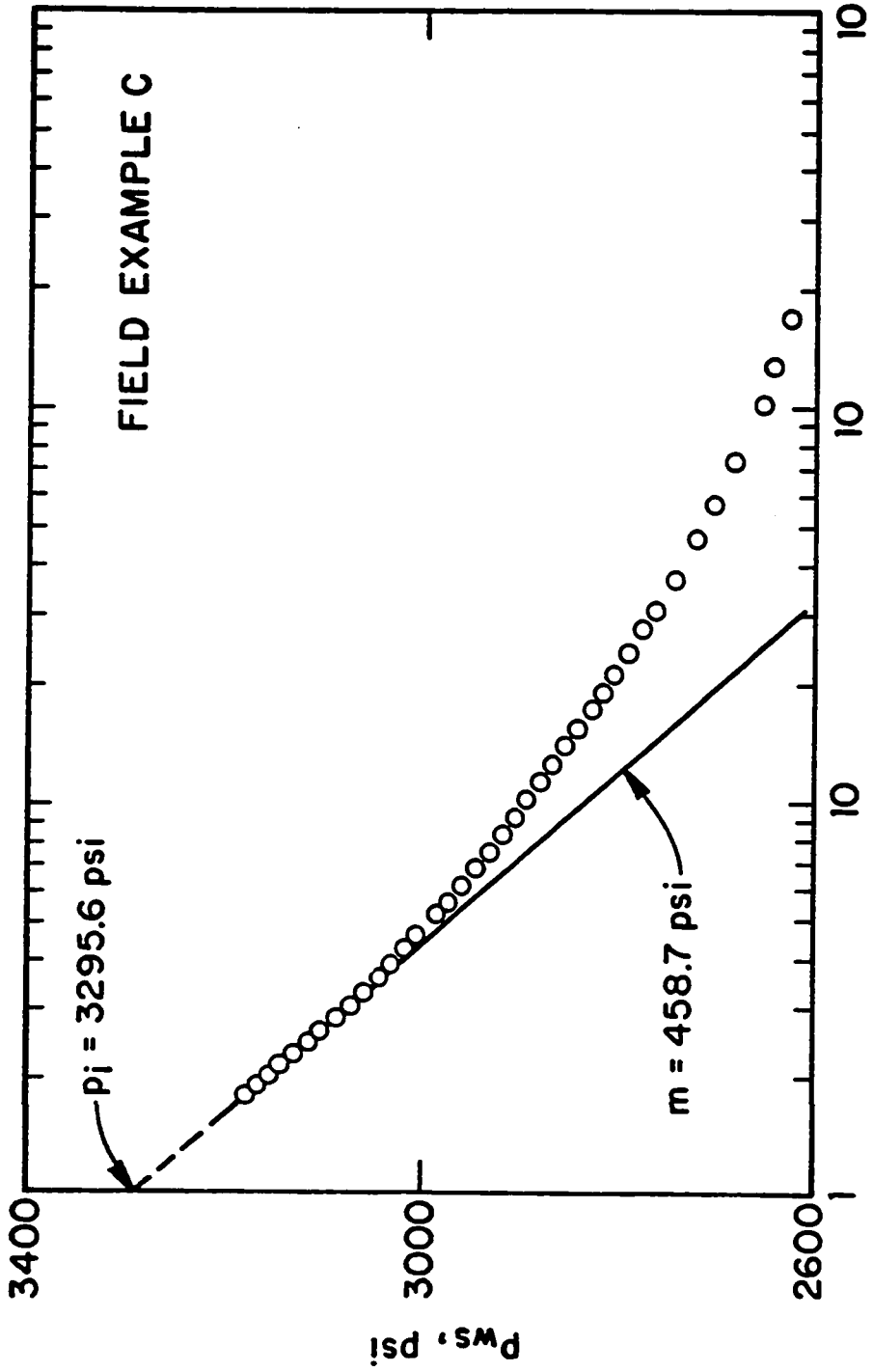

Fig. 3.4.5 - Horner plot; Field Example C.

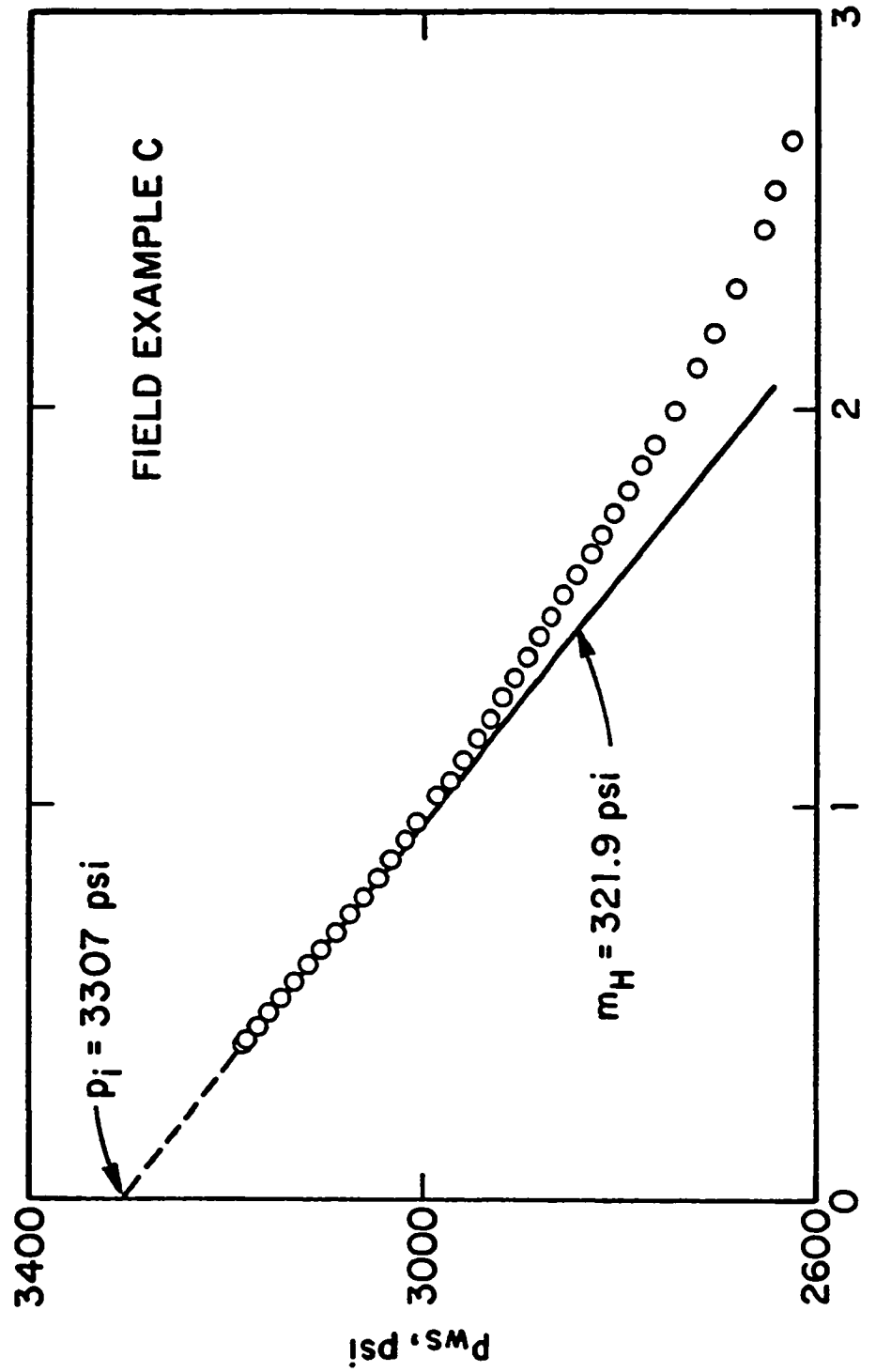

Fig. 3.4.6 - Conventional multi-rate plot; Field Example C.

$m_H = 321.9$ psi and $q_{sf}(\hat{t}_{n+1,p}) = 64.7$ RB/day (calculated from Eq. 3.3.76) in Eq. 3.2.14 gives

$$\frac{kh}{\mu} = \frac{162.6(64.7)}{321.9} = 32.7 \text{ md-ft/cp} \tag{3.4.7}$$

and $kh = 14.1$ md-ft. The extension of the straight line to $t_{mH} = 0$ gives $p_i = 3307$ psi. Using the above values of kh, p_i and m_H, one obtains $s = 0.7$. Note that the results obtained by the conventional multi-rate method using the material balance flow rates are in excellent agreement with the results of Methods 1 and 2.

In Table 3.4.2, we summarize the results obtained for this field example. The results of the flow period presented in this Table correspond to the results obtained by the converted convolution method. Note that the methods which account for rate variation during the flow period (Methods 1 and 2 and the conventional multi-rate) yield essentially the same results. The Horner method based on the average flow rate slightly overestimated the flow capacity and underestimated the initial reservoir pressure. As the slope in Fig. 3.4.5 is continuously decreasing, a longer buildup period would certainly have improved the results of the Horner method. Note that for the field data presented here, the rate variation during the flow period was not extremely severe (flow rate at shut-in is about 4 times smaller than the initial flow rate). For cases with larger rate variations, the Horner method might give completely erroneous results.

A more pronounced discrepancy exists between the results obtained from the flow period data and the buildup data. The difference in the calculated skin factor is caused by the discrepancy in the transmissibility values. For all field data we analyzed to date, the flow capacity calculated from the flow period data was consistently lower (30 to 50 %) than the respective value obtained from analysis of buildup data; see the results of Field Example B. One may be tempted to explain the causes of this difference as multiphase flow effects, clean up effects or the presence of a skin zone of finite thickness, but we believe that further research is needed to clearly resolve the sources of this discrepancy.

Table 3.4.2

Field Example C - Comparison of Results

Parameters	Method 1	Method 2	Multi-rate	Horner	Slug Test
kh/μ, md-ft/cp	30.6	31.6	32.7	37.8	21.1
kh, md-ft	13.2	13.6	14.1	16.3	9.1
skin	0.1	0.2	0.7	1.0	-1.2
p_i, psi	3315.2	3309	3307	3295.6	-

3.4.2 Example B

The example considered here was presented in Ref. 44 and corresponds to data measured during a drillstem test operation. The well was allowed to flow for approximately one hour and then it was shut-in for 2 hours. The flow data was analyzed in Chapter II. The measured buildup pressures are shown in the second column of Table 3.4.3. Other information about reservoir and well parameters are given in Table 2.4.3. In particular, $C_F = 0.0365$ bbl/psi, $\mu = 60$ cp, $\phi = 0.062$ and $r_w = 0.354$ ft.

The multi-rate times t_1 and t_2 are shown in Columns 3 and 4 of Table 3.4.3 and were obtained from Eqs. 3.3.16 and 3.3.31. The last Column of Table 3.4.1 gives the group $I(p_{ws})/\Delta t$ which is required for the application of Method 1; see Eq. 3.3.15. The integral $I(p_{ws})$ was performed using the composite trapezoidal integration formula given by Eq. 3.3.24.

The log-log plot of the pressure difference $[p_{ws} - p_{wf}(t_p)]$ and the pressure derivative $dp_{ws}/d\ln t_{eM}$ are shown in Fig. 3.4.7 by the circular and triangular data points, respectively. As discussed in the Practical Considerations section, the multi-rate time t_{eM} was computed using the flow rates obtained from Eq. 3.3.76. The pressure derivative of p_{ws} with respect to $\ln t_{eM}$ was obtained using the procedure suggested by Bourdet et al.[70] and no smoothing was applied to the data. Fig. 3.4.7 shows that the data is affected by wellbore storage for $t_{eM} < 0.1$ hours which corresponds approximately to $\Delta t < 0.1$ hours. It appears that the data is representative of radial flow geometry, therefore the new methods described in this Chapter can be applied.

The Method 1 plot for this field data is shown in Fig. 3.4.8. The circular data points shown in the figure represent the data of Column 5 of Table 3.4.3 plotted versus the multi-rate time t_1 shown in Column 3. A straight line is obtained for $t_1 < 0.55$ which corresponds to shut-in times satisfying $\Delta t > 0.5$ hours. As discussed previously, the existence of wellbore storage during buildup delays the beginning of

Table 3.4.3

Field Example B - Buildup Period

Δt hour	p_{ws} psi	t_1 dimensionless	t_2 dimensionless	$I(p_{ws})/\Delta t$ psi
2.200E-02	7.669E+02	8.43262E-01	1.86887E+00	7.39550E+02
2.600E-02	7.987E+02	8.37612E-01	1.84557E+00	7.46204E+02
3.400E-02	8.164E+02	8.26868E-01	1.80215E+00	7.60638E+02
4.100E-02	8.240E+02	8.18007E-01	1.76714E+00	7.70807E+02
5.300E-02	8.309E+02	8.03825E-01	1.71249E+00	7.83632E+02
6.700E-02	8.357E+02	7.88637E-01	1.65563E+00	7.94010E+02
8.400E-02	8.389E+02	7.71804E-01	1.59441E+00	8.02771E+02
1.060E-01	8.413E+02	7.52131E-01	1.52498E+00	8.10519E+02
1.320E-01	8.441E+02	7.31314E-01	1.45370E+00	8.16858E+02
1.660E-01	8.469E+02	7.07178E-01	1.37358E+00	8.22724E+02
1.870E-01	8.485E+02	6.93671E-01	1.32983E+00	8.25529E+02
2.090E-01	8.498E+02	6.80471E-01	1.28778E+00	8.28015E+02
2.350E-01	8.514E+02	6.65953E-01	1.24230E+00	8.30514E+02
2.640E-01	8.526E+02	6.50946E-01	1.19613E+00	8.32874E+02
2.950E-01	8.538E+02	6.36090E-01	1.15123E+00	8.35010E+02
3.340E-01	8.554E+02	6.18878E-01	1.10019E+00	8.37298E+02
3.720E-01	8.566E+02	6.03457E-01	1.05535E+00	8.39208E+02
4.180E-01	8.582E+02	5.86295E-01	1.00642E+00	8.41210E+02
4.700E-01	8.594E+02	5.68576E-01	9.56969E-01	8.43156E+02
5.280E-01	8.610E+02	5.50578E-01	9.07858E-01	8.45028E+02
5.900E-01	8.622E+02	5.33067E-01	8.61157E-01	8.46770E+02
6.620E-01	8.634E+02	5.14607E-01	8.13085E-01	8.48513E+02
7.740E-01	8.646E+02	4.89159E-01	7.48783E-01	8.50754E+02
8.350E-01	8.658E+02	4.76687E-01	7.18108E-01	8.51810E+02
9.380E-01	8.674E+02	4.57462E-01	6.71919E-01	8.53434E+02
1.051E+00	8.687E+02	4.38599E-01	6.27902E-01	8.55005E+02
1.181E+00	8.703E+02	4.19265E-01	5.84135E-01	8.56601E+02
1.325E+00	8.715E+02	4.00262E-01	5.42465E-01	8.58155E+02
1.486E+00	8.723E+02	3.81457E-01	5.02556E-01	8.59644E+02
1.666E+00	8.735E+02	3.62907E-01	4.64495E-01	8.61076E+02
1.870E+00	8.747E+02	3.44433E-01	4.27886E-01	8.62497E+02
2.098E+00	8.763E+02	3.26358E-01	3.93335E-01	8.63910E+02
2.189E+00	8.763E+02	3.19780E-01	3.81074E-01	8.64425E+02

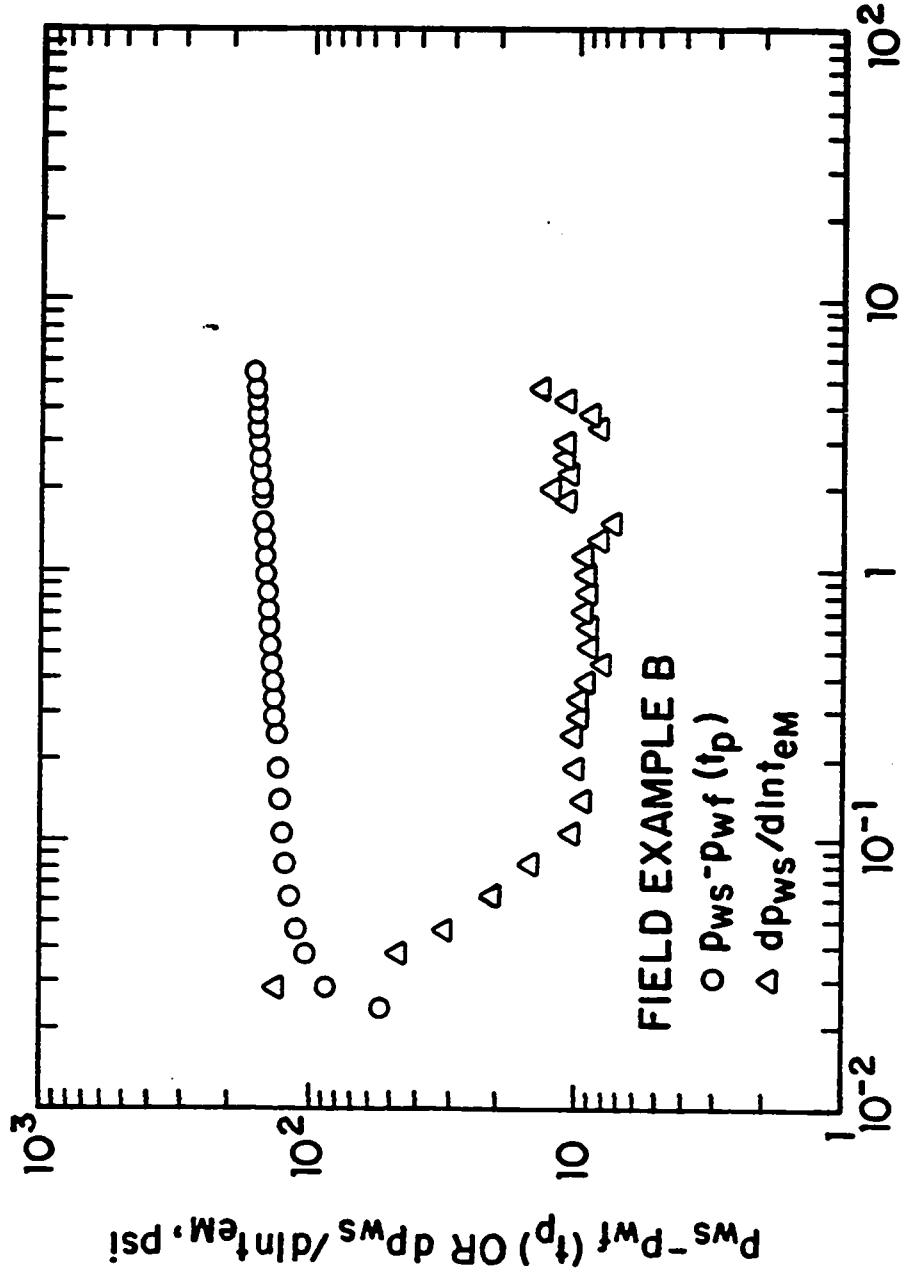

Fig. 3.4.7 - Log-log plot of buildup pressure rise and logarithmic derivative; Field Example B.

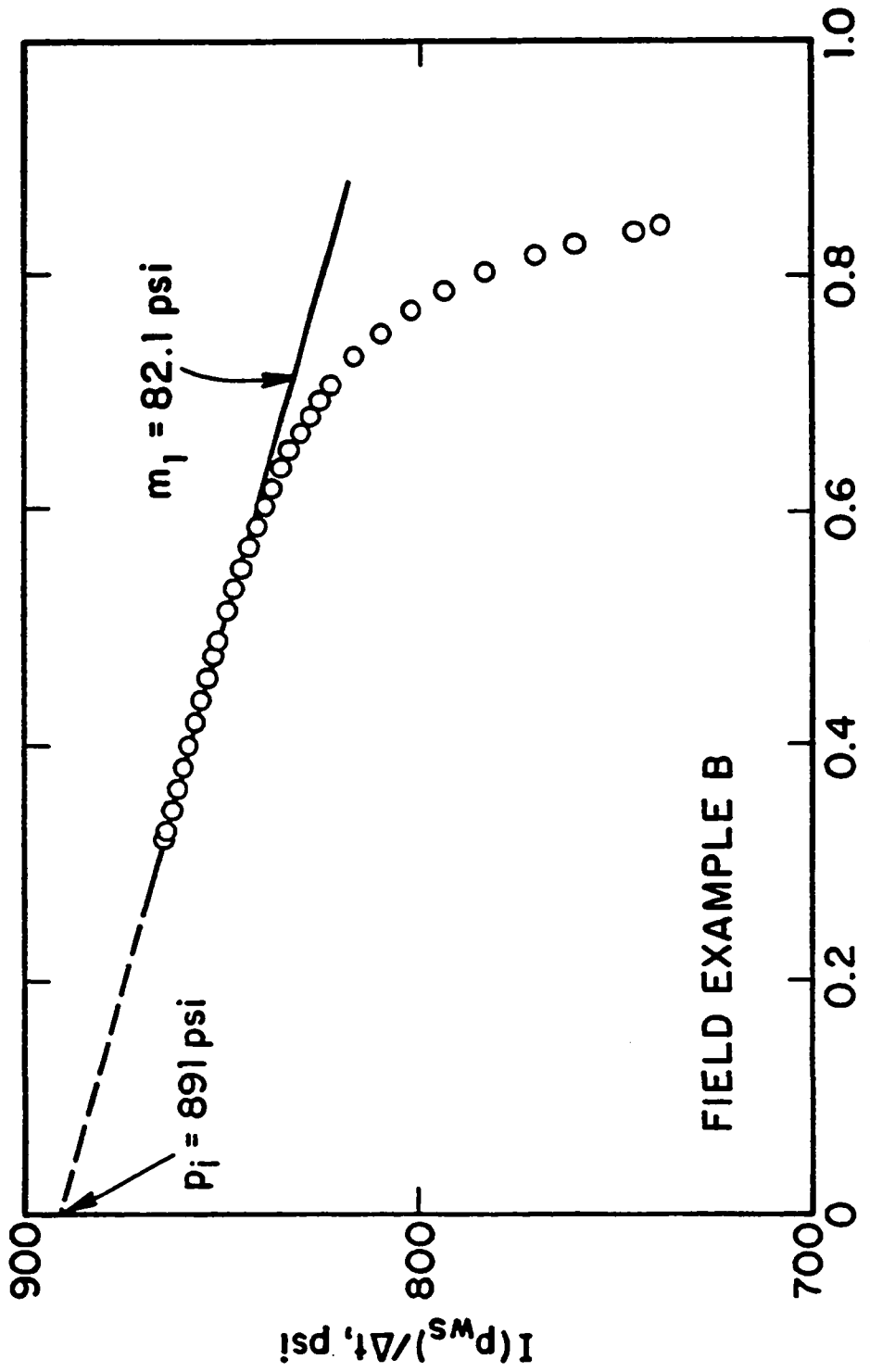

Fig. 3.4.8 - Method 1 Cartesian plot; Field Example B.

the proper straight of Method 1. From the slope value $m_1 = 82.1$ psi shown in Fig. 3.4.8, the transmissibility can be estimated by Eq. 3.3.17 as

$$\frac{kh}{\mu} = \frac{162.6}{82.1}\frac{(24)(0.0365)(712.2-142.4)}{1.126} = 878 \text{ md-ft/cp}, \tag{3.4.8}$$

which is equivalent to $kh = 52{,}700$ md-ft. Note that the extrapolation of the straight line shown in Fig. 3.4.8 gives $p_i = 891$ psi. The skin factor estimate is given by

$$s = 1.151\left\{\frac{891-535}{82.1} - (-0.149) - \log\left(\frac{878}{(0.062)(38)(10.2\times10^{-6})(0.354)^2}\right) + 3.23\right\} = -0.9 \tag{3.4.9}$$

Note that in the above computation we used $p_{avg} = 535$, obtained from Eq. 3.3.22, and that the value (-0.149) corresponds to the summation term in the right hand side of the skin equation (Eq. 3.3.21).

Fig. 3.4.9 presents the application of Method 2 to the field data. The buildup pressure versus the multi-rate time t_2 data are plotted as circular data points and correspond to the values of Column 4 in Table 3.4.3. For comparison purposes Fig. 3.4.9 also presents the Cartesian Method, indicated by the triangular data points. As shown in Fig. 3.4.4, a well defined straight line with slope $m_2 = 31.3$ psi is obtained for $t_2 < 0.8$. Note that most of the data points follow that straight line very closely, and its possible to draw a longer, and equally good, straight line through the circular data points for $t_2 < 1.4$. Note that the Cartesian Method performs better here than in the previous field example and a straight line can be drawn through the last points as shown by Ref. 44. Using the slope obtained from Method 2 in Eq. 3.3.32, gives

$$\frac{kh}{\mu} = \frac{162.6}{31.3}\frac{(24)(0.0365)(712.2-142.4)}{(2.3)1.126} = 1{,}000 \text{ md-ft/cp}, \tag{3.4.10}$$

which yields $kh = 60{,}000$ md-ft. The extrapolation of the straight line to $t_2 = 0$ gives $p_i = 888$ psi, which is only 3 psi lower than the initial reservoir pressure estimated by Method 1.

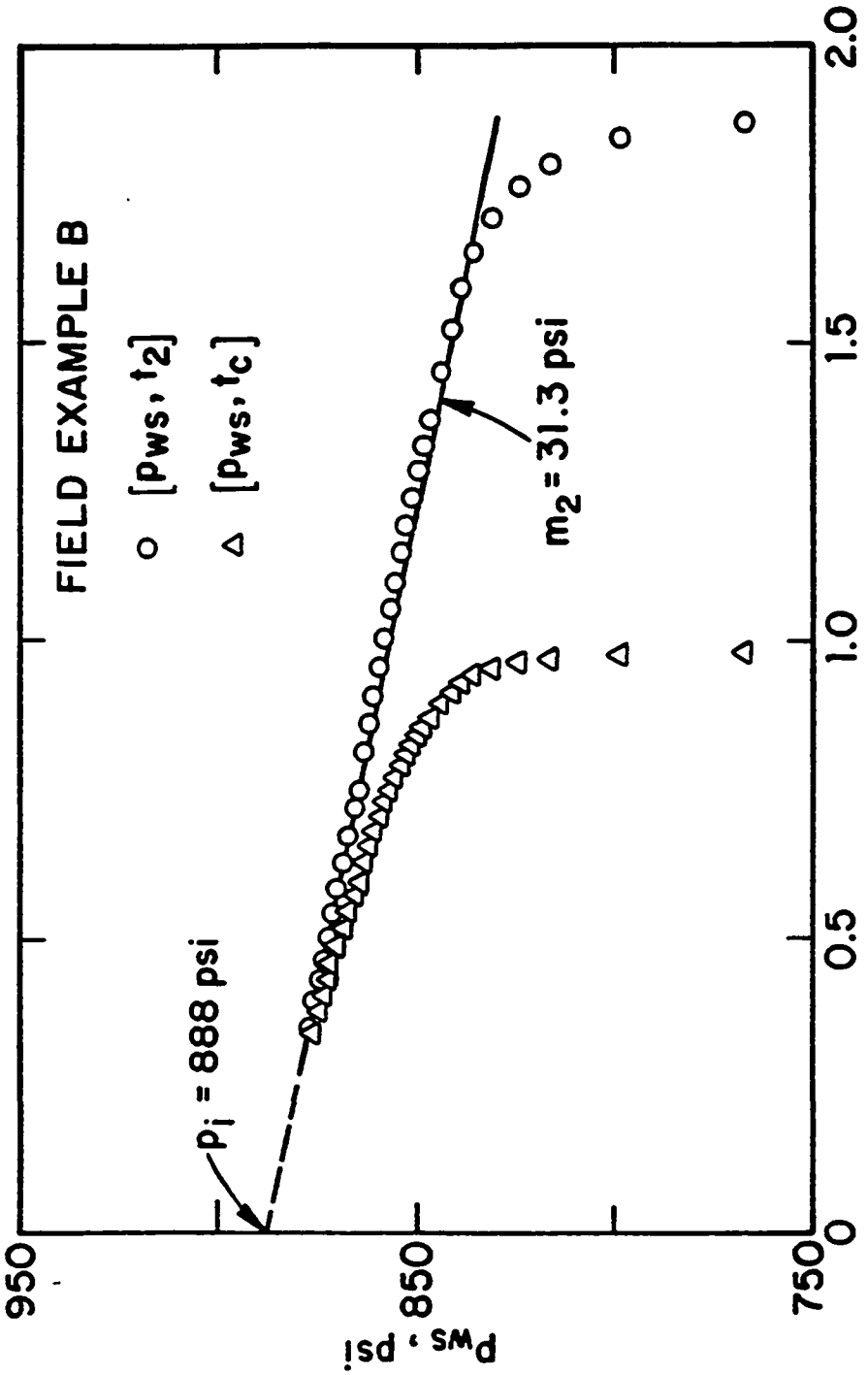

Fig. 3.4.9 - Comparison of Method 2 and Cartesian Method; Field Example B.

The skin factor from Method 2 is given

$$s = 1.151\left\{\frac{888-535}{(2.3)31.3} - (-0.149)\right.$$

$$\left. - \log\left(\frac{1000}{(0.062)(38)(10.2\times 10^{-6})(0.354)^2}\right) + 3.23\right\} = -0.3. \qquad (3.4.11)$$

Note that the kh and s values calculated from Method 2 are somewhat different from those obtained by Method 1.

The Horner plot for Example B is presented in Fig. 3.4.10. Note that in this field example the flow rate at the moment of shut-in is about 10 times smaller than the initial flow rate, therefore the rate variation has a strong effect on the shape of the Horner plot. Note that a straight line was drawn through the last data points and, as discussed in this Chapter, the computations based on such straight line should be based on the average flow rate. Further, as shown in Ref. 44, a second straight line can be obtained at early shut-in times with a slope value approximately equal to half of the value obtained by the first straight line. As discussed previously, this behavior can be erroneously interpreted as due the existence of a sealing fault close to the well.

Using the semilog slope value m = 55.1 psi, the transmissibility can be estimated by

$$\frac{kh}{\mu} = \frac{162.6}{55.1}\frac{(24)(0.0365)(712.2-142.4)}{1.1.26} \qquad (3.4.12)$$
$$= 1{,}309 \text{ md-ft/cp},$$

which gives kh = 78,540 md-ft. The initial reservoir pressure obtained from the Horner method is equal to 886 psi. The skin factor, using the modification presented by Ref. 35 and discussed in the previous field example, gives

$$s = 1.151\left\{\frac{886-427}{55.1}\right.$$

$$\left. - \log\left(\frac{1309(1.126)}{(0.062)(38)(10.2\times 10^{-6})(0.354)^2}\right) + 3.23\right\} = 3.3 \qquad (3.4.13)$$

Note that the flow capacity obtained by the Horner method exceeds the one obtained from Method 2 by approximately 30%.

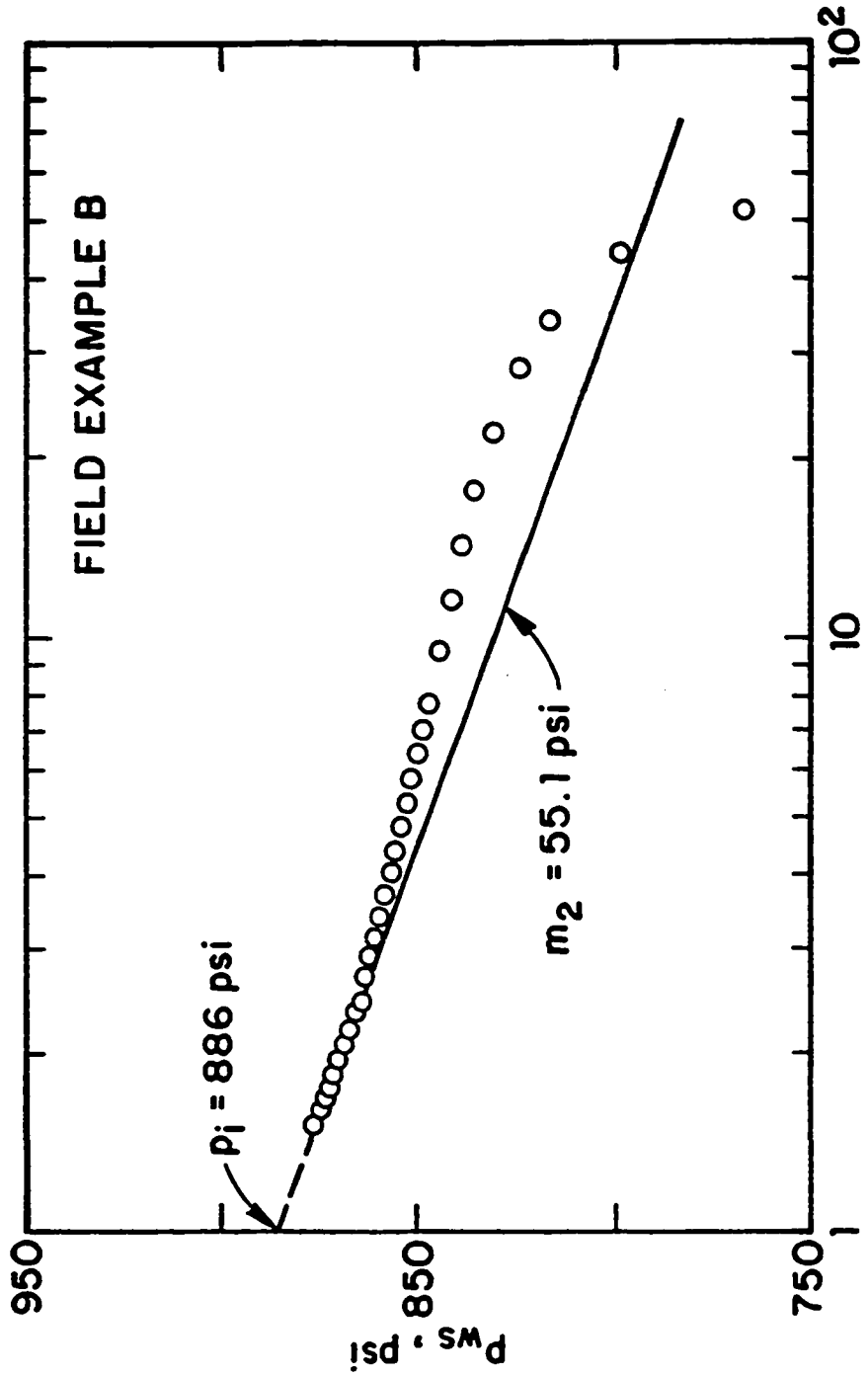

Fig. 3.4.10 - Horner plot; Field Example B.

Fig. 3.4.11 presents the conventional multi-rate method using the flow rates obtained from the material balance criteria. Note that by accounting for the rate variation during the flow period, the character of the buildup plot changes completely; compare with Fig. 3.4.10. From the slope value $m_H = 24.5$ psi and using the value of $q_{sf}(\hat{t}_{n+1,p})$ computed from Eq. 3.3.76, one obtains

$$\frac{kh}{\mu} = \frac{162.6(155.3)}{24.5} = 1{,}031 \text{ md-ft/cp} \tag{3.4.14}$$

and $kh = 61{,}860$ md-ft. An estimate for the initial reservoir pressure is obtained by extending the straight line to $t_{mH} = 0$ which gives $p_i = 888$ psi. The computation of the skin factor gives $s = 0.8$.

A summary of the results obtained by the different methods are presented in Table 3.4.4. Clearly, the results obtained by Method 2 and the conventional multi-rate method are in excellent agreement, whereas the results obtained by the Method 1 are not as good as in the Field Example C due the presence of wellbore storage during the buildup period. As discussed before (and illustrated in this example), the Horner method overestimates the flow capacity and underestimates the initial pressure p_i. The difference in the skin factor calculated by the Horner method is a direct consequence of the completely erroneous value of kh used in the computations.

For comparison purposes, Table 3.4.4 also includes the results obtained by Ref. 44 using the Cartesian Method. Note that the Cartesian Method does not provide a direct computation of the skin factor and the value reported in Table 3.4.4 was obtained by Ref. 44 using early drawdown pressure data.

As mentioned in the previous field example, the kh value obtained from the analysis of the flow period is approximately 50% lower than the one calculated from the buildup data; compare the results of Table 3.4.4 and 2.4.4.

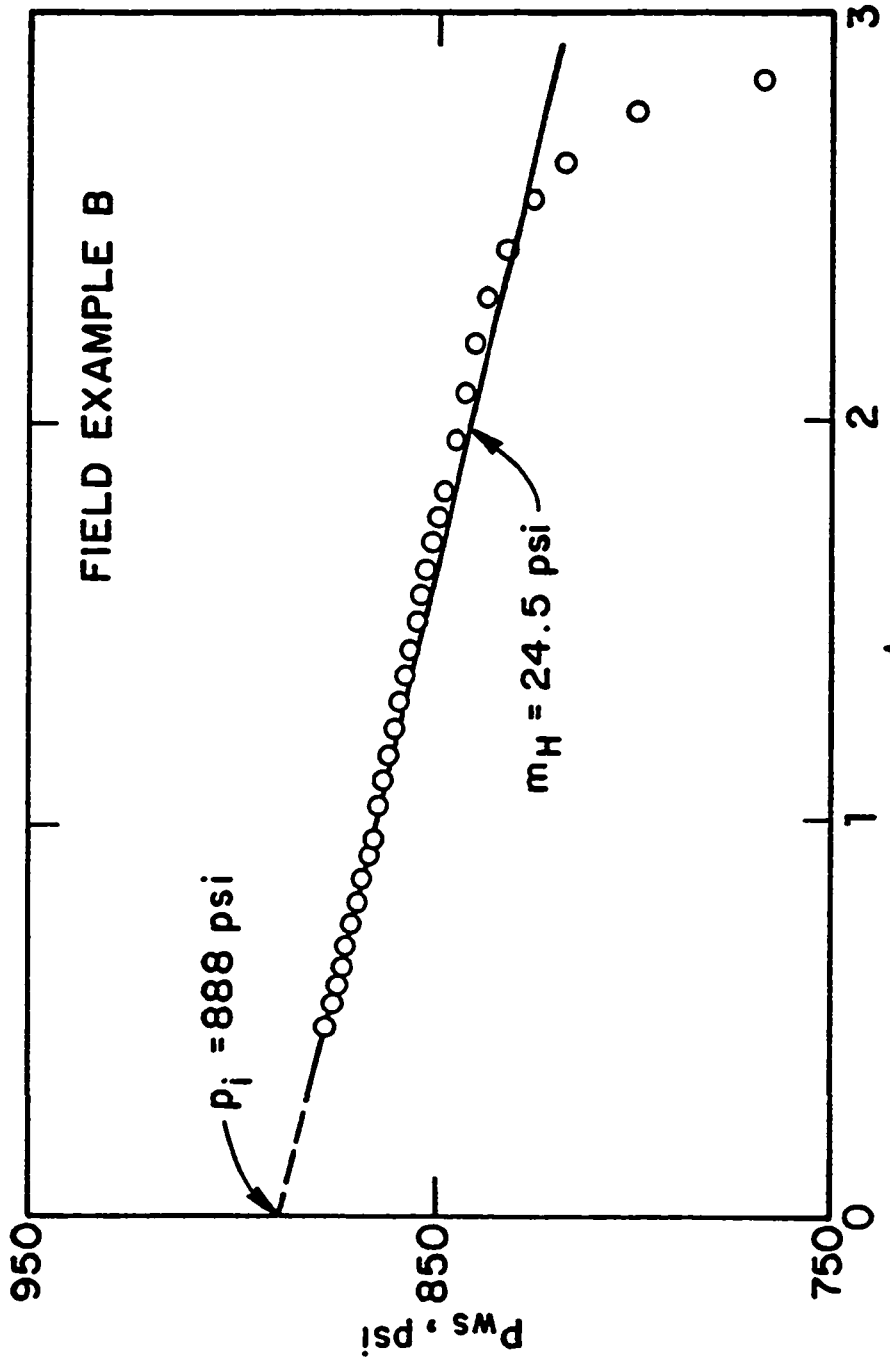

Fig. 3.4.11 - Conventional multi-rate plot; Field Example B.

Table 3.4.4

Field Example B - Comparison of Results

Parameters	Method 1	Method 2	Multi-rate	Horner	Cartesian
kh/μ, md-ft/cp	878	1,000	1,031	1,309	877
kh, md-ft	52,700	60,000	61,860	78,540	52,600
skin	-0.9	-0.3	0.8	3.3	-3.5
p_i, psi	891	888	888	886	892

CHAPTER IV
DECONVOLUTION ANALYSIS

In Chapters II and III new procedures for analyzing pressure data from slug and drillstem tests have been presented. However, some of methods developed in those Chapters assume that a particular flow regime exists in the reservoir. A more general analysis procedure for variable sandface problems can be constructed from Duhamel's principle, regardless of the well/reservoir flow geometry. In this approach, generally referred to as deconvolution methods, the measured pressure and rate data are used to generate the equivalent pressure data for constant sandface flow production.

In this Chapter, new deconvolution schemes designed for slug and DST applications are presented. The new algorithms do not require the measurement or direct computation of the flow rates during the flow and buildup periods. Several field examples are presented at the end of this Chapter.

4.1 Background and Theory

In this section, we review the application of the Bostic et al.[49] and the Kuĉuk and Ayestaran[50] deconvolution algorithms to slug and drillstem tests. In presenting this topic we follow closely the approach used by Thompson et al.[51]

Using the definitions of Chapter III and starting from Duhamel's principle, the dimensionless pressure solution for the DST problem is given by

$$p_{wD}(t_D) = \int_0^{t_D} q_D(\tau) \frac{dp^*_{wcD}}{dt_D}(t_D - \tau) d\tau. \qquad (4.1.1)$$

Note that in Eq. 4.1.1 p_{wD} denotes either a slug or buildup solution whereas q_D represents the DST sandface flow rate throughout the test.

Consider the time partition $[0, t_D]$ given by

$$0 = t_{0D} < t_{1D} < \cdots < t_{nD} < t_{n+1,D} = t_D. \qquad (4.1.2)$$

Recall that t_D represents the total elapsed dimensionless time since the start of the DST. With this notation, Eq. 4.1.1. becomes

$$\begin{aligned} p_{wD}(t_D) &= \sum_{j=0}^{n} \int_{t_{jD}}^{t_{j+1,D}} q_D(\tau) \frac{dp^*_{wcD}}{dt_D}(t_D - \tau) d\tau \\ &= \sum_{j=0}^{n} q_D(\hat{t}_{j+1,D}) \int_{t_{jD}}^{t_{j+1,D}} \frac{dp^*_{wcD}}{dt_D}(t_D - \tau) d\tau, \end{aligned} \tag{4.1.3}$$

where $\hat{t}_{j+1,D}$ is given by

$$\hat{t}_{j+1,D} = \theta_{j+1} t_{j+1,D} + (1 - \theta_{j+1}) t_{jD}. \tag{4.1.4}$$

Performing the integration and rearranging, Eq. 4.1.3 can be written as

$$\begin{aligned} \bar{p}_{wcD}(t_D) = \frac{p_{wD}(t_D)}{q_D(\hat{t}_{1D})} - \\ \sum_{j=1}^{n} \left(\frac{q_D(\hat{t}_{j+1,D}) - q_D(\hat{t}_{jD})}{q_D(\hat{t}_{1D})} \right) \bar{p}_{wcD}(t_D - t_{jD}). \end{aligned} \tag{4.1.5}$$

Eq. 4.1.5 represents a generalization[51] of the algorithm proposed by Bostic et al.[49] In applying Eq. 4.1.5, the results obtained by Thompson[71] indicate that one should choose $\theta_{j+1} = 1$ for all j, that is, $\hat{t}_{j+1,D} = t_{j+1,D}$. As discussed in Ref. 51, whenever $t_D - t_{jD} > t_{nD}$, where t_{nD} is the last value generated by Eq. 4.1.5, the computation of $p^*_{wcD}(t_D)$ requires an iterative procedure. Moreover, for the partition points satisfying $t_D - t_{jD} < t_{nD}$, the evaluation of the term $\bar{p}_{wcD}(t_D - t_{jD})$ generally requires interpolation. These problems are also discussed in Refs. 47 and 49.

Integrating Eq. 4.1.1 by parts, gives

$$\begin{aligned} p_{wD}(t_D) &= q_D(0^+) \bar{p}_{wcD}(t_D) + \int_0^{t_D} \frac{dq_D}{d\tau}(\tau) \bar{p}_{wcD}(t_D - \tau) d\tau \\ &= q_D(0^+) \bar{p}_{wcD}(t_D) + \int_0^{t_D} \frac{dq_D}{dt_D}(t_D - \tau) \bar{p}_{wcD}(\tau) d\tau, \end{aligned} \tag{4.1.6}$$

where $q_D(0^+)$ represents the limit of $q_D(t_D)$ as t_D approaches zero from the right. Eq. 4.1.6 is the starting point of the Kuĉuk and Ayestaran's deconvolution algorithm. With the time partition given by Eq. 4.1.2, Eq. 4.1.6 can be written as

$$p_{wD}(t_D) = q_D(0^+) \bar{p}_{wcD}(t_D) + \sum_{j=0}^{n} \int_{t_{jD}}^{t_{j+1,D}} \frac{dq_D}{dt_D}(t_D - \tau) \bar{p}_{wcD}(\tau) d\tau$$

$$= q_D(0^+)p^*_{wcD}(t_D) + \sum_{j=0}^{n}[q_D(t_D - t_{jD}) - q_D(t_D - t_{j+1,D})]\,p^*_{wcD}(\hat{t}_{j+1,D}). \quad (4.1.7)$$

For the slug or DST problem in which $q_D(0^+) \neq 0$, Ref. 51 recommends that one choose $\theta_{j+1} = 1$, or equivalently, $\hat{t}_{j+1,D} = t_{j+1,D}$, so that the flow rate at 0^+ is eliminated from the resulting equation. Using this result in Eq. 4.1.7 and solving for p^*_{wcD}, gives

$$p^*_{wcD}(t_D) = \frac{p_{wD}(t_D)}{q_D(t_D - t_{nD})} -$$

$$\sum_{j=0}^{n-1}\left[\frac{q_D(t_D - t_{jD}) - q_D(t_D - t_{j+1,D})}{q_D(t_D - t_{nD})}\right] p^*_{wcD}(t_{j+1,D}), \quad (4.1.8)$$

which represents the DST version of the deconvolution algorithm proposed by Ref. 50. Note that the recursive algorithm given by Eq. 4.1.8 does not require interpolation and iteration in p_{wcD}, however, if the flow rates are only known at the nodes of the time partition, it is necessary to interpolate the measured flow rates.

Note that the deconvolution algorithms given by Eqs. 4.1.8 and 4.1.5 are unconditionally stable[51,71] when the flow rate is a decreasing function of time, that is, an error in the p^*_{wcD} value at some point of the computation does not grow as subsequent values of p^*_{wcD} are calculated.

4.2 Analysis Procedures

The application of either Eq. 4.1.5 or Eq. 4.1.8 requires flow rate information. In slug test and DST operations this data can be obtained from a bottom-hole flow meter device but this is rarely done in standard field operations. An alternative approach is to compute the flow rates from the DST boundary condition given by Eq. 3.2.24, however, as mentioned previously, this requires the computation of pressure derivatives from field data. In the following sections, new deconvolution schemes are presented which account for the flow rate variation without resorting to pressure derivative computations.

4.2.1 Slug Test Real Space Deconvolution

The new deconvolution method presented here follows the same basic approach used in the development of the buildup Methods 1 and 2, that is, Duhamel's formula is rearranged in a convenient form so that the wellbore pressure derivatives are eliminated from the equations. In this section, we are concerned with the analysis of the flow period only. The buildup deconvolution scheme is considered later in this Chapter.

Integrating both side of Duhamel's principle given by Eq. 3.3.1 gives

$$\begin{aligned}\int_0^{t_D} p_{wD}(\tau)d\tau &= \int_0^{t_D} q_D(\tau)\ p^*_{wcD}(t_D-\tau)d\tau \\ &= \int_0^{t_D} q_D(t_D-\tau)\ p^*_{wcD}(\tau)d\tau \end{aligned} \tag{4.2.1}$$

Using the time partition given by Eq. 4.1.2, we can write Eq. 4.2.1 as

$$\int_0^{t_{n+1,D}} p_{wD}(\tau)d\tau = \sum_{j=0}^{n}\int_{t_{jD}}^{t_{j+1,D}} q_D(t_D-\tau)\ p^*_{wcD}(\tau)d\tau. \tag{4.2.2}$$

As p^*_{wcD} is a continuously differentiable function on each time sub-interval $[t_{jD}, t_{j+1,D}]$, the Taylor series expansion for $p^*_{wcD}(\tau)$ truncated at the first term gives

$$p^*_{wcD}(\tau) = p^*_{wcD}(\hat{t}_{j+1,D}) - (\hat{t}_{j+1,D}-\tau)\frac{dp^*_{wcD}}{dt_D}(\tilde{t}_{j+1,D}), \tag{4.2.3}$$

for $t_{jD} \le \tau \le t_{j+1,D}$, where $\hat{t}_{j+1,D}$ is given by Eq. 4.1.4 and $\tilde{t}_{j+1,D}$ satisfies

$$t_{jD} \le \tilde{t}_{j+1,D} \le t_{j+1,D}. \tag{4.2.4}$$

Substituting Eq. 4.2.3 in Eq. 4.2.2 gives

$$\int_0^{t_{n+1,D}} p_{wD}(\tau)d\tau = \sum_{j=0}^{n}\left\{p^*_{wcD}(\hat{t}_{j+1,D})\int_{t_{jD}}^{t_{j+1,D}} q_D(t_D-\tau)d\tau - e_{B,j+1}\right\}, \tag{4.2.5}$$

where

$$e_{B,j+1} = \int_{t_{jD}}^{t_{j+1,D}} q_D(t_D - \tau)(\hat{t}_{j+1,D} - \tau)\frac{dp^*_{wcD}}{dt_D}(\tilde{t}_{j+1,D})d\tau. \tag{4.2.6}$$

Using the slug test pressure integral definition given by Eq. 2.2.29 and solving Eq. 4.2.5 for $p^*_{wcD}(\hat{t}_{n+1,D})$, gives

$$p^*_{wcD}(\hat{t}_{n+1,D}) = \frac{I(p_{wD}) - \text{sum} + E_B}{\int_{t_{nD}}^{t_{n+1,D}} q_D(t_D - \tau)d\tau}, \tag{4.2.7}$$

where

$$\text{sum} = \sum_{j=0}^{n-1}\left\{p^*_{wcD}(\hat{t}_{j+1,D})\int_{t_{jD}}^{t_{j+1,D}} q_D(t_D - \tau)d\tau\right\} \tag{4.2.8}$$

and

$$E_B = \sum_{j=0}^{n} e_{B,j+1}. \tag{4.2.9}$$

Although our goal is to construct a deconvolution method for slug and DST problems, thus far, the recursive algorithm given by Eq. 4.2.7 is completely general and can be applied to any other well testing problem provided the dimensionless sandface flow rate, q_D, is defined appropriately.

For $t_D < t_{pD}$, the sandface flow rate is given by

$$q_D(t_D) = -C_{FD}\frac{dp_{wD}}{dt_D}. \tag{4.2.10}$$

Using Eq. 4.2.10, one can write

$$\begin{aligned}\int_{t_{jD}}^{t_{j+1,D}} q_D(t_D - \tau)d\tau &= -C_{FD}\int_{t_{jD}}^{t_{j+1,D}} \frac{dp_{wD}}{dt_D}(t_D - \tau)d\tau \\ &= C_{FD}\left[p_{wD}(t_D - t_{j+1,D}) - p_{wD}(t_D - t_{j,D})\right].\end{aligned} \tag{4.2.11}$$

For $j = n$, Eq. 4.2.11 gives

$$\int_{t_{nD}}^{t_{n+1,D}} q_D(t_D - \tau)d\tau = C_{FD}\left[1 - p_{wD}(t_D - t_{n,D})\right]. \tag{4.2.12}$$

Note that in Eq. 4.2.12, we used the fact that $p_{wD}(0) = 1$.

Using Eqs. 4.2.11 and 4.2.12 and assuming that the error term E_B can be neglected, we write a new deconvolution scheme for slug test data from Eq. 4.2.7 as

$$P_{FCND}(\hat{t}_{n+1,D}) = \frac{[I(p_{wD})/C_{FD}] - \text{sum 1}}{[1 - p_{wD}(t_D - t_{n,D})]}, \tag{4.2.13}$$

where sum 1 is defined by

$$\text{sum 1} = \sum_{j=0}^{n-1} \left\{ P_{FCND}(\hat{t}_{j+1,D}) \left[p_{wD}(t_D - t_{j+1,D}) - p_{wD}(t_D - t_{j,D}) \right] \right\}. \tag{4.2.14}$$

In Eqs. 4.2.13 and 4.2.14, we adopted the notation of Bostic et al.[49] and use P_{FCND} to denote the p''_{wcD} values calculated by the new deconvolution algorithm. Note that the key step in the derivation is provided by Eqs. 4.2.11 and 4.2.12, which eliminates the flow rate from the resulting equations. Also note that the new deconvolution scheme does not require interpolation and iteration in P_{FCND}. In most of the cases, it is necessary to interpolate the measured pressure data in order to evaluate the terms $p_{wD}(t_D - t_{j+1,D})$ in Eq. 4.2.14. Throughout, the algorithm given by Eq. 4.2.13 is referred to as Method A.

Following Ref. 49, P_{FCN} is defined as the pressure drop per unit flow rate for the constant sandface rate problem. Thus,

$$P_{FCND} = \frac{(kh/\mu)P_{FCN}}{141.2}, \tag{4.2.15}$$

where P_{FCN} is in psi/RB/day.

Using the dimensionless definitions given previously, the dimensional form of Eqs. 4.2.13 and 4.2.14 are given, respectively, by

$$P_{FCN}(\hat{t}_{n+1}) = \frac{[I(\Delta p)/24C_F] - \text{sum 2}}{[p_{wf}(t_{n+1} - t_n) - p_o]}, \tag{4.2.16}$$

and

$$\text{sum 2} = \sum_{j=0}^{n-1} \left\{ P_{FCN}(\hat{t}_{j+1}) \left[p_{wf}(t_{n+1} - t_j) - p_{wf}(t_{n+1} - t_{j+1}) \right] \right\}. \tag{4.2.17}$$

The field application of Eq. 4.2.16 requires the computation of $I(\Delta p)$ by some numerical integration procedure; see related discussion in the section 2.3.4 of Chapter

II. After generating the P_{FCN} values by the recursive application of Eq. 4.2.16, the data can then be analyzed using constant sandface flow rate methods.

Stability of Method A

An mentioned before, a deconvolution scheme is defined to be stable if an error ϵ in p^*_{wcD} at some point in the calculations does not result in an error greater than $|\epsilon|$ in subsequently computed values of p^*_{wcD}. For the sake of generality, we consider the stability of Method A in the form given by Eqs. 4.2.7 and 4.2.8.

Suppose that an error ϵ is introduced into the calculated value of $p^*_{wcD}(\hat{t}_{l+1,D})$ for some l, $0 \leq l \leq n-1$. Let $\tilde{p}^*_{wcD}$ denote the calculated value of p^*_{wcD}, then it follows from Eqs. 4.2.7 and 4.2.8 that

$$\tilde{p}^*_{wcD}(\hat{t}_{n+1,D}) = \frac{I(p_{wD}) + E_B}{\int_{t_{nD}}^{t_{n+1,D}} q_D(t_D - \tau)d\tau} - b_{l+1}\left[p^*_{wcD}(\hat{t}_{l+1,D}) + \epsilon\right] - \sum_{\substack{j=0 \\ j\neq l}}^{n-1}\left\{b_{j+1}p^*_{wcD}(\hat{t}_{j+1,D})\right\}, \tag{4.2.18}$$

where for convenience we defined b_{j+1} as

$$b_{j+1} = \frac{\int_{t_{jD}}^{t_{j+1,D}} q_D(t_D - \tau)d\tau}{\int_{t_{nD}}^{t_{n+1,D}} q_D(t_D - \tau)d\tau}. \tag{4.2.19}$$

The error in the calculated value of $p^*_{wcD}(\hat{t}_{n+1,D})$ caused by an error ϵ in the $p^*_{wcD}(\hat{t}_{l+1,D})$ value can then be obtained by subtracting Eq. 4.2.18 from Eq. 4.2.7 and is given by

$$E = p^*_{wcD}(\hat{t}_{n+1,D}) - \tilde{p}^*_{wcD}(\hat{t}_{n+1,D}) = b_{l+1}\epsilon. \tag{4.2.20}$$

The stability criterion requires that $|E| \leq |\epsilon|$, thus, from Eq. 4.2.20 one can see that the scheme is stable if and only if

$$|b_{l+1}| \leq 1; \qquad 0 \leq l \leq n-1. \tag{4.2.21}$$

II. After generating the P_{FCN} values by the recursive application of Eq. 4.2.16, the data can then be analyzed using constant sandface flow rate methods.

Stability of Method A

An mentioned before, a deconvolution scheme is defined to be stable if an error ϵ in p^*_{wcD} at some point in the calculations does not result in an error greater than $|\epsilon|$ in subsequently computed values of p^*_{wcD}. For the sake of generality, we consider the stability of Method A in the form given by Eqs. 4.2.7 and 4.2.8.

Suppose that an error ϵ is introduced into the calculated value of $p^*_{wcD}(\hat{t}_{l+1,D})$ for some l, $0 \leq l \leq n-1$. Let $\tilde{p}^*_{wcD}$ denote the calculated value of p^*_{wcD}, then it follows from Eqs. 4.2.7 and 4.2.8 that

$$\tilde{p}^*_{wcD}(\hat{t}_{n+1,D}) = \frac{I(p_{wD}) + E_B}{\int_{t_{nD}}^{t_{n+1,D}} q_D(t_D - \tau)d\tau} - b_{l+1}\left[p^*_{wcD}(\hat{t}_{l+1,D}) + \epsilon\right] - \sum_{\substack{j=0 \\ j\neq l}}^{n-1}\left\{b_{j+1}p^*_{wcD}(\hat{t}_{j+1,D})\right\}, \tag{4.2.18}$$

where for convenience we defined b_{j+1} as

$$b_{j+1} = \frac{\int_{t_{jD}}^{t_{j+1,D}} q_D(t_D - \tau)d\tau}{\int_{t_{nD}}^{t_{n+1,D}} q_D(t_D - \tau)d\tau}. \tag{4.2.19}$$

The error in the calculated value of $p^*_{wcD}(\hat{t}_{n+1,D})$ caused by an error ϵ in the $p^*_{wcD}(\hat{t}_{l+1,D})$ value can then be obtained by subtracting Eq. 4.2.18 from Eq. 4.2.7 and is given by

$$E = p^*_{wcD}(\hat{t}_{n+1,D}) - \tilde{p}^*_{wcD}(\hat{t}_{n+1,D}) = b_{l+1}\epsilon. \tag{4.2.20}$$

The stability criterion requires that $|E| \leq |\epsilon|$, thus, from Eq. 4.2.20 one can see that the scheme is stable if and only if

$$|b_{l+1}| \leq 1; \qquad 0 \leq l \leq n-1. \tag{4.2.21}$$

As the b_{j+1} terms are always greater than or equal to zero, Eq. 4.2.21 implies that we must have

$$\int_{t_{nD}}^{t_{n+1,D}} q_D(t_D - \tau)d\tau \geq \int_{t_{lD}}^{t_{l+1,D}} q_D(t_D - \tau)d\tau. \tag{4.2.22}$$

Using the mean value theorem for integrals, Eq. 4.2.22 can be written as

$$[t_{n+1,D} - t_{nD}] \geq \frac{q_D(t_D - \vartheta)}{q_D(t_D - \varsigma)}[t_{l+1,D} - t_{lD}], \tag{4.2.23}$$

where

$$t_{nD} \leq \varsigma \leq t_{n+1,D} \tag{4.2.24}$$

and

$$t_{lD} \leq \vartheta \leq t_{l+1,D}. \tag{4.2.25}$$

Based on Eqs. 4.2.24 and 4.2.25, it is clear that $(t_D - \varsigma) < (t_D - \vartheta)$, for all l, $0 \leq l \leq n-1$. Thus, if the flow rate is a decreasing function of time, we have $q_D(t_D - \vartheta) < q_D(t_D - \varsigma)$, and an upper bound for the inequality of Eq. 4.2.23 is given by

$$[t_{n+1,D} - t_{nD}] \geq [t_{l+1,D} - t_{lD}]; \qquad 0 \leq l \leq n-1. \tag{4.2.26}$$

Thus, if the flow rate decreases throughout the flow period, the scheme is stable provided that the time partition have equal or increasing time step sizes.

For the slug test problem under consideration, the stability criteria given by Eq. 4.2.26 provides a conservative upper bound. Using the results of Eqs. 4.2.11 and 4.2.12 in Eq. 4.2.22, one obtains the stability of Method A for slug test problems as

$$1 - p_{wD}(t_D - t_{nD}) \geq p_{wD}(t_D - t_{l+1,D}) - p_{wD}(t_D - t_{lD}), \tag{4.2.27}$$

for $0 \leq l \leq n-1$. The dimensional form of Eq. 4.2.27 is given by

$$p_{wf}(t_{n+1} - t_n) \geq p_o + \max_{0 \leq l \leq n-1} \{p_{wf}(t_{n+1} - t_l) - p_{wf}(t_{n+1} - t_{l+1})\}. \tag{4.2.28}$$

In programming, we should use the more rigorous stability criterion given by Eq. 4.2.28, however, the criterion given by Eq. 4.2.26 is useful for a quick inspection of the field data.

Truncation Errors in the Method A Scheme

In this sub-section we will present an upper bound on the local truncation error, $e_{B,j+1}$, and the global truncation error, E_B, in the new slug test deconvolution scheme.

Taking absolute values of both sides of Eq. 4.2.6 gives

$$|e_{B,j+1}| \leq \int_{t_{jD}}^{t_{j+1,D}} |q_D(t_D-\tau)||\hat{t}_{j+1,D}-\tau|\left|\frac{dp^*_{wcD}}{dt_D}(\tilde{t}_{j+1,D})\right|d\tau. \qquad (4.2.29)$$

Note that the following inequality holds

$$|\hat{t}_{j+1,D}-\tau| \leq (t_{j+1,D}-t_{jD}) \qquad (4.2.30)$$

for all values of τ and $\hat{t}_{j+1,D}$ satisfying $t_{jD} \leq \tau, \hat{t}_{j+1,D} \leq t_{j+1,D}$. Defining the time step size of the interval $[t_{j+1,D}-t_{jD}]$ as

$$\delta t_{j+1,D} = t_{j+1,D}-t_{jD}, \qquad (4.2.31)$$

it follows from Eq. 4.2.29 that

$$|e_{B,j+1}| \leq \max_{t_{jD}\leq\tau\leq t_{j+1,D}}\left\{|q_D(t_D-\tau)|\left|\frac{dp^*_{wcD}}{dt_D}(\tilde{t}_{j+1,D})\right|\right\}\delta t_{j+1,D}\int_{t_{jD}}^{t_{j+1,D}} d\tau$$

$$= \max_{t_{jD}\leq\tau\leq t_{j+1,D}}\left\{|q_D(t_D-\tau)|\left|\frac{dp^*_{wcD}}{dt_D}(\tilde{t}_{j+1,D})\right|\right\}(\delta t_{j+1,D})^2. \qquad (4.2.32)$$

Assuming that both dp^*_{wcD}/dt_D and q_D are bounded in every interval $[t_{j+1,D}-t_{jD}]$, there exists a positive constant K_{j+1} such that

$$|e_{B,j+1}| \leq K_{j+1}(\delta t_{j+1,D})^2. \qquad (4.2.33)$$

Eq. 4.2.23 indicates that the order of the local truncation error is $O[(\delta t_{j+1,D})^2]$.

Taking absolute values of both sides of Eq. 4.2.9 and using Eq. 4.2.33, gives

$$|E_B| \leq \sum_{j=0}^{n} K_{j+1}(\delta t_{j+1,D})^2. \qquad (4.2.34)$$

Define

$$K_{max} = \max_{0 \le j \le n} \{K_{j+1}\}, \tag{4.2.35}$$

and

$$\delta t_{D,max} = \max_{0 \le j \le n} \delta t_{j+1,D}, \tag{4.2.36}$$

then Eq. 4.2.33 yields

$$|E_B| \le K_{max}(\delta t_{D,max}) \sum_{j=0}^{n} \delta t_{j+1,D} = K_{max} t_D(\delta t_{D,max}) \tag{4.2.37}$$

which is $O(\delta t_{D,max})$.

4.2.2 Slug Test Laplace Space Deconvolution

Following ideas presented by Ref. 50, Roumboutsos and Stewart[53] presented a deconvolution scheme in which, the pressure and rate data are transformed into Laplace space where all computations are performed. The resulting p^*_{wcD} values are then inverted from Laplace space by some numerical inversion algorithm. A similar Laplace space convolution was also proposed by Guillot and Horne[71] for improving nonlinear regression analysis of field data using computer-based techniques. Here, we extend those ideas to slug test problems and a deconvolution scheme is presented which, similar to Method A, does not require measurement or direct computation of the flow rates.

Applying Laplace transforms to Duhamel's principle given by Eq. 4.1.1, gives

$$\bar{p}_{wD}(u) = u\bar{q}_D(u)\bar{p}^*_{wcD}, \tag{4.2.38}$$

where $\bar{p}_{wD}$ denotes the dimensionless wellbore pressure drop in Laplace space, $\bar{p}^*_{wcD}$ refers to the Laplace transform of the constant sandface flow rate solution, and u represents the Laplace variable. In Eq. 4.2.38 we used the fact that $p^*_{wcD}(0) = 0$.

Solving Eq. 4.2.38 for $\bar{p}^*_{wcD}$ and taking the inverse transform, we obtain

$$p^*_{wcD}(t_D) = \mathcal{L}^{-1}\left\{\frac{\bar{p}_{wD}(u)}{u\bar{q}_D(u)}\right\}, \tag{4.2.39}$$

where $\mathcal{L}$ is used to denote the Laplace transform operator, thus, $\mathcal{L}^{-1}$ denotes the inverse transform. Eq. 4.2.39 indicates that the constant sandface rate solution can be directly obtained by inverting the ratio of $\bar{p}_{wD}$ to $u\bar{q}_D$. This approach is, in principle, more efficient than real space deconvolution schemes since no recurrence formula is needed and hence, the stability of the algorithm is improved.

For the slug test problem, the Laplace transform of Eq. 4.2.10 gives

$$\bar{q}_D(u) = -C_{FD}[u\bar{p}_{wD}(u) - p_{wD}(0)]. \tag{4.2.40}$$

Using Eq. 4.2.40 in Eq. 4.2.39, gives

$$p^{\bullet}_{wcD}(t_D) = -\mathcal{L}^{-1}\left\{\frac{\bar{p}_{wD}(u)}{uC_{FD}[u\bar{p}_{wD}(u) - p_{wD}(0)]}\right\}. \tag{4.2.41}$$

Eq. 4.2.41 shows that the $p^{\bullet}_{wcD}$ values can be obtained from the measured slug test pressure data without explicitly computing the flow rates. In this Chapter, the deconvolution scheme given by Eq. 4.2.41 is referred to as Method B.

The next step for implementing Eq. 4.2.41 is to transform the p_{wD} data to the corresponding Laplace space data. Consider the time partition given by Eq. 4.1.2. Then, the piecewise linear approximation of a function $f(t_D)$ can be written as

$$f(\tau) = f_j + [\tau - t_{jD}]\dot{f}_{j+1}; \qquad t_{jD} \le \tau \le t_{j+1,D}, \tag{4.2.42}$$

for $0 \le j \le n$. In Eq. 4.2.42, f_j denotes the value of the function f evaluate at the node j and $\dot{f}_{j+1}$ represents the chord slope between two adjacent points in the partition and is defined by

$$\dot{f}_{j+1} = \frac{f_{j+1} - f_j}{t_{j+1,D} - t_{j,D}}; \qquad 0 \le j \le n. \tag{4.2.43}$$

The Laplace transform of a function f is defined as

$$\mathcal{L}\{f(t_D)\} = \bar{f}(u) = \int_0^{\infty} e^{-u\tau} f(\tau)d\tau = \lim_{T\to\infty}\int_0^{T} e^{-u\tau} f(\tau)d\tau. \tag{4.2.44}$$

With the time partition, the last integral in the right hand side of Eq. 4.2.44 can be written as

$$\int_0^{T} e^{-u\tau} f(\tau)d\tau = \sum_{j=0}^{n}\int_{t_{jD}}^{t_{j+1,D}} e^{-u\tau} f(\tau)d\tau. \tag{4.2.45}$$

By substituting Eq. 4.2.42 in Eq. 4.2.45 and performing the integration term by term, Ref. 53 obtained an expression for f in Laplace space. As the details of this derivation are somewhat tedious, we present here an interesting short-cut. From the operational properties of the Laplace transforms, we have

$$\mathcal{L}\{f'(t_D)\} = \lim_{T\to\infty} \int_0^T e^{-u\tau} f'(\tau) d\tau = u\bar{f}(u) - f(0), \tag{4.2.46}$$

which can be rearranged to give

$$\bar{f}(u) = \frac{1}{u}\left[\mathcal{L}\{f'(t_D)\} + f(0)\right]. \tag{4.2.47}$$

In Eq. 4.2.46 and 4.2.47, $f'(t_D)$ denotes the derivative of $f(t_D)$. With the time partition given by Eq. 4.1.2, one obtains the following approximation:

$$\int_0^{T=t_{n+1,D}} e^{-u\tau} f'(\tau) d\tau = \sum_{j=0}^{n} \int_{t_{jD}}^{t_{j+1,D}} e^{-u\tau} \dot{f}_{j+1} d\tau = \sum_{j=0}^{n} \dot{f}_{j+1} \int_{t_{jD}}^{t_{j+1,D}} e^{-u\tau} d\tau, \tag{4.2.48}$$

where the second equality in Eq. 4.2.48 follows from the fact that the chord slope is constant in each sub-interval $[t_{jD}, t_{j+1,D}]$. Performing the integration and taking the limit $T \to \infty$, Eq. 4.2.28 becomes

$$\int_0^{\infty} e^{-u\tau} f'(\tau) d\tau \approx \frac{1}{u}\left\{\sum_{j=0}^{n-1} \dot{f}_{j+1}\left[e^{-ut_{jD}} - e^{-ut_{j+1,D}}\right] + \dot{f}_{n+1} e^{-ut_{nD}}\right\}. \tag{4.2.49}$$

Note that to obtain Eq. 4.2.49, the function is extrapolated from $t_{n+1,D}$ to infinity using the last chord slope value as suggested by Ref. 53. Using Eq. 4.2.49 in Eq. 4.2.47 gives

$$\bar{f}(u) = \frac{f(0)}{u} + \frac{1}{u^2}\left\{\sum_{j=0}^{n-1} \dot{f}_{j+1}\left[e^{-ut_{jD}} - e^{-ut_{j+1,D}}\right] + \dot{f}_{n+1} e^{-ut_{nD}}\right\}, \tag{4.2.50}$$

which is the expression obtained by Roumboutsos and Stewart. Eq. 4.2.50 represents the Laplace transform of a function f obtained from a collection of discrete data points using a piecewise linear approximation and it can be applied to pressure and/or flow rate data.

The working equations of Method B for field applications are shown in the following. Using the definition of P_{FCND} given by Eq. 4.2.15, the dimensional form of Eq. 4.1.1 becomes

$$\Delta p(t) = \int_0^t q_{sf}(\tau) \frac{dP^*_{FCN}}{dt}(t-\tau)d\tau, \tag{4.2.51}$$

where the sandface flow rate, q_{sf}, is given by

$$q_{sf}(t) = -(24)C_F \frac{d\Delta p}{dt}. \tag{4.2.52}$$

Taking Laplace transforms of Eqs. 4.2.51 and 4.2.52 and combining the resulting equations as done previously, one obtains

$$\bar{P}_{FCN}(u) = -\left\{ \frac{\overline{\Delta p}(u)}{u(24)C_F[u\overline{\Delta p}(u) - \Delta p(0)]} \right\}, \tag{4.2.53}$$

where $\bar{P}_{FCN}$ denotes the Laplace transform of the constant rate solution and $\overline{\Delta p}$ represents the Laplace transform of the pressure difference $p_i - p_{wf}$. Given the slug test pressure versus time data, the P_{FCN} values in real space are obtained by first evaluating $\overline{\Delta p}$ from Eq. 4.2.50 and then by inverting Eq. 4.2.53 using a numerical inversion algorithm. Note that P_{FCN} values can be generated for any time t of interest and are not restricted to the knots of the time partition, however times greater than t_{n+1} should not be considered.

A comparison of the working equations of Method A (Eqs. 4.2.16 and 4.2.17) and Method B (Eqs. 4.2.53 and 4.2.50) shows that in Method A, the pressure measurements are added to the computation procedure as time increases, whereas in Method B, all the measured data are used at each point in the computation. Note, however, since the Laplace variable u is large when t is small, only the very first terms in the summation of Eq. 4.2.50 have a significant contribution to the $\bar{f}$ value at small times.

4.2.3 Buildup Real Space Deconvolution

In this section, deconvolution schemes for the analysis of DST buildup data are presented. It is important to mention that the approach used here assumes

that buildup flow rate measurements are not available. The proposed schemes consider the buildup period as an extension of the drawdown period so that pressure measurements from both drawdown and buildup are used in the computations.

If the buildup wellbore storage is known (or has been estimated by type curve techniques), we can directly apply the scheme presented in Section 4.2.1 by considering t_D as the total elapsed time since the beginning of the test and $I(p_{wD})$ as the pressure integral over the entire test history, that is,

$$I(p_{wD}) = \int_0^{t_D} p_{wD}(\tau)d\tau = \int_0^{t_{pD}+\Delta t_D} p_{wD}(\tau)d\tau. \tag{4.2.54}$$

In applying Eqs. 4.2.7 and 4.2.8, we need to evaluate the terms

$$\int_{t_{jD}}^{t_{j+1,D}} q_D(t_D-\tau)d\tau = \int_{t_D-t_{j+1,D}}^{t_D-t_{jD}} q_D(\tau)d\tau. \tag{4.2.55}$$

Recall that the flow rate versus time is given by

$$q_D(t_D) = \begin{cases} -C_{FD}\dfrac{dp_{wD}}{dt_D}, & t_D < t_{pD}; \\ -C_{SD}\dfrac{dp_{wD}}{dt_D}, & t_D > t_{pD}, \end{cases} \tag{4.2.56}$$

therefore several cases may arise when the flow rate is integrated over a time partition $[t_{jD}, t_{j+1,D}]$. Using the DST boundary condition given by Eq. 4.2.56, Eq. 4.2.55 gives

$$\int_{t_D-t_{j+1,D}}^{t_D-t_{jD}} q_D(\tau)d\tau =$$

$$\begin{cases} -C_{FD}[p_{wD}(t_D-t_{jD}) - p_{wD}(t_D-t_{j+1,D})], & (t_D-t_{jD}) \le t_{pD}\ ; \\ -C_{SD}[p_{wD}(t_D-t_{jD}) - p_{wD}(t_D-t_{j+1,D})], & (t_D-t_{j+1,D}) \ge t_{pD}\ , \end{cases} \tag{4.2.57}$$

and

$$\int_{t_D-t_{j+1,D}}^{t_D-t_{jD}} q_D(\tau)d\tau = -C_{FD}\left[p_{wD}(t_{pD}) - p_{wD}(t_D-t_{j+1,D})\right] -$$

$$C_{SD}\left[p_{wD}(t_D-t_{jD}) - p_{wD}(t_{pD})\right]; \quad (t_D-t_{j+1,D}) < t_{pD} < (t_D-t_{jD}). \tag{4.2.58}$$

Note that Eqs. 4.2.57 and 4.2.58 apply for all j, $0 \le j \le n$. The stability criteria and the bound for the local and global truncation errors are still given by Eqs. 4.2.22, 4.2.33 and 4.2.37, respectively.

Starting

show that t

given by

where sum 3

and

$$\begin{cases} 24\ C_F \\ 24\ C_S \\ 24\ C_F \\ 24\ C_S \end{cases}$$

for $0 \leq j \leq$

pressure.

In most

known and c

on the early

However, in

above schem

imation is ec

been used pr

As men

drawdown ar

it is common

order to capt

the buildup

step just bef

Eqs. 4.2.22 a

Starting with Eq. 4.2.7 with $p^*_{wcD}(\hat{t}_{j+1,D}) = P_{FCND}(\hat{t}_{j+1,D})$, it is easy to show that the dimensional form of Method A for analysis of DST buildup data is given by

$$P_{FCN}(\hat{t}_{n+1}) = \frac{I(\Delta p) - \text{sum 3}}{\int_{t_n}^{t} q_{sf}(t-\tau)d\tau}, \tag{4.2.59}$$

where sum 3 is defined by

$$\text{sum 3} = \sum_{j=0}^{n-1}\left\{P_{FCN}(\hat{t}_{j+1})\int_{t_j}^{t_{j+1}} q_{sf}(t-\tau)d\tau\right\}, \tag{4.2.60}$$

and

$$\int_{t_j}^{t_{j+1}} q_{sf}(t-\tau)d\tau =$$

$$\begin{cases} 24\ C_F[p_{wf}(t-t_j) - p_{wf}(t-t_{j+1})], & (t-t_j) \leq t_p\ ; \\ 24\ C_S[p_{wf}(t-t_j) - p_{wf}(t-t_{j+1})], & (t-t_{j+1}) \geq t_p\ ; \\ 24\ C_F[p_{wf}(t_p) - p_{wf}(t-t_{j+1})] + & \\ 24\ C_S[p_{wf}(t-t_j) - p_{wf}(t_p)], & (t-t_{j+1}) < t_p < (t-t_j)\ , \end{cases} \tag{4.2.61}$$

for $0 \leq j \leq n$. Note that in Eq. 4.2.61 p_{wf} may represent a drawdown or buildup pressure.

In most DST field applications, the buildup wellbore storage coefficient is unknown and cannot be estimated from the log-log plot (the unit slope line is missing on the early buildup response); see the field examples presented in Chapter III. However, in such cases, the assumption $C_F \gg C_S$ is generally satisfied, and the above scheme can be implemented by setting $C_S = 0$ in Eq. 4.2.61. This approximation is equivalent to neglect afterflow effects on the buildup response and has been used previously in the development of Methods 1 and 2 in Chapter III.

As mentioned previously, the stability criterion for the combined analysis of drawdown and buildup data using Method A is also given by Eq. 4.2.22. Note that it is common practice to increase the data sampling frequency just after shut-in in order to capture the early buildup pressure response. Therefore, the first points in the buildup period will have a time step size substantially smaller than the time step just before shut-in so that the stability criterion might not be satisfied (see Eqs. 4.2.22 and 4.2.23).

An alternative buildup scheme can be built which, in principle, improves the stability of the early buildup data. Consider the partition of interval $[0, t_{pD}]$ correspondent to the drawdown period as

$$0 = t_{0,pD} < t_{1,pD} < \cdots < t_{n,pD} < t_{n+1,pD} = t_{pD}. \tag{4.1.62}$$

For $t_D > t_{pD}$, Eq. 4.2.1 can be written as

$$\int_0^{t_D} p_{wD}(\tau)d\tau =$$

$$\int_0^{t_{pD}} q_D(\tau)\, p^{\bullet}_{wcD}(t_D - \tau)d\tau \; + \int_{t_{pD}}^{t_D} q_D(\tau)\, p^{\bullet}_{wcD}(t_D - \tau)d\tau. \tag{4.2.63}$$

Assuming that $q_D(t_D) = 0$ for $t_D > t_{pD}$ and using the time partition given by Eq. 4.1.62, Eq. 4.2.63 becomes

$$\begin{aligned}\int_0^{t_{pD}+\Delta t_D} p_{wD}(\tau)d\tau &= \int_0^{t_{pD}} q_D(t_{pD} - \tau)\, p^{\bullet}_{wcD}(\tau + \Delta t_D)d\tau \\ &= \sum_{j=0}^{n} \int_{t_{j,pD}}^{t_{j+1,pD}} q_D(t_{pD} - \tau)\, p^{\bullet}_{wcD}(\tau + \Delta t_D)d\tau.\end{aligned} \tag{4.2.64}$$

If $p^{\bullet}_{wcD}$ is a continuously differentiable function, the truncated Taylor series expansion for $p^{\bullet}_{wcD}(\tau + \Delta t_D)$ is given by

$$p^{\bullet}_{wcD}(\tau + \Delta t_D) = p^{\bullet}_{wcD}(\hat{t}_{j+1,pD} + \Delta t_D) - (\hat{t}_{j+1,pD} - \tau)\frac{dp^{\bullet}_{wcD}}{dt_D}(\xi), \tag{4.2.65}$$

where $\hat{t}_{j+1,pD}$ and ξ are given, respectively, by

$$\hat{t}_{j+1,pD} = \theta_{j+1} t_{j+1,pD} + (1 - \theta_{j+1}) t_{j,pD}, \tag{4.2.66}$$

and

$$t_{j,pD} + \Delta t_D \leq \xi \leq t_{j+1,pD} + \Delta t_D. \tag{4.2.67}$$

Substituting Eq. 4.2.65 into Eq. 4.2.64 gives

$$\int_0^{t_{pD}+\Delta t_D} p_{wD}(\tau)d\tau = \sum_{j=0}^{n} \Big\{ p^{\bullet}_{wcD}(\hat{t}_{j+1,pD} + \Delta t_D) \times$$

$$\int_{t_{j,pD}}^{t_{j+1,pD}} q_D(t_{pD}-\tau)d\tau - e_{B,j+1}\Big\}, \tag{4.2.68}$$

where

$$e_{B,j+1} = \int_{t_{j,pD}}^{t_{j+1,pD}} q_D(t_{pD}-\tau)(\hat{t}_{j+1,pD}-\tau)\frac{dp^*_{wcD}}{dt_D}(\xi)d\tau. \tag{4.2.69}$$

Using the pressure integral definition given by Eq. 4.2.54, one can solve Eq. 4.2.68 for $p^*_{wcD}(\hat{t}_{n+1,pD}+\Delta t_D)$

$$p^*_{wcD}(\hat{t}_{n+1,pD}+\Delta t_D) = \frac{I(p_{wD}) - \text{sum } 4 + E_B}{\int_{t_{n,pD}}^{t_{n+1,pD}} q_D(t_{pD}-\tau)d\tau}, \tag{4.2.70}$$

where

$$\text{sum } 4 = \sum_{j=0}^{n-1}\Big\{p^*_{wcD}(\hat{t}_{j+1,pD}+\Delta t_D)\int_{t_{j,pD}}^{t_{j+1,pD}} q_D(t_{pD}-\tau)d\tau\Big\} \tag{4.2.71}$$

and

$$E_B = \sum_{j=0}^{n} e_{B,j+1}. \tag{4.2.72}$$

The buildup deconvolution scheme given by Eqs. 4.2.70 and 4.2.71 is referred throughout as Method A1. Note that the above scheme generates p^*_{wcD} values only for times greater than $\hat{t}_{n+1,pD}$, however, Eq. 4.2.71 requires the evaluation of p^*_{wcD} at $\hat{t}_{j+1,pD}+\Delta t_D < \hat{t}_{n+1,pD}$ for some value of j. Thus, we must first generate the p^*_{wcD} values corresponding to the drawdown period by means of Method A or Method B and then apply Method A1 to the buildup data. In contrast to Method A, the scheme of Eq. 4.2.70 will generally require interpolation for evaluating the $p^*_{wcD}(\hat{t}_{j+1,pD}+\Delta t_D)$ terms. Also note that, the sandface flow rate integrals which appear in the right hand side of Eqs. 4.2.70 and 4.2.71 are given, respectively, by Eq. 4.2.12 and 4.2.11. Evaluation of these terms often requires interpolation.

Stability and Truncation Errors of Method A1

The stability analysis shown here follows the same steps used in the stability analysis of Method A. Suppose that an error ϵ is introduced in some $p^*_{wcD}(\hat{t}_{l+1,pD}+$

Δt_D) value for some l, $0 \le l \le n-1$. If $\tilde{p}^*_{wcD}$ denotes the calculated value of p^*_{wcD}, then from Eqs. 4.2.70 and 4.2.71 one can write

$$\tilde{p}^*_{wcD}(\hat{t}_{n+1,pD} + \Delta t_D) = \frac{I(p_{wD}) + E_B}{\int_{t_{n,pD}}^{t_{n+1,pD}} q_D(t_{pD} - \tau)d\tau} - b_{l+1}\left[p^*_{wcD}(\hat{t}_{l+1,pD} + \Delta t_D) + \epsilon\right]$$

$$- \sum_{\substack{j=0 \\ j \neq l}}^{n-1} \left\{ b_{j+1} p^*_{wcD}(\hat{t}_{j+1,pD} + \Delta t_D) \right\}, \qquad (4.2.73)$$

where b_{j+1} is defined by

$$b_{j+1} = \frac{\int_{t_{j,pD}}^{t_{j+1,pD}} q_D(t_{pD} - \tau)d\tau}{\int_{t_{n,pD}}^{t_{n+1,pD}} q_D(t_{pD} - \tau)d\tau}. \qquad (4.2.74)$$

Subtracting Eq. 4.2.73 from Eq. 4.2.70, the error in the calculated value of $p^*_{wcD}(\hat{t}_{n+1,pD} + \Delta t_D)$ caused by an error ϵ in $p^*_{wcD}(\hat{t}_{l+1,D} + \Delta t_D)$ is given by

$$E = p^*_{wcD}(\hat{t}_{n+1,pD} + \Delta t_D) - \tilde{p}^*_{wcD}(\hat{t}_{n+1,pD} + \Delta t_D) = b_{l+1}\epsilon, \qquad (4.2.75)$$

therefore the Method A1 scheme is stable if and only if

$$|b_{l+1}| \le 1; \qquad 0 \le l \le n-1. \qquad (4.2.76)$$

The flow rates are always positive quantities, therefore, we can write the stability criteria as

$$\int_{t_{n,pD}}^{t_{n+1,pD}} q_D(t_{pD} - \tau)d\tau \ge \int_{t_{l,pD}}^{t_{l+1,pD}} q_D(t_{pD} - \tau)d\tau. \qquad (4.2.77)$$

Note that the stability of the Method A1 is independent of the buildup partition used and depends only on the drawdown time partition. As shown previously, substituting the slug test boundary condition in Eq. 4.2.77, gives

$$1 - p_{wD}(t_{pD} - t_{n,pD}) \ge p_{wD}(t_{pD} - t_{l+1,pD}) - p_{wD}(t_{pD} - t_{l,pD}), \qquad (4.2.78)$$

for $0 \le l \le n-1$. The dimensional form of the above stability condition is given by

$$p_{wf}(t_p - t_{n,p}) \ge p_o + \max_{0 \le l \le n-1} \left\{ p_{wf}(t_p - t_{l,p}) - p_{wf}(t_p - t_{l+1,p}) \right\}. \qquad (4.2.79)$$

Eq. 4.2.77 - 4.2.79 indicate that if the last drawdown point satisfies the stability criteria of Eq. 4.2.28, then the buildup scheme given by Eq. 4.2.70 is stable for any buildup time partition. This represents the major advantage of Method A1 over Method A when performing a deconvolution for buildup data.

Following basic stability analysis procedure presented in Section 4.2.1, one can show that the upper bound for the local and global truncation errors of Method A1 are given, respectively, by

$$|e_{B,j+1}| \leq K_{j+1}(\delta t_{j+1,pD})^2. \tag{4.2.80}$$

and

$$|E_B| \leq K_{max} t_D (\delta t_{pD,max}), \tag{4.2.81}$$

where

$$\delta t_{j+1,pD} = t_{j+1,pD} - t_{j,pD} \tag{4.2.82}$$

and

$$\delta t_{pD,max} = \max_{0 \leq j \leq n} \delta t_{j+1,pD}. \tag{4.2.83}$$

The results of Eqs. 4.2.80 and 4.2.81 indicate that the order of the local truncation error is $O[(\delta t_{j+1,pD})^2]$ whereas the global truncation error is $O(\delta t_{pD,max})$.

Other Numerical Considerations

Here, we present and discuss an important aspect in the implementation of the Method A1. Consider the partition of the buildup time interval $[0, \Delta t_D]$ given by

$$0 = \Delta t_{0,D} < \Delta t_{1,D} < \cdots < \Delta t_{m,D} < \Delta t_{m+1,D} = \Delta t_D. \tag{4.2.84}$$

As mentioned in Ref. 59, it is computationally attractive to choose a buildup partition with increasing time steps since the wellbore pressure increases much faster at short times than at late times. However, the calculation of $p^*_{wcD}(\hat{t}_{n+1,pD} + \Delta t_{m+1,D})$ requires that the p^*_{wcD} terms in Eq. 4.2.71 be evaluated at $\hat{t}_{j+1,pD} + \Delta t_{m+1,D}$, and then, it is possible that for some j, $l \leq j \leq n-1$, the following expression holds

$$\hat{t}_{j+1,pD} + \Delta t_{m+1,D} > \hat{t}_{n+1,pD} + \Delta t_{m,D}, \tag{4.2.85}$$

if $\Delta t_{m+1,D} \gg \Delta t_{m,D}$. Eq. 4.2.85 indicates that all $p^*_{wcD}(\hat{t}_{j+1,pD}+\Delta t_{m+1,D})$ values for $j \geq l$ cannot be determined by interpolation since $p^*_{wcD}(\hat{t}_{n+1,pD}+\Delta t_{m+1,D})$ is not known. Rearranging Eq. 4.2.85, one can see that this problem will always occur whenever

$$\Delta t_{m+1,D} - \Delta t_{m,D} > \hat{t}_{n+1,pD} - \hat{t}_{n,pD}, \tag{4.2.86}$$

that is, whenever the buildup time step size is greater than the last time step of the drawdown partition.

One possibility here is to implement the iterative procedure used by Thompson et al.[51] in the Bostic et al.[49] deconvolution scheme. The procedure proposed here is based on an implicit interpolation idea presented in Ref. 47 which is equally good and simple to implement.

Neglecting the error term $e_{B,j+1}$, the right hand side of Eq. 4.2.68 can be written as

$$\sum_{j=0}^{n}\left\{p^*_{wcD}(\hat{t}_{j+1,pD}+\Delta t_D)\int_{t_{j,pD}}^{t_{j+1,pD}} q_D(t_{pD}-\tau)d\tau\right\} =$$

$$\sum_{j=0}^{l-1}\left\{p^*_{wcD}(\hat{t}_{j+1,pD}+\Delta t_D)\int_{t_{j,pD}}^{t_{j+1,pD}} q_D(t_{pD}-\tau)d\tau\right\}+$$

$$\sum_{j=l}^{n}\left\{p^*_{wcD}(\hat{t}_{j+1,pD}+\Delta t_D)\int_{t_{j,pD}}^{t_{j+1,pD}} q_D(t_{pD}-\tau)d\tau\right\}, \tag{4.2.87}$$

where l is the first point in the drawdown partition which satisfies Eq. 4.2.85. For $l \leq j \leq n-1$, the $p^*_{wcD}(\hat{t}_{j+1,pD}+\Delta t_{m+1,D})$ values are linearly interpolated between $p^*_{wcD}(\hat{t}_{n+1,pD}+\Delta t_{m,D})$ and $p^*_{wcD}(\hat{t}_{n+1,pD}+\Delta t_{m+1,D})$ by the expression

$$p^*_{wcD}(\hat{t}_{j+1,pD}+\Delta t_{m+1,D}) = [1-\chi_{j+1}]p^*_{wcD}(\hat{t}_{n+1,pD}+\Delta t_{m,D})+$$

$$\chi_{j+1}p^*_{wcD}(\hat{t}_{n+1,pD}+\Delta t_{m+1,D}), \tag{4.2.88}$$

where $p^*_{wcD}(\hat{t}_{n+1,pD}+\Delta t_{m,D})$ represents the last value computed p^*_{wcD} value, and χ_{j+1} is defined by

$$\chi_{j+1} = \frac{(\hat{t}_{j+1,pD}+\Delta t_{m+1,D})-(\hat{t}_{n+1,pD}+\Delta t_{m,D})}{(\hat{t}_{n+1,pD}+\Delta t_{m+1,D})-(\hat{t}_{n+1,pD}+\Delta t_{m,D})}, \tag{4.2.89}$$

for $l \leq j \leq n-1$. Using Eq. 4.2.88 in Eq. 4.2.87, gives

$$\sum_{j=0}^{n}\left\{p^{*}_{wcD}(\hat{t}_{j+1,pD}+\Delta t_D)\int_{t_{j,pD}}^{t_{j+1,pD}} q_D(t_{pD}-\tau)d\tau\right\} =$$

$$\sum_{j=0}^{l-1}\left\{p^{*}_{wcD}(\hat{t}_{j+1,pD}+\Delta t_D)\int_{t_{j,pD}}^{t_{j+1,pD}} q_D(t_{pD}-\tau)d\tau\right\}+$$

$$p^{*}_{wcD}(\hat{t}_{n+1,pD}+\Delta t_{m,D})\sum_{j=l}^{n}\left\{[1-\chi_{j+1}]\int_{t_{j,pD}}^{t_{j+1,pD}} q_D(t_{pD}-\tau)d\tau\right\}+$$

$$p^{*}_{wcD}(\hat{t}_{n+1,pD}+\Delta t_D)\sum_{j=l}^{n}\left\{\chi_{j+1}\int_{t_{j,pD}}^{t_{j+1,pD}} q_D(t_{pD}-\tau)d\tau\right\}. \qquad (4.2.90)$$

Using Eq. 4.2.90 in Eq. 4.2.68 and solving for $p^{*}_{wcD}(\hat{t}_{n+1,pD}+\Delta t_{m+1,D})$, gives

$$p^{*}_{wcD}(\hat{t}_{n+1,pD}+\Delta t_D) = \frac{I(p_{wD})-\text{sum } 5+E_B}{\sum_{j=l}^{n}\left\{\chi_{j+1}\int_{t_{j,pD}}^{t_{j+1,pD}} q_D(t_{pD}-\tau)d\tau\right\}}, \qquad (4.2.91)$$

where

$$\text{sum } 5 = \sum_{j=0}^{l-1}\left\{p^{*}_{wcD}(\hat{t}_{j+1,pD}+\Delta t_D)\int_{t_{j,pD}}^{t_{j+1,pD}} q_D(t_{pD}-\tau)d\tau\right\}+$$

$$p^{*}_{wcD}(\hat{t}_{n+1,pD}+\Delta t_{m,D})\sum_{j=l}^{n}\left\{[1-\chi_{j+1}]\int_{t_{j,pD}}^{t_{j+1,pD}} q_D(t_{pD}-\tau)d\tau\right\}. \qquad (4.2.92)$$

Note that Eq. 4.2.92 is completely general and can be applied, in principle, to any variable flow rate problem. For the DST problem, using Eqs. 4.2.11 and 4.2.12, neglecting the error term, E_B, and using the P_{FCND} notation, Eq. 4.2.91 becomes

$$P_{FCND}(\hat{t}_{pD}+\Delta t_D) = \frac{[I(p_{wD})/C_{FD}]-\text{sum } 6}{\sum_{j=l}^{n}\left\{\chi_{j+1}\left[p_{wD}(t_{pD}-t_{j+1,D})-p_{wD}(t_{pD}-t_{j,D})\right]\right\}}, \qquad (4.2.93)$$

where

$$\text{sum } 6 = \sum_{j=0}^{l-1}\left\{P_{FCND}(\hat{t}_{j+1,pD}+\Delta t_D)\left[p_{wD}(t_{pD}-t_{j+1,D})-p_{wD}(t_{pD}-t_{j,D})\right]\right\}+$$

$$P_{FCND}(\hat{t}_{pD}+\Delta t_{m,D})\sum_{j=l}^{n}\Big\{[1-\chi_{j+1}]\,[p_{wD}(t_{pD}-t_{j+1,D})-p_{wD}(t_{pD}-t_{j,D})]\Big\}. \tag{4.2.94}$$

Note that in Eqs. 4.2.93 and 4.2.94 we use the notation $\hat{t}_{pD}$ to denote $\hat{t}_{n+1,pD}$.

Using the dimensionless definitions given previously, the working equations for analyzing field data by Method A1 are given by

$$P_{FCN}(\hat{t}_p+\Delta t)=\frac{[I(\Delta p)/24C_F]-\text{sum 7}}{\sum_{j=l}^{n}\Big\{\chi_{j+1}\,[p_{wf}(t_p-t_{j,p})-p_{wf}(t_p-t_{j+1,p})]\Big\}}, \tag{4.2.95}$$

where $\hat{t}_p=\hat{t}_{n+1,p}$ and sum 7 is given by

$$\text{sum 7}=\sum_{j=0}^{l-1}\Big\{P_{FCN}(\hat{t}_{j+1,p}+\Delta t)\,[p_{wf}(t_p-t_{j,p})-p_{wf}(t_p-t_{j+1,p})]\Big\}+$$

$$P_{FCN}(\hat{t}_p+\Delta t_m)\sum_{j=l}^{n}\Big\{[1-\chi_{j+1}]\,[p_{wf}(t_p-t_{j,p})-p_{wf}(t_p-t_{j+1,p})]\Big\}. \tag{4.2.96}$$

In Eqs. 4.2.95 and 4.2.96, χ_{j+1} is defined as

$$\chi_{j+1}=\frac{(\hat{t}_{j+1,p}+\Delta t_{m+1})-(\hat{t}_p+\Delta t_m)}{(\hat{t}_p+\Delta t_{m+1})-(\hat{t}_p+\Delta t_m)}. \tag{4.2.97}$$

As mentioned by Ref. 47, if the constant rate solution p^*_{wcD} represents a radial flow problem, it would be more appropriate to use a logarithm interpolation instead. In such a case, Eq. 4.2.97 is given by

$$\chi_{j+1}=\frac{\log\{(\hat{t}_{j+1,p}+\Delta t_{m+1})/(\hat{t}_p+\Delta t_m)\}}{\log\{(\hat{t}_p+\Delta t_{m+1})/(\hat{t}_p+\Delta t_m)\}}, \tag{4.2.98}$$

4.2.4 Results

Here, computer generated data is used to verify the performance of the new deconvolution schemes presented in this Chapter. The drawdown and buildup responses considered in this section assume a fully penetrating well in a homogeneous and infinite reservoir, represented by the IBVP given by Eqs. 3.2.17 - 3.2.22. The

dimensionless pressure solutions were obtained from Eq. 2.2.17, for the drawdown (slug test) period, and from Eq. 3.2.26 for the buildup period.

Three cases were chosen to illustrate the effect of skin and wellbore storage on the results obtained by the deconvolution schemes:

Case 1A - $t_{pD} = 10^4; C_{FD} = 10^3; C_{SD} = 10; s = 0.$

Case 2A - $t_{pD} = 10^4; C_{FD} = 10^3; C_{SD} = 10; s = 10.$

Case 3 - $t_{pD} = 10^5; C_{FD} = 10^4; C_{SD} = 10^2; s = 10.$

Note that Cases 1A and 2A were considered previously in the Results section of Chapter III. In this section, p^*_{wcD} is used to denote the constant sandface flow rate dimensionless solution and it is presented in all figures as a solid line. We use the notation P_{FCND} to represent the constant rate solution calculated by the proposed deconvolution schemes and it is shown as circular data points in all figures presented here. In all cases, the drawdown and buildup partitions are chosen such that the stability criteria for Methods A and A1 are always satisfied.

Fig. 4.2.1 presents a comparison for the drawdown period of Case 1A between p^*_{wcD}, shown by the solid line, and the P_{FCND} values, presented as circular data points, obtained by the deconvolution scheme given by Eq. 4.2.13 (Method A) using $C_{FD} = 10^3$ and the p_{wD} values obtained from Eq. 2.2.17. Here, and in all applications of Methods A and A1, the P_{FCND} values are computed with $\theta_{j+1} = 0.5$ for all j (see Eqs. 4.1.4 and 4.2.14). Note that in Fig. 4.2.1 the p^*_{wcD} solution is plotted versus $t_D = t_{n+1,D}$, whereas P_{FCND} is graphed versus $\hat{t}_{n+1,D}$. The results of Fig. 4.2.1 indicates that, with the exception of the two first points, the agreement between solutions is excellent.

Fig. 4.2.2 presents the results for P_{FCND} obtained by Method B for the same Case 1A of Fig. 4.2.1. These values were obtained using the Laplace space deconvolution approach of Eqs. 4.2.41 and 4.2.50. The P_{FCND} values in real space were obtained by inverting the results of Eq. 4.2.41 using the Stehfest algorithm[54]. Note that here, both p^*_{wcD} and P_{FCND} solutions are plotted versus the dimensionless time $t_D = t_{n+1,D}$. As in Fig. 4.2.1, the agreement of the two solutions is excellent except at the first two points.

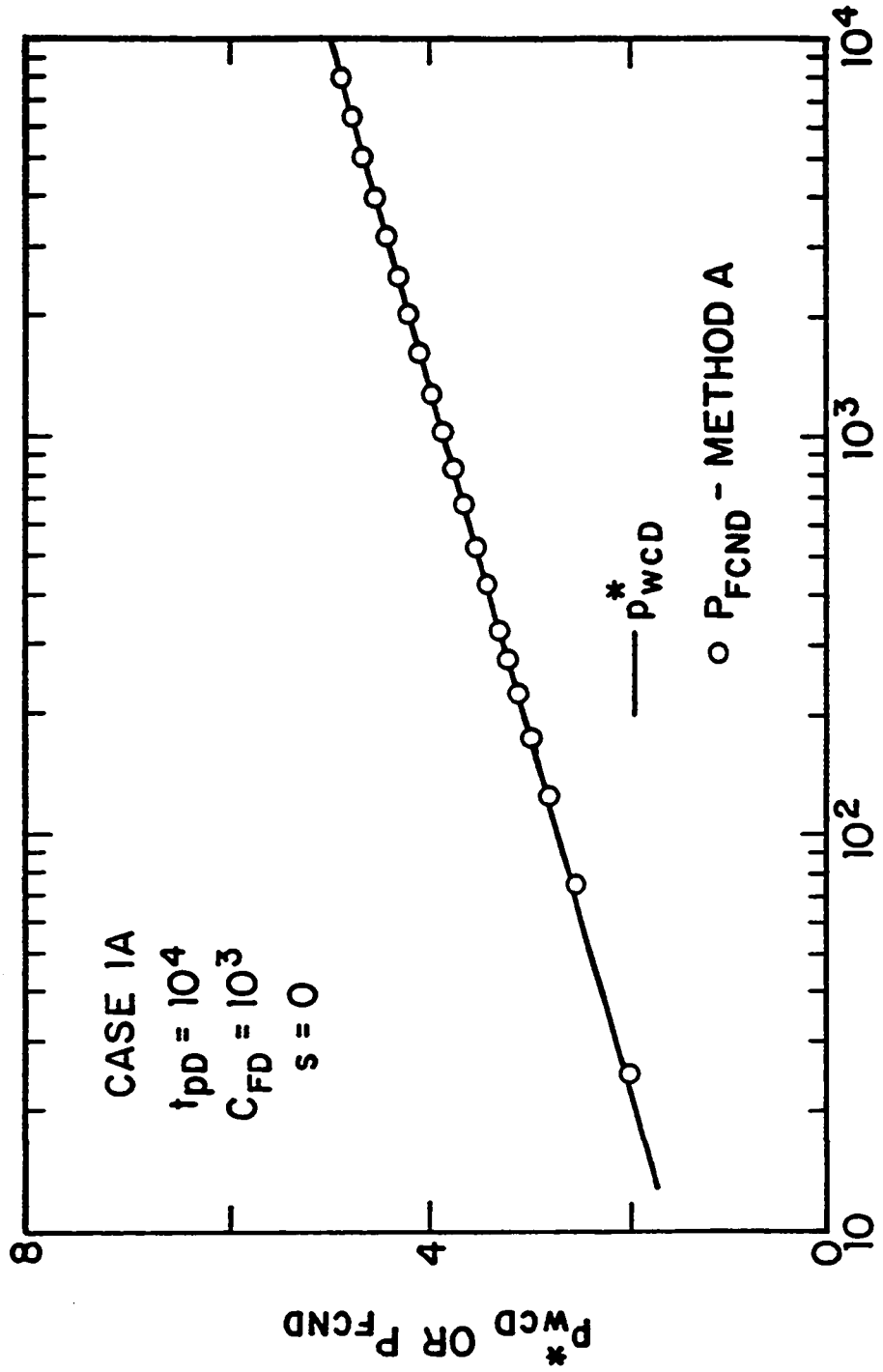

Fig. 4.2.1 - Correlation of deconvolution scheme Method A; Case 1A - flow period.

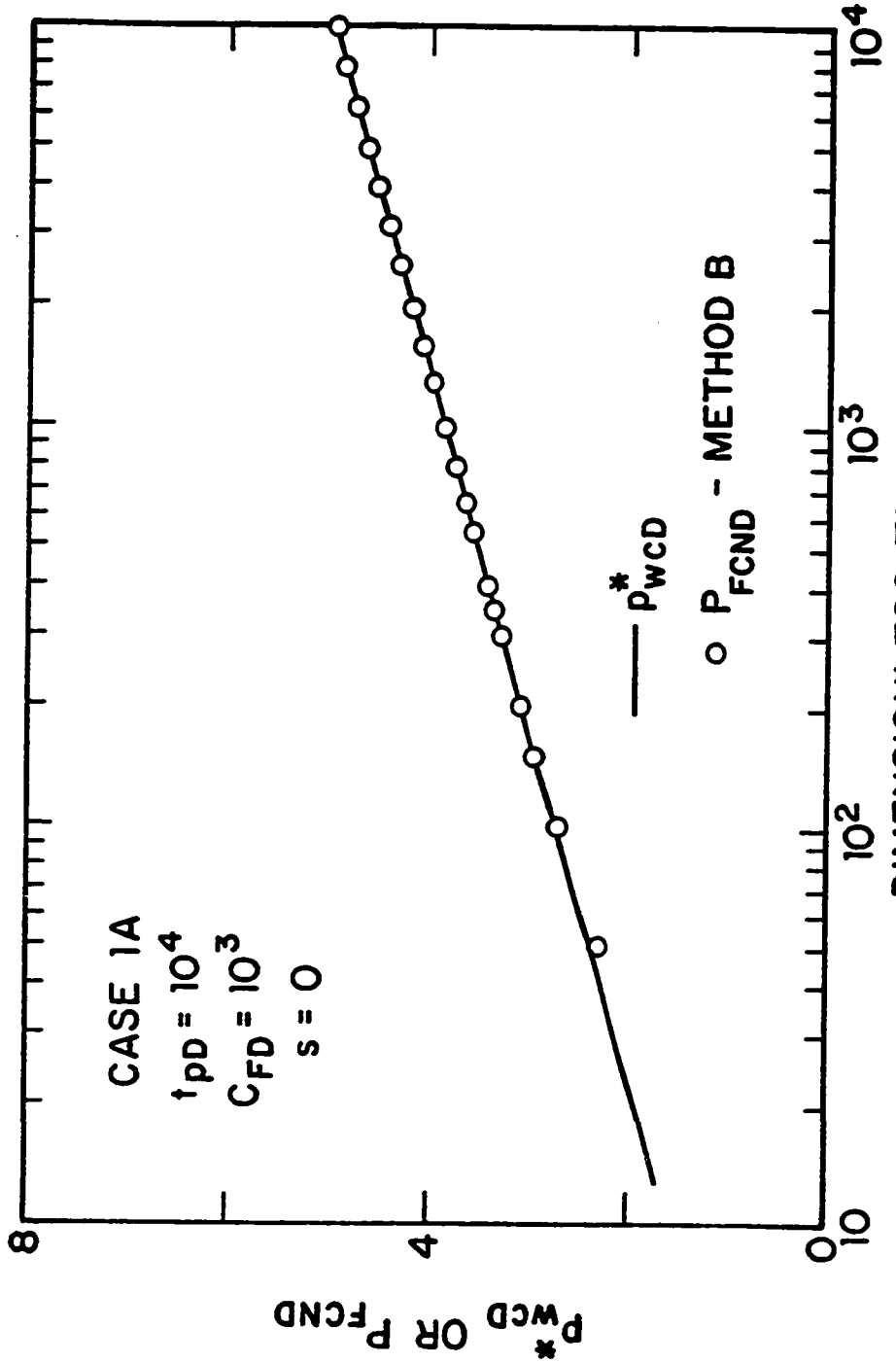

Fig. 4.2.2 - Correlation of deconvolution scheme Method B; Case 1A - flow period.

The application of Method A for the drawdown and buildup periods of Case 1A is presented in Fig. 4.2.3. As discussed previously, Method A considers the buildup period as an extension of the drawdown period, and thus, t_D represents the total elapsed time. In Fig. 4.2.3, the P_{FCND} values correspondent to the buildup period ($t_D > 10^4$) are calculated from Eqs. 4.27, 4.2.8 4.2.57 and 4.2.58, using the actual values of the wellbore storage coefficients, that is, $C_{FD} = 10^3$ and $C_{SD} = 10$. Note that for times less than $t_D = 10^5$, corresponding to $\Delta t_D = 9 \times 10^4$, the buildup P_{FCND} data is in perfect agreement with the p^*_{wcD} solution. However, the P_{FCND} data in the time period $10^5 < t_D < 2 \times 10^5$ is slightly less accurate due to the sudden increase (by a factor of 10) on the time step size at $t_D = 10^5$; see the local truncation error bound, Eq. 4.2.33.

As discussed previously, if an estimate for the buildup wellbore storage coefficient is not available, the computations still can be performed by setting $C_{SD} = 0$ in the equations of Method A. Fig. 4.2.4 presents such computations for Case 1A, and shows that the agreement is quite good; compare with Fig. 4.2.3. Fig. 4.2.5 shows the results of Fig. 4.2.4 correspondent to the buildup portion only, that is, for $t_D > 10^4$. The results shown in Fig. 4.2.5 indicate that the $C_{SD} = 0$ assumption works very well in the present case, especially for $t_D < 10^5$. For times greater than $t_D = 10^5$, the computed values from Method A are shifted slightly above the p^*_{wcD} solution due to the increase in the buildup time step size as discussed previously.

Fig. 4.2.6 presents a semilog plot of P_{FCND} computed from Method A1 (Eq. 4.2.93) for the buildup period of Case 1A. As discussed in section 4.2.3, Method A1 implicitly assumes that $C_{SD} = 0$ and it generates P_{FCND} values for the buildup period only. The P_{FCND} values for $t_D < 10^4$ used in the calculations were obtained from Method A, that is, the results presented in Fig. 4.2.6 were obtained by first applying Method A (Eq. 4.2.13) to the flow period data and then Method A1 was applied to the buildup data. Fig. 4.2.6 shows that the agreement with the constant sandface flow rate solution, p^*_{wcD}, is excellent during the whole span of the buildup period. Note that the increase in the buildup time step size by a factor of 10 at $t_D = 10^5$ does not introduce significant errors in the P_{FCND} computations; compare

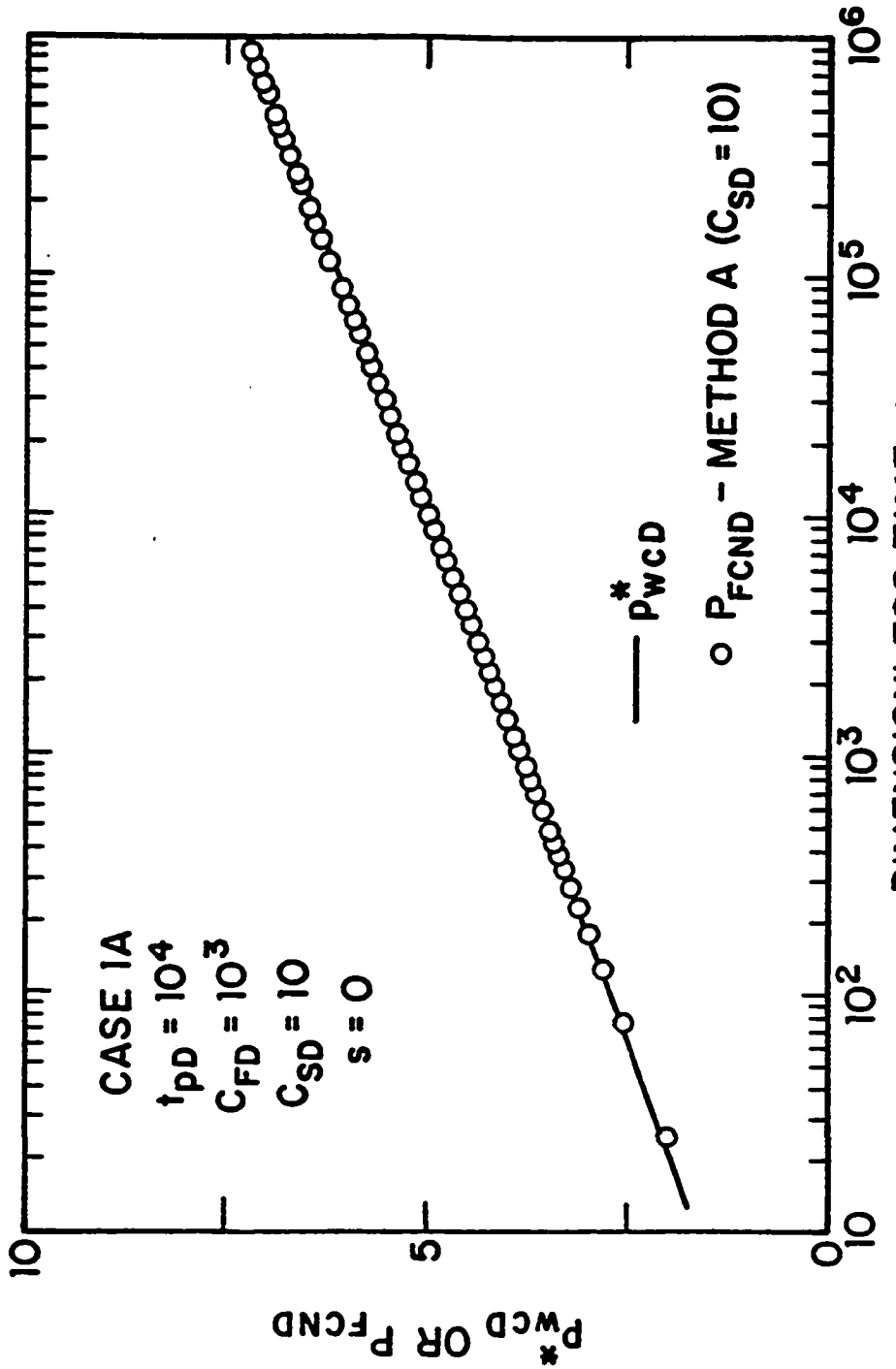

Fig. 4.2.3 - Correlation of deconvolution scheme Method A using $C_{SD} = 10$; Case 1A - flow and buildup periods.

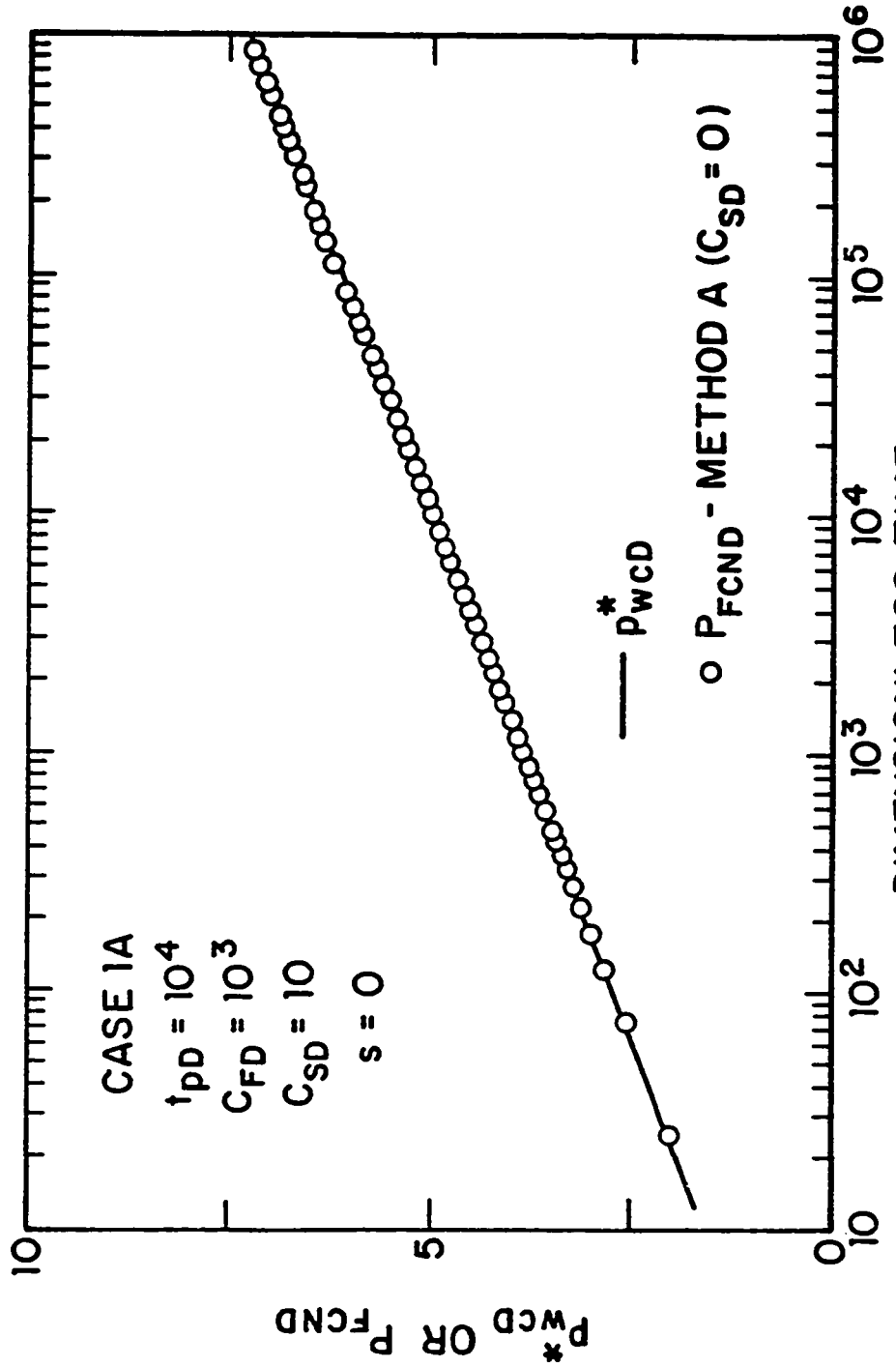

Fig. 4.2.4 - Correlation of deconvolution scheme Method A using $C_{SD} = 0$; Case 1A - flow and buildup periods.

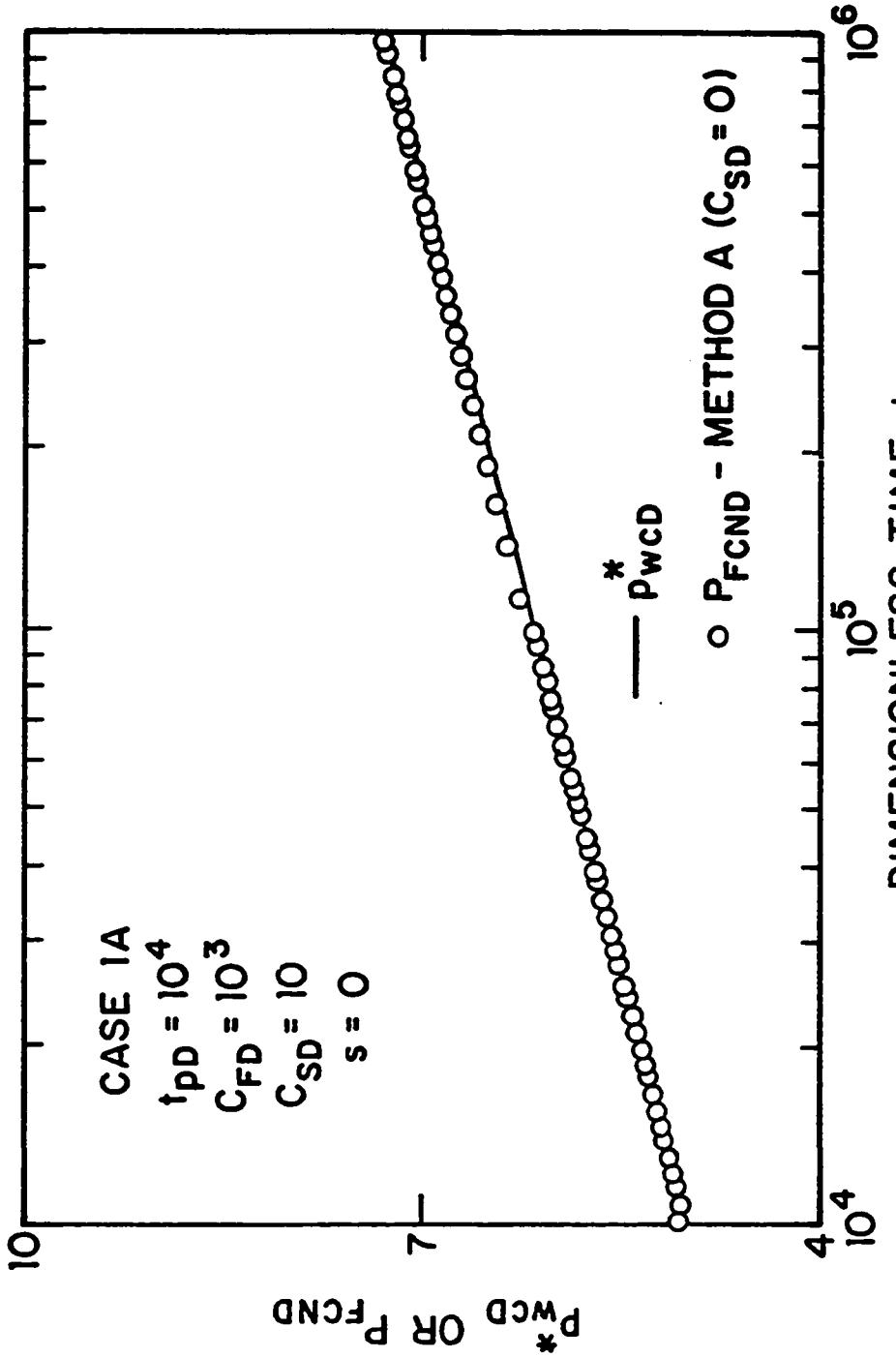

Fig. 4.2.5 - Correlation of deconvolution scheme Method A using $C_{SD} = 0$; Case 1A - buildup period.

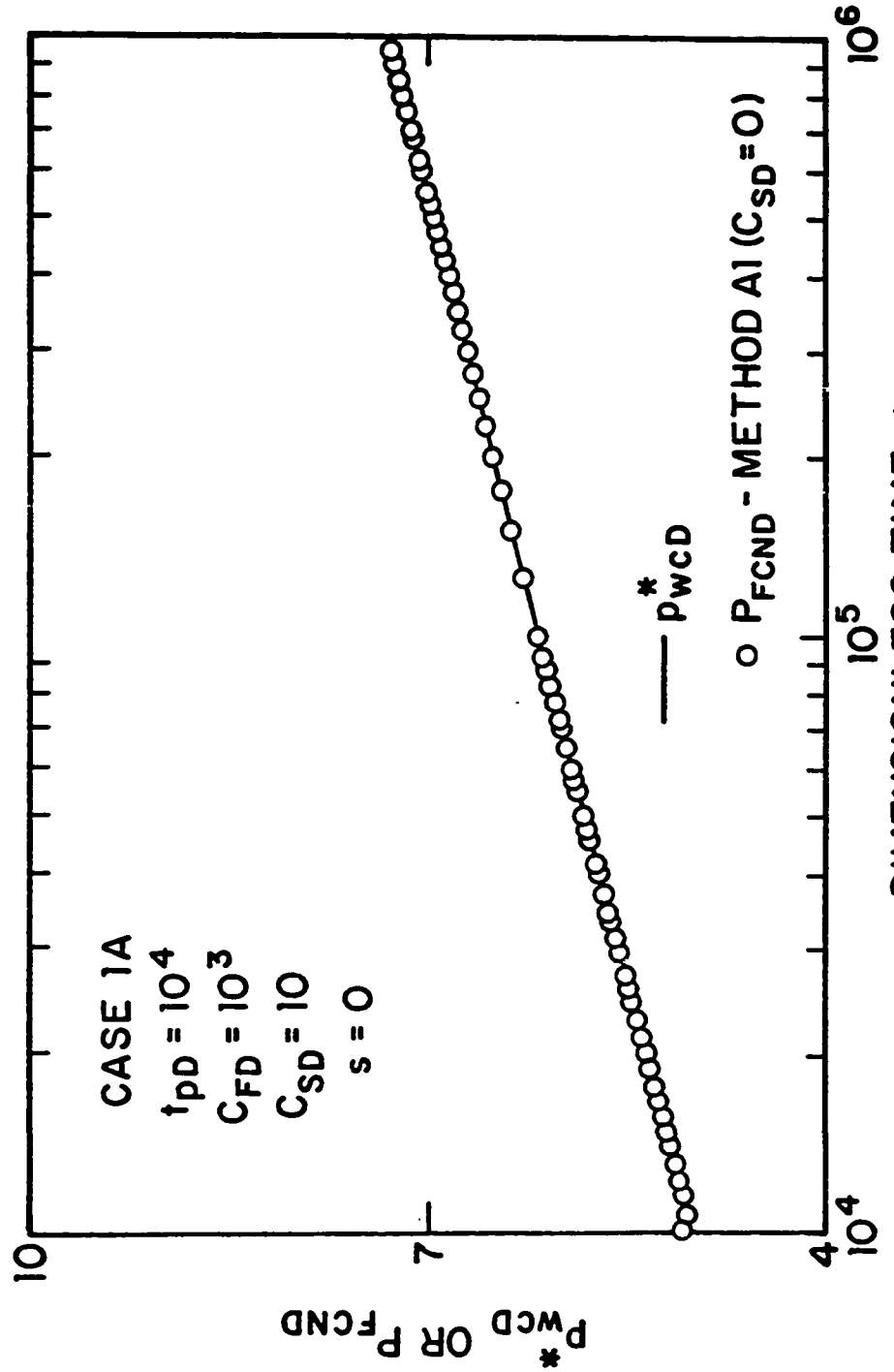

Fig. 4.2.6 - Correlation of deconvolution scheme Method A1; Case 1A - buildup period.

with the results of Method A in Fig. 4.2.5. Note that the local and global truncation errors of Method A depends on both drawdown and buildup time partitions whereas the truncation errors in Method A1 is independent of the buildup time partition.

Fig. 4.2.7 presents a semilog plot of the results obtained by Method A for the flow period of Case 2A. The computed P_{FCND} values correlate extremely well with the constant sandface flow rate solution, except the first point which slightly underestimate the correct value.

The results for the data of Case 2A using the deconvolution procedure of Method B is shown in Fig. 4.2.8. The agreement with the p^*_{wcD} solution is as good as the one obtained by Method A for most of the span of the data. For times approaching the producing time $t_{pD} = 10^4$, the P_{FCND} values computed by Method B becomes less accurate. Moreover, for times greater than $t_D > 8.5 \times 10^3$ the computed values begins to decrease with time. This behavior may be caused by the extrapolation of the pressure data beyond the producing time necessary to obtain an approximation to the pressure drop in Laplace space. As discussed in section 4.2.2, the deconvolution scheme in Laplace space uses all the information of the time interval $[0, \infty]$ in the computation of every single point, however, the P_{FCND} values for times approaching $t_{pD} = 10^4$ are more affected by the extrapolation. This "tail effect" may also be caused by the type of approximation used (i.e., piecewise linear) to convert real space data into Laplace space data and/or insufficient accuracy in the numerical Laplace space inversion. This point needs further investigation.

Fig. 4.2.9 presents the combined results for the drawdown and buildup periods obtained by Method A using $C_{FD} = 10^3$ and $C_{SD} = 10$. As one can see, the results are excellent for the entire span of drawdown and buildup data. In contrast to Case 1A, the buildup time step size was kept under control so that the P_{FCND} values remained accurate throughout the buildup period; compare with Fig. 4.2.3.

The results using $C_{SD} = 0$ in the computations of Method A for Case 2A are shown in Fig. 4.2.10. Fig. 4.2.11 presents the P_{FCND} values pertaining to the the buildup period only. The presence of a high skin factor causes the $C_{SD} = 0$

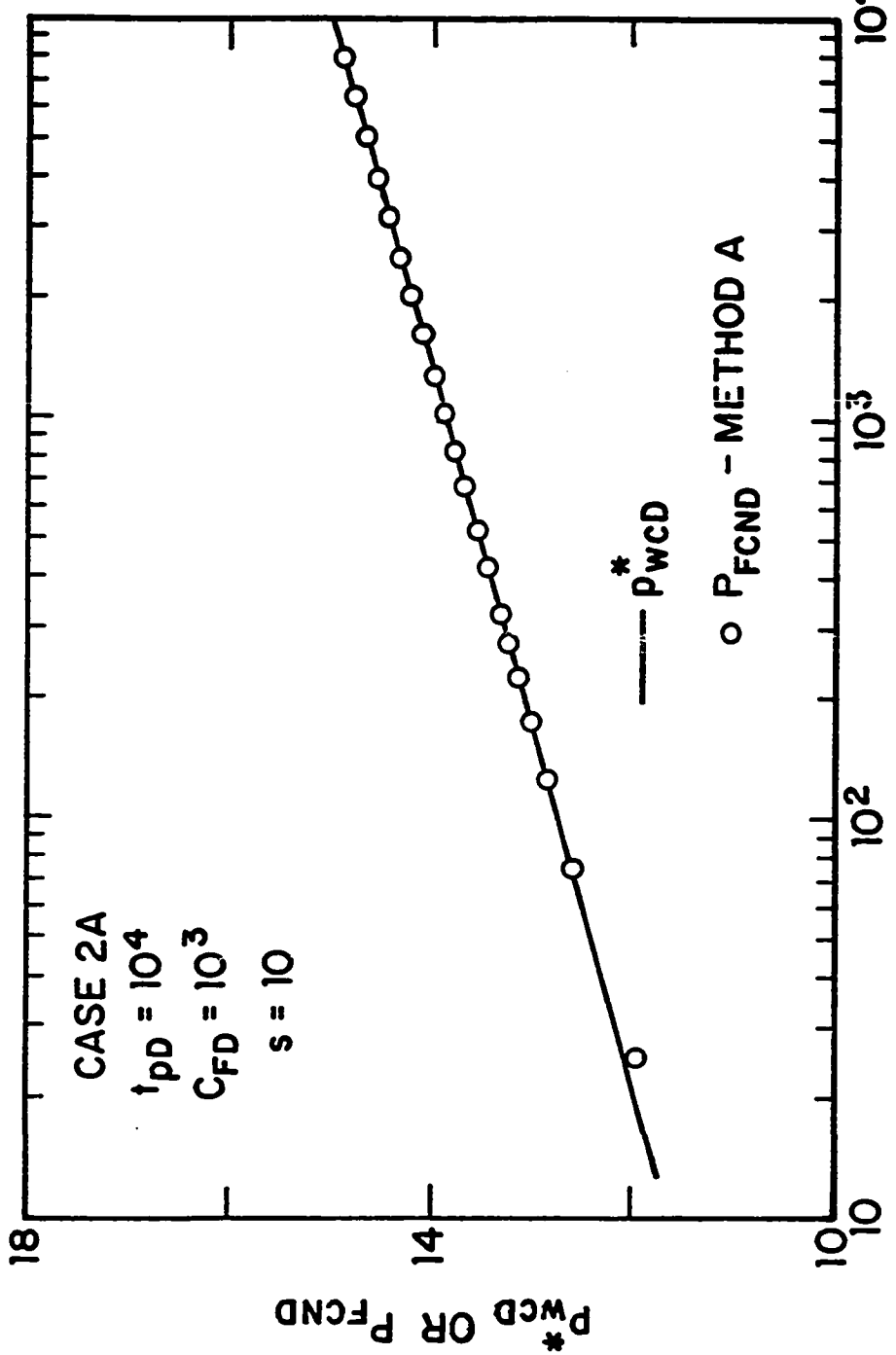

Fig. 4.2.7 - Correlation of deconvolution scheme Method A; Case 2A - flow period.

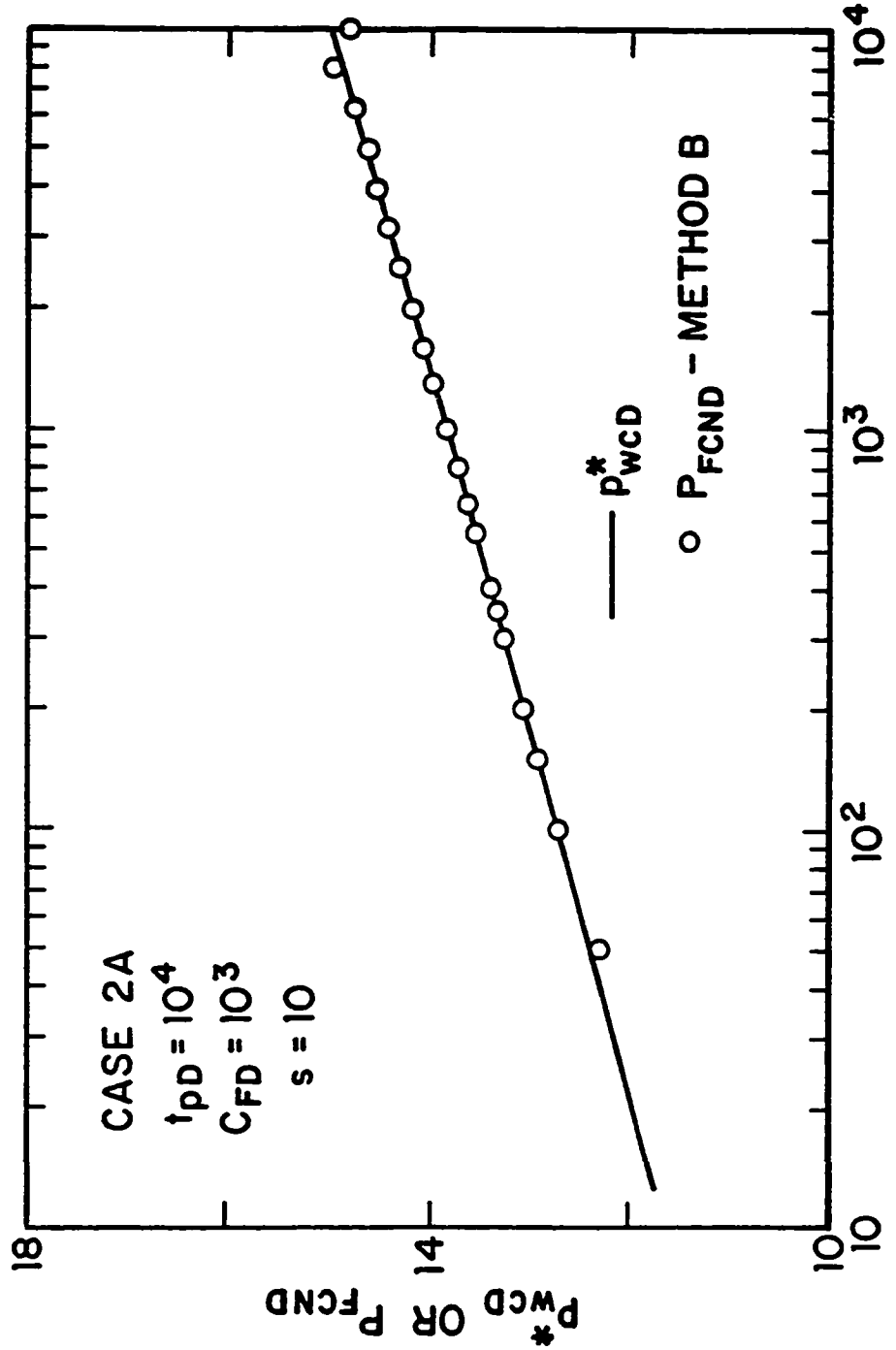

Fig. 4.2.8 - Correlation of deconvolution scheme Method B; Case 2A - flow period.

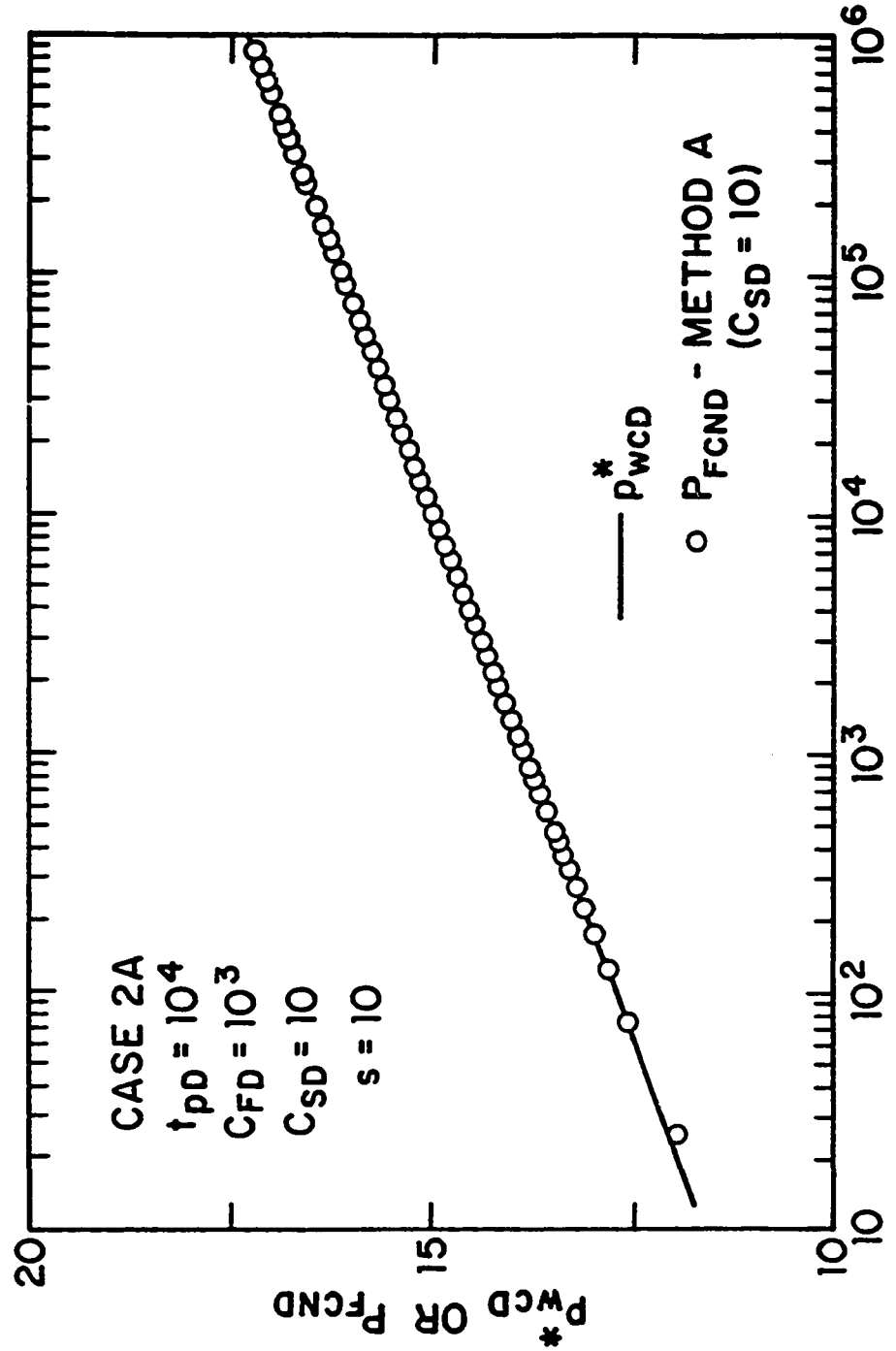

Fig. 4.2.9 - Correlation of deconvolution scheme Method A using $C_{SD} = 10$; Case 2A - flow and buildup periods.

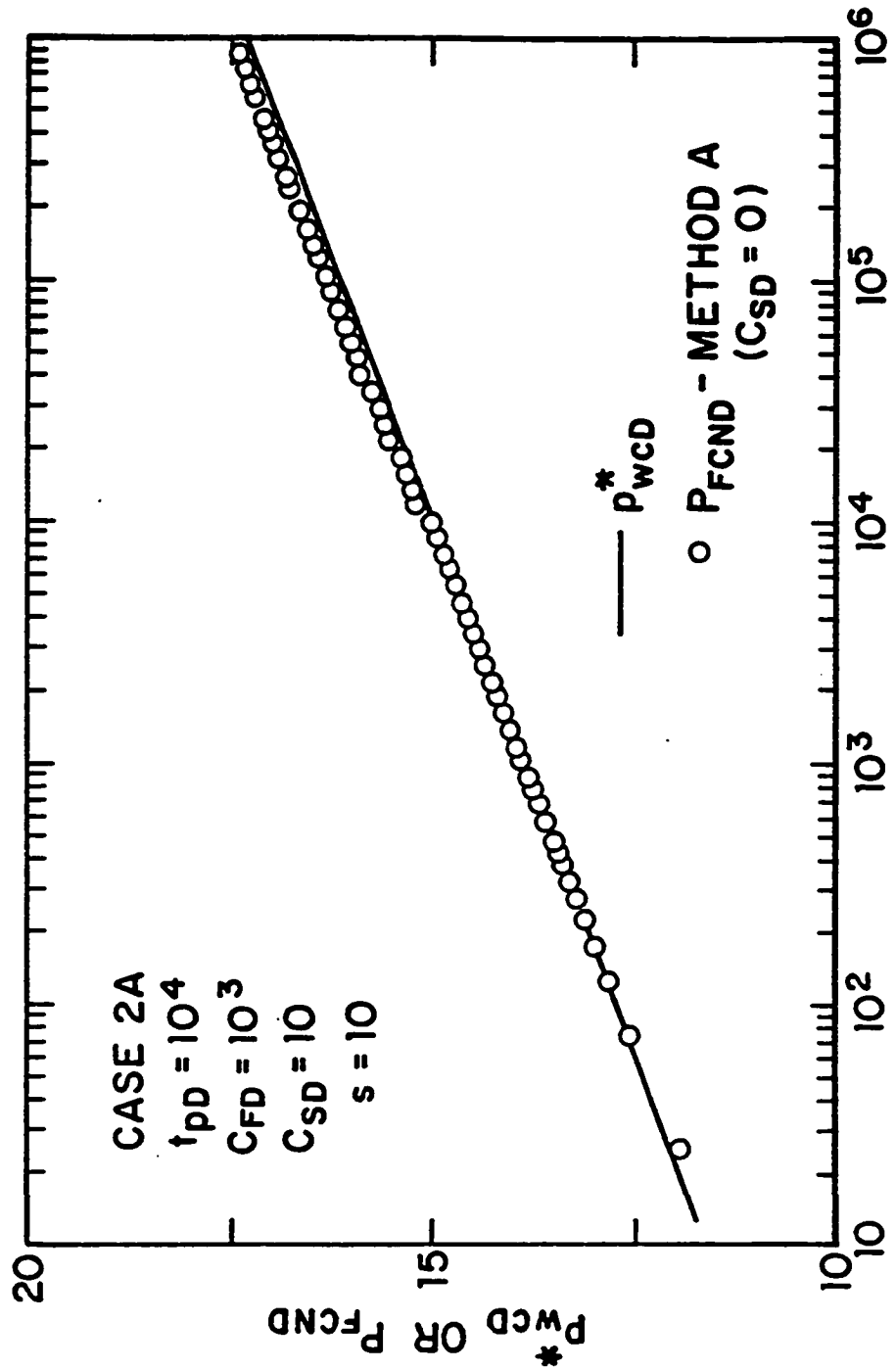

Fig. 4.2.10 - Correlation of deconvolution scheme Method A using $C_{SD} = 0$; Case 2A - flow and buildup periods.

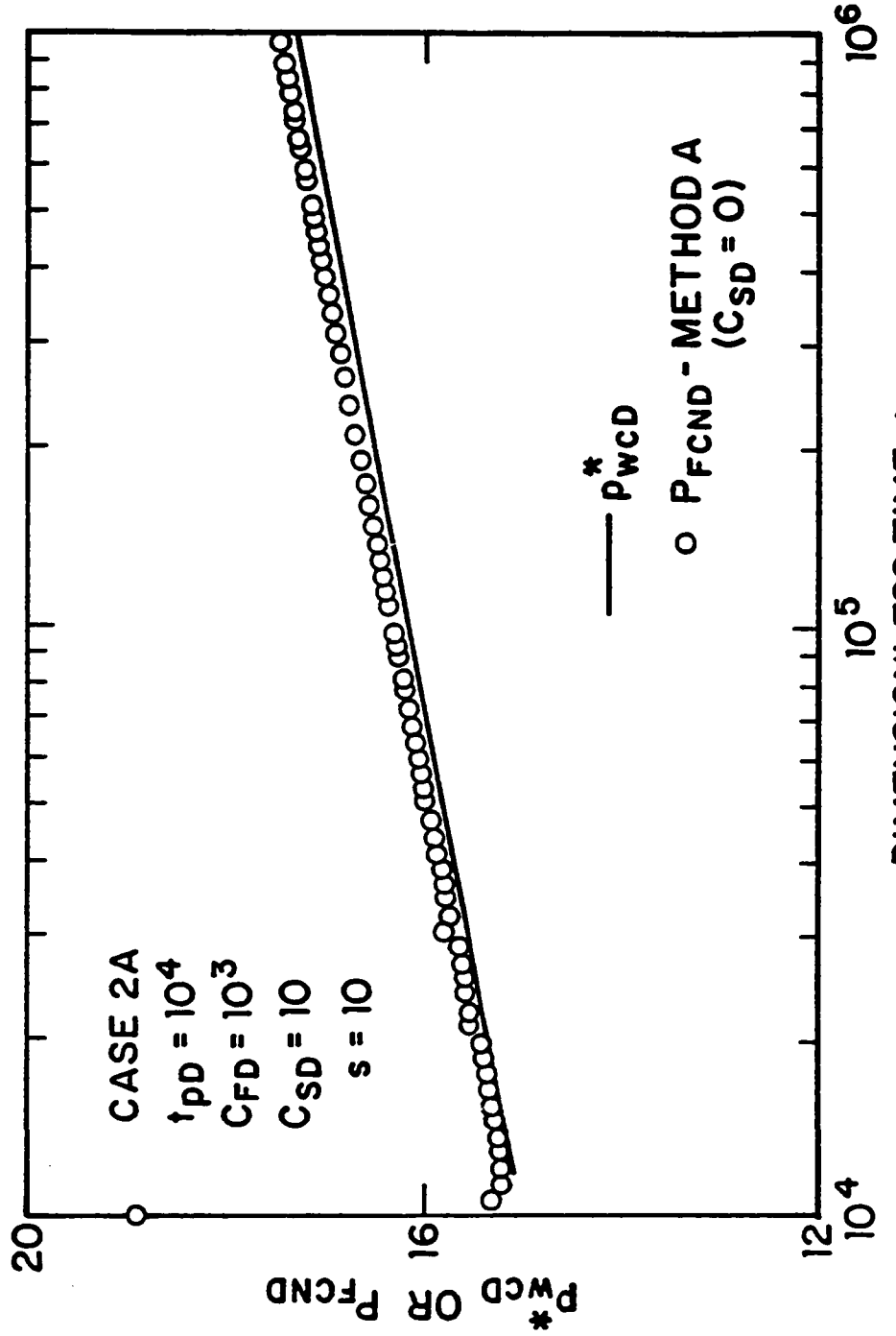

Fig. 4.2.11 - Correlation of deconvolution scheme Method A using $C_{SD} = 0$; Case 2A - buildup period.

approximation to be less accurate than in Case 1A shown before (see Fig. 4.2.5), however, the P_{FCND} values are nearly parallel to the p^*_{wcD} solution and slightly displaced (by approximately 0.18 units) above the correct solution. The results of Fig 4.2.10 indicate that application of the $C_{SD} = 0$ approximation for the buildup data of Case 2A provides the correct flow capacity but a slightly overestimated skin factor.

The results obtained by Method A1 deconvolution scheme for the buildup data of Case 2A are presented in Fig. 4.2.12. As in Case 1A, the buildup computations use drawdown P_{FCND} values obtained by Method A; see related discussion of Fig. 4.2.6. Similar to Method A shown before, the P_{FCND} data is slightly displaced above the correct solution shown by the solid line. Note that the computed data present localized spots of loss in accuracy, in particular at $t_D = 2 \times 10^4$ and $t_D = 3 \times 10^4$, however the overall performance of the scheme is not affected.

Fig. 4.2.13 presents results for the drawdown data of Case 3 using Method A. As in Cases 1A and 2A, the correlation with the constant rate solution is excellent. The application of Method B deconvolution scheme to the same set of data is presented in Fig. 4.2.14, which shows an excellent agreement for times less than $t_D = 4 \times 10^4$. For times greater than this value, the computed values are less accurate and for $t_D > 8.5 \times 10^4$, the calculated P_{FCND} bends downward. This "tail effect" was also seen in the results of Case 2A; see discussion of Fig. 4.2.8.

The combined analysis of drawdown and buildup data by Method A using the correct value of the buildup wellbore storage coefficient is shown in Fig. 4.2.15. Note that only data corresponding to the buildup period is shown here. The buildup P_{FCND} values are less accurate for $t_D > 10^6$ due to an increase in time step size, see Fig. 4.2.3.

The application of Method A using $C_{SD} = 0$ for Case 3 is presented in Fig. 4.2.16 where the P_{FCND} values for both drawdown and buildup data are shown as circular data points. Fig. 4.2.17 shows in more detail the semilog plot for the buildup period and the same features observed in Fig. 4.2.11 (Case 2A) are also present here. Note that a straight line drawn through the P_{FCND} data points for

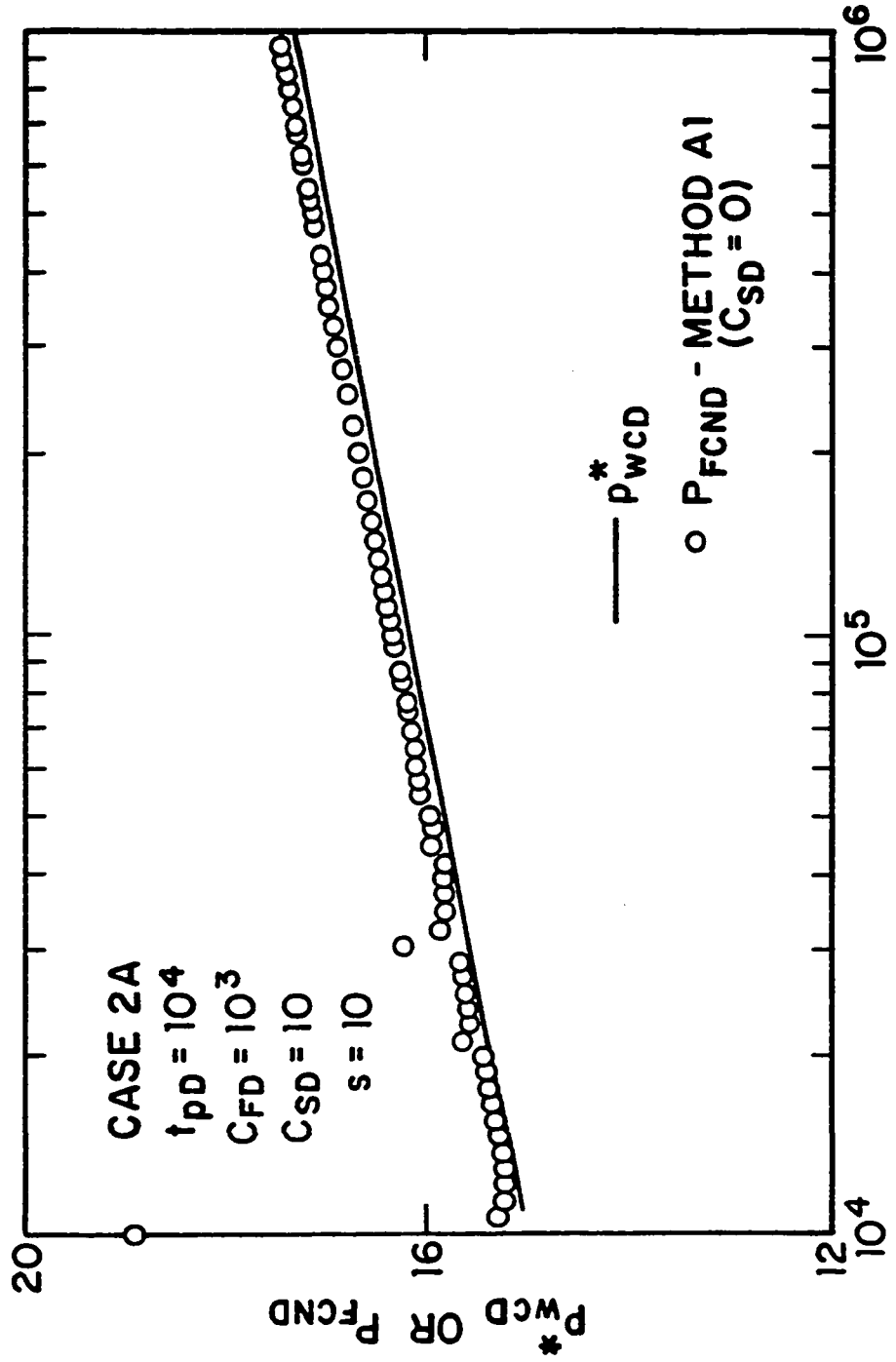

Fig. 4.2.12 - Correlation of deconvolution scheme Method A1; Case 2A - buildup period.

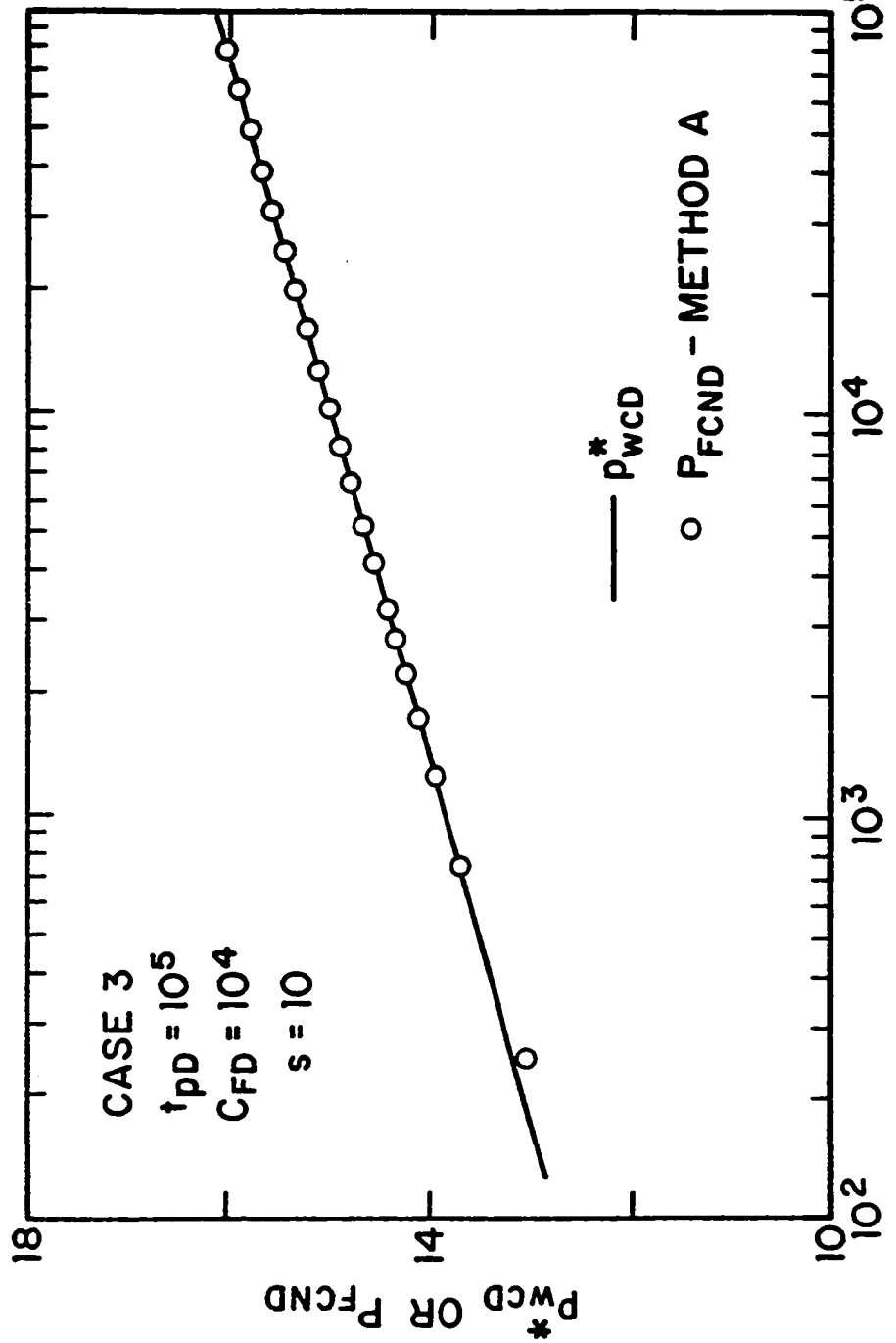

Fig. 4.2.13 - Correlation of deconvolution scheme Method A; Case 3 - flow period.

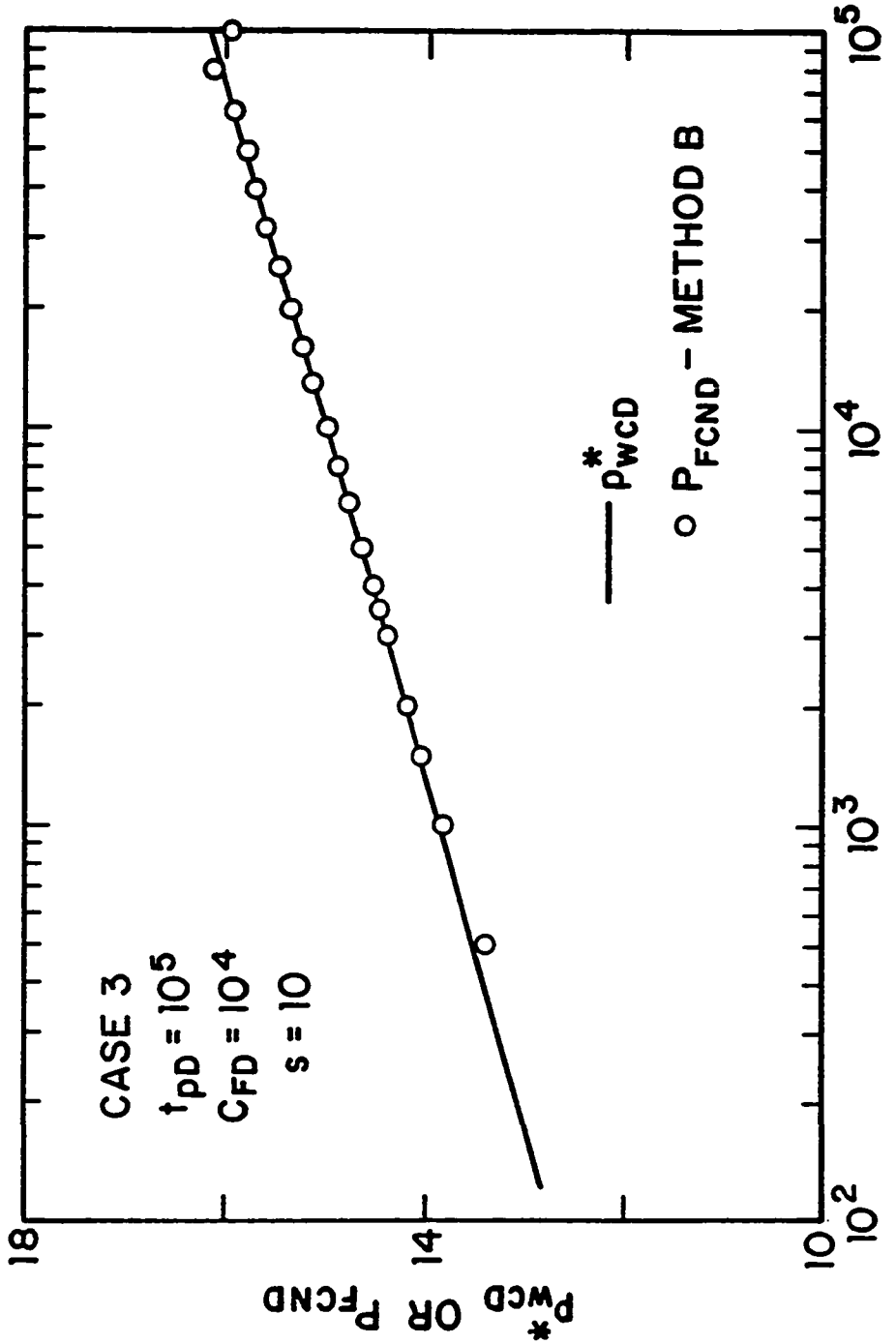

Fig. 4.2.14 - Correlation of deconvolution scheme Method B; Case 3 - flow period.

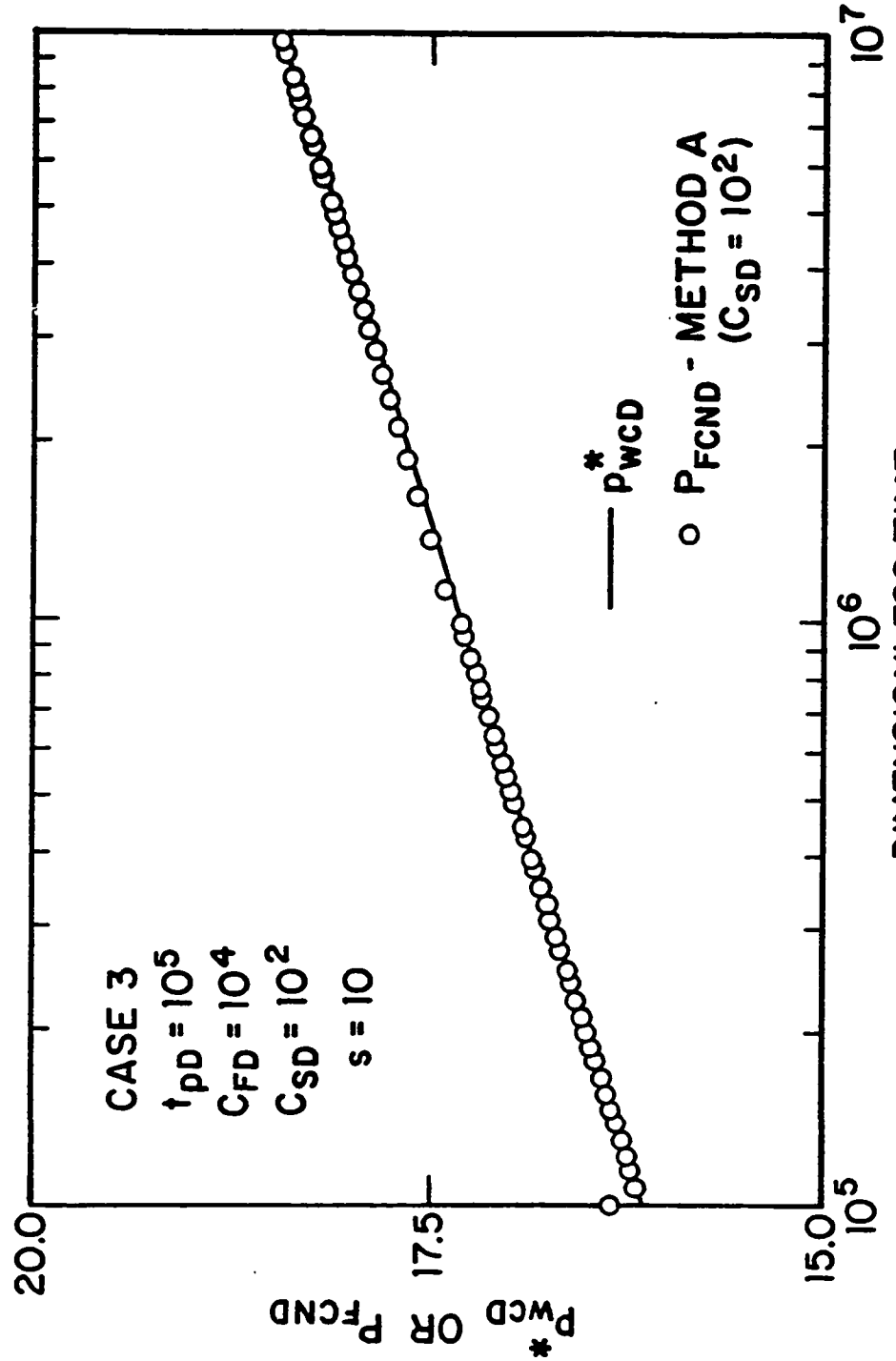

Fig. 4.2.15 - Correlation of deconvolution scheme Method A using $C_{SD} = 10^2$; Case 3 - buildup period.

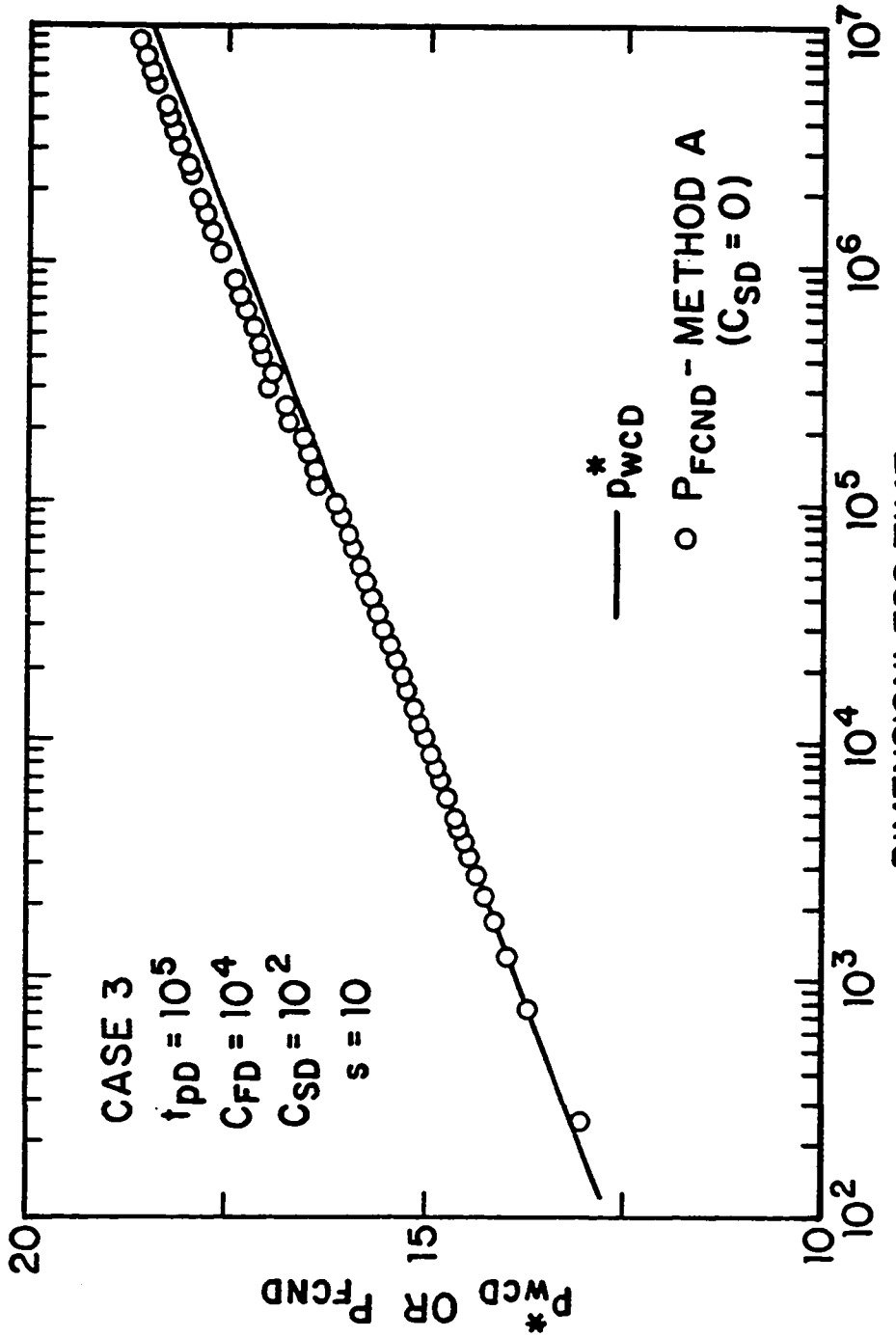

Fig. 4.2.16 - Correlation of deconvolution scheme Method A using $C_{SD} = 0$; Case 3 - flow and buildup periods.

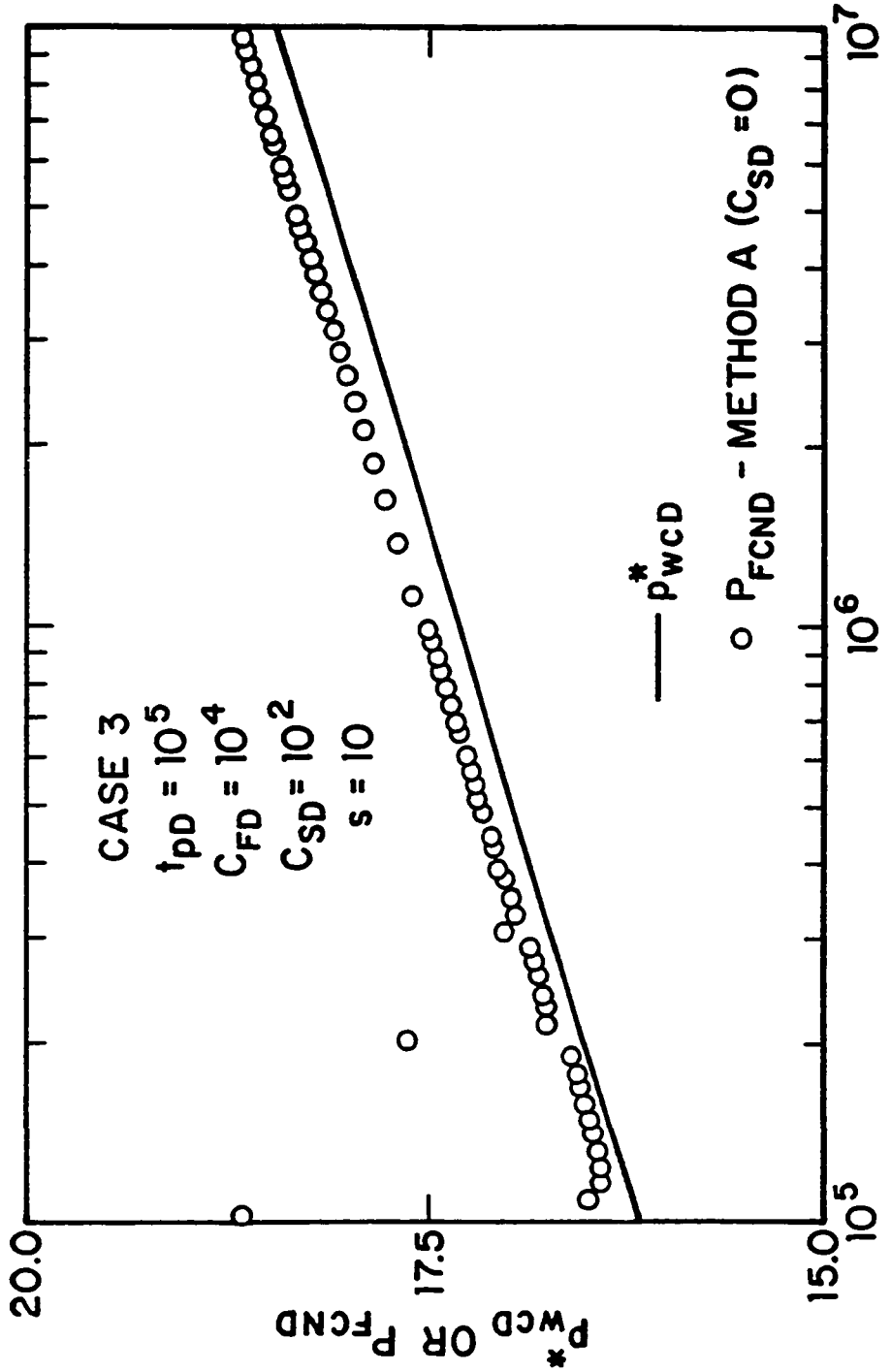

Fig. 4.2.17 - Correlation of deconvolution scheme Method A using $C_{SD} = 0$; Case 3 - buildup period.

$t_D > 2 \times 10^5$ yields a semilog slope slightly greater than the correct 1.151 value and shifted approximately 0.22 units above the correct p^*_{wcD} solution. Similar to the behavior exhibited by Method A1 in Fig. 4.2.12, some points clearly present a loss in accuracy. This behavior is also present in the results obtained from Method A1 shown in Fig. 4.2.18. In Fig. 4.2.18, a sudden error in the computed value of P_{FCND} occurs at $t_D = 2 \times 10^5$, however the subsequent oscillation is damped out as time increases due to the stability of the scheme.

The results of Figs. 4.2.1 - 4.2.18 provide some guidelines for applying the new deconvolution schemes. The P_{FCND} computation for slug test or DST flow data does not present major problems if the analysis is performed using Method A. The Laplace space approach of Method B exhibits a "tail effect", and thus, one should be aware of this behavior when analyzing field data using this deconvolution scheme. If the buildup wellbore storage coefficient can be estimated to some degree of accuracy, the combined analysis of drawdown and buildup data can be performed successfully with Method A when the buildup time step size is not increased too rapidly. If C_{SD} is not known, setting C_{SD} to zero provides a very good approximation for all practical purposes and gives excellent results for non-damaged wells. As shown in Case 2A, truncation errors in Method A1 are independent of the buildup partition, which represents an advantage in terms of field applications. As shown in section 4.2.3 of this Chapter, the stability of this scheme is also independent of the buildup partition used. However, the application for computer generated data indicates that Method A1 tends to yield more oscillatory P_{FCND} values than does Method A.

4.3 Field Applications

In this subsection, we analyze the field examples of Chapters II and III using the new deconvolution schemes presented in this Chapter.

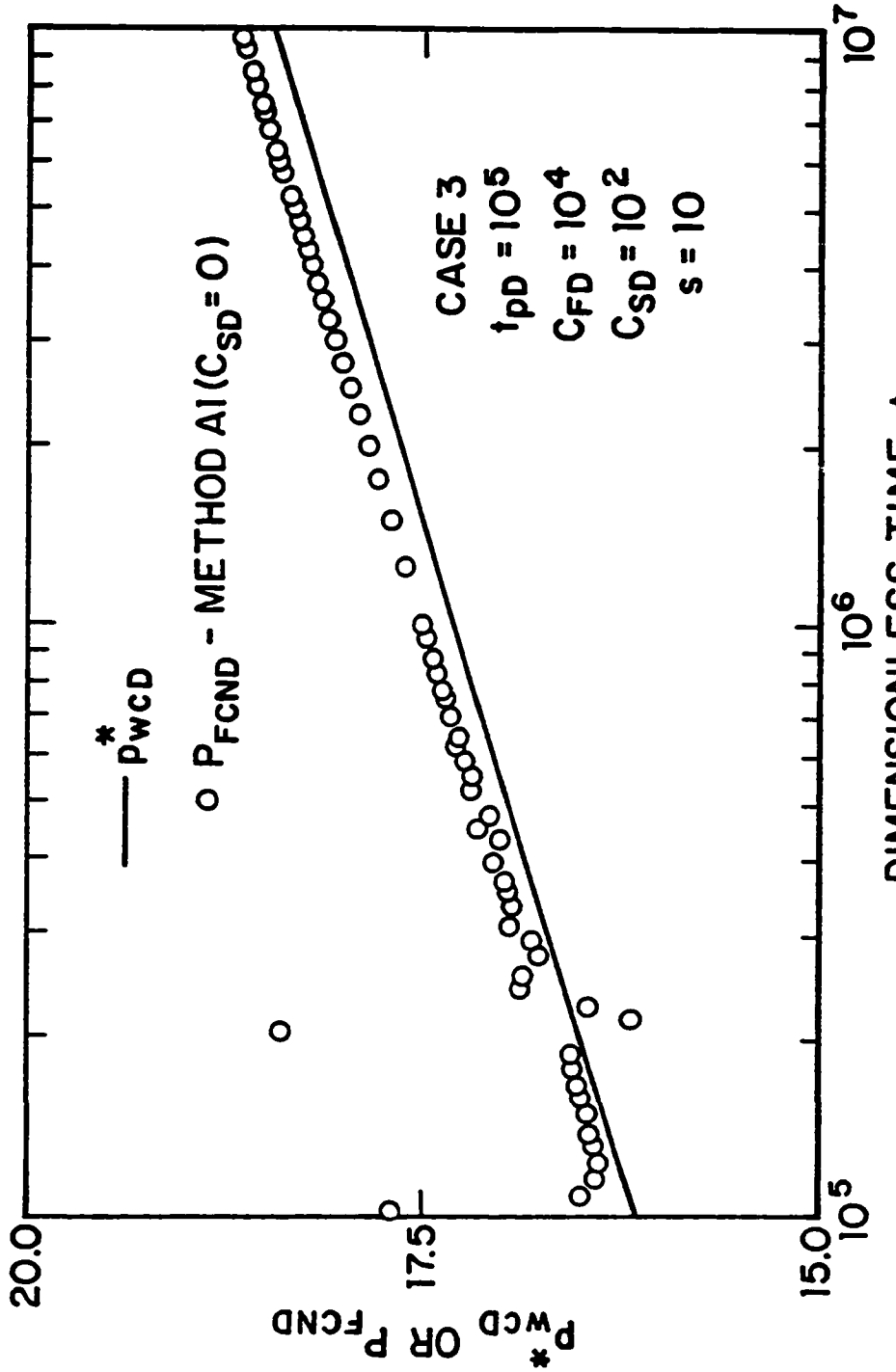

Fig. 4.2.18 - Correlation of deconvolution scheme Method A1; Case 3 - buildup period.

4.3.1 Example A

As explained in section 2.4.1 of Chapter II, this data pertains to a slug test conducted after a perforation run in underbalanced conditions. The measured pressure versus time data as well as other test data were presented in Table 2.4.1. This data will be analyzed here using the deconvolution schemes given by Methods A and B.

Table 4.3.1 presents the P_{FCN} versus time data obtained from the application of Method A; see Eqs. 4.2.16 and 4.2.17. The computations shown in Table 4.3.1 are based on $p_i = 3427.5$ psi and $p_o = 3165$. The integral of the slug test pressure was constructed using the trapezoidal rule as discussed in Chapter II; see section 2.3.4. In Table 4.3.1 we employ the notation $\hat{t}$ to indicate the computed values given by $\hat{t}_{j+1}$ with $\theta_{j+1} = 0.5$; see Eq. 4.1.4. A quick look at Table 2.4.1 indicates that all points (except the one at $t = 2.5$ minutes) satisfies the stability criterion given by Eq. 4.2.26.

Fig. 4.3.1 presents the semilog plot of P_{FCN} versus $\hat{t}$, shown as circular data points. The behavior of the data for times $\hat{t} < 7$ minutes is caused by the oscillation in the measured pressure due to the explosion of the perforating charges. If the data is representative of radial flow geometry, p^*_{wcD} is given by the standard semilog equation and Eq. 4.2.15 becomes

$$\frac{(kh/\mu)}{141.2} P_{FCN}(\hat{t}\,) = 1.151 \log(\hat{t}\,) + \tilde{s}, \tag{4.3.1}$$

where $\tilde{s}$ is given by Eq. 2.3.28. Eq. 4.3.1 suggests that a semilog plot of P_{FCN} versus $\hat{t}$ yields a straight line with slope m given by

$$m = \frac{162.6}{(kh/\mu)}, \tag{4.3.2}$$

where the slope m is in psi/bbl/day.

Returning to Fig. 4.3.1, a well-defined semilog straight line with slope $m =$ 0.835 psi/bbl/day is obtained for the time period $7 < \hat{t} < 40$ minutes. As discussed

Table 4.3.1

Field Example A - Method A

$\hat{t}$ minutes	P_{FCN} psi/bbl/day	$\hat{t}$ minutes	P_{FCN} psi/bbl/day
0.416500E-01	0.1308561E+00	0.775000E+01	0.1861997E+01
0.166650E+00	0.4999240E+00	0.825000E+01	0.1879461E+01
0.333350E+00	0.7531043E+00	0.875000E+01	0.1917931E+01
0.458350E+00	0.7861847E+00	0.925000E+01	0.1922868E+01
0.583350E+00	0.7279130E+00	0.975000E+01	0.1945317E+01
0.708350E+00	0.6508853E+00	0.102500E+02	0.1959839E+01
0.791650E+00	0.7459177E+00	0.107500E+02	0.1968818E+01
0.875000E+00	0.1072303E+01	0.112500E+02	0.1995009E+01
0.958350E+00	0.9352702E+00	0.117500E+02	0.1992858E+01
0.104165E+01	0.1193806E+01	0.122500E+02	0.2025152E+01
0.112500E+01	0.1239113E+01	0.127500E+02	0.2029838E+01
0.120835E+01	0.1136258E+01	0.132500E+02	0.2056770E+01
0.129165E+01	0.1061898E+01	0.137500E+02	0.2075113E+01
0.137500E+01	0.1128110E+01	0.142500E+02	0.2081036E+01
0.145835E+01	0.9380620E+00	0.147500E+02	0.2101368E+01
0.154165E+01	0.1077509E+01	0.152500E+02	0.2085289E+01
0.162500E+01	0.1390777E+01	0.157500E+02	0.2116017E+01
0.170835E+01	0.1162469E+01	0.165000E+02	0.2127068E+01
0.179165E+01	0.1461825E+01	0.175000E+02	0.2149490E+01
0.187500E+01	0.1578678E+01	0.185000E+02	0.2172732E+01
0.195835E+01	0.1303676E+01	0.195000E+02	0.2189598E+01
0.204165E+01	0.1273096E+01	0.205000E+02	0.2207943E+01
0.212500E+01	0.1460402E+01	0.215000E+02	0.2226987E+01
0.220835E+01	0.1063887E+01	0.225000E+02	0.2247846E+01
0.229165E+01	0.1276711E+01	0.235000E+02	0.2254209E+01
0.241665E+01	0.1148545E+01	0.245000E+02	0.2281174E+01
0.254165E+01	0.1511922E+01	0.255000E+02	0.2296064E+01
0.262500E+01	0.1903251E+01	0.265000E+02	0.2309163E+01
0.270835E+01	0.1415028E+01	0.275000E+02	0.2315896E+01
0.279165E+01	0.1717693E+01	0.285000E+02	0.2334017E+01
0.287500E+01	0.1909803E+01	0.295000E+02	0.2341270E+01
0.295835E+01	0.1149301E+01	0.325000E+02	0.2392403E+01
0.325000E+01	0.1211472E+01	0.375000E+02	0.2437358E+01
0.375000E+01	0.1519536E+01	0.425000E+02	0.2476379E+01
0.425000E+01	0.1722780E+01	0.475000E+02	0.2505061E+01
0.500000E+01	0.1815713E+01	0.522500E+02	0.2518016E+01
0.575000E+01	0.1813688E+01	0.570000E+02	0.2533949E+01
0.625000E+01	0.1836218E+01	0.620000E+02	0.2561227E+01
0.675000E+01	0.1820661E+01	0.670000E+02	0.2564765E+01
0.725000E+01	0.1851344E+01	0.720000E+02	0.2576449E+01

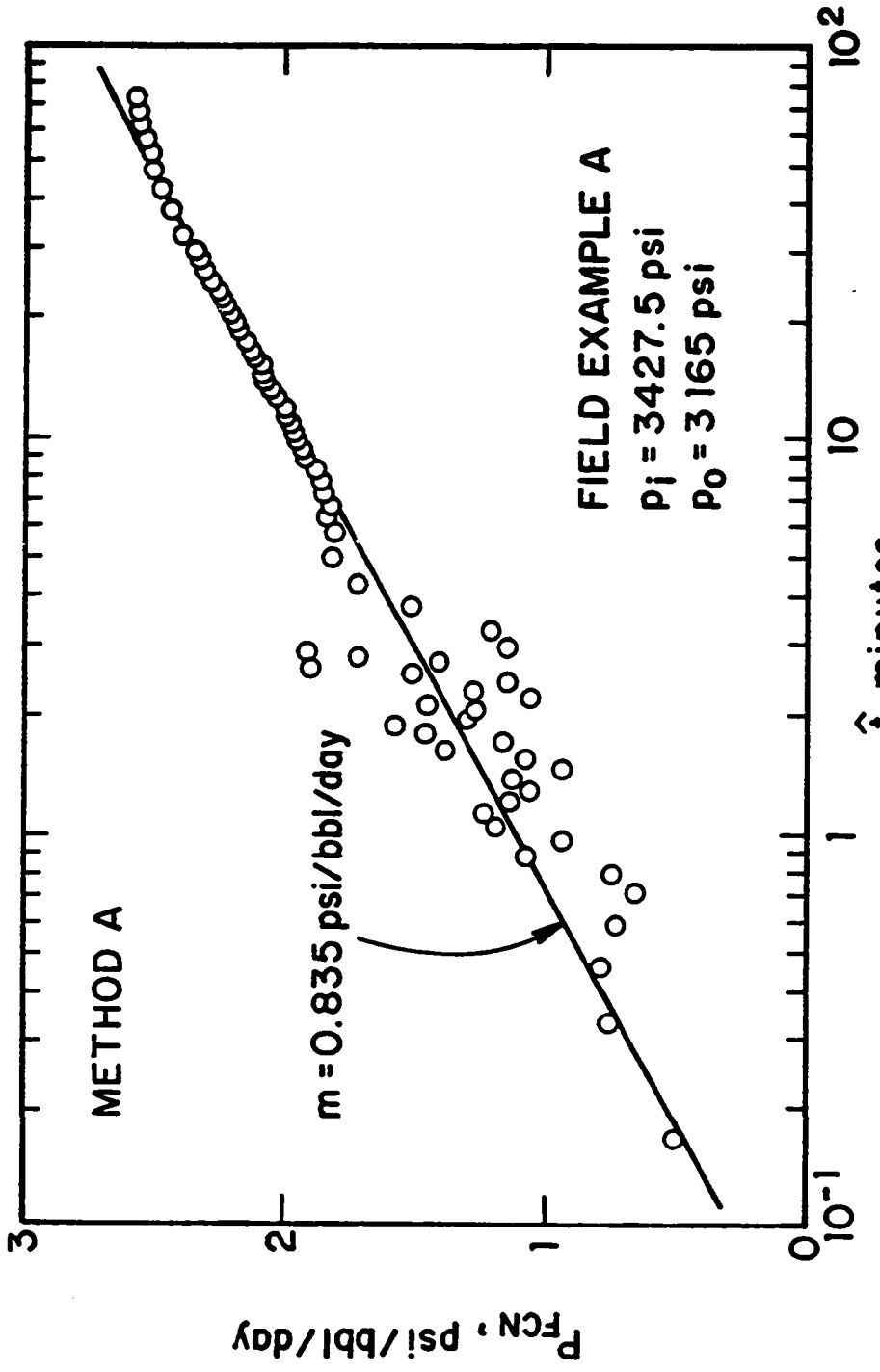

Fig. 4.3.1 - Semilog plot of P_{FCN} computed from Method A; Field Example A.

in Section 2.4.1, at late times the data bends downward because the pressure measurements are not sufficiently accurate; also see Figs. 2.4.4 and 2.4.5. Using the slope value indicated in Fig. 4.3.1, the transmissibility can be estimated by

$$\begin{aligned}\frac{kh}{\mu} &= \frac{162.6}{0.835} \\ &= 194.7 \text{ md-ft/cp},\end{aligned} \tag{4.3.3}$$

which gives $kh = 79.6$ md-ft. An equation for the skin factor can be obtained by rearranging Eq. 4.3.1 and is given by

$$s = 1.151\left\{\frac{P_{FCN}(t^*)}{m} - \log\left(\frac{kt^*}{\phi\mu c_t r_w^2}\right) + 3.23\right\}, \tag{4.3.4}$$

where $[t^*, P_{FCN}(t^*)]$ is any point on the straight line. Selecting the point $t^* = 21.5$ minutes, $P_{FCN}(t^*) = 2.227$ psi/bbl/day on the straight line, the skin factor can be estimated from Eq. 4.3.4 as

$$s = 1.151\left\{\frac{2.227}{0.835} - \log\left(\frac{194.7(21.5/60)}{(0.45)(39.37)(23\times10^{-6})(0.354)^2}\right) + 3.23\right\} = -0.27. \tag{4.3.5}$$

Fig. 4.3.2 shows the application of Method B to the same field data. The circular data points represent the P_{FCN} values shown in Table 4.3.2. As discussed in section 4.2.2, the slug test pressure difference $p_i - p_{wf}$ is converted to Laplace space using the approximation suggested by Ref. 53 and given by Eq. 4.2.50. The P_{FCN} values are obtained from the inversion of Eq. 4.2.53 using Stehfest's algorithm[54]. Note that the noise present in the measured data is substantially reduced by the application of this scheme. In all cases we tried, we noticed that this approach tends to smooth the data, which in principle is good, but one can erroneously interpret such smooth behavior as some kind of reservoir heterogeneity. The behavior of the P_{FCN} data obtained by Method A does not leave any room for misinterpretation; see Fig. 4.2.1. In any case, in Fig. 4.3.2, a semilog straight line through the data points corresponding to the time period $8 < t < 40$ minutes gives a slope $m = 0.839$ psi/bbl/day. Substituting this value in Eq. 4.3.2 and solving for the transmissibility, gives

$$\begin{aligned}\frac{kh}{\mu} &= \frac{162.6}{0.839} \\ &= 193.8 \text{ md-ft/cp},\end{aligned} \tag{4.3.6}$$

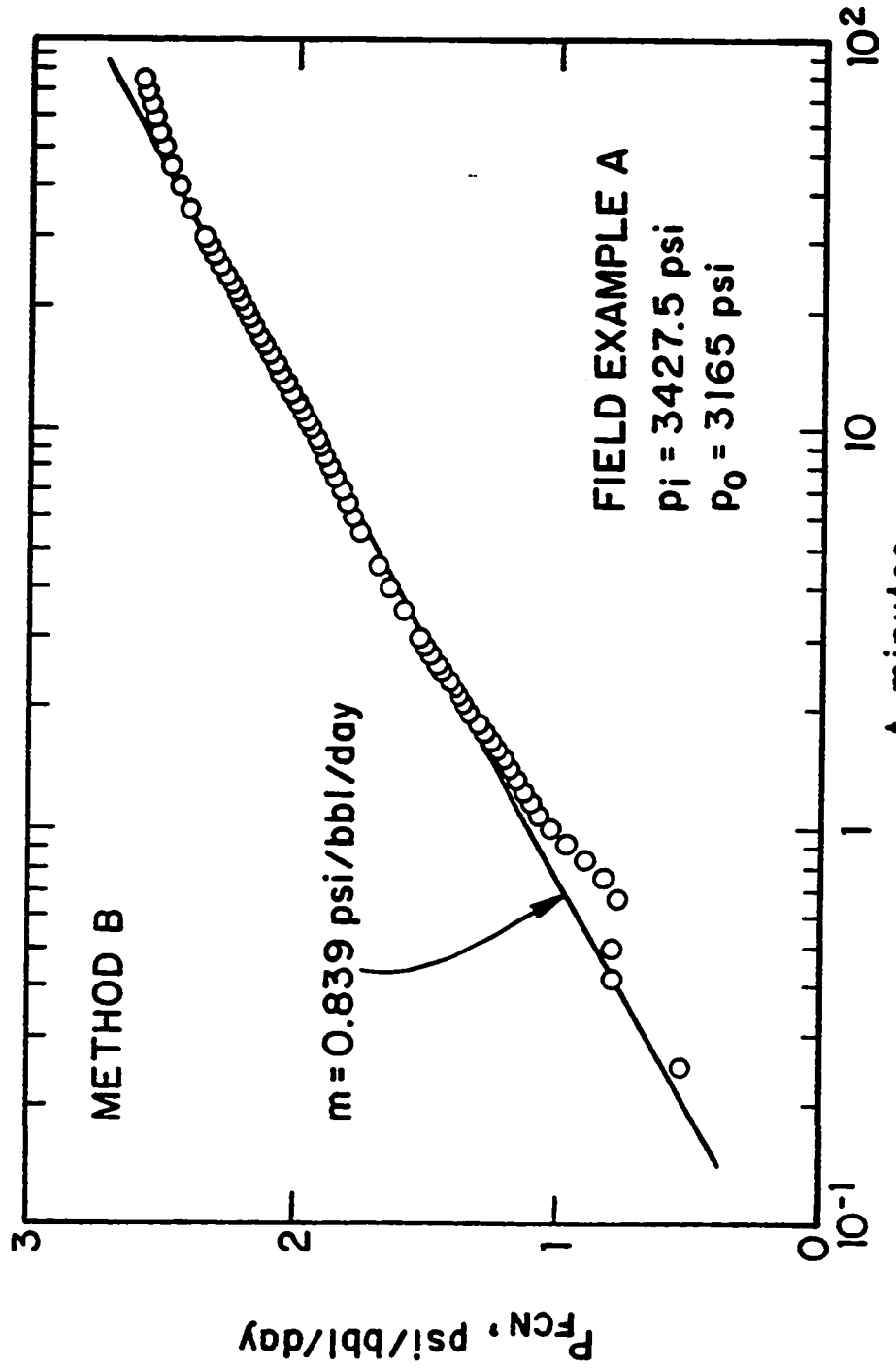

Fig. 4.3.2 - Semilog plot of P_{FCN} computed from Method B; Field Example A.

Table 4.3.2

Field Example A - Method B

t minutes	P_{FCN} psi/bbl/day	t minutes	P_{FCN} psi/bbl/day
0.83300E-01	0.21206E+00	0.80000E+01	0.18758E+01
0.25000E+00	0.54064E+00	0.85000E+01	0.18951E+01
0.41670E+00	0.79792E+00	0.90000E+01	0.19138E+01
0.50000E+00	0.80203E+00	0.95000E+01	0.19319E+01
0.66670E+00	0.77899E+00	0.10000E+02	0.19495E+01
0.75000E+00	0.82924E+00	0.10500E+02	0.19664E+01
0.83330E+00	0.90058E+00	0.11000E+02	0.19828E+01
0.91670E+00	0.96959E+00	0.11500E+02	0.19986E+01
0.10000E+01	0.10256E+01	0.12000E+02	0.20139E+01
0.10833E+01	0.10684E+01	0.12500E+02	0.20285E+01
0.11667E+01	0.11019E+01	0.13000E+02	0.20427E+01
0.12500E+01	0.11301E+01	0.13500E+02	0.20563E+01
0.13333E+01	0.11561E+01	0.14000E+02	0.20695E+01
0.14167E+01	0.11813E+01	0.14500E+02	0.20822E+01
0.15000E+01	0.12064E+01	0.15000E+02	0.20945E+01
0.15833E+01	0.12314E+01	0.15500E+02	0.21064E+01
0.16667E+01	0.12561E+01	0.16000E+02	0.21179E+01
0.17500E+01	0.12803E+01	0.17000E+02	0.21400E+01
0.18333E+01	0.13036E+01	0.18000E+02	0.21608E+01
0.19167E+01	0.13260E+01	0.19000E+02	0.21806E+01
0.20000E+01	0.13472E+01	0.20000E+02	0.21995E+01
0.20833E+01	0.13673E+01	0.21000E+02	0.22175E+01
0.21667E+01	0.13862E+01	0.22000E+02	0.22348E+01
0.22500E+01	0.14040E+01	0.23000E+02	0.22514E+01
0.23333E+01	0.14208E+01	0.24000E+02	0.22674E+01
0.25000E+01	0.14516E+01	0.25000E+02	0.22829E+01
0.25833E+01	0.14657E+01	0.26000E+02	0.22979E+01
0.26667E+01	0.14793E+01	0.27000E+02	0.23124E+01
0.27500E+01	0.14922E+01	0.28000E+02	0.23263E+01
0.28333E+01	0.15046E+01	0.29000E+02	0.23398E+01
0.29167E+01	0.15165E+01	0.30000E+02	0.23527E+01
0.30000E+01	0.15281E+01	0.35000E+02	0.24095E+01
0.35000E+01	0.15909E+01	0.40000E+02	0.24533E+01
0.40000E+01	0.16447E+01	0.45000E+02	0.24858E+01
0.45000E+01	0.16902E+01	0.50000E+02	0.25098E+01
0.55000E+01	0.17603E+01	0.54500E+02	0.25268E+01
0.60000E+01	0.17879E+01	0.59500E+02	0.25428E+01
0.65000E+01	0.18124E+01	0.64500E+02	0.25578E+01
0.70000E+01	0.18348E+01	0.69500E+02	0.25728E+01
0.75000E+01	0.18558E+01	0.74500E+02	0.25884E+01

which yields kh = 79.3 md-ft. At t^* = 21 minutes, the correspondent value of $P_{FCN}(t^*)$ on the straight line is 2.218 psi/bbl/day. Using these values in the the skin equation, one obtains

$$s = 1.151\left\{\frac{2.218}{0.839} - \log\left(\frac{193.8(21/60)}{(0.45)(39.37)(23\times 10^{-6})(0.354)^2}\right) + 3.23\right\} = -0.29. \tag{4.3.7}$$

The transmissibility and skin values calculated from Methods A and B are in excellent agreement with results obtained in Chapter II; compare with the results presented in Table 2.4.2.

4.3.2 Example B

The field data considered here pertains to a DST operation reported by Ref. 44. The measured pressure versus time data for the drawdown and buildup periods are shown in Tables 2.4.3 and 3.4.3, respectively. We begin by analyzing the flow period data.

Fig. 4.3.3 presents the application of the deconvolution scheme given by Eqs. 4.2.16 and 4.2.17 (Method A) using $\theta_{j+1} = 0.5$ for all points. Note that the data in Fig. 4.3.3 pertains to the flow period only. The P_{FCN} values presented in Table 4.3.3 are based on p_i = 892 psi and p_o = 142.4 psi. It is important to mention that, as one can see in Table 2.4.3, the time step size is reduced from the initial 0.022 hours value to approximately 0.008 hours, therefore the stability criterion given by Eq. 4.2.26 is not satisfied. Actually, based on the more rigorous criterion of Eq. 4.2.28, the scheme stability is not satisfied for the computation of the first five P_{FCN} values. Using linear interpolation, more points were added in the time interval [0,0.022] in order to satisfy the stability condition and the P_{FCN} computations were repeated. The results obtained were practically the same, and thus, the results shown in Fig. 4.3.3 are not affected by errors introduced in computing the P_{FCN} values of the first points.

A good semilog straight line with slope m = 0.298 psi/bbl/day is shown in Fig. 4.3.3. From Eq. 4.3.2, the transmissibility is given by

$$\frac{kh}{\mu} = \frac{162.6}{0.298} = 546 \text{ md-ft/cp}, \tag{4.3.8}$$

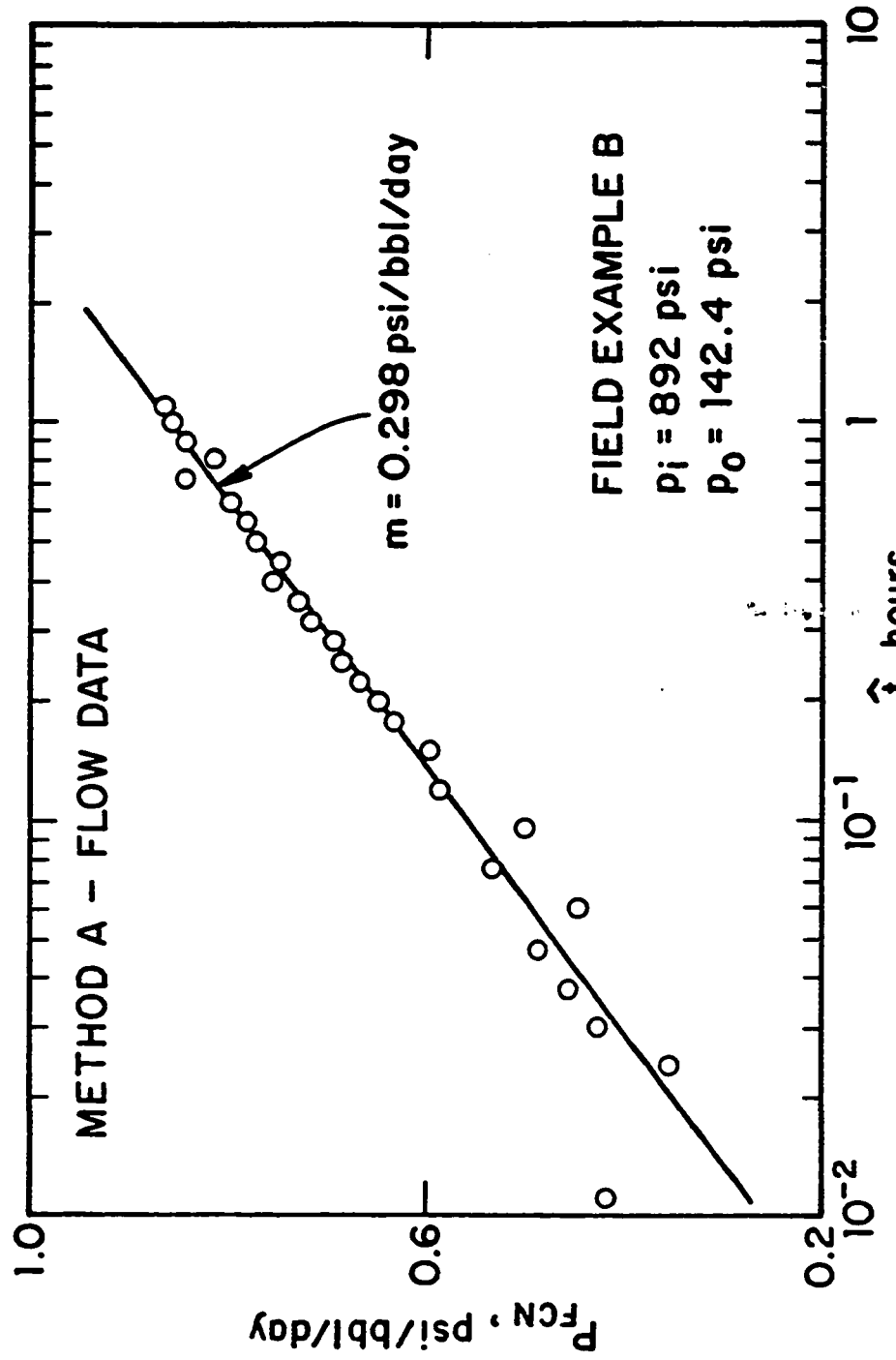

Fig. 4.3.3 - Semilog plot of P_{FCN} computed from Method A; Field Example B - flow period.

Table 4.3.3

Field Example B - Flow Period

Method A

$\hat{t}$ hours	P_{FCN} psi/bbl/day
1.1000E-02	4.172505E-01
2.4000E-02	3.530816E-01
3.0000E-02	4.248787E-01
3.7500E-02	4.547060E-01
4.7000E-02	4.856765E-01
6.0000E-02	4.446669E-01
7.5500E-02	5.333126E-01
9.5000E-02	4.997669E-01
1.1900E-01	5.856256E-01
1.4900E-01	5.958458E-01
1.7650E-01	6.322365E-01
1.9800E-01	6.483361E-01
2.2200E-01	6.669717E-01
2.4950E-01	6.852240E-01
2.7950E-01	6.931795E-01
3.1450E-01	7.164268E-01
3.5300E-01	7.284649E-01
3.9500E-01	7.549850E-01
4.4400E-01	7.466231E-01
4.9900E-01	7.705921E-01
5.5900E-01	7.811247E-01
6.2600E-01	7.964856E-01
7.1800E-01	8.423453E-01
8.0450E-01	8.131290E-01
8.8650E-01	8.417715E-01
9.9450E-01	8.555780E-01
1.0885E+00	8.636397E-01

or equivalently, kh = 32,738 md-ft. Note that the P_{FCN} values in Fig. 4.3.3 exhibit more scatter than the results obtained by the converted rate-normalized and converted convolution methods shown in Figs. 2.4.9 and 2.4.10. However, the circular data points in Fig. 4.3.3 follow the semilog straight line for all times, whereas, the data shown in Figs. 2.4.9 and 2.4.10 take approximately 0.1 hours to join their respective straight lines.

Using the values $t^* = 0.2795$ hours and $P_{FCN}(t^*) = 0.693$ psi/bbl/day taken from the straight line shown in Fig. 4.3.3, the skin factor can be estimated as

$$s = 1.151\left\{\frac{0.693}{0.298} - \log\left(\frac{546(0.2795)}{(0.062)(38)(10.2\times10^{-6})(0.354)^2}\right) + 3.23\right\} = -2.5. \tag{4.3.9}$$

The results obtained by Method B are presented in Fig. 4.3.4 and in Table 4.3.4. The P_{FCN} values are obtained directly from Eqs. 4.2.50 and 4.2.53 using the Stehfest algorithm. As discussed in Field Example A, the P_{FCN} values obtained from this deconvolution scheme exhibit less scatter; compare Figs. 4.3.4 and 4.3.3. Note that in Fig. 4.3.4 the last two points are slightly shifted below the semilog straight line due to the "tail effect" discussed previously.

Using the slope value $m = 0.293$ psi/bbl/day, the transmissibility is given by

$$\begin{aligned}\frac{kh}{\mu} &= \frac{162.6}{0.293} \\ &= 555 \text{ md-ft/cp},\end{aligned} \tag{4.3.10}$$

and the flow capacity is given by kh = 33,300 md-ft. Taking $t^* = 0.264$ hours, the value of $P_{FCN}(t^*)$ on the straight line is 0.692 psi/bbl/day. Using these values in Eq. 4.3.4, gives

$$s = 1.151\left\{\frac{0.692}{0.293} - \log\left(\frac{555(0.264)}{(0.062)(38)(10.2\times10^{-6})(0.354)^2}\right) + 3.23\right\} = -2.4. \tag{4.3.11}$$

The results obtained for the flow period of Example B using the Methods A and B are in good agreement with the results obtained by the analysis procedures of Chapter II; see Table 2.4.4.

We now address the analysis of the buildup period data. Fig. 4.3.5 presents a log-log plot of the combined drawdown and buildup P_{FCN} values obtained by

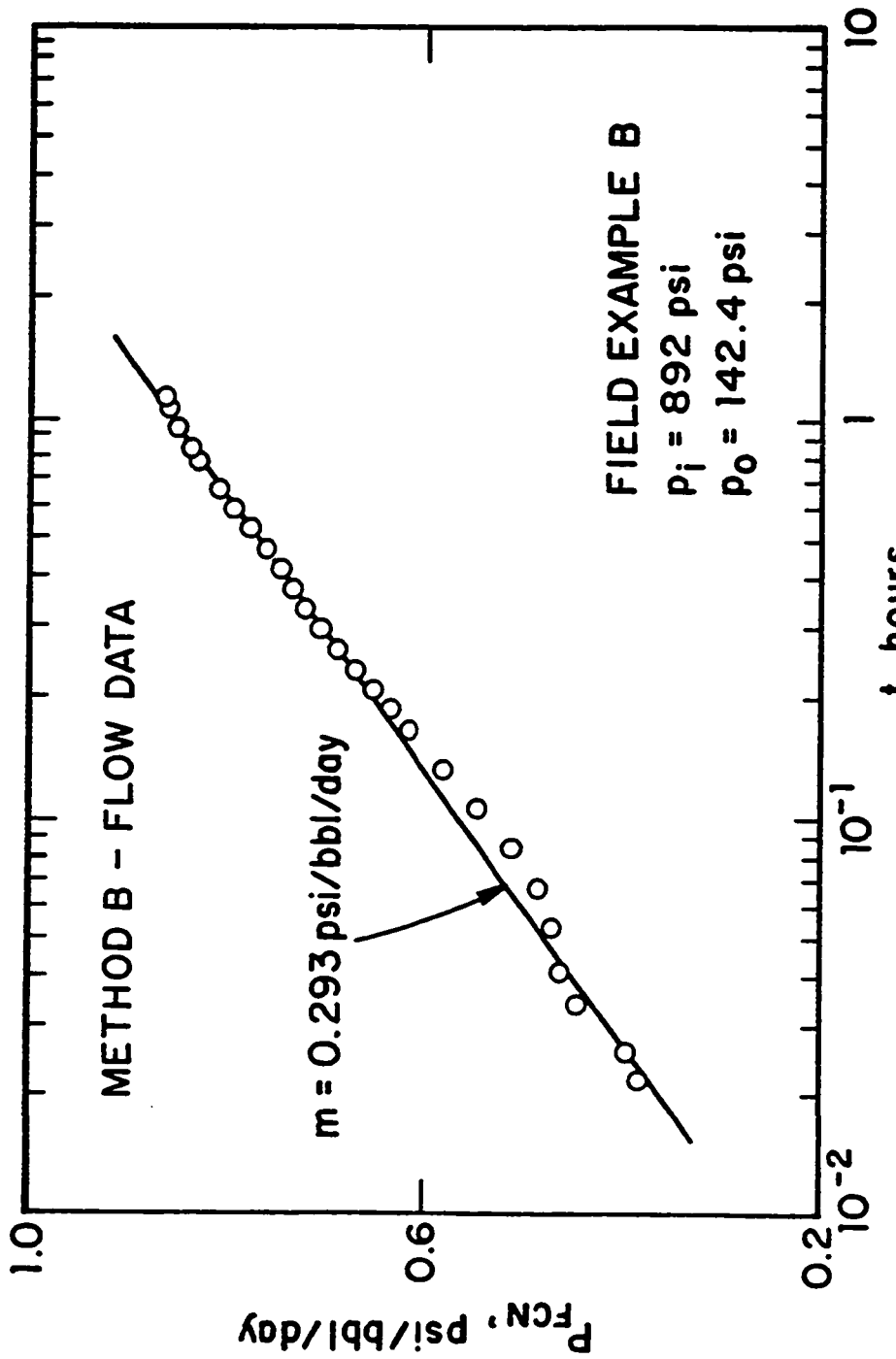

Fig. 4.3.4 - Semilog plot of P_{FCN} computed from Method B; Field Example B - flow period.

Table 4.3.4

Field Example B - Flow Period

Method B

t hours	P_{FCN} psi/bbl/day
0.22000E-01	0.38479E+00
0.26000E-01	0.39662E+00
0.34000E-01	0.44575E+00
0.41000E-01	0.46390E+00
0.53000E-01	0.47215E+00
0.67000E-01	0.48651E+00
0.84000E-01	0.51277E+00
0.10600E+00	0.54905E+00
0.13200E+00	0.58311E+00
0.16600E+00	0.61920E+00
0.18700E+00	0.63802E+00
0.20900E+00	0.65544E+00
0.23500E+00	0.67384E+00
0.26400E+00	0.69185E+00
0.29500E+00	0.70783E+00
0.33400E+00	0.72331E+00
0.37200E+00	0.73511E+00
0.41800E+00	0.74796E+00
0.47000E+00	0.76252E+00
0.52800E+00	0.77862E+00
0.59000E+00	0.79437E+00
0.66200E+00	0.81006E+00
0.77400E+00	0.83004E+00
0.83500E+00	0.83923E+00
0.93800E+00	0.85208E+00
0.10510E+01	0.86149E+00
0.11260E+01	0.86451E+00

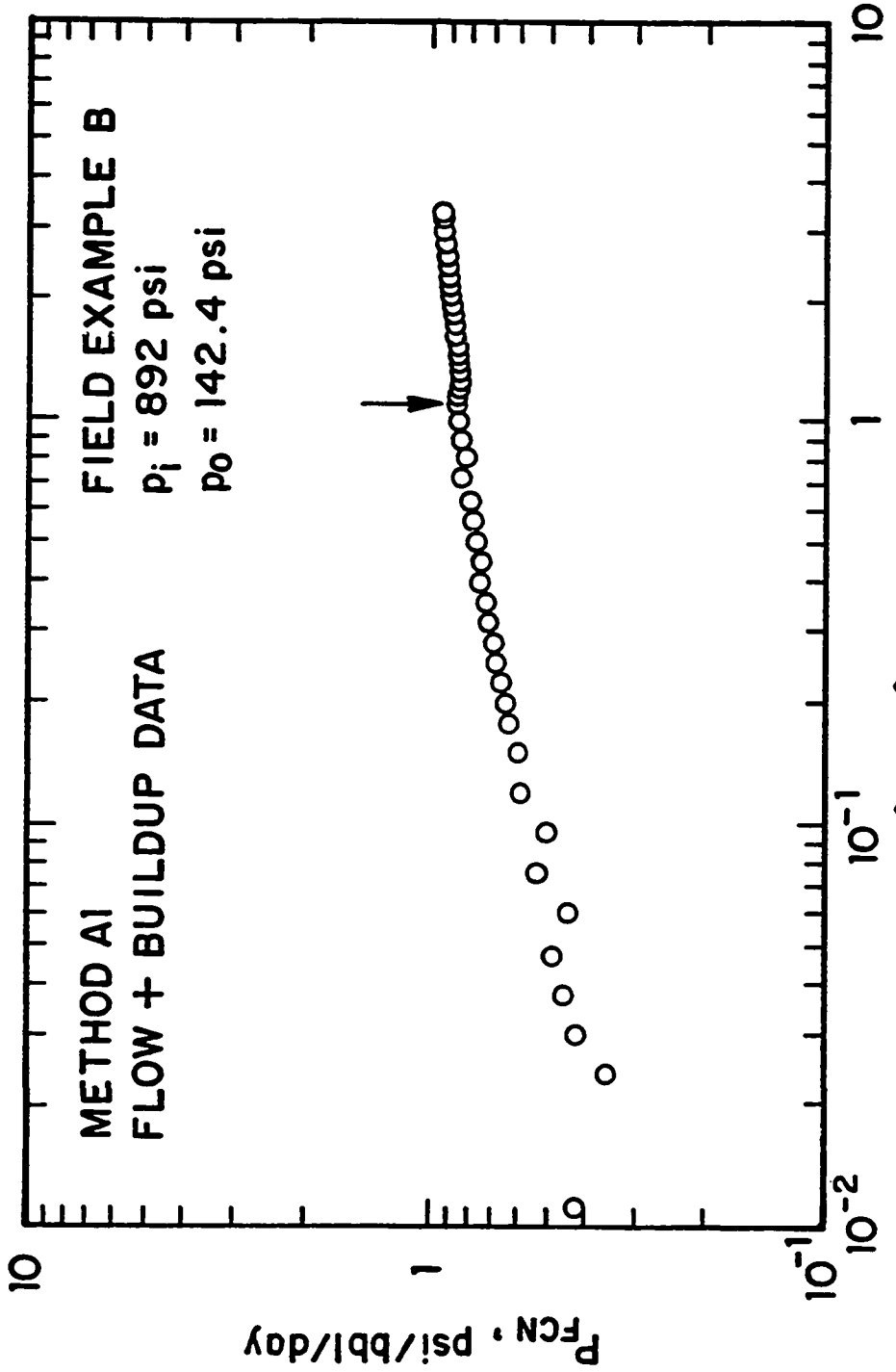

Fig. 4.3.5 - Log-log plot of P_{FCN} computed from Method A1; Field Example B - flow and buildup periods.

Method A1. As discussed previously, the computation of buildup P_{FCN} values shown in Table 4.3.5 uses the drawdown P_{FCN} values obtained by Method A. Note that in Fig. 4.3.5 the drawdown P_{FCN} values are plotted versus $\hat{t}$, whereas the buildup values are graphed versus the time $\hat{t}_p + \Delta t$; see Eq. 4.2.95. The arrow in Fig. 4.3.5 indicates the beginning of the buildup. Fig. 4.3.6 presents the semilog plot of the same data shown in Fig. 4.3.5. Fig. 4.3.6 clearly indicates that the buildup data does not follow exactly the trend of the drawdown data, which also explains the difference in results obtained in Chapters II and III. Even though the buildup period is twice as long as the flow period, the buildup data is compressed in Fig. 4.3.6 due to the nature of the logarithmic time scale. Fig. 4.3.7 presents a Cartesian plot of P_{FCN} versus $\log(\hat{t}_p + \Delta t)$, where a fairly good straight line is obtained with slope $m = 0.216$ psi/bbl/day. The approach used in this Chapter considers the buildup data as a flow period, therefore Eqs. 4.3.1 and 4.3.4 are still applicable. Then, the transmissibility estimate is given by

$$\begin{aligned} \frac{kh}{\mu} &= \frac{162.6}{0.216} \\ &= 753 \text{ md-ft/cp}, \end{aligned} \tag{4.3.12}$$

which gives $kh = 45{,}180$ md-ft. Selecting the point $[t^* = 1.92, P_{FCN}(t^*) = 0.887]$ on the straight line, Eq. 4.3.4 gives

$$s = 1.151\left\{\frac{0.887}{0.216} - \log\left(\frac{753(1.92)}{(0.062)(38)(10.2\times 10^{-6})(0.354)^2}\right) + 3.23\right\} = -1.5. \tag{4.3.13}$$

We also applied Method A to the buildup data by assuming $C_S = 0$; see Eqs. 4.2.59 - 4.2.61. The results of this computation are presented in Fig. 4.3.8 and Table 4.3.6. A fairly good straight line is also obtained in Fig. 4.3.8 and the results obtained by Method A appear to follow the straight line closer at early times than the P_{FCN} values obtained by Method A1. From Tables 2.4.3 and 3.4.3, one can verify that the last time step size in the drawdown time partition is 0.075 hours, whereas, the first buildup time step is equal to 0.022 hours, therefore the stability criterion is not satisfied at that point. If the stability condition given by Eq. 4.2.22 is applied to the buildup data, one can verify that 12 out of the first 13 points

Table 4.3.5

Field Example B - Buildup Period

Method A1

$\hat{t}_p + \Delta t$ hours	P_{FCN} psi/bbl/day
0.11105E+01	0.87480550
0.11145E+01	0.87494800
0.11225E+01	0.87442580
0.11295E+01	0.87333430
0.11415E+01	0.87180100
0.11555E+01	0.86742720
0.11725E+01	0.86396760
0.11945E+01	0.85160320
0.12205E+01	0.84427820
0.12545E+01	0.84379090
0.12755E+01	0.84916880
0.12975E+01	0.85348900
0.13235E+01	0.85402920
0.13525E+01	0.85536850
0.13835E+01	0.85358820
0.14225E+01	0.85781800
0.14605E+01	0.85991510
0.15065E+01	0.85897790
0.15585E+01	0.86668210
0.16165E+01	0.87429770
0.16785E+01	0.87255750
0.17505E+01	0.87826830
0.18625E+01	0.88630010
0.19235E+01	0.88705000
0.20265E+01	0.89574600
0.21395E+01	0.89904310
0.22695E+01	0.90625510
0.24135E+01	0.90750100
0.25745E+01	0.91337380
0.27545E+01	0.91966630
0.29585E+01	0.92644480
0.31865E+01	0.93350080
0.32775E+01	0.93618710

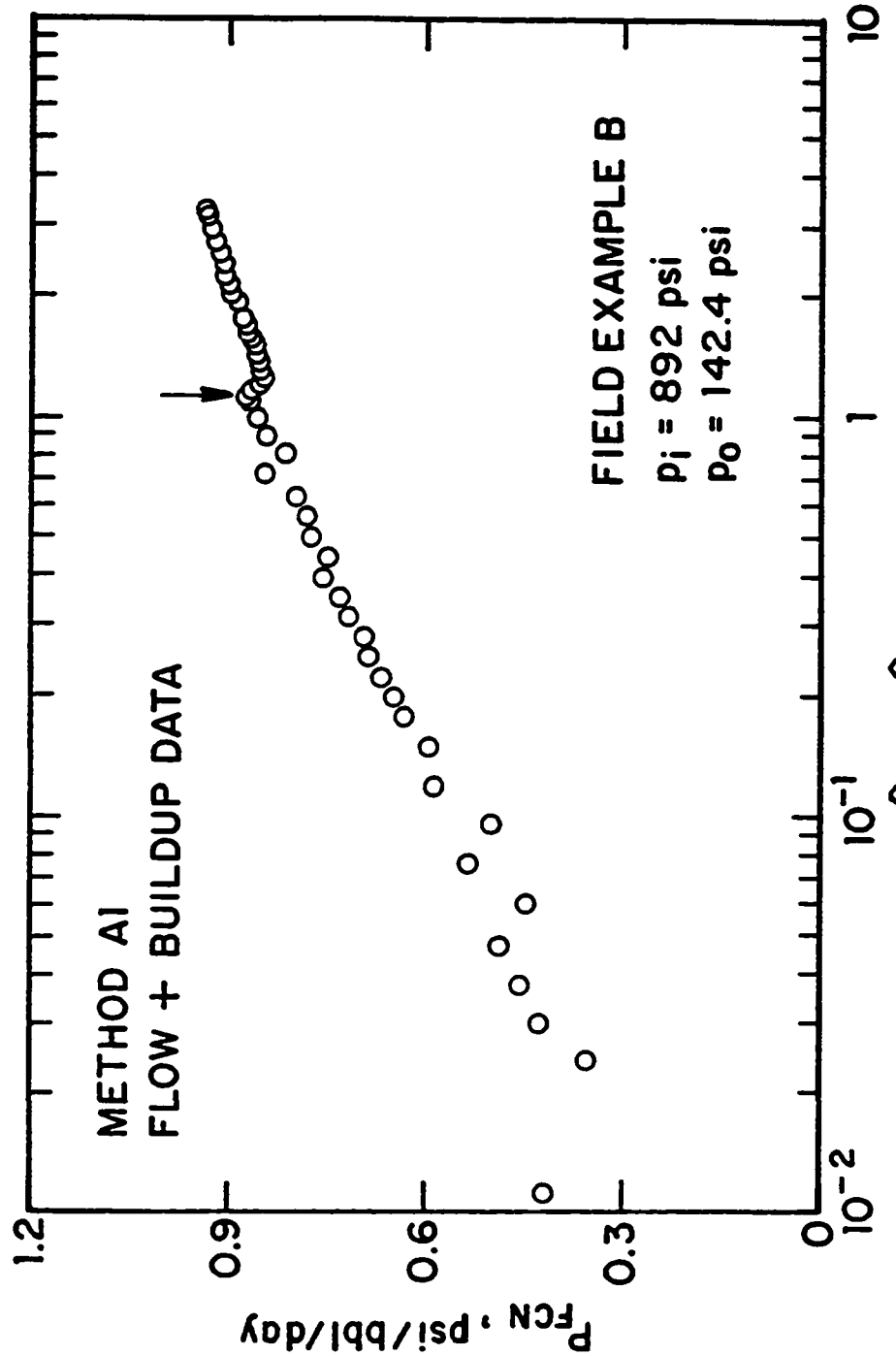

Fig. 4.3.6 - Semilog plot of P_{FCN} computed from Method A1; Field Example B - flow and buildup periods.

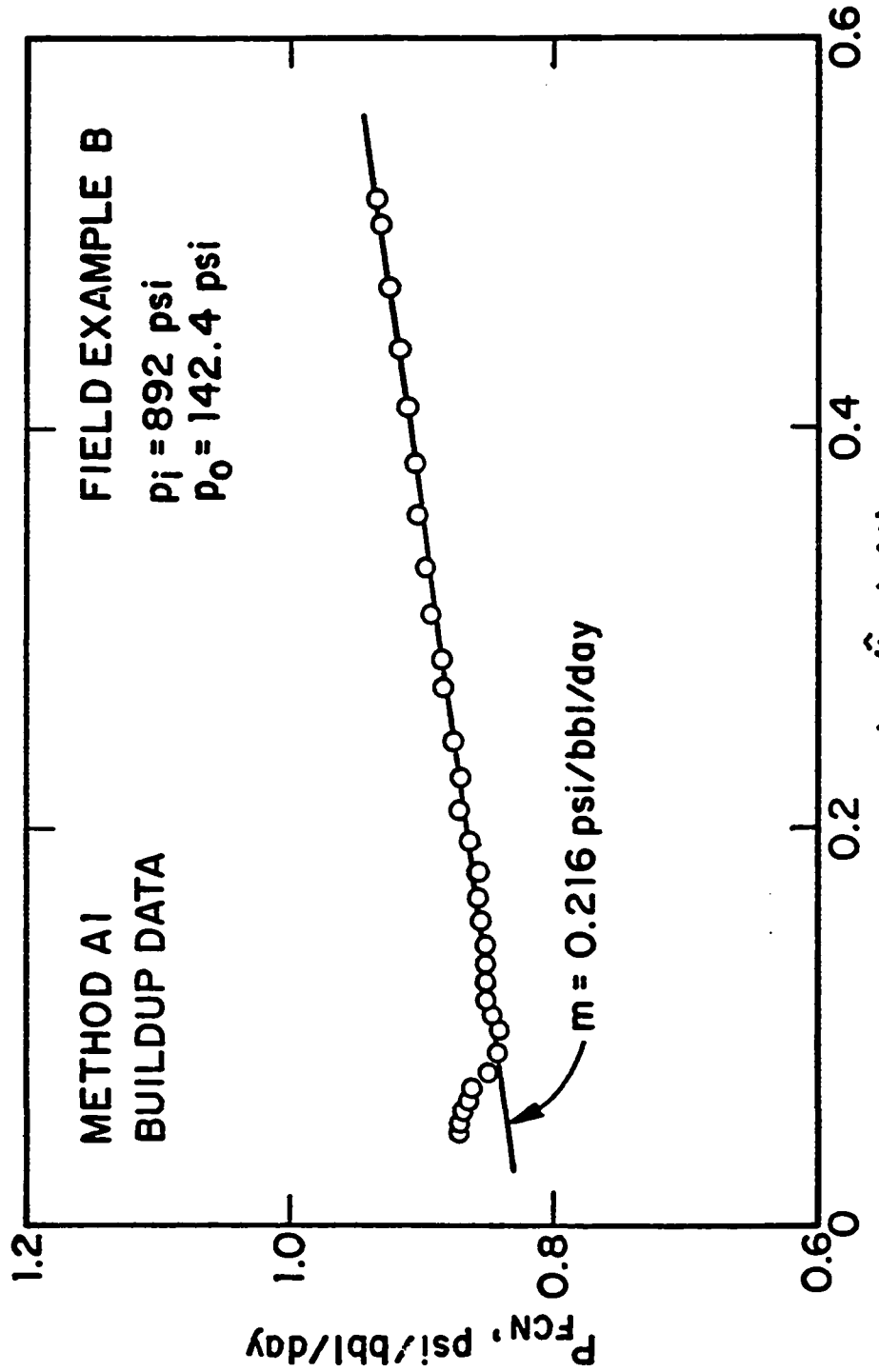

Fig. 4.3.7 - Cartesian plot of P_{FCN} computed from Method A1; Field Example B - buildup period.

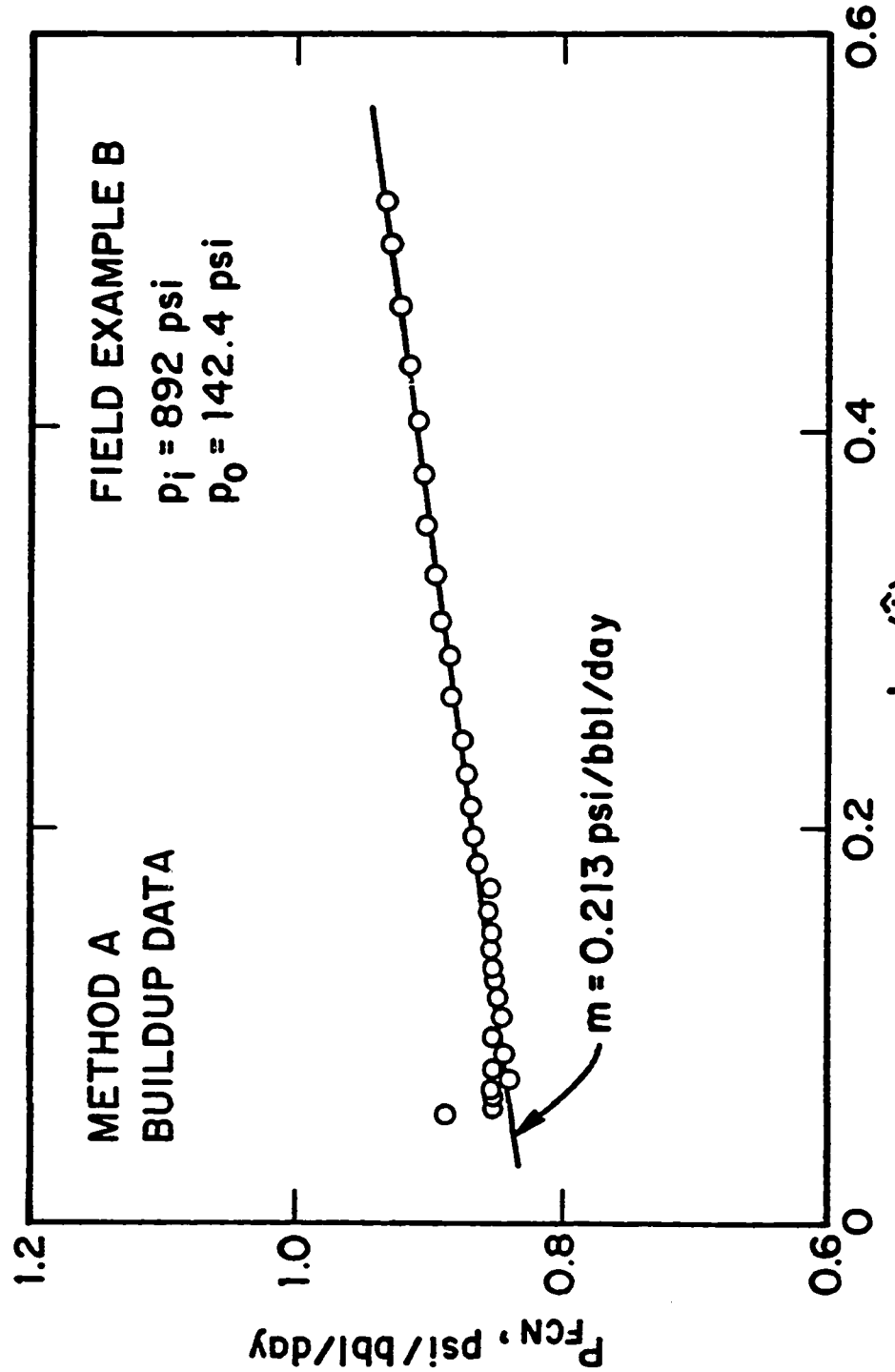

Fig. 4.3.8 - Cartesian plot of P_{FCN} computed from Method A; Field Example B - buildup period.

Table 4.3.6

Field Example B - Buildup Period

Method A - $C_S = 0$

$\hat{t}$ hours	P_{FCN} psi/bbl/day
0.11370E+01	0.88960820
0.11500E+01	0.85409560
0.11560E+01	0.85203750
0.11635E+01	0.85118140
0.11730E+01	0.85418650
0.11860E+01	0.83991950
0.12015E+01	0.85263360
0.12210E+01	0.84409530
0.12450E+01	0.85354500
0.12750E+01	0.84559990
0.13025E+01	0.84948070
0.13240E+01	0.85222990
0.13480E+01	0.85426120
0.13755E+01	0.85446190
0.14055E+01	0.85544010
0.14405E+01	0.85713860
0.14790E+01	0.85547750
0.15210E+01	0.86456150
0.15700E+01	0.86795090
0.16250E+01	0.87085970
0.16850E+01	0.87393290
0.17520E+01	0.87752760
0.18440E+01	0.88615930
0.19305E+01	0.88747430
0.20125E+01	0.89434940
0.21205E+01	0.89917750
0.22420E+01	0.90489660
0.23790E+01	0.90721330
0.25315E+01	0.91188440
0.27020E+01	0.91806070
0.28940E+01	0.92475370
0.31100E+01	0.93173400
0.32695E+01	0.93544690

do not satisfy the inequality of Eq. 4.2.22. Note that the stability of Method A1 does not depend on the time partition used in the buildup period, and in this field example, as the stability criterion is satisfied for the last point of the drawdown period, Method A1 is completely stable; see Eqs. 4.2.77 - 4.2.79. Based on the above discussion and from the comparison of Figs. 4.3.7 and 4.3.8, it appears that one may relax the enforcement of the stability condition in applying Method A for both drawdown and buildup applications.

Using the slope value indicated in Fig. 4.3.8, the transmissibility can be estimated as

$$\begin{aligned} \frac{kh}{\mu} &= \frac{162.6}{0.213} \\ &= 763 \text{ md-ft/cp}, \end{aligned} \tag{4.3.14}$$

which yields $kh = 45{,}780$ md-ft. Selecting the point $[t^* = 1.93, P_{FCN}(t^*) = 0.887]$ on the straight line, the skin factor is given by

$$s = 1.151\left\{\frac{0.887}{0.213} - \log\left(\frac{763(1.93)}{(0.062)(38)(10.2\times 10^{-6})(0.354)^2}\right) + 3.23\right\} = -1.5. \tag{4.3.15}$$

A comparison of the results obtained by Methods A and A1 indicates a nearly perfect agreement. Table 4.3.7 summarizes the results obtained for this field example using the deconvolution schemes proposed in this Chapter. Although we obtained different results for the drawdown and buildup periods, the discrepancy is not so severe as observed when applying the methods of Chapters II and III to the same field example.

4.3.2 Example C

The field example shown here also corresponds to data measured from a drillstem test operations and was previously considered in Chapters II and III. The measured pressure versus time data were presented in Tables 2.4.5 and 3.4.1.

The application of Method A for the flow period of Field Example C is shown in Fig. 4.3.9. Note that the unusual wave shape is not caused by stability problems since all points in the drawdown partition satisfy the condition given by 4.2.28. The

Table 4.3.7

Field Example B - Comparison of Results

Parameters	Flow Period		Buildup Period	
	Method A	Method B	Method A1	Method A
kh/μ, md-ft/cp	546	555	753	763
kh, md-ft	32,738	33,300	45,180	45,7[illegible]
skin	-2.5	- 2.4	-1.5	-1.5

Table 4.3.7

Field Example B - Comparison of Results

	Flow Period		Buildup Period	
Parameters	Method A	Method B	Method A1	Method A
kh/μ, md-ft/cp	546	555	753	763
kh, md-ft	32,738	33,300	45,180	45,780
skin	-2.5	- 2.4	-1.5	-1.5

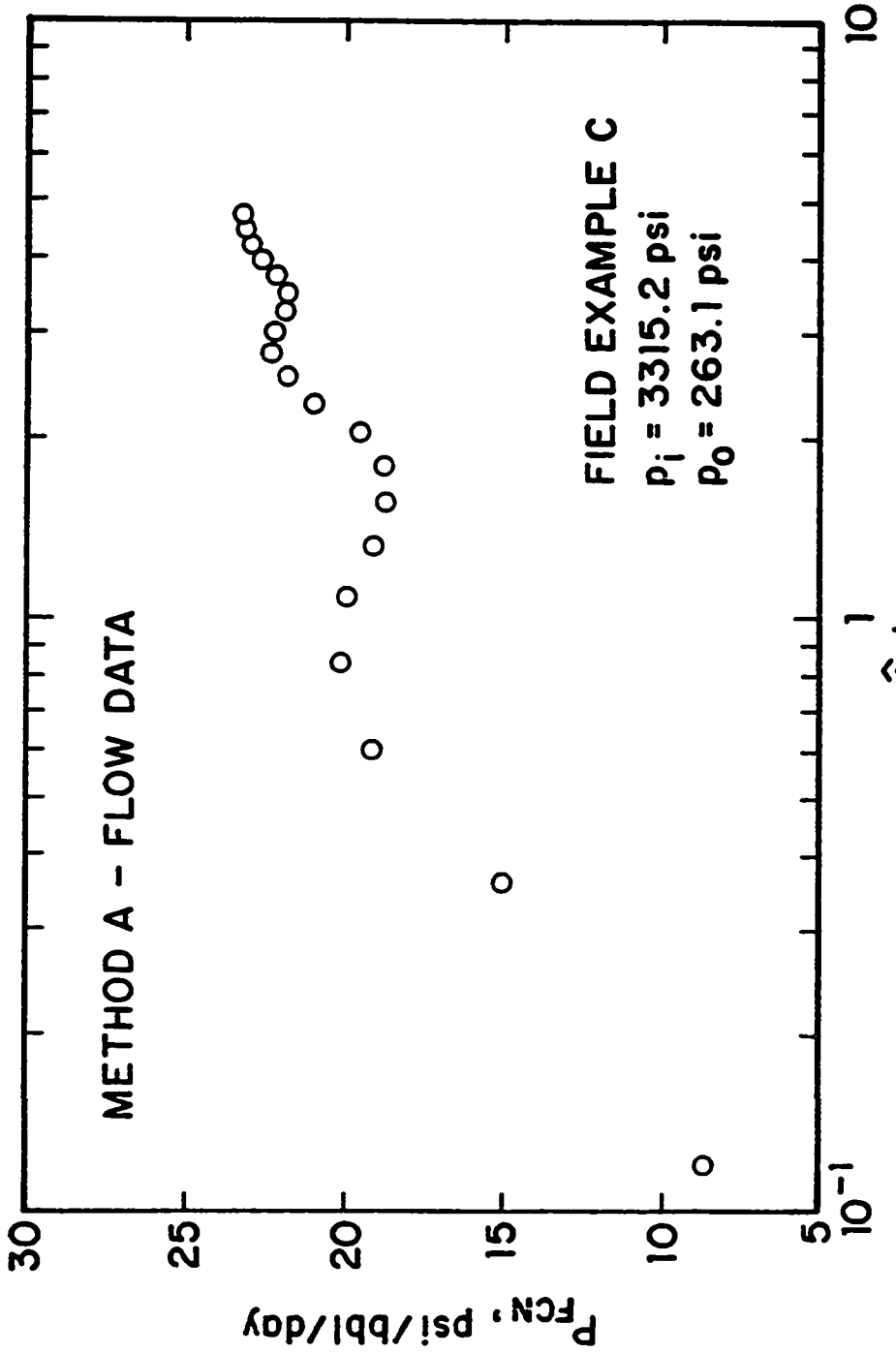

Fig. 4.3.9 - Semilog plot of P_{FCN} computed from Method A; Field Example C - flow period.

results obtained by Method B are shown in Fig. 4.3.10, which presents the same shape shown by the data in Fig. 4.3.9.

Fig. 4.3.11 presents the combined plot of drawdown and buildup P_{FCN} values calculated from Method A1. The arrow in the figure indicates the time correspondent to the beginning of the buildup period. Note that the data in the buildup period also presents the same oscillatory behavior displayed by the drawdown data. Fig. 4.3.12 presents the buildup data in more detail. Note that an "average" straight line line could be draw through the data (with results close to the ones obtained in Chapter III). However, such analysis would be highly questionable and is not presented here.

This example shows that the application of deconvolution methods can reveal additional features to apparently normal field data. To the best of our knowledge, the behavior exhibited by the P_{FCN} data in this field example not does not match any constant sandface flow rate solution presented in the literature to date.

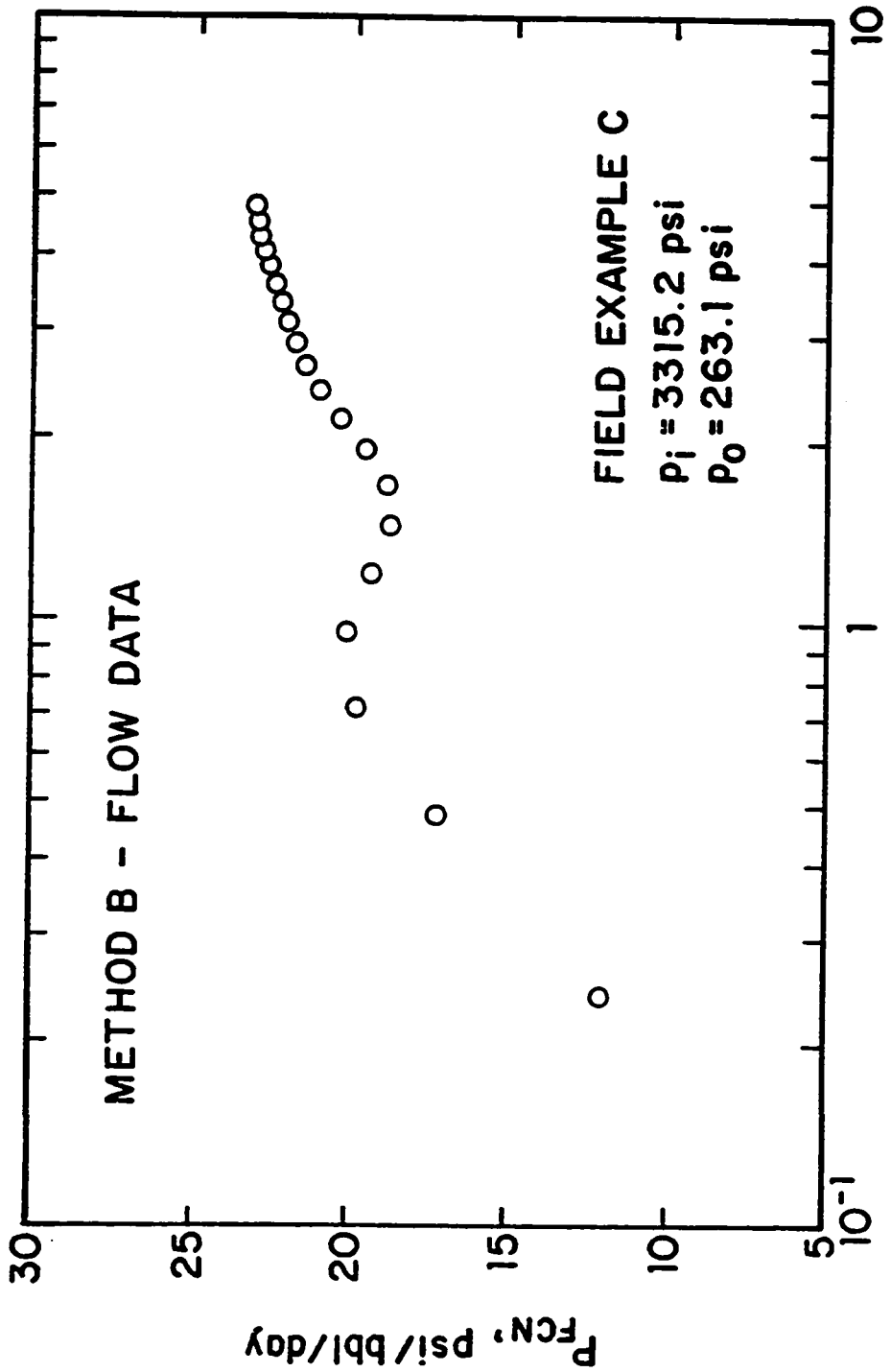

Fig. 4.3.10 - Semilog plot of P_{FCN} computed from Method B; Field Example C - flow period.

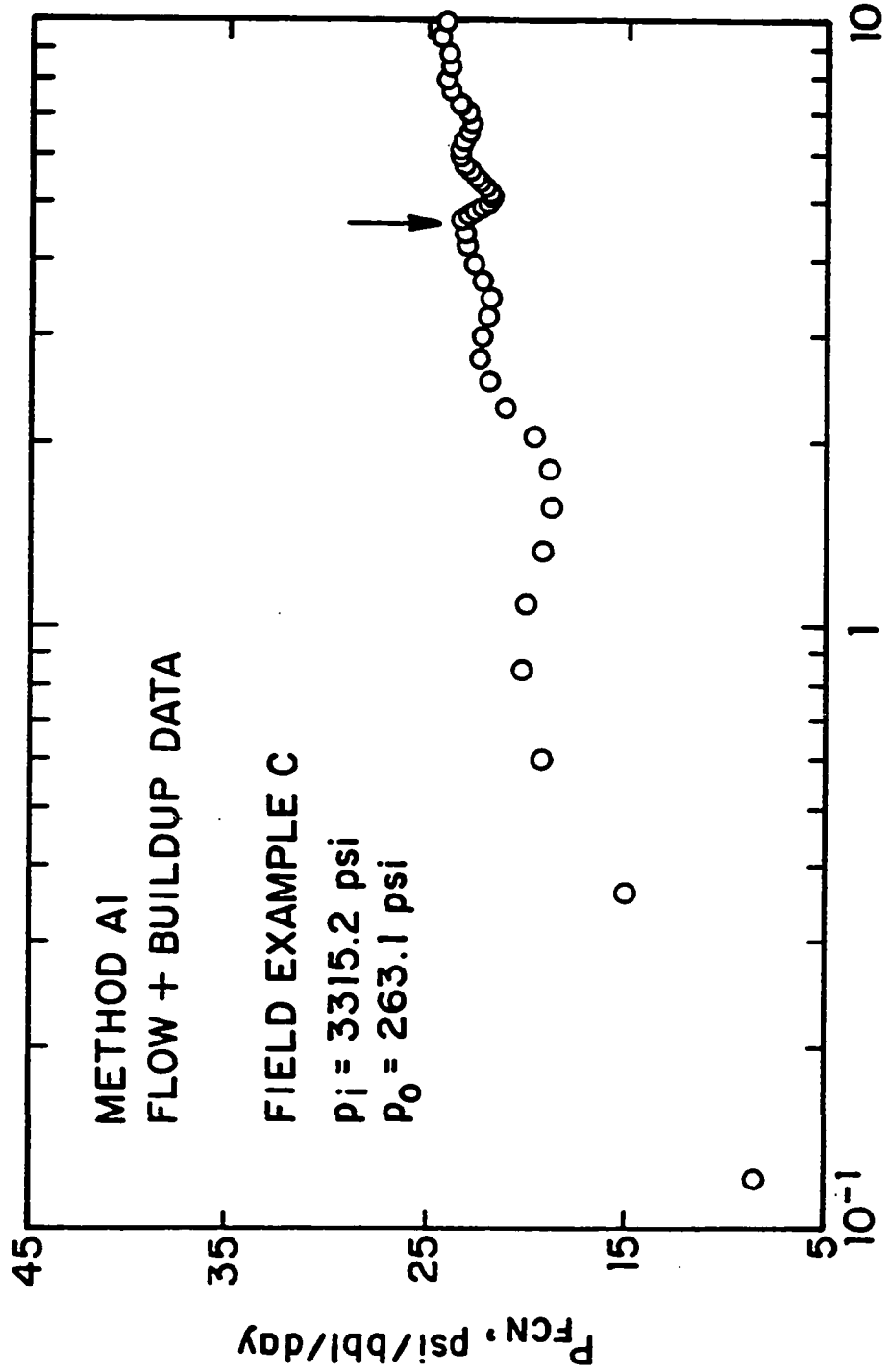

Fig. 4.3.11 - Semilog plot of P_{FCN} computed from Method A1; Field Example C - flow and buildup periods.

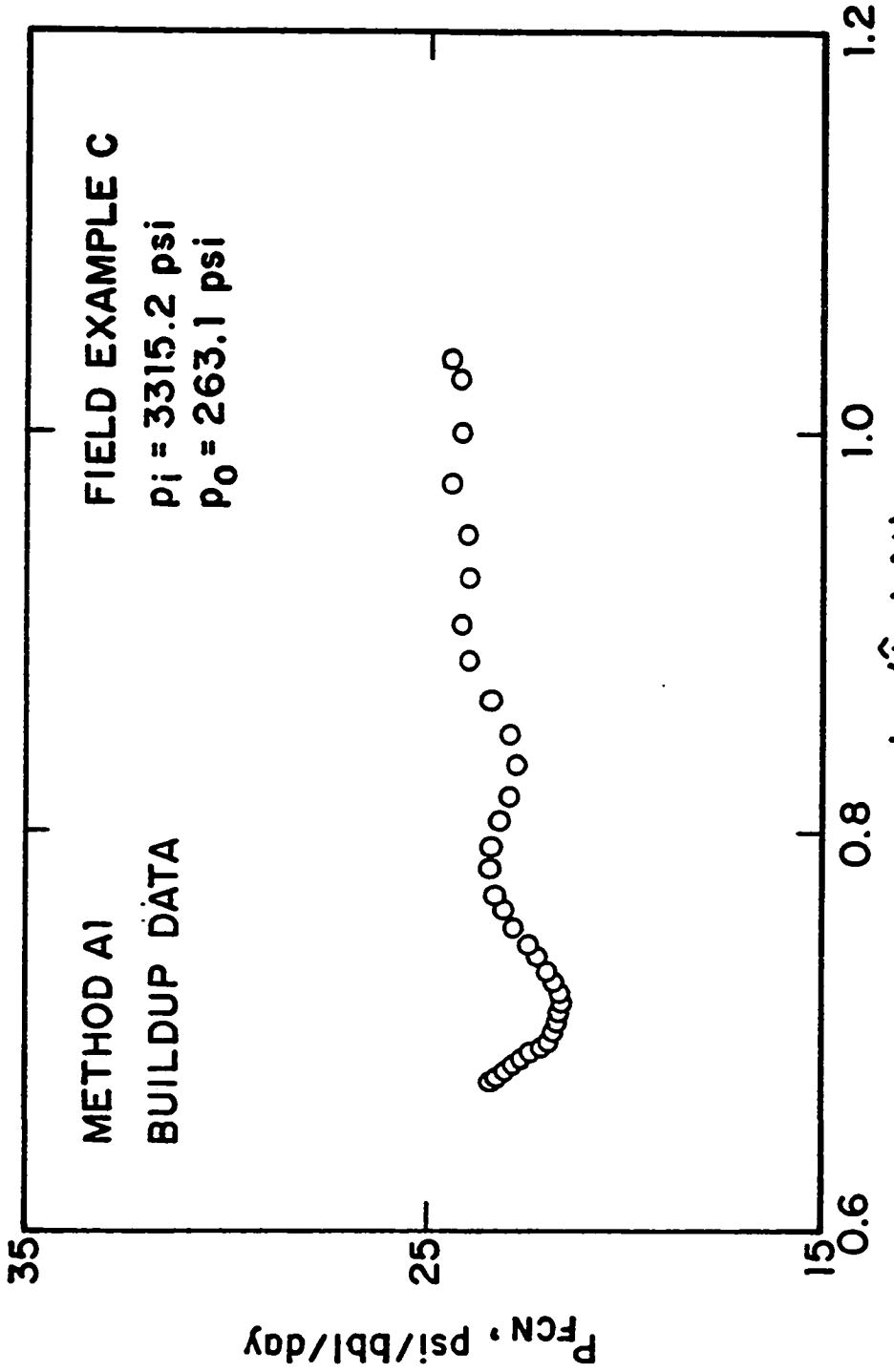

Fig. 4.3.12 - Cartesian plot of P_{FCN} computed from Method A1; Field Example C - buildup period.

CHAPTER V
CONCLUSIONS

The objective of this work has been to present new procedures for analyzing pressure data obtained from slug and drillstem tests. In this work, we considered only cases where the wellbore fluid does not reach the surface during the flow period. All methods proposed in this work do not require the measurement of the sandface flow rate versus time data.

Starting from Duhamel's principle, a general relationship between the slug test dimensionless pressure solution and the constant rate wellbore storage and skin dimensionless solution has been derived. Based on this result, we showed that the slug test response can be converted to an equivalent constant rate, wellbore storage and skin problem by integrating the measured slug test pressure over the producing time. Once the equivalent constant rate data are obtained from the new procedure, it was shown that these data can be analyzed using standard constant rate analysis procedures. In particular, we presented procedures for analyzing slug test pressure data using constant rate wellbore storage and skin type curves, therefore, slug test type curves are no longer needed. The general relationship established in this work clearly indicates that the slug test data represents an equivalent constant rate test of short duration, in which most of the data is strongly affected by wellbore storage. In terms of field applications, this result implies that if the fluid recovery is not large a unique match with the type curves cannot be easily obtained. For such cases, we presented procedures for applying the rate-normalization and convolution (superposition, multi-rate) methods to the converted data without resorting to direct measurement or computation of the sandface flow rate. Several field examples were presented to illustrate the applicability of the new procedure.

In DST operations, if the wellbore fluid does not reach the surface during the flow period, the analysis of the subsequent buildup pressure data is generally difficult due the combined effects of variable flow rate and short producing time. In

this work, two new straight-line methods (Method 1 and Method 2) for analyzing such buildup data have been presented. The new methods account for the flow rate variation during the flow period, however, no direct measurement of the sandface flow rate nor its determination from the liquid recovery are needed. Several sets of computer generated data were used to compare the performance of the new straight-line methods with conventional techniques such as the Horner method. We also extended the application of the multi-rate equivalent time to the analysis of DST buildup data and presented a more rigorous justification for using drawdown type curves in the analysis of buildup pressure data. The new straight-line methods were also applied to two sets of buildup field data.

Some of the methods presented in this work are strictly applicable for radial flow geometries. For cases when this condition is not satisfied, we developed new deconvolution schemes designed for slug and DST applications. All the new schemes are based on a particular rearrangement of Duhamel's principle so that no measurement or direct computation of the flow rate is required. We also presented an alternative scheme for analyzing pressure buildup data for cases in which the buildup wellbore storage coefficient is not known and cannot be accurately estimated. We also considered the numerical aspects of the proposed deconvolution schemes. For illustrative purposes, we analyzed several field examples using the new deconvolution algorithms.

Based on this work the following conclusions are warranted:

(1) A new procedure which exactly converts the measured slug or DST flow pressure data into equivalent constant surface flow rate pressure data has been presented. Specifically, the integration of the slug test pressure over the producing time gives the equivalent pressure change that would be obtained if the well were produced at constant surface flow rate. Moreover, by multiplying the measured slug test pressure data by the producing time one generates the logarithmic pressure derivative of the constant surface rate wellbore storage and skin problem without resorting to numerical differentiation schemes. Since the new procedure avoids numerical differentiation of data and the converted

data is obtained by integration of the measured slug test pressure data, the converted data will typically be free of noise.

(2) After the equivalent constant surface rate data is computed, one can use wellbore storage and skin pressure and pressure derivative type curves to identify the appropriate reservoir/well system represented by the field data. Reservoir parameters can then be determined by using well known constant rate analysis techniques without resorting to conventional slug test analysis procedures.

(3) If the slug test data is sufficiently long, that is, if a large fluid recovery is obtained during the flow period, the appropriate wellbore storage and skin pressure derivative type curve can be used to determine the desired parameters. In this regard, Onur and Reynolds' wellbore and skin type curve simplifies the type-curve matching procedure since the field data plot is moved only in one direction. However, we should first construct a log-log plot of the converted pressure and pressure derivative since it can help to identify when a type-curve match is most likely to be successful.

(4) If the converted slug test data is of "short" duration, that is, the converted slug test data is strongly dominated by wellbore storage, a unique match of field data with such type curves is very difficult. However, the rate-normalization method and/or the traditional multi-rate analysis based on the converted slug test data generated by our new method can still be successfully applied in determining reservoir properties, as shown in one of the field examples.

(5) Two new straight-line methods, referred to as Method 1 and Method 2, for analyzing drillstem test buildup data have been presented. The proposed methods account for both producing time and the rate variation effect, however, contrary to the conventional multi-rate approach, the new methods do not require direct measurement of the sandface flow rate or its computation from the liquid level recovery. If the buildup wellbore storage-skin group $C_{SD}\exp(2s)$ is small, the correct straight line is obtained shortly after the well is closed-in. From the slope of the straight line of either method, both the flow capacity and the formation damage can be estimated. The reservoir initial pressure can be obtained directly from the extrapolation of the straight line.

(6) If the group $C_{SD}\exp(2s)$ is large, the beginning of the proper straight line for Method 1 or Method 2 will be delayed and longer shut-in times are needed before the correct straight line is reached. Method 1 is more affected by the presence of wellbore storage and skin, since this method is based on the pressure integration over the entire buildup pressure history. For those cases, if the buildup wellbore coefficient can be estimated from a log-log plot of the buildup pressure rise versus the multi-rate equivalent time, modified versions of Methods 1 and 2 have been presented which account for afterflow effects on the pressure buildup response. Computer generated data shows that the modified Method 1 gives better results, however the implementation of this technique requires knowledge of the initial reservoir pressure.

(7) Field and computer generated data show that the decline in the flow rate during the DST flow period generally causes the Horner method to approach the correct straight line from above, whereas the Cartesian Method will always reach the proper straight line from below. In terms of field applications, this observation indicates that the Horner method will often underestimate the initial reservoir pressure and overestimate the flow capacity, whereas the Cartesian Method will tend to overestimate p_i and underestimate kh. Therefore, for cases where the rate variation is large during the flow period, the application of the Horner and Cartesian Methods are not recommended.

(8) Often in a dual shut-in DST, the Horner plot yields an estimated value of the initial reservoir pressure from the second shut-in which is lower than the p_i estimated from the first buildup period. As shown in this work, one should consider the effect of the flow rate decline during the preceding flow period as the most plausible cause.

(9) The working equations for Methods 1 and 2 presented in this work, are strictly applicable for transient radial flow. The validity of these straight line methods should be always verified with log-log plots of $\tilde{p}_{sD}$ and $\tilde{p}'_{sD}$ versus the multi-rate equivalent time.

(10) Three deconvolution schemes have been developed for the analysis of slug and DST data. Two methods (Method A and Method A1) perform all the computations in real space, whereas in Method B, the calculations are done in Laplace space. Application of these schemes to field data indicates that Method B provides smooth results, however, if the original data is noisy, this scheme will produce a very smooth curve which can be misinterpreted as caused by some sort of reservoir heterogeneity. As shown by field and computer generated data, Method B presents a "tail effect", that is, results obtained for the last points in the time partition are not accurate. This behavior may be caused by the extrapolation of the data beyond the last measured value, the type of approximation used (piecewise linear) or lack of accuracy in the numerical Laplace space inversion scheme used. This point needs further investigation. The Method B deconvolution scheme presented in this work is only applicable for the analysis of drawdown data. A similar algorithm for the analysis of DST buildup data can also be derived, however, the problems described above need to be solved before attempts are made to construct such a scheme.

(11) Method A does not present the problems of Method B, however our derivations indicate that Method A is stable provided that the time partition has equal or increasing time step sizes. Method A is applicable for analysis of drawdown and buildup data, however, because of the common practice of increasing the sampling data frequency during the early stages of the buildup period, the first points in the buildup partition have a time step size substantially smaller than the time step just before shut-in so that the stability criterion is not satisfied. Based on a field example presented in this work, it appears that the enforcement of the stability criterion can be relaxed.

(12) If the buildup wellbore storage coefficient cannot be estimated, it has been shown that by setting C_{SD} to zero in the deconvolution equations of Method A provides a very good approximation for practical applications. Computer generated data showed that, in general, the correct flow capacity is obtained whereas the skin factor is slightly overestimated. An alternative buildup deconvolution scheme (Method A1) has been also proposed, in which $C_{SD} = 0$

is implicitly assumed. In this method, the truncation errors and the stability criteria are independent of the buildup partition used, which represents, at least in principle, an advantage in terms of field applications. However, computer generated data indicated that Method A1 tends to yield more oscillatory results than does Method A.

(13) A field example showed that the application of deconvolution methods can reveal additional features not apparent when analyzing field data by other techniques. Therefore, this technique should be applied to the analysis of slug and drillstem tests data whenever possible.

(14) Further research is needed to explain discrepancy between the results obtained from the flow and buildup periods.

NOMENCLATURE

Symbol

B = formation volume factor, RB/STB.

C, C_F = slug test or DST drawdown wellbore storage coefficient, RB/psi.

C_S = buildup wellbore storage coefficient, RB/psi.

C_D = slug test dimensionless wellbore storage coefficient, Chapter II.

C_D = constant rate dimensionless wellbore storage coefficient, Chapter III.

C_{FD} = dimensionless drawdown wellbore storage coefficient.

C_{SD} = dimensionless buildup wellbore storage coefficient.

c_t = total system compressibility, psi^{-1}.

c_{wf} = wellbore fluid compressibility, psi^{-1}.

h = formation thickness, ft.

k = permeability, md.

m_D = dimensionless slope.

m_{cD} = dimensionless slope.

m_c = slope of Cartesian Method, psi.

m_H = slope of conventional multi-rate method, psi.

m_1 = slope of Method 1, psi.

m_2 = slope of Method 2, psi.

m = slope.

$p(r,t)$ = pressure at r and t, psi.

p_{avg} = average flowing pressure, psi.

p_i = initial reservoir pressure, psi.

p_o = initial wellbore pressure, psi.

p_w = wellbore pressure, psi.

p_{wf} = flowing wellbore pressure, psi.

p_{ws} = shut-in wellbore pressure, psi.

P_{FCN} = pressure drop per unit flow rate from deconvolution, psi/bbl/day.

p_D = slug test dimensionless pressure drop.

p_{sD} = dimensionless pressure buildup change.

$\tilde{p}_{sD}$ = DST dimensionless buildup pressure rise.

$\tilde{p}'_{sD}$ = logarithmic derivative of $\tilde{p}_{sD}$.

p_{cD} = constant surface rate dimensionless pressure drop.

p^*_{cD} = constant sandface rate dimensionless pressure solution.

p_{scD} = constant rate dimensionless pressure buildup change.

$\tilde{p}_{scD}$ = constant rate dimensionless buildup pressure rise.

p_{wD} = dimensionless wellbore pressure.

p_{wcD} = constant surface rate dimensionless wellbore pressure.

p'_{wcD} = logarithmic derivative of p_{wcD}.

p^*_{wcD} = constant sandface rate dimensionless wellbore pressure solution.

P_{FCND} = constant sandface rate solution obtained by deconvolution.

q = constant surface flow rate, STB/day.

q_D = slug test or DST dimensionless sandface flow rate.

q_{cD} = dimensionless sandface flow rate for the constant surface rate problem.

q_{sf} = slug test or DST sandface flow rate, RB/day.

q_{sfc} = sandface flow rate under constant surface rate production, RB/day.

r_p = radius of the drill pipe, ft.

r_w = wellbore radius, ft.

r_D = dimensionless radial distance.

s = skin factor.

t = total elapsed time, hours.

t_c = $t_p/(t_p + \Delta t)$.

t_{mH} = conventional multi-rate time, dimensionless.

t_{ms} = slug test multi-rate time, dimensionless.

t_p = producing time, hours.

t_1 = Method 1 multi-rate time, dimensionless.

t_2 = Method 2 multi-rate time, dimensionless.

t_{pD} = dimensionless producing time.

t_{cD} = Cartesian Method dimensionless time.

t_{HD} = Conventional multi-rate dimensionless time.

t_{1D} = Method 1 dimensionless time.

t_{2D} = Method 2 dimensionless time.

t_{eD} = dimensionless equivalent drawdown time.

t_{eMD} = dimensionless multi-rate equivalent drawdown time.

t_{msD} = converted slug test multi-rate dimensionless time.

t_D = dimensionless time.

V_w = wellbore volume, bbl.

$I(\Delta p)$ = integral of the slug test pressure data, psi-hour.

$I(p_{ws})$ = time integral of buildup pressure data, psi-hour.

$I(p_{sD})$ = integral of the dimensionless pressure buildup change.

$I(p_{wD})$ = integral of the dimensionless wellbore pressure.

μ = viscosity, cp.

ϕ = porosity, fraction.

ρ = fluid density, lbm/ft^3.

γ = Euler's constant (0.57722).

Δp = pressure change, psi.

$\Delta p'$ = logarithmic derivative of pressure change, psi.

Δt = elapsed shut-in time, hours.

Δt_D = dimensionless shut-in time.

Δp_{skin} = additional pressure drop due the skin, psi.

REFERENCES

1. Ferris, J. G. and Knowles, D. B.: "The Slug Test for Estimating Transmissibility," *U.S.Geol. Surv. Ground Water Note, 26* (1954) 1-7.
2. Cooper, H. H. Jr., Bredehoeft, J. D. and Papadopulos, I. S.: "Response of a Finite Diameter Well to an Instantaneous Charge of Water," *Water Resour. Res., 3*(1), (1967) 263-269.
3. van Poollen, H. K. and Weber, J. B.: "Data Analysis for High Influx Wells," paper SPE 3017 presented at the 1970 SPE Annual Fall Meeting, Houston, Oct. 4-7.
4. Kohlhaas, C. A.: "A Method for Analyzing Pressures Measured During Drillstem-Test Flow Periods," *Trans. AIME, 253* (1972) 1278-1282.
5. Ramey, H. J. Jr. and Agarwal, R. G.: "Annulus Unloading Rates as Influenced by Wellbore Storage and Skin Effect," *Trans. AIME, 253* (1972) 453-463.
6. van Everdingen, A. F.: "The Skin Effect and Its Influence on the Productive Capacity of a Well," *Trans. AIME, 198* (1953) 171-176.
7. Hurst, W.: "Establishment of the Skin Effect and Its Impediment to Fluid Flow Into a Well Bore," *Pet. Eng., 25* (Oct. 1953) B 6-16.
8. Ramey, H. J. Jr., Agarwal, R. G. and Martin I.:"Analysis of 'Slug Test' or DST Flow Period Data," *J. Can. Pet. Tech., 14* (July-Sept. 1975) 37-47.
9. Earlougher, R. C. Jr. and Kersch, K. M.: "Analysis of Short-Time Transient Test Data by Type-Curve Matching," *Trans. AIME, 257* (1974) 793-800.
10. Sageev, A.: "Slug Test Analysis," *Water Resour. Res., 22*(8), (1986) 1323-1333.
11. Faust, C. R. and Mercer, J. W.: "Evaluation of Slug Tests in Wells Containing a Finite-Thickness Skin," *Water Resour. Res., 20*(4), (1984) 504-506.
12. Moench, A. F. and Hsieh, P. A.: Comment on "Evaluation of Slug Tests in Wells Containing a Finite-Thickness Skin," *Water Resour. Res., 21*(9), (1985) 1459-1461.

13. Bredehoeft, J. D. and Papadopulos, S. S.: "A Method for Determining the Hydraulic Properties of Tight Formations," *Water Resour. Res., 16*(1), (1980) 233-238.

14. Barker, J. A. and Black, J. H.: "Slug Tests in Fissured Aquifers," *Water Resour. Res., 19*(6), (1983) 1558-1564.

15. Mateen, K. and Ramey, H. J. Jr.: "Slug Test Data Analysis in Reservoirs With Double Porosity Behavior," paper SPE 12779 presented at the 1984 California Regional Meeting of SPE of AIME, Long Beach, Cal., April 11-13.

16. Sageev, A. and Ramey, H. J. Jr.: "On Slug Test Analysis in Double-Porosity Reservoirs," paper SPE 15479 presented at the 1986 SPE Annual Technical Conference and Exhibition, New Orleans, Oct. 5-8.

17. Dougherty, D. E. and Babu, D. K.: "Flow to a Partially Penetrating Well in a Double-Porosity Reservoir," *Water Resour. Res., 20*(8), (1984) 1116-1122.

18. Karasaki, K., Long, J. C. S. and Witherspoon, P. A.: "Analytical Models of Slug Tests," *Water Resour. Res., 24*(1), (1988) 115-126.

19. Agarwal, R. G., Al-Hussainy R. and Ramey, H. J. Jr.: "An Investigation of Wellbore Storage and Skin Effect in Unsteady Liquid Flow: I. Analytical Treatment," *Trans. AIME, 249* (1970) 279-290.

20. Gringarten, A. C., Bourdet, D. P., Landel, P. A. and Kniazeff, V. J.: "A Comparison Between Different Skin and Wellbore Storage Type Curves for Early-Time Transient Analysis," paper SPE 8205 presented at the 1979 SPE Annual Technical Conference and Exhibition, Las Vegas, Sept. 23-26.

21. Bourdet, D. P., Whittle, T. M., Douglas, A. A. and Pirard, Y. M.: "A New Set of Type Curves Simplifies Well Test Analysis," *Word Oil* (May 1983) 95-106.

22. Onur, M. and Reynolds, A. C.: "A New Approach for Constructing Type Curves for Well Test Analysis," *SPE Formation Evaluation* (March 1988) 197-206.

23. Duong, A. N.: "A New Set of Type Curves for Well Test Interpretation Using the Pressure Derivative Ratio," paper SPE 16812 presented at the 1987 SPE Annual Technical Conference and Exhibition, Dallas, Sept. 27-30.

24. Gladfelter, R. E., Tracy, G. W. and Wilsey, L. E.: "Selecting Wells Which Will Respond to Production-stimulation Treatment," *Drill. and Prod. Prac.*, API (1955) 117-128.

25. Aron, G. and Scott, V. H.: "Simplified Solution for Decreasing Flow in Wells," *Proc. Am. Soc. Civ. Eng., 91*(HY 5), (1965) 1-13.

26. Winestock, A. G. and Colpitts, G. P.: "Advances in Estimating Gas Well Deliverability," *J. Can. Pet. Tech., 4* (July-Sept. 1965) 111-119.

27. Ramey, H. J. Jr.: "Non-Darcy Flow and Wellbore Storage Effects in Pressure Buildup and Drawdown of Gas Wells," *J. Pet. Tech.* (Feb. 1965) 223-233.

28. Ramey, H. J. Jr.: "Verification of the Gladfelter-Tracy-Wilsey Concept For Wellbore Storage-Dominated Transient Pressures During Production," *J. Can. Pet. Tech., 15* (April-June 1976) 84-85.

29. Cooper, H. H. Jr. and Jacob, C. E.: "A Generalized Graphical Method for Evaluating Formation Constants and Summarizing Well-Field History," *Trans. AGU, 27*(4), (1946) 526-534.

30. Odeh, A. S. and Jones, L. G.: "Pressure Drawdown Analysis, Variable Rate Case," *Trans. AIME, 234* (1965) 960-964.

31. Stewart, G., Wittmann, M. J. and Meunier, D.: "Afterflow Measurement and Deconvolution in Well Test Analysis," paper SPE 12174 presented at the 1983 SPE Annual Technical Conference and Exhibition, San Francisco, Oct. 5-8.

32. Black, W. M.: "A Review of Drill-Stem Testing Techniques and Analysis," *J. Pet. Tech.* (June 1956) 21-30.

33. van Poollen, H. K.: "Status of Drill-Stem Testing Techniques and Analysis," *J. Pet. Tech.* (April 1961) 333-339.

34. McAlister, J. A., Nutter, B. P. and Lebourg, M.: "A New System of Tools for Better Control and Interpretation Of Drill-Stem Tests," *J. Pet. Tech.* (Feb. 1965) 207-214.

35. Matthews, C. S. and Russel, D. G.: *Pressure Buildup and Flow Tests in Wells,* Monograph Series, SPE, Dallas(1967) **1.**

36. Earlougher, R. C. Jr.: *Advances in Well Test Analysis,* Monograph Series, SPE, Dallas(1977) **5.**

37. Erdle, J. C.: "Current Drillstem Testing Practices: Design, Conduct and Interpretation," paper SPE 13182 presented at the 1984 SPE Annual Technical Conference and Exhibition, Houston, Sept. 16-19.

38. Horner, D. R.: "Pressure Build-Up in Wells," *Reprint Series*, SPE, Dallas(1967) 9, 25-43.

39. Odeh, A. S. and Selig, F.: "Pressure Build-Up Analysis, Variable Rate Case," *J. Pet. Tech.* (July 1963) 790-794.

40. Dolan, J. P., Einarsen, Charles A. and Hill, G. A.: "Special Applications of Drill-Stem Test Pressure Data," *Trans. AIME, 210* (1957) 318-324.

41. Streltsova, T. D.: *Well Testing in Heterogeneous Formations,* John Wiley & Sons, New York (1988) Chapter 4.

42. Odeh, A. S. and Nabor, G. W.: "The Effect of Production History on Determination Of Formation Characteristics From Flow Tests," *Reprint Series*, SPE, Dallas(1967) 9, 167-174.

43. Soliman, M. Y.: "New Technique for Analysis of Variable Rate or Slug Test," paper SPE 10083 presented at the 1981 SPE Annual Technical Conference and Exhibition, San Antonio, Oct. 5-7.

44. Correa, A. C. and Ramey, H. J. Jr.: "A Method for Pressure Buildup Analysis of Drillstem Tests," paper SPE 16802 presented at the 1987 SPE Annual Technical Conference and Exhibition, Dallas, Sept. 27-30.

45. Soliman, M. Y.: "Analysis of Buildup Tests With Short Producing Time," *SPE Formation Evaluation* (Aug. 1986) 363-371.

46. Churchill, R. V.: *Operational Mathematics,* third edition, Mc Graw Hill, New York (1972) 247-249.

47. Jargon, J. R. and van Poollen, H. K.: "Unit Response Function From Varying-Rate Data," *Trans. AIME, 234* (1965) 965-969.

48. Pascal, H. and Quillian, R. G.: "New Method for Predicting Deliverability From Variable-Rate Drawdown Data," paper SPE 7932 presented at the 1979 SPE Symposium on Low-Permeability Gas Reservoirs, Denver, May 20-22.

49. Bostic, J. N., Agarwal, R. G. and Carter, R. D.:"Combined Analysis of Post-fracturing Performance and Pressure Buildup Data for Evaluating an MHF Gas Well," *J. Pet. Tech.* (Oct. 1980) 1711-1719.

50. Kuĉuk, F. and Ayestaran, L.: "Analysis of Simultaneously Measured Pressure and Sandface Flow Rate in Transient Well Testing," *J. Pet. Tech.* (Feb. 1985) 323-334.

51. Thompson, L. G., Jones, J. R. and Reynolds, A. C.: "Analysis of Pressure Buildup Data Influenced by Wellbore Phase Redistribution," *SPE Formation Evaluation* (October 1986) 435-452.

52. Thompson, L. G. and Reynolds, A. C.: "Analysis of Variable-Rate Well-Test Pressure Data Using Duhamel's Principle," *SPE Formation Evaluation* (October 1986) 453-469.

53. Roumboutsos, A. and Stewart, G.: "A Direct Deconvolution or Convolution Algorithm for Well Test Analysis," paper SPE 18157 presented at the 1988 SPE Annual Technical Conference and Exhibition, Houston, Oct. 2-5.

54. Stehfest, H.: "Algorithm 368, Numerical Inversion of Laplace Transforms," *Comm. of the ACM, 13(1),* (1970) 47-49.

55. van Everdingen, A. F. and Hurst, W.: "The Application of the Laplace Transformation to Flow Problems in Reservoirs," *Trans. AIME, 186* (1949) 305-324.

56. Papadopulos, I. S. and Cooper, H. H. Jr.: "Drawdown in a Well of Large Diameter," *Water Resour. Res., 3*(1), (1967) 241-244.

57. Cinco-Ley, H. *et al.:* "Analysis of Pressure Tests Through the Use of Instantaneous Source Response Concepts," paper SPE 15476 presented at the 1986 SPE Annual Technical Conference and Exhibition, New Orleans, Oct. 5-8.

58. Ayoub, J. A., Bourdet, D. P. and Chauvel, Y. L.: "Impulse Testing," *SPE Formation Evaluation* (Sept. 1988) 534-546.

59. Thompson, L. G.: *Analysis of Variable Rate Pressure Data Using Duhamel's Principle,* PhD dissertation, U. of Tulsa, Tulsa, OK, (1985).

60. Tariq, S. M. and Ayestaran, L.: "Analyses and Applications of Pressure, Flowrate, and Temperature Measurements During a Perforating Run," pa-

per SPE 15475 presented at the 1986 SPE Annual Technical Conference and Exhibition, New Orleans, Oct. 5-8.

61. Simmons, J. F.:"Interpretation of Underbalanced Surge Pressure Data by Rate-Time Convolution," paper SPE 15477 presented at the 1986 SPE Annual Technical Conference and Exhibition, New Orleans, Oct. 5-8.
62. Burden, R. S., Faires, J. D. and Reynolds, A. C.: *Numerical Analysis,* second edition, Prindle, Weber and Schmidt, Boston (1981) Chapter 4.
63. Waller, H. N. Jr. and Krase, L. D.: "A North Sea Application of Slug Testing for Quick Reservoir Analysis,"paper SPE 15480 presented at the 1986 SPE Annual Technical Conference and Exhibition, New Orleans, Oct. 5-8.
64. Theis, C. V.: "The Relationship Between the Lowering of the Piezometric Surface and the Rate and Duration of Discharge of a Well Using Ground-Water Storage," *Reprint Series*, SPE, Dallas(1980) **14**, 27-32.
65. Press, W. H., Flannery, B. P., Teukolsky, S. A. and Vetterling, W. T.: *Numerical Recipes,* Cambridge University Press, New York (1986) Chapter 4.
66. Ramey, H. J. Jr.: "Practical Use of Modern Well Test Analysis," paper SPE 5878 presented at the 1976 California Regional Meeting, Long Beach, April 8-9.
67. Agarwal, R.G.: " A New Method to Account for Producing Time Effects when Drawdown Type Curves Are Used to Analyze Pressure Buildup and Other Test Data," paper SPE 9289 presented at the 1980 SPE Annual Technical Conference and Exhibition, Dallas, Sept. 21-24.
68. Kazemi, H.: "Damage Ratio from Drill-Stem Tests With Variable Back Pressure," paper SPE 1458 presented at the 1966 California Regional Meeting, Santa Barbara, Nov. 17-18.
69. Maier, L. F.: "Recent Developments in the Interpretation and Application of DST Data," *J. Pet. Tech.* (Nov. 1962) 1213-1222.
70. Bourdet, D., Ayoub, J. A., and Pirard, Y. M.: "Use of Pressure Derivative in Well Test Interpretation," paper SPE 12777 presented at the 1984 California Regional Meeting, Long Beach, April 11-13.

71. Guillot, A. Y. and Horne, R. N.: "Using Simultaneous Downhole Flow-Rate and Pressure Measurements to Improve Analysis of Well Tests," *SPE Formation Evaluation* (March 1986) 217-226.

APPENDIX A
GENERAL SLUG TEST SOLUTION

Here, a general relationship between the slug test dimensionless pressure solution and the equivalent constant surface rate dimensionless solution is derived. The slug test pressure solution for any well/reservoir system can be written in terms of the pressure solution for constant sandface production by using Duhamel's formula, that is,

$$p_D(t_D, r_D, C_D, s) = \int_0^{t_D} q_D(\tau) \frac{\partial p^*_{cD}}{\partial t_D}(t_D - \tau, r_D) d\tau, \qquad (A-1)$$

which is Eq. 2.2.18 in Chapter II. Applying Laplace transforms to Eq. A-1, we obtain

$$\bar{p}_D(u, r_D) = u\bar{q}_D(u)\bar{p}^*_{cD}(u, r_D), \qquad (A-2)$$

where $\bar{p}_D$ denotes the slug test solution in Laplace space, $\bar{p}^*_{cD}$ refers to the Laplace transform of the constant sandface rate dimensionless pressure solution, and u represents the Laplace variable. Note that we used the fact that

$$p^*_{cD}(0, r_D) = 0 \qquad (A-3)$$

in the derivation of Eq. A-2.

Similarly, the wellbore version of Eq. A-2 is given by

$$\bar{p}_{wD}(u) = u\bar{q}_D(u)\bar{p}^*_{wcD}(u). \qquad (A-4)$$

The Laplace transform of the slug test boundary condition, Eq. 2.2.19, is given by

$$\bar{q}_D(u) = [1 - u\bar{p}_{wD}(u)]C_D. \qquad (A-5)$$

Using Eq. A-5 in Eqs. A-2 and A-4, gives, respectively,

$$\bar{p}_D(u, r_D) = [1 - u\bar{p}_{wD}(u)]uC_D\bar{p}^*_{cD}(u, r_D) \qquad (A-6)$$

and

$$\bar{p}_{wD}(u) = [1 - u\bar{p}_{wD}(u)]uC_D\bar{p}^*_{wcD}(u). \qquad (A-7)$$

Solving Eq. A-7 for $\bar{p}_{wD}$ gives

$$\bar{p}_{wD}(u) = uC_D\left[\frac{\bar{p}^*_{wcD}(u)}{1 + u^2C_D\bar{p}^*_{wcD}(u)}\right]. \qquad (A-8)$$

Eq. A-8 relates the wellbore slug test solution to the constant sandface rate dimensionless pressure solution. A more general result can be obtained by using Eq. A-8 in Eq. A-6, which gives

$$\bar{p}_D(u, r_D) = uC_D\left[\frac{\bar{p}^*_{cD}(u, r_D)}{1 + u^2C_D\bar{p}^*_{wcD}(u)}\right]. \qquad (A-9)$$

The general constant rate wellbore storage and skin solution can be obtained by following a similar procedure. Starting from Duhamel's formula, Eq. 2.2.21, the application of the Laplace transform gives

$$\bar{p}_{cD}(u, r_D) = u\bar{q}_{cD}(u)\bar{p}^*_{cD}(u, r_D), \qquad (A-10)$$

which applied at the wellbore gives

$$\bar{p}_{wcD}(u) = u\bar{q}_{cD}(u)\bar{p}^*_{wcD}(u). \qquad (A-11)$$

The Laplace transform of the constant rate boundary condition, Eq. 2.2.22, is given by

$$\bar{q}_{cD}(u) = \frac{1}{u}[1 - u^2C_D\bar{p}_{wcD}(u)]. \qquad (A-12)$$

Using Eq. A-12 in Eqs. A-10 and A-11, we obtain, respectively,

$$\bar{p}_{cD}(u, r_D) = [1 - u^2C_D\bar{p}_{wcD}(u)]\bar{p}^*_{cD}(u, r_D) \qquad (A-13)$$

and

$$\bar{p}_{wcD}(u) = \frac{\bar{p}^*_{wcD}(u)}{1 + u^2C_D\bar{p}^*_{wcD}(u)}. \qquad (A-14)$$

Using Eq. (A-14) in Eq. (A-13), gives

$$\bar{p}_{cD}(u, r_D) = \frac{\bar{p}^*_{cD}(u, r_D)}{1 + u^2C_D\bar{p}^*_{wcD}(u)}, \qquad (A-15)$$

which relates the constant surface and constant sandface rate pressure solutions at any position r_D in the reservoir.

By combining Eqs. A-9 and A-15, the constant sandface solution p^*_{cD} can be eliminated from the equations to obtain the following result:

$$\bar{p}_D = uC_D\bar{p}_{cD}. \qquad (A-16)$$

Note that Eq. A-16 relates the slug test solution to the constant surface flow rate solution in Laplace space. By taking the inverse Laplace transform of both sides of Eq. A-16, we find that

$$p_D(t_D, r_D, C_D, s) = C_D\frac{\partial p_{cD}}{\partial t_D}(t_D, r_D, C_D, s), \qquad (A-17)$$

which is Eq. 2.2.24 in Chapter II. The above relationship is completely general and forms the basis of the new analysis procedure for slug test data.